Etude numérique du comportement dynamique de microparticules à membrane hyperélastique chargées de liquide et soumises à des sollicitations hémodynamiques et des contraintes vasculaires

Imane El Jirari

HESAM UNIVERSITÉ

Arts et Métiers Sciences et Technologies

ÉCOLE DOCTORALE SCIENCES ET MÉTIERS DE L'INGÉNIEUR

Laboratoire angevin de mécanique procédès et innovation - Campus d'Angers

THÈSE

présentée par : **EL JIRARI Imane**

soutenue le : **07 juillet 2022**

pour obtenir le grade de : **Docteur d'HESAM Université**

préparée à : **École Nationale Supérieure d'Arts et Métiers**

Discipline : **Mécanique, génie mécanique, génie civil**
Spécialité : **Mécanique**

Computational study of dynamical behaviour of liquid-filled hyperelastic microparticles flowing under haemodynamical and vascular constraints

THÈSE dirigée par :
Monsieur AMMAR Amine

et co-encadrée par :
Monsieur EL BAROUDI Adil

Jury

M. Zoubeir LAFHAJ	Professeur des Universités, UMR 9013, Ecole Centrale de Lille	Président
M. Cyrille ALLERY	Professeur des Universités, UMR 7356 CNRS, Université de La Rochelle	Rapporteur
M. Lalaonirina RAKOTOMANANA-RAVELONARIVO	Professeur des Universités, UMR 6625 CNRS, Université de Rennes 1	Rapporteur
Mme. Christelle METIVIER	Maitresse de conférence-HDR, UMR 7563, Université de Lorraine	Examinatrice

THÈSE

À mes parents Rachida et Jamal

À ma défunte grande-mère Rabha

Résumé

Cette thèse est dédiée à l'étude du comportement dynamique de microparticules à membrane hyperélastique chargées d'une substance liquide et soumises à des contraintes hémodynamiques et vasculaires. L'étude qui est basée sur une modélisation numérique suffisamment fidèle aux conditions physiologiques a pour but de combler le manque d'études sur la réponse mécanique de microparticules en écoulement dans des vaisseaux sanguins distensibles (hyperélastiques), en particulier dans une artériole et une artère coronaire. Les travaux menés dans le cadre de cette thèse ont contribué à l'étude de l'influence de la distensibilité vasculaire sur le mécanisme de migration latérale dans une artériole ainsi que sur le partitionnement de microparticules soumises à un écoulement pulsatile au niveau d'une bifurcation coronarienne. Par ailleurs, les résultats obtenus sont fort susceptibles d'aider à améliorer les performances des microparticules à usage thérapeutique, notamment en apportant des éléments de réponses quant aux conditions favorisant les complications liées à un tel usage. Le problème instationnaire d'interaction fluide-structure est résolu suivant le formalisme arbitrairement lagrangien eulérien.

Mots-clés : Microparticule, interaction fluide-structure, paroi vasculaire, écoulement sanguin, hyperélasticité, modélisation numérique, microfluidique.

Abstract

In this thesis the dynamical behaviour of microparticles made of a thin hyperelastic membrane enclosing a liquid medium and subjected to haemodynamical solicitations is studied by means of a physiologically (and reasonably) realistic numerical modelling. The aim is to fill the gap in studies addressing the mechanical response of microparticles flowing in distensible human blood vessels particularly in arterioles and coronary arteries. In the arteriole we have investigated the influence of an isolated and a muscle-embodied arteriolar wall on a single centred microparticle and more interestingly, on the lateral migration mechanism of a couple of microparticles. The influence of arteriolar distensibility on particle-particle interaction during the lateral migration is further studied in addition to particle-wall interaction while varying the relevant nondimensional parameters namely, the ratio of the suspending fluid viscous forces to the membrane shear resistance, the viscosity ratio between internal and external fluids and the confinement. Another contribution of the present work is the appraisement of the dynamical behaviour of microparticles partitioning in the left coronary bifurcation under the action of pulsatile blood flow. The emphasis is on the prediction of the preferred branch of microparticles interacting with blood pulsatility, with contiguous microparticles and with the wobbling coronary wall depending on the initial vertical offset and on membrane shear resistance. For both considered blood vessels, the contribution of vascular wall distensibility is highlighted through comparison with rigid vascular walls. The physical quantities of interest are microparticle velocity, deformation, trajectory and elastic stored energy, to name just a few. Considering the therapeutic context, the risk of clustering, adhesion to wall and premature burst are assessed. The unsteady fluid structure-interaction problem is solved within the Arbitrary Lagrangian Eulerian framework and calculations are performed using Comsol Multiphysics® based on a monolithic approach.

Keywords : Microparticle, fluid-structure interaction, vascular wall, blood flow, numerical modelling, microfluidics, lateral migration, hyperelasticity, targeted drug delivery, ALE method.

Scientific communication

Published papers

[A01] El Jirari I, El Baroudi A, Ammar A. 2021. Numerical investigation of the dynamical behavior of a fluid-filled microparticle suspended in human arteriole. *Journal of Biomechanical Engineering* **143**(5). (doi: 10.1115/1.4049955)

[A02] El Jirari I, El Baroudi A, Ammar A. 2021. Effect of arteriolar distensibility on the lateral migration of liquid-filled microparticles flowing in a human arteriole. *Journal of Mechanics in Medicine and Biology* **21**(8). (doi: 10.1142/S0219519421500627)

Ready for submission

[A03] El Jirari I, El Baroudi A, Ammar A. Predictive dynamical behaviour of liquid-filled microparticles partitioning in the vicinity of a coronary bifurcation under pulsatile blood flow and arterial distensibility.

Oral presentation

"Predictive behaviour of liquid-filled microparticles in the vicinity of coronary bifurcation" at the symposium on aeroelasticity, fluid-Structure interaction, and vibrations (14-15th October 2021).

Poster communication

"Lateral migration of a hyperelastic microparticle confined in human arteriole" at the 45ème congrès de la société de biomécanique (26-28th October 2020).

Contents

List of Tables

List of figures

Glossary of main symbols

$\dot{E}_i$ Internal energy time-derivative.

Q Heat flux.

$\mathbf{W}$ Mechanical work.

$\dot{e}_i$ Specific internal energy.

ρ Density.

$\boldsymbol{\sigma}$ Cauchy stress tensor.

$\mathbf{D}$ Velocity gradient.

T Temperature.

ψ Specific Helmotz free energy.

W Density of elastic strain energy.

$\mathbf{F}$ Deformation gradient tensor.

$\mathbf{P}$ First Piola-Kirchoff stress tensor.

$\mathbf{S}$ Second Piola-Kirchoff stress tensor.

$\mathbf{E}$ Lagrangian strain tensor.

J Deformation gradient determinant.

$\bar{I}_1$ First invariant of $\mathbf{C}$.

$\bar{I}_2$ Second invariant of $\mathbf{C}$.

$\mathbf{C}$ Right Cauchy-Green deformation tensor.

C_{ij} Material parameters.

D_i Material parameters.

α_i Material parameters.

λ_m Chain locking stretch.

J_m Stretchering limiting value.

C Area compressibility modulus.

G_s Surface shear modulus.

h Membrane thickness.

R Microparticle radius.

E Young modulus.

G Shear modulus.

K Bulk modulus.

E_s Surface shear modulus.

K_s Surface bulk modulus.

ν_s Poisson ratio.

κ_b Bending stiffness.

$\tilde{\kappa}_b$ nondimensional bending stiffness.

τ Reduced volume.

H Enthalpy.

p pressure.

Re Reynolds number.

α Womersley number.

ω Angular frequency.

R_X Material domain.

R_x Spatial domain.

$\hat{R}_\chi$ Referential domain.

χ Referential coordinates.

x Spatial coordinates.

X Material coordinates.

Φ Application for mapping between the spatial domain and the referential domain.

Ψ Application for mapping between the referential domain and the material domain.

t Time.

t_f Final time.

$\hat{\mathbf{v}}_m$ Mesh velocity.

$\mathbf{c}$ Convective velocity.

$\boldsymbol{\omega}$ Referential velocity.

$\mathbf{b}$ Specific body force vector.

η Dynamic viscosity.

λ Damping factor.

Introduction

Context

The application of mechanical engineering and physics concepts to medicine and biology has gained a growing interest given the issues at stake. Examples include targeted drug delivery and biological cell manipulation and characterisation. These examples are deliberately given since both involve artificial or biological microparticles flowing in a constrained environment and subjected to hydrodynamical forces. The definition of microparticles is herein provided via defining microencapsulation.

The latter consists in coating an active substance using a thin membrane by means of procedures that could be mechanical (e.g. co-extrusion[1]), physio-chemical (e.g. ionotropic gelation [2]) or chemical (e.g. interfacial cross-linking polymerization [3]). Depending on their size, the resulting spherical structures are called nanoparticles or microparticles. The membrane is made of a network of cross-linked [1] polymer chains (e.g. polydimethylsiloxane, poly-L-lysine, alginate, polyacrylates, polylactic-coglycolic acid), protein chains (e.g. human serum albumin HSA, ovalbumin) or lipid molecules. Microparticles made of lipid membrane are called vesicles and the ones made of polymer and/or proteins are referred to as capsules.

Nano/microparticles are widely used in many industrial fields like in food industry as antibacterial compounds, in pharmaceutical as therapeutic vectors and in cosmetics as cleansing micelles. Advantages include active substance preventing from inactivation during manufacturing or storage and the controlled substance release in a targeted environment. The enclosed substance is bound to be released either by membrane rupture (triggered by a predetermined condition like temperature or pressure threshold) or by diffusing through pores when the membrane is of porous nature. A promis-

[1] Cross-linking refers to the insertion of bonds to link polymer or protein chains.

ing application of nano/microparticles in the pharmaceutical field is the targeted drug delivery. It is a non-invasive treatment based on direct injection of drug-loaded nano/microparticles called therapeutic vectors in blood circulation. Once injected intra-arterialy/venously, therapeutic vectors move under the action of blood flow to reach a specific target. Then, the coated drug is released either by membrane bursting or via the pores of the membrane. Examples of prominent targeted treatments are tumours, diabetes [4] and heart attack [5]. The chemoembolization is a local treatment of malignant tumours employed by physicians to counter chemotherapy or other invasive treatments. During the procedure, therapeutic vectors containing anticancerous substance like irinotecan or doxorubicin are intra-arterially injected via a micro-catheter. The procedure is ray-guided to monitor the path of injected therapeutic vectors [6]. The main therapeutic advantages of chemoembolization are a maximized concentration of tumour-absorbed drug and a reduced toxicity to healthy tissues as well as a reduced incidence of systemic side effects [7]. Targeted drug delivery is biologically-inspired, viz. by the mechanism of endocytosis-exocytosis and the red blood cell RBC. The endocytosis is the immunological process by which a cell uses its membrane to engulf and surround particles of interest in the extracellular fluid environment. The formed vesicle (of radius $0.5-5$ μm) migrates toward the core of the cell to be destructed. The vesicular transport in the opposite direction is known as exocytosis during which the secretory vesicle releases proteins or debris in the extracellular fluid environment. Concerning the RBC, it is a natural encapsulated system (a thin deformable membrane enclosing an aqueous haemoglobin solution) whose main role is oxygen delivery.

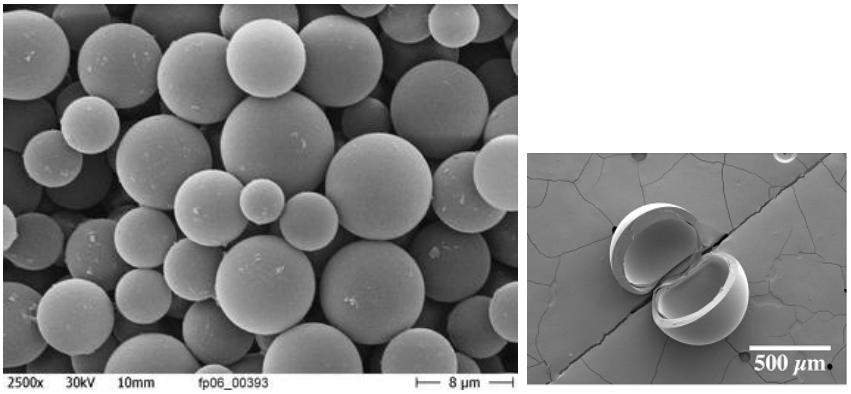

Figure 1: Microparticles image [2]produced by scanning electron microscopy, left, and solid membrane rupture and liberation of an aqueous inner core [3]

[3]Image from www.chemeurope.com
[3]Image provided by University of Illinois at Urbana-Champaign.

Objective

The targeted drug delivery techniques are employed with good therapeutic outcomes but still require a continuous monitoring for rapid care in the case of complications like clustering and premature or tardive membrane burst that pose a serious health issues [4]. Further studies are required to optimize the procedure, to extend it to other affected zones, to remedy the contraindications and to shed light on the mechanisms behind the commonly encountered complications or at least on the conditions that favour their occurrence. To achieve this, it is necessary to include haemorheological and haemodynamical characteristics. The best choice would certainly be an *in vivo* approach, but it is discarded by the scientific community due to evident ethical problems. An alternative is to mimic physiological conditions by applying an *in vitro* approach. However, arterial wall biophysical properties and geometrical characteristics of the vascular network like tapering, tortuosity and bifurcations are very difficult or even impossible to reproduce experimentally. It addition to this, such approach is costly and requires important material and human resources. The *in silico* approach based on numerical modelling and simulation permits to overcome the aforementioned limitations, it is employed as an alternative or an auxiliary approach in biophysics and biomechanical engineering. The *in silico* studies rest on two pillars for an accurate representation of the complex physical phenomena in human circulatory system: the robustness and the "well-posedness". It might be a predictive tool of dynamical behaviour of therapeutic vectors, pharmacokinetics (i.e. drug profile and concentration) and to understand the ambiguous mechanisms behind complications of targeted drug treatments. Furthermore, a parametric numerical modelling allows scientists and engineers to time-efficiently assess the role of a group of parameters on the evolution of a wide range of physical quantities.

The aim of the present work is to investigate the dynamical behaviour of microparticles made of a deformable protein membrane and enclosing a liquid core in their interaction with blood flow and vascular walls. Physical quantities of interest include deformation, velocity and trajectories. Blood vessels we are interested in are an arteriole and a coronary artery, physiological conditions therein are respected to the extent that information are available is literature. The dynamical behaviour of microparticles in flow was extensively studied while excluding the contribution on the confining vascular walls on the overall mechanical response of microparticles. To the best of our knowledge, the

[4] A comprehensive review of encountered complications in chemoembolization is found in [8].

few studies investigating microparticles flowing in blood vessels considered capillaries (microvessels characterized by a thin rigid wall) motivated by a convenient confrontation with experimental analysis that is made by mimicking the capillary by a rigid microchannel. We have consequently made a point of including the contribution of thicker and distensible vascular walls. We have examined among others, the mechanism of lateral migration and the partitioning at a bifurcation in the presence of distensible vascular walls. Furthermore, the particle-particle interaction is studied in a cell-train while assessing the risk occurrence of clustering, adhesion to walls and premature membrane rupture. As the particle-particle interaction is studied in literature while considering "flocks" of microparticles, we have accordingly limited the interaction to three microparticles to fill in the missing studies. The fluid-structure interaction problem is solved using the Arbitrary Lagrangian-Eulerian method in Comsol Multiphysics ® based on a finite element analysis.

The manuscript is organised as following :

- Chapter 1: The first chapter is dedicated to soft membrane mechanical properties and the hyper-elastic constitutive laws describing their mechanical response to applied stresses. Measurement techniques of membrane elastic properties are briefly reviewed as well as the extracted moduli. We are interested in red blood cells and artificial microparticles because of their common physical properties and dynamical similarities. Some aspects of dynamical behaviour of microparticles subjected to hydrodynamical forces are given. Centred and off-centred microparticles are presented distinctly due to the relevance of the initial position on the dynamical behaviour during microparticles course in wall-bounded flows;

- Chapter 2: The second chapter deals with dynamical and rheological properties of blood (haemodynamic and hemorheology) and mechanical properties of vascular walls focusing on arteriolar walls and coronary walls;

- Chapter 3: In this last chapter, the conducted works within the thesis are exposed. The chapter opens by presenting the numerical method employed to solve the strongly-coupled fluid-structure interaction problem. It follows by clarifying the applied assumptions. The chapter closes by thesis findings presented as two published research papers and a third paper ready for submission.

Chapter 1

Soft membrane mechanics

Content

1.1 Generalities on soft membrane mechanics

Membrane physical and mechanical properties are a primary determinants of microparticles response to external stresses. Biological tissues like proteins and natural and synthetic polymers are able to sustain large deformation rates without internal energy dissipation. This behaviour is described by hyperelastic constitutive laws, including non-linear stress-strain response of materials subjected to high deformation and geometrical non-linearities. The elasticity of protein and polymer cross-linked membranes is purely entropic [9, 10] which means that their elasticity arises from conformational entropy induced by external stress (i.e. change in molecules shape and dynamics). In order to store the mechanical energy induced by deformation, the chains end-to-end distance increases and the entropy is diminished. We present hereafter some relevant properties of polymer and protein membranes (solid membranes), both consist of a chain-like macromolecules connected via entanglements or cross-links.

Polymer materials are known to exhibit strain-softening behaviour under cyclic loading (Mullins effect) and strain-hardening under large strains. The first behaviour is believed to result from the viscoelastic component of polymer materials and to the alteration in the macromolecular structure [11]. Depending on the tacticity, the second behaviour arises from crystallinity or from finite chain extensibility and is found to be influenced by temperature and molecular concentration [12].

Strain-softening of proteins is shown to results from irreversible structural damage [13, 14]. Concerning strain-hardening of proteins and other biological tissues, it is found to be related to biotensegrity [1] preserve [15] and allows cells to sustain large deformation without damage. Examples comprise human collagen (type I [16] and type II [17]), fibrin [18], actin filament [19] and spectrin [20]. The strain-hardening is due to bending rigidity [21] that limits sliding. With that being said, the strain-hardening is found to strongly depend on the applied stress and on the concentration of protein and cross linker *i*) it has been shown that actin filament network of plasma (biological cell membrane) is strain-hardening under moderate strain amplitudes and strain-softening under high strain amplitudes [21] *ii*) in [10] strain-hardening of bundled and cross-linked actin filaments is found to depend on concentrations of protein and cross linker and to vanish below a concentration threshold.

[1] The ability of some biostructures to auto-stabilize by balancing compression and tension forces.

1.1.1 Overview on hyperelatsic laws

Constitutive laws describing the response of hyperelastic solid are based on phenomenological background (e.g Mooney-Rivlin, Ogden, Gent), on experimental background (e.g. Hart-Smith) or on physical background (e.g. neo-Hookean, Aruda-Boyce). Phenomenological laws are based on mathematical development of the elastic-strain energy density while physically-motivated laws are based on a micro-mechanistically approach. Let $\dot{E}_i$ denotes the internal energy time-derivative, Q the heat flux and W the mechanical work per unit volume. The first law of thermodynamics gives :

$$\dot{E}_i = Q + \dot{\mathrm{W}} \tag{1.1}$$

In terms of specific internal energy $\dot{e}_i$ we write:

$$\rho(\dot{e}_i - Q) = \boldsymbol{\sigma} : \mathbf{D} \tag{1.2}$$

where ρ is density. The term on the right yielding the Cauchy stress tensor $\boldsymbol{\sigma}$ and the velocity gradient $\mathbf{D}$ corresponds to the stress power. Bearing in mind the second principle of thermodynamics relating entropy time-derivative $\dot{S}$ and temperature T to heat flux ($\dot{S} \geq Q/T$), we obtain the Clausius–Duhem inequality:

$$\rho(\dot{e} - T\dot{s}) \leq \boldsymbol{\sigma} : \mathbf{D} \tag{1.3}$$

where $\dot{s}$ is the specific entropy time-derivative. An isothermal reversible elastic transformation gives the equality:

$$\rho(\dot{e} - T\dot{s}) = \boldsymbol{\sigma} : \mathbf{D} \tag{1.4}$$

The elastic entropy is the special case where stress power decreases the quantity $|T\dot{s}|$. The specific Helmholtz free energy ψ is defined as:

$$\psi = e - Ts \tag{1.5}$$

$$\rho\dot{\psi} = \boldsymbol{\sigma} : \mathbf{D} \tag{1.6}$$

Let $W{=}\rho\psi$ denotes the strain energy density function. A hyperelastic solid is defined as a material whose specific free energy depends only on strain:

$$W = W(\mathbf{F}) \tag{1.7}$$

in which $\mathbf{F}$ is the deformation gradient tensor. Different expressions of stress tensor are obtained by partial differentiation of W, thus defining the first Piola-Kirchoff stress tensor $\mathbf{P}$, the second Piola-Kirchoff stress tensor $\mathbf{S}$ and $\boldsymbol{\sigma}$

$$\mathbf{P} = \frac{\partial W}{\partial \mathbf{F}} \quad , \quad \mathbf{S} = \frac{\partial W}{\partial \mathbf{E}} \quad , \quad \boldsymbol{\sigma} = J^{-1}\frac{\partial W}{\partial \mathbf{F}}\mathbf{F}^T \tag{1.8}$$

where $\mathbf{E}$ is the Lagrangian strain tensor and $J{=}\det\mathbf{F}$. For an isotropic hyperelastic material, W is function of $\bar{I}_1$ and $\bar{I}_2$ corresponding to the first and the second invariant of the right Cauchy-Green tensor $\mathbf{C}{=}\mathbf{F}\mathbf{F}^T$

$$W = W(\mathbf{C}) = W(\bar{I}_1, \bar{I}_2, \bar{I}_3) = W(\bar{I}_1, \bar{I}_2, J) \tag{1.9}$$

The generalized polynomial form of energy density function is given by:

$$W = \sum_{i,j=0}^{n} C_{ij}(\bar{I}_1 - 3)^i(\bar{I}_2 - 3)^j + \sum_{i=1}^{n}\frac{1}{D_i}(J-1)^{2i} \tag{1.10}$$

in which C_{ij} and D_i are material parameters. From a physical point of view W is a measure of the energy stored in the solid during the deformation and released as the initial non-deformed shape is recovered. From (1.10), n-order constitutive laws with a phenomenological or a physical background are established for appropriate constants. We concisely present the most commonly used hyperelastic law to model soft membrane mechanical response to applied external stresses including strain-softening laws (e.g. Mooney-Rivlin and neo-hookean) and strain-hardening laws (e.g. Arruda-Boyce and Gent).

Mooney-Rivlin MR [22, 23] . The first order MR law is obtained by setting parameters C_{ij} with $i = j$ to 0, the obtained form corresponds to the 2-parameters MR law:

$$W^{\mathrm{MR}} = C_{10}(\bar{I}_1 - 3) + C_{01}(\bar{I}_2 - 3) + \frac{1}{D_1}(J-1)^2 \tag{1.11}$$

Material constants are determined by curve-fitting of uni/multiaxial extension or shear loading results. The choice of the test depends on the number of parameters to fit. The 3, 5 and 9-parameter MR law are obtained with higher n-order (n=3). It is admitted that the MR law accurately describes behaviour of hyperelastic solids for strains about 100–200% [24].

Neo-Hookean NH[25]. The NH law is the special case of MR law where $C_{01} = 0$:

$$W^{\mathrm{NH}} = C_{10}(\bar{I}_1 - 3) + \frac{1}{D_1}(J-1)^2 \tag{1.12}$$

The NH law was originally obtained by applying the "molecular chain theory" to the derivation of W. It is based on a Gaussian end-to-end distance distribution assumption (i.e. the freely joined chain model where the units are randomly directed and randomly rotate) and is seen as a Gaussian distribution that gives an estimation of the number of conformation. The freely-rotating chain model is more realistic since the units rotate with determined angles limiting the chain extensibility and the possible conformations. The end-to-end length distribution is non-Gaussian and the number of possible conformations is limited. The Gaussian model accurately describes the stress-stretch up to low stretches but for moderate to high stretches the non-Gaussian character get more pronounced (see [26, 27]) and is captured by strain-hardening laws.

Ogden [28]. Higher strains (700%) could be handled by the Ogden law expressed in terms of the principal stretch ratio $\lambda_{i=1,2,3}$ as:

$$W^{\mathrm{OG}} = \sum_{i=1}^{n} \frac{G_i}{2}(\lambda_1^{\alpha_i} + \lambda_2^{\alpha_i} + \lambda_3^{\alpha_i} - 3) + \frac{1}{D_1}(J-1)^2 \tag{1.13}$$

where α_i are material constants empirically determined. The stability requires the fulfilment of the condition $G_i\alpha_i > 0$. For small strains $G = \sum_{i=1}^{n} G_i\alpha_i/2$. Ogden law is equivalent the the NH law when n=1 and α_1=2 and to the 2-parameters MR law for n=2, α_1=2 and α_2=-2. Depending on parameters n and α_i, Ogden law could be either strain-softening or strain-hardening [29].

Arruda-Boyce [30]. The Arruda-Boyce law (8-chain model) is based on stretching an eight-chain polymeric network system in a cube. This model accounts of chain extensibility limit by introducing the chain locking stretch λ_m:

$$W^{\mathrm{AB}} = C_1 \sum_{i=1}^{5} \frac{\alpha_i}{{\lambda_m}^{2i-2}} ({\bar{I}_1}^i - 3^i) + \frac{1}{D_1}(\frac{J^2-1}{2} - lnJ) \tag{1.14}$$

Gent [27]. Gent law could be seen as an extension of the NH law in such a way it takes into account the maximum chain extensibility and thus, the non-Gaussian character of end-to-end distribution. For this purpose, the stretchering limiting value J_m of the quantity $\bar{I}_1 - 3$ (J_m is of the order of 10^2) is introduced:

$$W^{\mathrm{GT}} = -\frac{G}{2} J_m ln(1 - \frac{\bar{I}_1 - 3}{J_m}) + \frac{1}{D_1}(\frac{J^2-1}{2} - lnJ) \tag{1.15}$$

With assuming an infinite chain extensibility (i.e. $J_m \to \infty$) the Gent model is equivalent to the NH law.

STZC[2] law [31]. The bidimensional STZC law was first postulated to describe the sphering [3] of the RBC. In contrast to the aforementioned laws of tridimensional origin where the compressibility is implicitly embodied in law formulation, the STZC law adds independently the area compressibility through the areal stiffness (or area compressibility modulus) C as:

$$W^{\mathrm{STZC}} = \frac{G_s}{4}(\frac{1}{2} I_{1,SK}^2 + 2I_{1,SK} - 2I_{2,SK} + C I_{2,SK}^2) \quad ; \quad C > -1.2 \tag{1.16}$$

in which the surface shear modulus G_s satisfies G_s=$(1 + 2C)$. This law deals with very thin membranes for which the continuum assumption is no more satisfied in the transverse direction. The strain-hardening character of the STZC law becomes increasingly marked as C incrases ($C >> 1$ for the RBC). The STZC law is consistent with the "fluid mosaic model" for cellular membranes and is in excellent agreement with experimental results of uniaxial tensile test performed on RBC membrane (see [32]). In this same paper, authors demonstrate that the 2-parameters MR law is not suitable to properly capture the mechanical response of such membranes.

[2]The STZC law was developed conjointly by Skalak, Tozeren, Zarda and Chien but is often referenced in literature as Skalak law.

[3]RBCs swell when immersed in fluid whose osmolarity is less than that of the inner liquid.

1.1.2 Mechanical properties of soft membranes

1.1.2.1 Elastic properties of capsules

Membrane of capsules are made of a network of cross-linked molecules of polymers (e.g. polydimethylsiloxane, poly-L-lysine, alginate, polyacrylates, polylactic-co-glycolic acid) or protein (e.g. HSA, ovalbumin). Physical properties of membrane are inherently determined by the manufacturing process which could be mechanical (e.g. co-extrusion), physio-chemical (e.g. ionotropic gelation) or chemical (e.g. interfacial cross-linking polymerization). The elastic proprieties of the membrane and the rheology of the internal core determine the global properties of microparticles (capsules and vesicles) and consequently their mechanical response to external applied stresses (e.g. compression, shear and tension). A direct comparison between the mechanical behaviour of microparticles made of protein or polymer is meaningless since the molecular nature is not the sole determinant of membrane elastic properties. In fact, elastic proprieties are found to depend on protein concentration [33], on polymer concentration [34], on cross-linking degree [35, 36] (the cross-linking degree and molecules concentration unequivocally increase membrane stiffness) and on microparticle size [33]. Moreover, membrane shear resistance is found to rise non-linearly with geometric properties of the microparticle (thickness h and radius R) [37]. Membrane fragility, thinness and instability make it very sensitive to forces applied by the measurement techniques thus, the intrinsic mechanical properties interfere with applied forces and gives rise to different elastic properties depending on the employed measurement technique [38, 35]. There is a general consensus that protein membranes designed for capsules are strain-softening [39, 40] and their mechanical response is accurately described by the NH law. Polymeric membrane exhibits strain-hardening under extensional or compression forces [38, 41].

Membrane elastic properties are determined by means of several techniques based on measuring microparticle deformation under a determined local or global stress and chosen on the basis of membrane size and fragility. The most popular measurements techniques of millimeter-sized particles include squeezing technique [4] [41], micropipette aspiration [5] [42], atomic force microscopy AFM [6][33], spinning-drop tensiometer [7] [35, 36] (see ref [34] for micron-sized particles) and extensional experiment

[4]Squeezing technique consists of compressing a microparticle between to parallel plates and measuring the separating distance to deduce membrane expansion modulus.

[5]Micropipette aspiration consists of applying a suction force using a small tube (micropipette) to a small portion of the membrane and to retrieve its elastic properties by measuring the aspired (pinched) length in the micropipette.

[6]AFM technique consists of assessing membrane elastic properties by measuring its resistance to indentations of a tip.

[7]Spinning drop technique was first developed for studying elastic properties of droplets and was later extended to

in a four-roll apparatus [43]. Mechanical properties of micron-sized particles are mainly extracted by microfluidic methods that were first introduced in [40]. Technically, this involves flowing microparticles in microfluidic channel of transversal dimension is comparable to microparticle diameter and in monitoring deformation, volume and velocity changes. Membrane properties are retrieved by means of inverse analysis (via numerical model) and further with choosing *ad hoc* constitutive law to fit extracted experimental profiles and to relate the stretching to tensions experienced by the membrane.

The relevant elastic moduli are the Young modulus E, the shear modulus G and the bulk modulus K. Due to the thinness of the membrane, surface moduli ($G_s = Gh$, $E_s = Eh$ and $K_s = Kh$) are often preferred. Assuming membrane incompressibility ($\nu_s \to 0.5$) we have $E_s = 3G_s$ and $K_s \to \infty$. The bidimensional incompressible form of (1.12) is given as:

$$W_s^{\mathrm{NH}} = \frac{G_s}{2}(\bar{I}_1 - 3) \tag{1.17}$$

Capsules with polymer membrane

In the squeezing experiment of millimetre-sized alginate capsule, E_s is found to jump from 6.5 N/m to 32.9 N/m as the cross-linking degree increases [35]. In this same paper and for identical capsules, the Young moduli extracted from the spinning experiment are 4 to 5 times less that those obtained by the squeezing experiment since the centrifugal forces in the spinning apparatus tend to modify the cross-linking degree. In [42], micropipette aspiration technique gives $E = 15.5$ kPa. In [38] squeezing millimetre-sized silicone membranes found the surface Young modulus to vary from 20 to 28.6 kPa (corresponding to the range of $0.14 - 0.2$ N/m), the extensional flow measurement gives larger values (37.5% larger at most). For a hydrogel polymer membrane flowing in a rectangular cross-section microchannel with two different cross-linking degrees, retrieved elastic moduli are estimated to $G = 13$ Pa, $K = 66$ Pa for the lowest cross-liking degree and to $G = 33$ Pa, $K = 79$ Pa for the highest one [44].

Capusles with protein membrane

For protein membrane (ovalbumin) flowing in a circular cross-section channel, the experimental curves fitted with NH law and STZC law ($C = 1$) gives $G_s = 0.07$ N/m but for higher flow strength,

microparticles. The technique consists of placing the microparticle of interest in a rotating tube and to measure membrane elasticity from microparticle deformation induced by the generated centrifugal forces. This technique requires the use of a microscope.

STZC law could not fit the experimental curve using a constant G_s [40]. Authors concluded that STZC law is inappropriate to describe the mechanical response of protein membrane at large deformation states. This finding together with strain-softening of protein membranes was ulteriorly confirmed in [39]. The surface shear modulus found with the same microfluidic measurement technique in [45, 46] is of the same order ($G_s \approx 0.026-0.242$ N/m). In [33], authors extend the extensional flow technique used in [38] to micron-sized capsule. They found for albumin membrane (not to confuse with ovalbumin) $G_s = 0.002 - 5$ N/m and with the AFM technique $E = 0.02 - 1$ MPa. The surface shear modulus is found to rise with a factor 2000 for a factor 3.5 in capsule radius.

Hybrid protein-polymer membrane

The compression of HSA-alginate membrane [37] with varying thicknesses gives $E = 108 - 176$ kPa. Authors surprisingly found Young modulus to rise non-linearly with increasing h, thus the thick hybrid membrane to obey an elastomeric behaviour (i.e. strain hardening). The STZC law ($C = 0$) has proved suitable to fit the experimental curves and to model the strain-hardening exhibited by HSA-alginate capsule before bursting [8] [41]. Depending on h, the extracted moduli are in the range of $K = G = 45.3 - 64.7$ kPa ($K_s = G_s = 1.6 - 4.4$ N/m). However, for SK ($C = 2$) and the NH law the membrane exhibits strain-softening. The microfluidic technique estimates the Young modulus in the range of $8 - 60$ kPa ($E_s = 0.26 - 1.8$ N/m) [48]. The bending stiffness κ_b characterizing flexural resistance is directly related membrane thickness:

$$\kappa_b = \frac{Eh^3}{12(1-\nu^2)} \tag{1.18}$$

The nondimensionnal form of κ_b is known as the inverse Föppl-von Kármán-number:

$$\tilde{\kappa}_b = \frac{h^2}{12(1-\nu^2)R^2} \tag{1.19}$$

For artificial membrane with homogeneous wall $\tilde{\kappa}_b$ is comprised between 0.00005 and 0.001 [49].

[8] The bursting would deserve a dedicated thesis. Since it is not *per se* addressed in the present work, we simply note that it is believed to results from 'the non-existence of a steady equilibrium state between elastic and viscous forces'[47] and is often preceded by membrane thinning and/or tip development.

1.1.2.2 Red blood cells and vesicles

Erythrocyte or RBC is the principal formed element of blood (about 45%). It is an anucleolus cell containing haemoglobin solution (cytoplasm) and suspended in the liquid portion of blood (plasma). The principal function of RBC is oxygen delivery. Its membrane consists of a phospholipid bilayer [9] embedded of proteins and anchored to a skeleton of spectrin filament network (see [50, 51]). The enclosed haemoglobin solution is Newtonian and incompressible. The normal shape of RBC is a biconcave disc, a special solution of the "shape equation of lipid vesicle". This peculiar shape corresponds to the minimizing of the Helfrich bending energy [52]. From a physiological point of view, the human RBC might have developed the biconcave shape to maximize its area, thus to optimize oxygen delivery in small blood vessels. It was suggested in [53] that the biconcave shape limits the rotation in large blood vessels and then the apparition of eddy currents [10]. The metastable configuration of the biconcave disc shape is the stomatocyte shape (cup-like shape) [52] (Figure 1.1). The RBC is easily deformable ($10 - 100$ pN [54]) ant its global mechanical properties are primarily determined by the phospholipid bilayer and the skeleton.

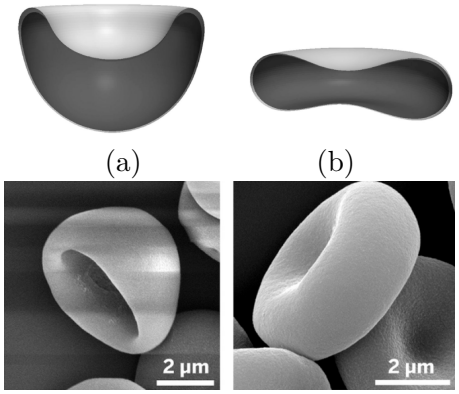

Figure 1.1: Image of a RBC showing the stomatocyte shape (a),(c) and the biconcave disc shape (b),(d). From www.cen.acs.org, credits to Bryan Kaehr.

The phospholipid bilayer behaves as a bidimensional fluid described by the biological "fluid mosaic

[9] A phospholipid bilayer is made of sequences of phospholipid molecules (two lipid tails attached to one phosphorus head) forming a mirror-reflection sheets. The head is hydrophile and the tails are hydrophobe, then the assembly is called amphiphile.

[10] The biconcave profile implies that much of the mass is distributed in the periphery. This increases the moment of inertia of the RBC and subsequently renders the RBC less prone to rotate during flow in the large blood vessels.

model" (phospholipids are free to move as a fluid molecules while the proteins are anchored). It is in the liquid crystal phase where molecules are preferentially oriented. The conferred fluidity implies that the phospholipid bilayer is devoid of shear resistance but at the same time, the resistance to area expansion is important [31] (membrane resistance to area change is significantly larger that its shear resistance (see Table 1.1). This causality was further confirmed in [55, 56]. The phospholipid bilayer is semi-permeable and has the property of selective permeability.

The skeleton is topologically organized as a hexagonal and pentagonal network of spectrin filaments. This structure is devoid of bending rigidity but shear resistant. The measured moduli are K_s^{sk}=9.7± 3.4 μN/m and G_s^{sk}=5.7± 2.3 μN/m [57]. The skeleton shear resistance is found to arise from the intrinsic shear resistance of individual spectrin filaments [57] and from the particular network topology [56]. Authors attribute the whole RBC shear resistance to the skelton [56, 58]. Thus, RBC shear resistance is skeleton-originate. The properties combined of phospholipid bilayer and spectrin skeleton make the RBC membrane shear resistant, highly deformable, resistant to area expansion and incompressible. These properties allow the RBC to sustain large strains in the microvascular system composed by capillaries without collapsing [59].

Table 1.1: Mechanical properties of red blood cells

Mechanical properties	values	Techniques
Membrane viscosity (mN.s/m)	0.036*	Micropipette [60]
Cytoplasm viscosity (Pa.s)	0.0032 ± 0.003	Rotational viscometer [61]
Bending stiffness (N.m)	2.10^{-19}	Micropipette [62]
Shear modulus (μN/m)	6.6	Micropipette [63]
Area expansion modulus (N/m)	0.353 ± 0.121	Micropipette [64]
Young modulus (kPa)	26	AFM[65]

* At 37°C. The bulk membrane viscosity is estimated to 0.022 Pa.s [66]

Vesicle membrane consists of one or more phospholipid layers that spontaneously curve is contact with aqueous medium as a consequence of the amphiphilic character of the layer: the membrane self-assembles into a spherical shape in such a way that the hydrophobic tails are not in contact with the aqueous medium. The final shape (e.g. bilayered liposome and monolayered micelle) is also determined by a geometrical packing parameter. Vesicular membrane is comparable to a RBC membrane devoid of skeleton and thus acts as a bidimensional fluid. The resting shapes of initially spherical vesicles are characterized by the reduced volume $\tau = V/V_{sphere} \leq 1$ (or reduced area) quantifying the degree of

deflating in comparison to a sphere. Examples are given in Figure 1.2 showing a stomatocyte ($\tau \approx 0.4$) an oblate shape ($\tau \approx 0.6$) and a prolate-like shape ($\tau \approx 0.8$) [67].

(a) (b) (c)

Figure 1.2: Few resting shapes of vesicles (a) stomatocyte (b) oblate-biconcave (c) prolate.

1.2 Microparticles immersed in fluid

1.2.1 In resting fluid

We are here interested in bifurcation which corresponds to the sudden topological change of a dynamic system under a very small change in a parameter called the bifurcation parameter. Bifurcation parameters of microparticle freely suspended in a fluid medium at rest are the mechanical pressure and the osmotic pressure. The mechanical pressure control consists in varying the pressure acting on the immersed microparticle whose resulting deformation corresponds to enthalpy H minimization:

$$H = E_i + pV \tag{1.20}$$

where E_i is internal energy and p pressure. As applied pressure increases, the membrane shall decreases its volume to minimize the enthalpy. At a critical pressure, initially spherical microparticles become buckled and develop a dimple (snap-through buckling). The curvature of the dimple increases by increasing pressure. For gas-filled membranes and at a second critical pressure, the opposite sides of the buckled shape are self-contacting (could not be observed for liquid-filled shells due to the liquid incompressibility).

The osmotic pressure control is limited to permeable and semi-permeable membranes. The osmolarity is defined as the total solute concentration in a solution (solvent+solute) and tonicity as the osmotic pressure gradient between two solutions separated by a semi-permeable membrane, it gives the ability of a solution to induce solvent movement from a side to another. The solvent (water),

moves from the low to the high solute concentration zone passing through the semi-permeable membrane. This water movement gives rise to an osmotic pressure. The osmotic pressure control consists in varying the solute concentration of the suspending fluid medium. The shape of the semi-permeable membrane evolves from the sphere to the rear-dimpled shape (or double-dimpled shape) but without the fully collapsed self-contacted sides observed in mechanical pressure control [68]. A well-known example of osmolarity controlled bifurcation is the RBC submerged in a non-isotonic solution: in hypnotic solution where solute concentration is higher inside the haemoglobin solution, water enters the RBC that swells and possibly bursts, in a hypertonic solution water flows out of the RBC that develops spicules on its surface. Comprehensive study on mechanical pressure control and osmotic pressure control of initially spherical microparticles is found in [68] and on osmotic pressure control in [69].

1.2.2 In flowing fluid

The global dynamical response of microparticles subjected to hydrodynamical constraints depends on several elements including suspending fluid inertia, membrane elasticity, confinement and on the rheology of the enclosed fluid. In this section, we report the most commonly observed behaviours of confined centred and off-centred microparticles subjected to a simple shear flow (1.21) and to Poiseuille flow (1.22). More detailed information related to this topic are found in research papers presented in Chapter 3.

$$v_s = \dot{\gamma} y \tag{1.21}$$

where y is ordinate and $\dot{\gamma}$ the shear rate

$$v_p = 4 v_{max} \frac{y}{H}(1 - \frac{y}{H}), \quad 0 \leq y \leq H \tag{1.22}$$

in which H is the height of the microchannel/bood vessel and v_{max} the peak velocity (at $y = H/2$)

1.2.2.1 Centred microparticles

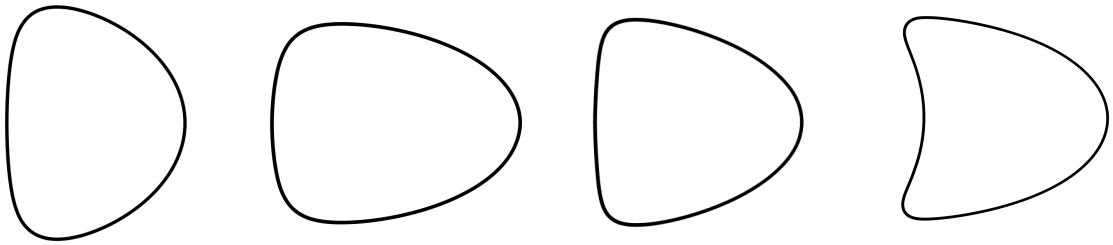

Figure 1.3: Examples of deformed shapes exhibited by an initially disc-shaped centred microparticle flowing in a wall-bounded Poiseuille flow.

The dynamical behaviour of initially spherical-shaped microparticles immersed in parabolic (Poiseuille) flow was extensively studied in literature profiting from the development of microfluidic devices and the growth of interest. Microparticle deformation remains symmetrical about the channel centreline. Under low stresses, the initial convex rear-end progressively decreases and becomes flattened. For moderate stresses, a concave dimpled rear-end is progressively developed simultaneously to a tight front. The microparticle is then bullet-like shaped. As applied stress increases the rear-end convexity further increases giving rise to a deeper dimple and a tighter front resembling a parachute shape. This shape transition schematised in Figure 1.3 was reported analytically, numerically and experimentally by several authors for artificial microparticles [70, 71, 48, 72] and for RBCs [73, 74].

At low stresses, microparticle suspended in shear flow elongates, tilts and adopts an ellipsoidal shape (Figure 1.4). The angle of inclination with respect of the channel centreline initially of 90° continuously decreases. The microparticle is likely to exhibit a tank-treading motion defined as a rotation mode where the membrane continually rotates about the interior fluid in a tank-tread manner, whence the appellation. Consequently, the interior fluid elements rotates in a purely rotational manner. At moderate to high stresses, the microparticle is more stretched and develops an upper and a lower tip aligned with streamlines [75]. As observed experimentally and numerically, wrinkles are often formed on membranes subjected to shear flow. Wrinkles relaxes with increasing membrane bending stiffness [76].

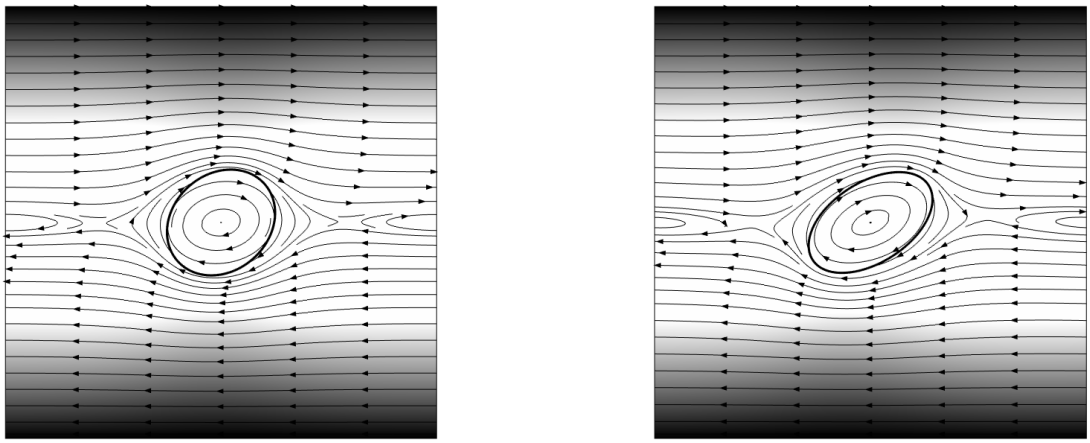

Figure 1.4: Deformation of an initially disc-shaped microparticle in shear flow at t=0.05 s (left) and t=0.27 s (right). Darker shades are higher velocity zones and lighter ones lower velocity zones.

Another mode of rotation that could be observed when a centred microparticle is subjected to a simple shear flow is the tumbling motion during which the microparticle flips about its centre of mass as illustrated in Figure 1.5. Unlike the tank-treading during which the microparticle acts as fluid, the microparticle has a rigid-body behaviour during the tumbling motion. Both rotation modes are observed either for centred and off-centred microparticles. Other peculiar motions are further reported like swinging [77] and vacillating [78].

1.2.2.2 Off-centred microparticles

Off-centred microparticles are known to drift away from the nearest wall by undergoing a lateral migration which is an intricate mechanism employed in a multitude of bio-cellular manipulation techniques like fractionation[79], filtration [80] and focusing [81]. Microparticle migration path, velocity and equilibrium positions are found to depend on several intrinsic elements and flow conditions: elastic properties of the microparticle [82, 83], inertia [84, 85], viscosity contrast between internal and external fluids [86, 87], confinement [83, 87] and on the initial microparticle position [88]. Lateral migration is a crucial mechanism in blood circulation where RBCs migrate towards the blood vessel centerline while white blood cells whose membrane is significantly stiffer undergo a sidewalls migration called margination (necessary for the immunological process of diapedesis[11]). In microcirculation, lateral

[11]Diapedesis refers to white blood cells wall margination followed by a vascular wall-crossing (extravasation) into inflammatory surrounding tissues. This process might occur for RBC in some abnormal conditions.

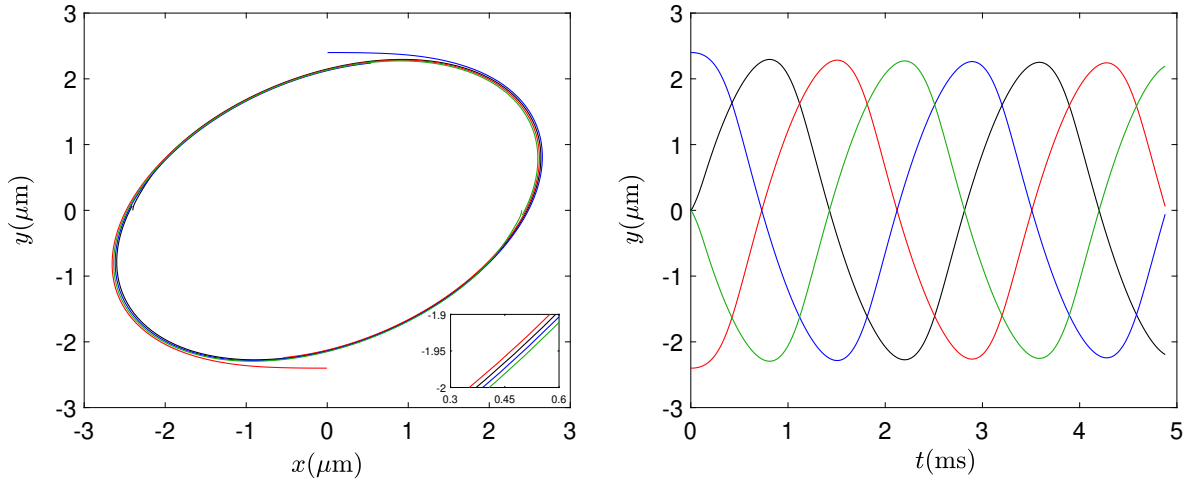

Figure 1.5: Microparticles exhibiting tumbling motion. Each colour is for a material point localized in the membrane and defined by its spatial coordinates x and y.

migration owes the creation of a lubrication cell-free layer, enabling an easier motion of the RBC is such confined zone where the blood vessel size is comparable to that of the confined RBC and even smaller. As for microparticles, RBCs might exhibit tank-treading during the lateral migration. In the absence of inertia or for a finite inertia, the lateral migration of neutrally-buoyant microparticles suspended in a wall-bounded Poiseuille flow results from an interplay of three lateral forces *i*) the wall-induced lift force (or confinement-induced force) resulting from the disturbance of flow field induced by the presence of the microparticle and its reflection at the wall *ii*) the deformability induced-lift and *iii*) the shear gradient lift force due to the curvature of undisturbed fluid velocity profile. Unlike the deformation induced lift and the wall-induced lifts forces, this force pushes the microparticle towards the nearest wall. For non-neutrally buoyant microparticle and/or for inertial flow, Rubinow-Keller lift (due to slip-rotation lift force) and Saffman lift force (due to the interaction of slip velocity and shear) are additionally involved in forces interplay.

Deformable microparticles exhibit fore-aft asymmetrical shapes which are auspicious to migration due to the pressure gradient between the fore and the aft. Unlike the bullet or the parachute shape, fore-aft asymmetrical shapes are also asymmetrical about the channel centreline. The bullet and the parachute shapes (or intermediary symmetrical shapes) are recovered after the migration stops and the microparticle reaches the centreline of the channel. A well-known fore-aft asymmetrical deformation

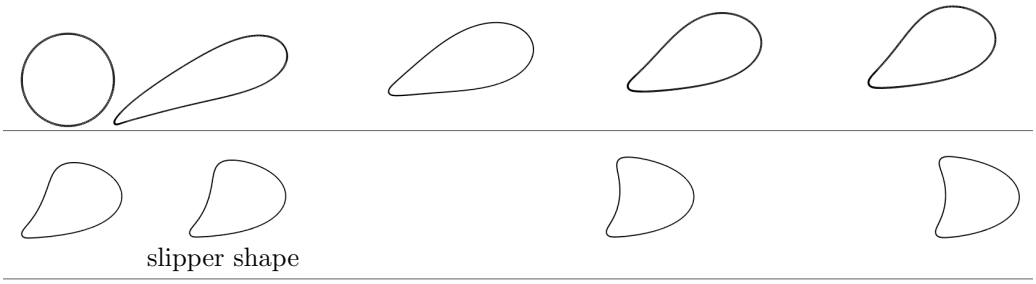

Figure 1.6: Microparticle undergoing lateral migration near a rigid wall.

is the slipper shape displayed in Figure 1.6. It results from a stability losing [89] and is reported for artificial microparticles as well as for RBCs. This shape is particularly propitious for migration and could even be accompanied with a tank-treading motion is some specific conditions, for instance below a critical ratio of external fluid viscosity to internal fluid viscosity [90]. During the process of lateral migration and beyond a shear resistance threshold, the microparticle is likely to develop the cusp-like instability (a localized highly deformed zone morphologically resembling a cusp). This instability is also observed in droplet formation. During migration the cusp (or at least the pointy end/tip) acts as an appendix tail and offers a hydrodynamical shape so that the microparticle drifts with less resistance to the flow. For drug-loaded microparticle, such instability could however be a risk of premature burst since this zone concentrates an important stress. However, at early times in the existence of the cusp, the latter tends to expand toward the wall therefore temporary decelerating the microparticle.

Chapter 2

Basic concepts of vascular physiology

Content

2.1 Arterial walls biomechanics

Blood vessels are soft tissues, like ligaments and skin. The arterial blood system is made up of muscular and elastic large arteries and arterioles while the venous system carrying deoxygenated blood is composed of large veins and venules. These two systems are connected via capillaries, a single layered microvessels with a height comparable (or less) to that of the RBC. Within the framework of the thesis, focus is on arterial blood vessels. The vascular walls are structurally and chemically different depending on the function of the vessel. Generally speaking, the arterial wall is divided into three layers: the tunica intima, tunica media and tunica adventitia (tunica externa). The first is the innermost layer lining the lumen (the domain of the blood vessel through which blood flows), it is mainly composed of endothelial cells. The second is composed of smooth muscle. The third is the outermost layer made of collagen and elastin both providing the ability to experience large deformations to regulate blood flow. The layers are separated by two internal elastic lamina. The vascular wall constituents are heterogeneously dispatched on the different layers according to the function of the artery. Large and medium arteries are able to dilate their lumen by arterial wall thinning (vasodilation) or oppositely, to narrow it by arterial wall thickening (vasoconstriction). Both mechanisms are controlled by the contraction of the smooth muscle and aim to control blood pressure (i.e. to adapt blood flow whatever the situation). Furthermore, arteries and arterioles experience expansion whereas muscular arteries whose main role is resistance to blood flow are relatively less prone to expand than elastic arteries.

Few experimental studies were conducted to extract the mechanical properties of vascular walls due to legal-related restrictions on human tissues experimentation, ethical limitations and delicate manipulation. Such experiments are compounded by anatomical and biochemical variations from a specimen to another as well as the extrinsic sensibility of biological soft tissues. Thus, explaining the paucity of data related to mechanical properties of human arterial walls in literature. On a microscopic scale, arterial walls are a fibrous-like structure whose fibres have dispersed orientations and distribution [91]. Anisotropic formalism is convenient to capture this nature. However, depending on fibrousness degree, on fibres orientation and above all on the application of interest, arterial wall could be considered as homogeneous and isotropic. As an illustration, the isotropic formulation has been proven sufficiently accurate under a restricted range of loading (see [92] and [93]). Arterial walls has demonstrated a strong non-linear behaviour [94, 91] due to their physiological structure and their

ability to sustain large deformation ranges. It has been revealed that similarly to the RBCs and proteins, arterial walls exhibit stain-hardening to prevent rupture in some particular conditions like high blood pressure [92]. Furthermore, arterial walls are incompressible since they are water-rich.

The wall shear stress WSS is defined as the pressure exerted tangentially by blood on the arterial wall, it forms with blood pressure the most important haemodynamical forces. Regarding the effect of vascular layer number in numerical modelling, it has been shown that the WSS acting on a lipid plaque in the left main coronary artery is quite similar if considering a mono-layered or a multi-layered coronary wall [95]. As for soft membranes, arterial elasticity is described within hyperelasticity framework. The NH law is found to accurately model mechanical response of elastinous constituents of arterial walls [96] (a modification of the NH law is proposed in [97] to take into account the failure energy). However, the MR law is preferred when larger expansion is predicted. A valuable work on experimental extraction of arterial wall mechanical proprieties is found in [91], where layer-specific mechanical properties are determined by means of uniaxial tensile tests. The corresponding material constants C_{ij} adequate for a modelling using the 5-parameters MR law were obtained by curve fitting [95] (see Table 2.1), it gives the expression of W as:

$$W = C_{01}(\bar{I}_2 - 3) + C_{10}(\bar{I}_1 - 3) + C_{11}(\bar{I}_1 - 3)(\bar{I}_2 - 3) + C_{20}(\bar{I}_1 - 3)^2 + C_{02}(\bar{I}_2 - 3)^2 + \frac{1}{D}(J-1)^2 \qquad (2.1)$$

Table 2.1: Coronary wall proprieties (from [95, 91])

Coronary layers	$H(\mu\text{m})$	$\rho(\text{kg/m}^3)$	C_{10}(Pa)	C_{01}(Pa)	C_{11}(Pa)	C_{20}(Pa)	C_{02}(Pa)
Intima	230	1150	2.04E5	2.23E5	3.71E6	1.37E6	2.37E6
Media	310	〃	1.17E5	1.28E5	6.72E5	2.24E5	5.69E5
Adventitia	340	〃	1.89E5	2.02E5	1.38E6	4.59E5	1.34E6

To the best of our knowledge, experimental data on mechanical properties of human arterioles is lacking in literature. From a physiological point of view, the arteriolar wall could be regarded as a single layered wall. More precisely, arteriolar constituents are found to be functionally interdependent and dynamically interconnected thus making the frontiers separating arteriolar layers muddled [98]. This observation is condoned by other physiologists in [99] who consider the wall in smallest arterioles to be limited to a single incomplete intimal layer made of smooth cells, dismissed of tunica adventitia and the tunica media. Regarding their mechanical response to flow, arterioles reveal distensibility

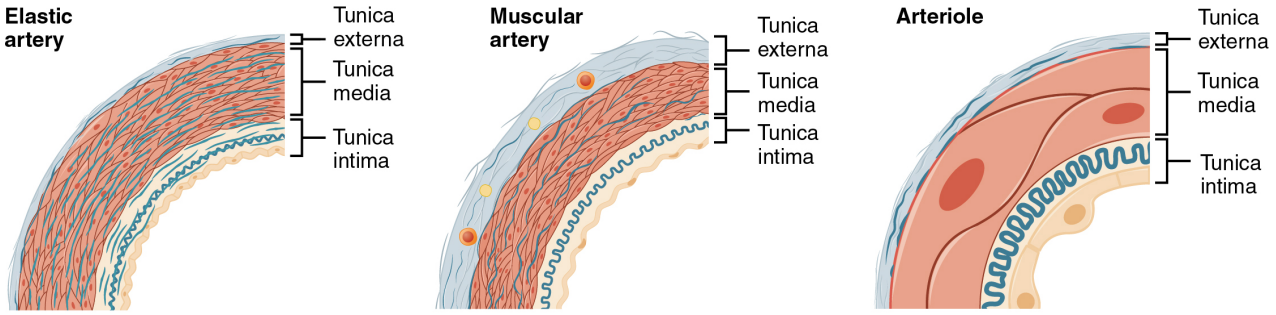

Figure 2.1: Simplified representation of layers composing arterial and arteriolar walls [1]

capabilities [100, 101] that are less important in comparison with large arteries.

2.2 Arterial haemorheology and haemodynamic

Human blood is a suspension of cells called formed elements in a yellowish aqueous liquid (plasma). Formed elements are the RBCs, the leucocytes (white blood cells) and the thrombocytes (platelets). The RBCs are the most numerous cells of formed elements (volume concentration of 45% to 1% for others elements). The rheological properties of blood are determined by the inherent mechanical proprieties of formed elements and cell-cell interaction. They include shear-thining [102], thixotropicity [103] and viscoelasticity [104]. Shear-thinning is a consequence of the shear rate-mediated process of aggregation and desegregation of RBCs: at low shear rates RBCs cluster and form long structures called *rouleaux* that disaggregate at sufficiently higher shear rates. As a consequence, the whole blood viscosity increases during the aggregation and decreases during the desegregation. Above a shear rate of 100 s^{-1}, the shear-thinning character vanishes and the blood viscosity approaches the asymptomatic values of 3.45 mPa.s [105]. Blood viscoelasticity is also attributed to the RBCs [106] as well as blood incompressibility. It is admitted that blood is laminar at $Re<2000$ and turbulent at $Re>3000$ [107]. However, turbulence might appear locally (and occasionally) for instance in stenotic arteries [108].

The study of the cellular interaction of blood components as well as haemodynamical and haemorheological proprieties at micro-scale requires a multiphase flow model [109]. Nevertheless, considering blood as a homogeneous single phased fluid is largely sufficient and allows scientists to free from haematocrit (percentage of RBCs to whole blood volume) variation [110].

[1] Image from anatomy and physiology (p:1241), access provided by the open educational resources unit of Oregon State University.

A heartbeat consists of the phase called systole during which the heart contracts to fill with blood, subsequently followed by the diastole phase during which blood is ejected out of the heart. We focus here on the arterial system whose relevant mechanical properties are the distensibility and the compliance. The first is related to arterial wall elasticity while the second reflects the pulse-damping function, that is, compliant blood vessels are inevitably distensible. Due to their vicinity with the heart, large blood vessels alternate expansion (at systole) and recoil (at diastole) to propagate blood in the arterial circulation. Blood pulsatile behaviour decays farther away from the heart until it is transformed into a steady continuous flow, as a result of arterial compliance. This phenomenon is known as "Windkessel effect"(wind chamber) and ensures a steady irrigation of small and medium blood vessels throughout a heartbeat which implies that the unsteady effects could be neglected in small blood vessels but not in larger ones [111].

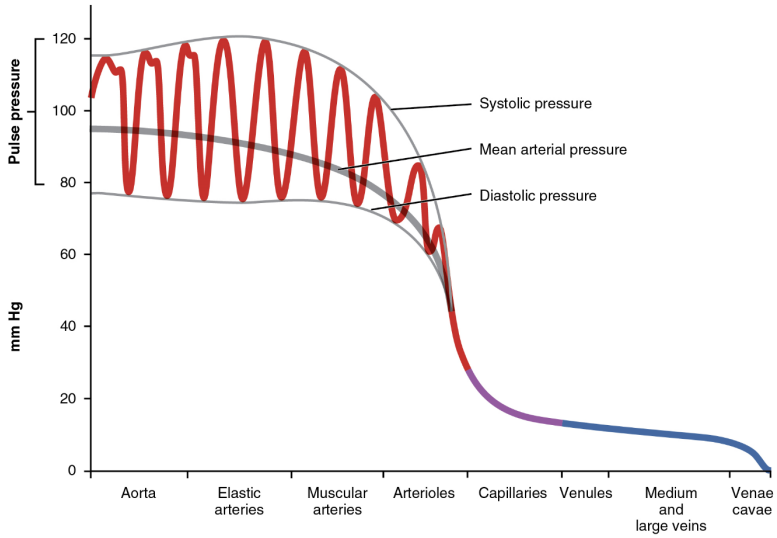

Figure 2.2: Pulsatile character of blood in human blood vessels [2]

.

The cyclic behaviour in the arterial vascular network is quantified by the nondimensional Womersley number α representing the ratio of unsteady inertial forces to viscous forces ($\alpha \approx 2.72$ in coronary arteries and $\alpha \approx 0.016$ in arterioles). The Womersley number further indicates the axial velocity profiles: for $\alpha \leq 2$ unsteadiness is neglected and the flow is parabolic while for $\alpha \geq 10$ velocity profile is blunted. Velocity profile is also impacted by the viscosity of blood, for example, in large arteries

[2]Image from anatomy and physiology (p:1226), access provided by the open educational resources unit of Oregon State University.

where the shear-thinning character of blood is pronounced the velocity profile is somewhat flattened.

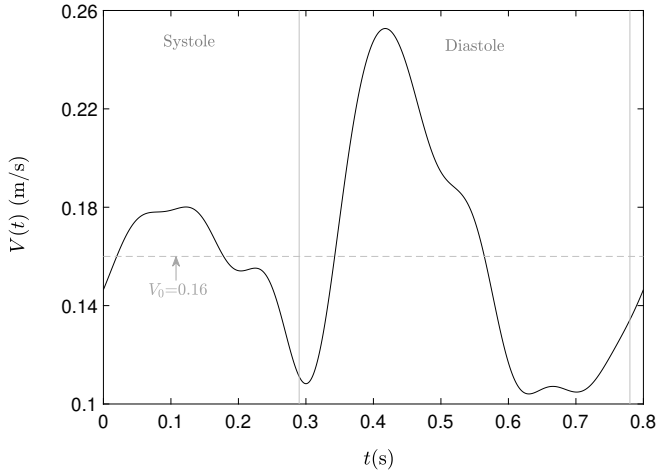

Figure 2.3: Signal of instantaneous velocity $V(t)$ in the LCA showing the systole (t <0.29 s) and the diastole (0.29< t(s)<0.78). The peak velocity is attained at t=0.42 s and the minimum at t=0.63 s.

The Windkessel model introduced by Frank in [112] is the simplest model of blood pulsatility. A limit of Windkessel model is its failure to properly model blood flow during the systole phase [113]. Later, Womersley has developed a more sophisticated mathematical model reasonably complete in a series of paper both for rigid and elastic arteries [114, 115, 116]. However, the developed flow suffers from being too complex to be employed in numerical modelling. An alternative solution was proposed in [117] where pulsatile blood instantaneous velocity in the human left coronary artery LCA was clinically measured by the Doppler technique. The resituated signal $V(t)$ is given in Figure 2.3. To obtain quantitative data permitting the numerical reinstitution of the desired signal, a Fourier transformation is applied to $V(t)$ [118]:

$$V(t) = V_0 + \sum_{n=1}^{8} V_n cos(n\omega t) + W_n sin(n\omega t) \quad , \tag{2.2}$$

where $V_0 = 0.16$ m/s is the average blood velocity throughout a heartbeat and $\omega \approx 7.85$ rad/s the angular frequency.

The coefficients V_n and W_n are expressed as:

$$V_n = \frac{2}{N} \sum_{k=1}^{N-1} cos(n\omega k\delta t) \quad , 0 \leq k \leq N-1 \tag{2.3}$$

$$W_n = \frac{2}{N} \sum_{k=1}^{N-1} sin(n\omega k\delta t) \quad , 0 \leq k \leq N-1 \tag{2.4}$$

in which V_k (of N=100) are samples of $V(t)$ and δt time-interval. Numerical values of V_n and W_n are provided in Table 2.2. The pulsatile Poiseuille flow is readily expressed as:

$$V = 6V(t)\frac{y}{H}(1 - \frac{y}{H}) \quad , \tag{2.5}$$

The finally obtained flow is a very good compromise between simple numerical implementation and realistic physiological conditions in the LCA.

Table 2.2: Numerical values of coefficients V_n and W_n [118].

n	V_n (m/s)	W_n (m/s)
0	0.15634	0
1	-0.02995	0.00808
2	0.02458	0.03887
3	-0.01182	-0.00838
4	0.00985	0.00280
5	-0.01009	0.00313
6	0.00618	-0.00113
7	0.00133	0.000874
8	-0.00360	-0.000235

Chapter 3

Hyperelastic microparticles in human blood vessels

Content

3.1 Arbitrary Lagrangian Eulerian ALE method for fluid-structure interaction

3.1.1 An overview on the ALE method

To solve the interaction between the deformable membrane, the surrounding fluid and the inner fluid, several numerical methods are employed. The most popular one is the immersed boundary method IBM, a non-conforming method originally introduced by Peskin [119] to describe the interaction between cardiac valves and blood flow. The IBM method treats the membrane as an elastic fiber formed by a series of Lagrangian massless markers immersed in a Eulerian mesh gird through which the fluid domain flows. The membrane is able to move through the fixed mesh gird. The IBM method has the flaw of being consistent only with very thin membranes and with viscous flows, that is, with inertialess conditions. Moreover, the membrane is not treated as a physical entity but is approximated using Dirac functions. The fluid domain is usually solved by the finite difference method [120] or by the lattice Boltzmann method [121] while membrane elastic force is usually obtained by the finite element method. A modification of the IBM method to accurately describe deformation of thick immersed boundaries is proposed in [122] and to account of inertia in [88] (both methods are based on a hybrid formulation). Alternatively to IBM, the arbitrary Lagrangian Eulerian ALE method could be used. It is a conforming method developed by [123, 124, 125] among others. The ALE method involves a continuous rezoning and is non-straightforward to implement. It is hence employed by fewer authors [126, 127, 128, 129, 130, 131]. The is no restriction neither on membrane inertia nor on flow inertia. Since the fluid mesh and the membrane mesh are coincident, an important deformation induces an important mesh distortion. This method is used in this work to solve the interaction between the arterial wall, the blood domain, the membrane and the enclosed fluid. The mesh is allowed to move to track deformation and displacement of the moving deformable boundary. In the following section, we concisely present generalities on mathematical formalism of the ALE method as well as details on the numerical modelling of microparticles immersed in blood and confined in blood vessels. Calculations are performed on Comsol Multiphysics® commercial package. For the mathematical background and further calculus details on the hereafter presented ALE formalism, the interested reader is referred to research papers [132, 133, 124, 134, 135] and to dedicated PhD theses [136, 137].

The ALE method combines the advantages of the purely Eulerian description and the purely Lagrangian description. It is indeed a generalisation of both descriptions. The distinguishing feature of the ALE method is that the computational gird is neither purely Lagrangian (independent on material domain R_X) nor purely Eulerian (independent on spatial domain R_x), thus, a third referential domain is introduced to be taken as a reference namely, the referential domain $\hat{R}_\chi$. The subscripts χ, x and X identify referential gird coordinates (or ALE coordinates), spatial coordinates and material coordinates, respectively.

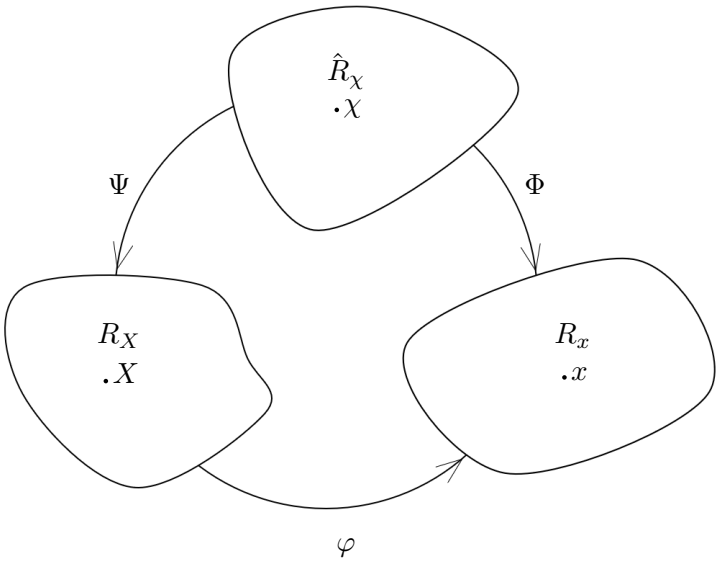

Figure 3.1: Mesh description in the ALE method and the related mappings.

The referential domain $\hat{R}_\chi$ is mapped into the spatial domain by Φ as following:

$$\Phi : R_\chi \times x[0, t_f[\longrightarrow R_x \times x[0, t_f[$$

$$(\chi, t) \longrightarrow \Phi(\chi, t) = (x, t)$$

The main feature of the ALE method is that the mesh is allowed to move with an arbitrary velocity $\hat{\mathbf{v}}_m$ (independently on the material velocity) which follows from the gradient of x variation:

$$\frac{\partial \Phi_x}{\partial(\chi, t)} = \begin{bmatrix} \frac{\partial x}{\partial \chi} \\ \frac{\partial x}{\partial t} \end{bmatrix} = \begin{bmatrix} \frac{\partial x}{\partial \chi} \\ \hat{\mathbf{v}}_m \end{bmatrix} \tag{3.1}$$

The relative velocity of the moving gird to the material velocity is known as the convective velocity c:

$$\mathbf{c} = \mathbf{v} - \hat{\mathbf{v}}_{\mathrm{m}} \tag{3.2}$$

The referential domain is mapped to the material domain by Ψ:

$$\Psi : R_X \times x[0, t_f[\longrightarrow R_\chi \times x[0, t_f[$$
$$(X, t) \longrightarrow \Psi(X, t) = (\chi, t)$$

We further introduce the particle velocity in $\hat{R}_\chi$, that is, the referential velocity $\boldsymbol{\omega}$. It is readily obtained from the gradient of χ variation:

$$\frac{\partial \Psi_\chi^{-1}}{\partial(\chi, t)} = \begin{bmatrix} \frac{\partial \chi}{\partial X} \\ \frac{\partial \chi}{\partial t} \end{bmatrix} = \begin{bmatrix} \frac{\partial \chi}{\partial X} \\ \boldsymbol{\omega} \end{bmatrix} \tag{3.3}$$

The velocities [1] involved in the ALE description are related by:

$$\mathbf{c} = \mathbf{v} - \hat{\mathbf{v}}_m = \frac{\partial x}{\partial \chi} \cdot \boldsymbol{\omega} \tag{3.4}$$

At this point we present the fundamental equation of ALE formulation that gives the variation of a physical quantity f in terms of its material derivative and its spatial derivative as:

$$\frac{\partial f}{\partial t}|_X = \frac{\partial f}{\partial t}|_\chi + \frac{\partial f}{\partial x} \cdot \mathbf{c} \tag{3.5}$$

3.1.1.1 Conservation laws

The differential form of conservation laws expressed in the ALE framework is straightforwardly obtained by replacing material velocity by convective velocity in the convective terms of the classical conservation laws for mass, momentum and total energy:

[1] $\mathbf{c} = 0$ in Lagrangian description, $\mathbf{c} = \mathbf{v}$ in Eulerian description and $\boldsymbol{\omega} = \hat{\mathbf{v}}_m$ when mesh motion is purely translational.

$$\begin{aligned}
\frac{\partial \rho}{\partial t}|\chi + \mathbf{c}\cdot\nabla\rho &= -\rho\nabla\cdot\mathbf{v} \\
\rho\Big(\frac{\partial \mathbf{v}}{\partial t}|\chi + (\mathbf{c}\cdot\nabla)\mathbf{v}\Big) &= \nabla\cdot\boldsymbol{\sigma} + \rho\mathbf{b} \\
\rho\Big(\frac{\partial E}{\partial t}|\chi + \mathbf{c}\cdot\nabla E\Big) &= \nabla\cdot\Big(\boldsymbol{\sigma}\cdot\mathbf{v}\Big) + \rho\mathbf{b}
\end{aligned} \tag{3.6}$$

where $\mathbf{b}$ is the specific body force vector. The variational form of conservation laws within the ALE framework is obtained by exploiting the Reynolds transport theorem expressed as:

$$\frac{\partial}{\partial t}|_\chi \int_{V_t} f dV = \int_{V_t} \frac{\partial f}{\partial t} dV + \int_{\partial V_t} f \quad \hat{\mathbf{v}}_m \cdot \mathbf{n} \quad dS \tag{3.7}$$

where V_t is an arbitrary control volume whose boundary ∂V_t moves with velocity $\hat{\mathbf{v}}_m$. Then, the equations of interest are obtained by substituting f in (3.7) by ρ, $\rho\mathbf{v}$ or ρE for mass conservation, momentum conservation and total energy conservation, respectively (details are found in [133, 138]). Finally, the conservation laws of interest are written in the ALE formulation as:

$$\begin{aligned}
\frac{\partial}{\partial t}|\chi \int_{V_t} \rho \quad dV + \int_{\partial V_t} \rho \quad \mathbf{c}\cdot\mathbf{n} \quad dS &= 0 \\
\frac{\partial}{\partial t}|\chi \int_{V_t} \rho\mathbf{v} \quad dV + \int_{\partial V_t} \rho\mathbf{v} \quad \mathbf{c}\cdot\mathbf{n} \quad dS &= \int_{V_t} (\nabla\cdot\boldsymbol{\sigma} + \rho\mathbf{b}) \quad dV \\
\frac{\partial}{\partial t}|\chi \int_{V_t} \rho E \quad dV + \int_{\partial V_t} \rho E \quad \mathbf{c}\cdot\mathbf{n} \quad dS &= \int_{V_t} (\mathbf{v}\cdot\rho\mathbf{b} + \nabla\cdot(\boldsymbol{\sigma}\cdot\mathbf{v})) \quad dV
\end{aligned} \tag{3.8}$$

in which $\mathbf{n}$ is the outer normal vector.

3.1.1.2 Governing equations

Before addressing the variational formulation of the coupled fluid-structure interaction problem, we first present the governing equations and the variational formulation of the fluid and the structure distinctly in sub-problems. We also recall that in ALE formulation the referential time derivative substitutes to all material time derivatives to take account of the convective velocity based on (3.5). For the reader's convenience, neither the structure sub-problem is further subdivided to represent the membrane and the vascular wall nor the fluid sub-problem is subdivided to represent the suspending blood and the fluid core. For both sub-problems, body forces are neglected.

The fluid domain assumed to be incompressible is specified by Navier-Stokes equations and the Cauchy stress tensor of fluid $\boldsymbol{\sigma}_f$:

$$\begin{aligned} &\rho_f \left(\frac{\partial \mathbf{v}_f}{\partial t}|_\chi + (\mathbf{v}_f - \hat{\mathbf{v}}_m) \cdot \nabla \mathbf{v}_f \right) = \nabla \boldsymbol{\sigma}_f \\ &\nabla \cdot \mathbf{v}_f = 0 \\ &\boldsymbol{\sigma}_f = -p\mathbf{I} + \eta[\nabla \mathbf{v}_f + (\nabla \mathbf{v})_f^T)] \end{aligned} \tag{3.9}$$

where $\mathbf{v}_f$ is fluid velocity, ρ_f fluid density, $\mathbf{I}$ the identity tensor and η dynamic viscosity. The structure which is treated as a hyperelastic solid is specified by giving the momentum conservation and the second Piola-Kirchoff stress tensor $\mathbf{S}$:

$$\begin{aligned} &\rho_s \frac{\partial^2 \mathbf{u}_s}{\partial t^2}|_\chi = \nabla \cdot (\mathbf{FS}) \\ &\mathbf{S} = 2\frac{\partial W}{\partial \mathbf{C}} = J\mathbf{F}^{-1}\boldsymbol{\sigma}_s\mathbf{F}^{-T} \end{aligned} \tag{3.10}$$

where ρ_s is structure density, $\mathbf{u}_s$ structure displacement and $\boldsymbol{\sigma}_s$ the Cauchy stress tensor of the structure.

The kinematic interface boundary condition describing continuity of velocities and the dynamic interface boundary condition describing continuity of tractions are imposed at the fluid-structure interface. In ALE formulation an extra interface boundary condition is required to specify that the normal referential velocity must vanish at the fluid-structure interface ($\boldsymbol{\omega} \cdot \mathbf{n} = 0$).

3.1.1.3 Variational formulation

Let V^f denotes the space of trial solution of $\mathbf{v}_f$ and p and Q^f the trial weighting space of test time-dependant test functions $\hat{\mathbf{v}}^f$ and $\hat{\mathbf{q}}$. Considering a fluid occupying a domain $\hat{\Omega}_f$ in its ALE configuration and $\hat{\Gamma}_f$ the fluid part of the fluid-structure interface, the variational formulation of the fluid sub-problem in ALE formulation is given by:

Find $\{\mathbf{v}_f, p\} \in V^f$ that verifies $\forall \left\{\hat{\mathbf{v}}^f, \hat{\mathbf{q}}\right\} \in Q^f$

$$\int_0^{t_f}\int_{\hat{\Omega}_f}\rho_f\frac{\partial \mathbf{v}_f}{\partial t}|_\chi\cdot\hat{\mathbf{v}}^f \quad dVdt+\int_0^{t_f}\int_{\hat{\Omega}_f}\rho_f(\mathbf{v}_f-\hat{\mathbf{v}}_m)\cdot\nabla\mathbf{v}_f\cdot\hat{\mathbf{v}}^f \quad dVdt-\int_0^{t_f}\int_{\hat{\Omega}_f}p\nabla\hat{\mathbf{v}}^f \quad dVdt$$
$$+\int_0^{t_f}\int_{\hat{\Omega}_f}\nabla\hat{\mathbf{v}}^f\eta\nabla\mathbf{v}_f \quad dVdt+\int_0^{t_f}\int_{\hat{\Omega}_f}\hat{\mathbf{q}}\nabla\cdot\mathbf{v} \quad dVdt=\int_0^{t_f}\int_{\hat{\Gamma}_f}\hat{\mathbf{v}}^f \quad \boldsymbol{\sigma}_f\cdot\mathbf{n} \quad dSdt \tag{3.11}$$

Let V^s stands for the space of trial solution of $\mathbf{u}_s$ and $\mathbf{u}$ for a time-independent test function. The variational formulation of the structure sub-problem is formulated in Lagrangian configuration as:

Find $\mathbf{u}_s \in V^s$ that verifies $\forall\ \mathbf{u} \in Q^s$

$$\int_0^{t_f}\int_{\Omega_s}\rho_s\frac{\partial^2\mathbf{u}_s}{\partial t^2}\mathbf{u} \quad dVdt+\int_0^{t_f}\int_{\Omega_s}\nabla\mathbf{u}(\mathbf{FS}) \quad dVdt=\int_0^{t_f}\int_{\Gamma_s}\mathbf{u} \quad \boldsymbol{\sigma}_s\cdot\mathbf{n} \quad dSdt \tag{3.12}$$

The formulation of the fluid-structure problem is obtained by summing (3.11) and (3.12)

Find $\{\mathbf{v}_f, p\}$ and $\mathbf{u}_s$ such that:

$$\int_0^{t_f}\int_{\hat{\Omega}_f}\rho_f\frac{\partial \mathbf{v}_f}{\partial t}|_\chi\cdot\hat{\mathbf{v}}^f \quad dVdt+\int_0^{t_f}\int_{\hat{\Omega}_f}\rho_f(\mathbf{v}_f-\hat{\mathbf{v}}_m)\cdot\nabla\mathbf{v}_f\cdot\hat{\mathbf{v}}^f \quad dVdt-\int_0^{t_f}\int_{\hat{\Omega}_f}p\nabla\hat{\mathbf{v}}^f \quad dVdt$$
$$+\int_0^{t_f}\int_{\hat{\Omega}_f}\nabla\hat{\mathbf{v}}^f\mu\nabla\mathbf{v}_f \quad dVdt+\int_0^{t_f}\int_{\hat{\Omega}_f}\hat{\mathbf{q}}\nabla\cdot\mathbf{v} \quad dVdt-\int_0^{t_f}\int_{\hat{\Gamma}_f}\hat{\mathbf{v}}_f \quad \boldsymbol{\sigma}_f\cdot\mathbf{n} \quad dSdt$$
$$+\int_0^{t_f}\int_{\Omega_s}\rho_s\frac{\partial^2\mathbf{u}_s}{\partial t^2}|_\chi\mathbf{u} \quad dVdt$$
$$+\int_0^{t_f}\int_{\Omega_s}\nabla\mathbf{u}(\mathbf{FS}) \quad dVdt-\int_0^{t_f}\int_{\Gamma_s}\mathbf{u} \quad \boldsymbol{\sigma}_s\cdot\mathbf{n} \quad dSdt$$
$$+\int_0^{t_f}\int_{\hat{\Gamma}}\boldsymbol{\sigma}_f\cdot\mathbf{n} \quad \hat{\mathbf{v}}_f \quad dSdt-\int_0^{t_f}\int_{\Gamma}\boldsymbol{\sigma}_s\cdot\mathbf{n} \quad \mathbf{u} \quad dSdt=0 \tag{3.13}$$

The equation system (3.13) could be solved as a fully coupled monolithic system [139] or as a staggered system [140]. In this work the first approach is adopted in sight of its stability and accuracy properties [141] and foremost for its ability to maintain conservation at interface [142]. Furthermore, for robustness concerns the second approach is not the best choice when the problem involves an incompressible fluid interacting with a thin solid and when the enclosed fluid undergoes complex deformation [143] which is typically the studied system (a thin hyperelastic membrane enclosing an incompressible droplet and immersed in a incompressible fluid).

3.1.2 Smoothing and rezoning

Mesh elements are of Taylor-hood type (triangular elements approximating the velocity on a quadratic basis and pressure on a linear basis P2/P1) known for satisfying the Ladyzhenskaya-Babuš ka-Breezi (LBB) condition [144]. Instead of presenting mesh convergence tests and mesh statistics, we thought it is more insightful to present features relative to mesh motion: smoothing and rezoning. Smoothing techniques are algorithms that aim to minimize mesh distortion by resolving *ad hoc* equations while maintaining nodal connectivity. Hereafter are presented smoothing methods employed in this work.

The simplest smoothing method is the Laplace smoothing which consists in solving a Laplace operator for spatial coordinates x and y:

$$\nabla^2 x = 0 \tag{3.14}$$

$$\nabla^2 y = 0$$

The unsteady form of Laplace smoothing solves the pair:

$$\frac{\partial^2}{\partial X^2}\frac{\partial x}{\partial t} + \frac{\partial^2}{\partial Y^2}\frac{\partial x}{\partial t} = 0 \tag{3.15}$$

$$\frac{\partial^2}{\partial X^2}\frac{\partial y}{\partial t} + \frac{\partial^2}{\partial Y^2}\frac{\partial y}{\partial t} = 0$$

The Laplace smoothing could result in a mesh spillover during vertex relocation. To deal with this, Winslow proposed an inverted form of above-equations [145] (i.e. the dependant variable and the independent ones are interchanged) thus, the system to solve is given by the pair:

$$\frac{\partial^2}{\partial x^2}\frac{\partial X}{\partial t} + \frac{\partial^2}{\partial y^2}\frac{\partial X}{\partial t} = 0 \tag{3.16}$$

$$\frac{\partial^2}{\partial x^2}\frac{\partial Y}{\partial t} + \frac{\partial^2}{\partial y^2}\frac{\partial Y}{\partial t} = 0$$

The Winslow smoothing was later extended to unstructured mesh in [146]. A Higher mesh deformation is managed by the hyperelastic smoothing inspired by the NH law (3.17) or the Yeoh smoothing (3.18) inspired from the eponym hyperelastic law. Unlike Laplace and Winslow smoothing methods, hyperelastic methods are not based on vertex relocation but on limiting (from the outset)

mesh deformation to maintain an acceptable element aspect ratio.

$$W_{sm}^{\mathrm{NH}} = \int_{\Omega} \frac{G}{2} C_{10}(\bar{I}_1 - 3) + \frac{1}{D_1}(J-1)^2 dV \tag{3.17}$$

$$W_{sm}^{\mathrm{YH}} = \frac{1}{2} \int_{\Omega} C_{10}(\bar{I}_1 - 3) + C_{20}(\bar{I}_1 - 3)^2 + C_{30}(\bar{I}_1 - 3)^2 + K(J-1)^2 dV \tag{3.18}$$

All material parameters in (3.17) and (3.18) are artificial. At very larger deformations, the Yeoh smoothing is patently the most powerful tool to minimise element distortion since we can turn it to a strain-hardening smoothing by controlling the stiffening factor C_{20}. However, we are not far of convergence problems with the Yeoh smoothing, in view of its important non-linearity. We wisely 'juggle' with the above-mentioned smoothing methods to conciliate computational cost and convergence issues.

Rezoning or remeshing is the generation of a new mesh with improved quality from the deformed gird. During the procedure, the velocity, the pressure, the internal energy and the stress are updated on the new generated mesh by means of remapping algorithm. Remeshing becomes necessary when mesh quality falls below a predetermined threshold of distortion, quality or squeezeness. It helps to avoid an extremely small mesh elements but might be a source of struggling, specifically when it generates interpolation errors. Comsol Multiphysics® offers the capability to automatize the remeshing procedure, that is triggered by a user-defined geometrical threshold x_t of element quality (3.19) or distortion (3.20).

$$min\left(1 - max\left[\frac{\theta - \theta_e}{180}; \frac{\theta_e - \theta}{\theta_e}\right]\right) \leq x_t \tag{3.19}$$

where θ is the angle over a vertex in the element and θ_e is the angle of the corresponding vertex in an ideal element (i.e. zero skewness).

$$\sqrt{\frac{tr\mathbf{F}^T\mathbf{F}}{2J} - 1} > x_t \tag{3.20}$$

It is important to note that the presence in the ALE conservation equations of transport terms accounting for mesh velocity for arbitrary grid velocities of the fluid nodes guarantees conservation of mass, momentum and energy during the continuous rezoning process. A method of mesh velocity update during remeshing procedure is found in [124].

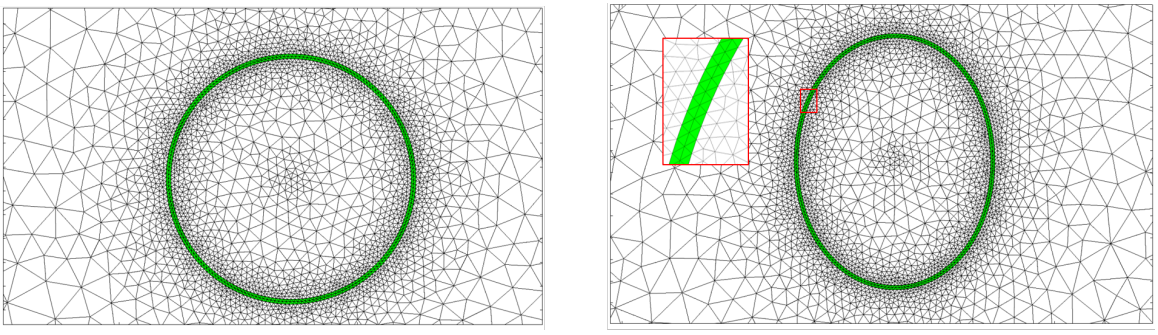

Figure 3.2: Conforming mesh in the ALE method, the green surface corresponds to the immersed solid and the white one to the fluid domain. Left: initial shape, right: deformed shape.

3.1.3 Time-integration

Equations are time-updated using the implicit multistep Backward differentiation formula BDF [147] following the scheme:

$$\Sigma_{i=0}^{k} \alpha_i u_{n-i} = \beta_0 \delta t f(t_n, u_n) \tag{3.21}$$

where u_n is a gird function approximating the solution of the boundary value problem, α and β coefficients determined is such a way they meet stability requirement (conditioned by $k > 6$) [2] and δt time-interval. In this work, $k \leq 2$ (3.22), this was chosen as a compromise between damping and stability concerns (higher k-order leads to stability issues and lower k-order are known to cause damping issues). One can notice that BDF-1 is equivalent to the Backward Euler method and Adam-Moulton scheme. However for $k = 2$ Adam-Moulton and BDF methods has different order of accuracy and stability zones.

$$\begin{aligned} &\text{BDF}-1 \quad (k = 1, \alpha_0 = 1, \alpha_1 = -1, \beta_0 = 1) \rightarrow u_n = u_{n-1} + \delta t f(t_n, u_n) \\ &\text{BDF}-2 \quad (k = 2, \alpha_0 = 1, \alpha_1 = -\frac{4}{3}, \alpha_2 = \frac{1}{3}, \beta_0 = 1) \rightarrow u_n = \frac{4}{3}u_{n-1} - \frac{1}{3}u_{n-2} + \frac{2}{3}\delta f(t_n, u_n) \end{aligned} \tag{3.22}$$

We should specify that for all performed calculations, the geometry is of first shape order. A prior, geometry shape order was set to 2, but tenacious and repetitive mesh-inversion errors occur. The Comsol Multiphysics® user guide warns about this predictable error and recommends to lower the geometry shape order to one.

[2] $k \leq 5$ in Comsol Multiphysics®

3.1.4 Newton's damped method

The variables are updated at each time-step using Newton's damped non-linear method [148]. It is a modification of the Newton method to include a damping factor λ (the Newton method is retrieved for $\lambda = 1$). A major propriety of this damped version is that it has a global convergence properties. We opt for this method to enforce convergence at reasonably small time-steps ($\delta t = 0.01 - 1$ ms) and to avoid the spurious force that was reported by some authors [149, 137]. We first vary λ in the range $1 - 10^{-5}$ then in $10^{-9} - 10^{-5}$ to enforce convergence when higher-non linearities are involved. This method is based on a damping reduction algorithm, where the key parameter is the error E_N.

Let $\mathbf{u}_0$ [3] stands for the initial guess and δu for the Newton step. For a new iteration $\mathbf{u}_1 = \mathbf{u}_0 + \lambda\delta\mathbf{u}$ the iterative solver computes E_N from the following:

$$Df(x)E_N = -f(\mathbf{u}_1) \tag{3.23}$$

where $Df(x)$ is the Jacobian matrix and $f(\mathbf{u}_1)$ the residual vector of the solution vector u_1. If E_N is smaller than the relative error E_r, $\mathbf{u}_1$ is recomputed till the condition $E_N > E_r$ is satisfied. The non-linear failures are dealt with the non-linear controller [150] that enables an efficient time-step control in the BDF method and ensures that the accuracy time-step h_{acc} remains smaller than the stability time-step h_{stab}.

3.2 Research results

3.2.1 Assumptions

In this work blood is considered as homogeneous (single phase flow), which is a commonly accepted simplification on a coarse enough scale in large and medium vessels (e.g. coronary arteries). However, in the arteriole where the characteristic size of the microparticle and that of the RBC are comparable, the assumption of homogeneous blood is hardly justifiable but nevertheless excused for the following reasons *i*) we are interested in blood as an external hydrodynamical load acting on microparticles disregarding the cellular interaction of formed elements *ii*) densities of plasma, RBCs and microparticles are of the same order (1110 ± 87 kg/m^3) *iii*) considering the plasma as the suspending fluid requires

[3] In the original Newton's damped method [148] u is specified as a function while in Comsol it is specified as a vector within the damping algorithm. Comsol actually uses a modified version of the the original method.

the modelling of the RBCs but also of white blood cells, which requires an enormous computational cost not borne by the computer installation provided (calculations abruptly crash when considering a couple of RBCs in view of mesh refinement at membranes);

To circumvent the issue of unavailable data on mechanical proprieties of arteriolar wall, the latter is modelled as a nearly-incompressible neo-Hookean solid as in [151]. However, the paper concerned do not specify the origin of the employed material parameters, we then validate the model through comparison with experimental data related on dilation of human arterioles [100]. Unlike the coronary wall, the arteriolar wall is restricted to a single layer (the intima) a simplification condoned by *i*) no related data are forthcoming in literature *ii*) the smallest arterioles herewith considered do not have a tunica external and the tunica media is limited to a single incomplete layer of smooth cells [99] *iii*) arteriolar wall constituents are functionally interdependent and dynamically interconnected making the frontiers blurred between the three layers [98];

Since we are not interested in vascular wall from a purely physiological/biological point of view but only as a confinement environment and an external solid load exerted on microparticles, we estimate the assumption of isotropy to be reasonably acceptable;

The assigned density of 1150 kg/m^3 is taken as an intermediate value between 1000 kg/m^3 and 1300 kg/m^3 employed in [95] and [152], respectively;

The bidimensional modelling is supported by the following items *i*) a confrontation between experimental and numerical investigation conducted in [45] revealed that a bidimensional model is enough accurate to describe dynamical behaviour of a microparticle flowing in a circular channel *ii*) three dimensional effects are shown to be negligible for microparticles whose thickness to radius ratio do not exceed 5% (here we have a ratio of 4%) [37] *iii*) available numerical facilities do not permit the 3D modelling and in-house cluster and CCIPL [4] could not profit from the lab-available licence (a locked single user Comsol Multiphysics® licence), we also requested access to the cluster of CCUB [5] that was accepted but the anterior available version of Comsol Multiphysics® do not handle the system modelling;

Microparticle membrane is considered as a protein-reticulated membrane and described as a neo-Hookean solid (strain-softening) that was demonstrated to be appropriate for such membranes [40]. It

[4] Le centre de calcul intensif des Pays de la Loire.
[5] Le centre de calcul de l'université de Bourgogne.

is indeed a capsule since the membrane is solid although we prefer the generic term of microparticle;

The radius to thickness ratio is also established in [76] as a threshold (5%) below which the bending stiffness do not show a substantial effect on the overall dynamical behaviour of the considered microparticle, it is the reason why bending stiffness effect in not explicitly addressed in the present work.

3.2.2 Produced research papers

3.2.2.1 A01

Numerical investigation of the dynamical behavior of a fluid-filled microparticle suspended in human arteriole

I. El Jirari

LAMPA, Arts et Metiers Institute
of Technology, HESAM University,
49035 Angers, France

A. El Baroudi

LAMPA, Arts et Metiers Institute
of Technology, HESAM University,
49035 Angers, France

A. Ammar

LAMPA, Arts et Metiers Institute
of Technology, HESAM University,
49035 Angers, France

ABSTRACT

The study of artificial microparticles (capsules and vesicles) has gained a growing interest with the emergence of bioengineering. One of their promoting applications is their use as therapeutic vectors for drug delivery, when capsules and vesicles release their capacity in a targeted environment. The dynamic behavior of capsules and vesicles in confined or unbounded flows was widely studied in the literature and their mechanical response was truthfully described using constitutive laws with good agreement with experiences. However, in a context of biological application, to our knowledge, none of published studies investigating the mechanical response of deformable microparticle took into account the real physiological conditions: the rheological properties of blood such as carrying fluid and the mechanical properties of blood vessels. In this paper, we consider a hyperelastic microparticle suspended in human arteriole. We investigate the deformation of the microparticle resulting from its interaction with blood flow and the arteriolar wall using various capillary numbers and respecting physiological properties of blood and arterial wall. The influence of the blood viscosity model (Newtonian vs shear-thinning) is investigated and a comparison with a rigid microchannel and a muscle-embedded arteriole are carried out. The fluid structure interaction (FSI) problem is solved using Arbitrary Lagrangian Eulerian (ALE) method. Our simulations have revealed that the arteriolar wall distensibility deeply influences both the deformation and velocity of the microparticle: the deformation strongly increases while the velocity decreases in comparison to an infinitely rigid wall. In the context of therapeutic procedure of targeted drug-delivery, a particular attention should be addressed to these observations, in particular for their implication in the burst mechanism.

1 Introduction

Microencapsulation is the industrial process by which a droplet or a solid is enclosed by a thin elastic membrane, resulting in structures called microparticles. The membrane of a microparticle bursts under predetermined conditions allowing a controlled and targeted release of the inner contain. The application field of microparticles as delivery system includes cosmetics, pharmaceutics and food. Microparticles are used as pharmaceutical vehicle in targeted drug delivery process for non-invasive cancer treatments [1–3], diabetes [4] and heart attack [5]. In the procedure of targeted drug delivery, microparticles are injected into arterial bloodstream (e.g the hepatic artery for transarterial chemoembolization (TACE) [6] and the coronary arteries for thrombus dissolution [5]). Once the microparticle is injected, it flows in varied size and nature blood vessels till it reaches its target (e.g. tumor), a robust and reliable prediction of the mechanical behavior of microparticle (velocity, surface

tensions acting on membrane, deformation, burst...) and fluid kinetics (diffusion, convection, concentration of the released inner drug) in interaction with vascular wall and blood stream are essential to ensure a proper, efficient and safe functioning of the targeted drug-delivery procedure. Attention also should be addressed on local perturbation due to the presence of the microparticle (i.e. wall shear stress, pattern of blood flow...). Prediction and evaluation of drug-eluting microparticle behavior are conducted by means of in-vitro [7–9] and in-vivo [10] studies. Above-mentioned studies are conducted by physicians and focused on the pharmacokinetic behavior of the released drug without any consideration of mechanics. Interestingly, the present study proposes an alternative in-silico approach that could be complementary of in-vivo and in-vitro studies, by providing an upstream prediction of the mechanical behavior of the microparticle in its interaction with blood flow and vascular wall without tricky experimental protocols and limitations imposed by regulation related to animal experimentation. Furthermore, microparticles constitute an efficient biomimetic system to understand the mechanical properties of biological microparticles such as the red blood cell (RBC). The study of mechanical properties of RBCs and their dynamical response to applied external flow has profited from the enhancement of microfluidic devices where microchannels mime the vascular system [11, 12]. RBC is a biological cell formed by an elastic membrane (phospholipid bilayer attached to a spectrine skeleton) enclosing hemoglobin solution. Due to its finite thickness, only the deformation of median surface is considered. RBC membrane is characterized by three elastic moduli: surface shear modulus $G_s = 2.5\ \mu\mathrm{N/m}$ [13], surface extension modulus $K = 300 - 500\ \mathrm{mN/m}$ [14–16] and bending rigidity (also called bending energy) $B = 5 - 150\ \mathrm{K_bT}$ [17, 18]. In the microcirculation, RBCs are highly deformed from their initial biconcave shape. Depending on the blood flow strength and inner diameter of microvessel, RBCs take the shape of a bullet, a parachute or a slipper [19–21].These characteristic shapes are also observed for artificial microparticles like vesicles and capsules [22–25]. Vesicle membrane is lipidic and acts like a bidimensional incompressible fluid (i.e. zero shear elasticity). In contrast, polymeric membrane of capsule is solid and shear resistant. Capsule's membrane obeys to Lagrangian elastic laws. Instead of a reference configuration, vesicle membrane is characterized by an initial curvature which means a bending resistance. Mechanical properties of microparticles are obtained by different methods among them squeezing microparticle between two parallel plates [25, 26], spinning capsule experiment [27] flowing in a capillary tube [24, 28], micropipette aspiration [29], and compression [30]. In literature, membrane is assumed to obey different hyperelastic constitutive laws that describe hyperelasticity in terms of a strain energy potential which defines the strain energy stored in the material per unit of reference volume: Skalak (SK) [31–33], Evans-Skalak (ES) [32], Mooney-Rivlin (MR) [34], Neo-Hookean (NH) [35–37] and Yeoh [26]. For small strains, all of aforementioned hyperelastic laws reduce to the elastic Hook's law [38]. Skalak law was first introduced to model the large deformation and area incompressibility of biological membrane [39], this law adds non-linearly the area dilatation to the shear deformation. Evans law (or Evans-Skalak law) [40] was introduced later to simplify SK law by adding linearly the area dilatation to the shear deformation. Due to its 3D origin, MR is strain-softening. NH law is derived from MR and Yeoh law is a higher-order extension of the NH law [41]. SK law is strain-hardening, hence, for similar hydrodynamic constraints a membrane obeying SK law is less deformed than the one obeying MR law [33] or NH law [24]. Besides constitutive law, microparticle deformation depends on viscosities ratio [42], the section of the microfluidic channel [36], membrane thickness [43], confinement [22, 25] and bending rigidity [44, 45].

In his Phd thesis [46], Tahiri introduced a local elastic law to take into account the contribution of the wall, nonetheless, without any consideration of the mechanical properties of the arterial wall. In this paper, we chose not to distinguish between a capsule and a vesicle (even if capsules are sometimes used to designate both artificial particles). Henceforth, the generic term microparticle is used to describe a Newtonian and incompressible fluid enclosed by a thin hyperplastic membrane.

In this study and in a context of medical application, we respect mechanical properties of arteriolar wall and the rheological/dynamical properties of blood flow in a human arteriole. The study is carried out using Arbitrary Lagrangian Eulerian Method implemented on Comsol Multiphysics [47].

2 Physical model description and modeling

The studied problem is schematically represented by a thin membrane enclosing an internal fluid, freely suspended in a confined external flow (blood). The arteriole is represented using a rectangular channel on which we distinguish the lumen and the arteriolar wall (see Fig. 1). The flow is defined using an inlet velocity (at Γ_i) and a zero outlet normal stress (at Γ_o). The top-bottom right and left edges of the arterial wall are fixed. Three fluid-structure interfaces are identified: external fluid-membrane/internal fluid-membrane (Γ_{fm}) and external fluid-arterial wall (Γ_{fa}).

2.1 Blood model

Blood is known to behave like a shear-thinning fluid in regions when shear rate $\dot{\gamma}$ is below $100\,\mathrm{s}^{-1}$ [48–50], above this value, blood viscosity tend to a constant Newtonian viscosity $\eta = 0.0035\,\mathrm{Pa\cdot s}$. In an arteriole, the shear rate exceeds significantly $100\,\mathrm{s}^{-1}$ [51, 52] and blood is Newtonian. Even if non-Newtonian blood in the arteriole is physiologically implausible, we studied besides the Newtonian blood a specific case where blood is shear-thinning, the aim being to evaluate the effect of blood viscosity model on microparticle deformation. A Carreau model is used to describe the shear thinning of

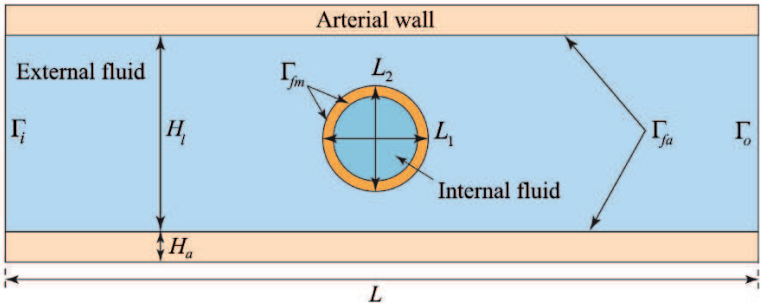

Fig. 1. Schematic description of the FSI problem.

blood:

$$\eta = \eta_\infty + (\eta_0 - \eta_\infty)\left[1 + (\lambda\dot{\gamma})^2\right]^{\frac{n-1}{2}} \tag{1}$$

where the coefficients $\eta_\infty = 0.0035\,\mathrm{Pa}\cdot\mathrm{s}$, $\eta_0 = 0.056\,\mathrm{Pa}\cdot\mathrm{s}$, $\lambda = 3.313\,\mathrm{s}$ and $n = 0.3568$ were provided from [53]. Due to cardiac contractions, blood flow is pulsed, mainly in the arterial circulation. The disentisibility of arterial wall damps the pulsation of blood and transform the pulsatile flow into a continued flow (Windkessel effect). In biofluid mechanics, the importance of cyclic behavior in a pulsatile flow is quantified by Womersley number (α) [54]. This nondimensional number can be interpreted as the ratio of the unsteady forces to the viscous forces. Blood velocity profile depends on the Womersley number: for small and medium-sized arteries ($1 < \alpha < 10$) [55], flow is dominated by viscous effects and the profile is parabolic. For $\alpha > 10$, the unsteadiness dominates the flow, hence, velocity profile becomes blunted [56]. In the arteriole the Womersley number is approximately $\alpha = 0.016$, then we considered a steady Poiseuille flow described as:

$$v_i = 6v_0\frac{y}{H_l}\left(1 - \frac{y}{H_l}\right) \quad \text{at } (\Gamma_i) \tag{2}$$

where $v_0 = 10\,\mathrm{cm/s}$ is the average velocity in the arteriole and $H_l = 30\,\mu\mathrm{m}$ the height of the rigid channel/arteriole. The value of H_l corresponds to the inner diameter (lumen) of a human arteriole and the corresponding arterial wall thickness is $H_a = 20\,\mu\mathrm{m}$ [57]. In the absence of body forces, the incompressible flow is governed by the continuity and Navier-Stokes equations as given below

$$\nabla\cdot\mathbf{v} = 0\,, \quad \rho\left[\frac{\partial\mathbf{v}}{\partial t} + (\mathbf{v}\cdot\nabla)\,\mathbf{v}\right] = \nabla\cdot\boldsymbol{\sigma}$$

where $\rho = 1050\,\mathrm{kg/m^3}$ is the fluid density, $\mathbf{v}$ is the velocity field, $\boldsymbol{\sigma}$ is the total stress tensor in the incompressible fluid which could be expressed as :

$$\boldsymbol{\sigma} = -p\mathbf{I} + \eta\left[\nabla\mathbf{v} + (\nabla\mathbf{v})^T\right]$$

where p is the fluid pressure, $\mathbf{I}$ is the identity tensor and η is the fluid dynamic viscosity.

2.2 Arterial wall model

The arterial wall consists of collagen, elastin and smooth muscle cells distributed and oriented differently on three distinct layers: the intima, the media and the adventice [58]. Layer-specific mechanical properties of human coronary artery include nonlinearity, inelasticity and anisotropy [59]. In their work on in vitro determination of layer-specific mechanical properties of human coronary arteries [59], Holzapfel and co-workers observed that the intima showed a significant thickening, a load-bearing capacity and a mechanical strength compared to the media and the adventitia. Moreover, the inclusion of the three layers in blood vessel modeling has a insignificant contribution on the shear stress [60]. Furthermore, frontiers between the three layers are blurred in the arteriole [61]. For aforementioned reasons, we chose to restrict arterial wall model

to the intima. In this work, the thickness of the arteriolar wall is assigned to $20\,\mu$m [57]. For reasons related to computational cost, we consider a section of a human arteriole ($L = 300\,\mu$m). The arterial wall is assumed to be hyperelastic, homogenous and incompressible, the equation describing the motion is governed by

$$\rho_a \frac{\partial^2 \mathbf{u}^{(a)}}{\partial t^2} = \nabla \cdot \boldsymbol{\sigma}^{(a)} \tag{3}$$

where ρ_a is the arterial wall density, $\mathbf{u}^{(a)}$ the displacement vector and $\boldsymbol{\sigma}^{(a)}$ the Cauchy stress tensor. In addition, the constitutive relation can be written readily in terms of Cauchy stress tensor and strain-energy density function

$$\boldsymbol{\sigma}^{(a)} = J^{-1}\mathbf{F}\frac{\partial W^{(a)}}{\partial \mathbf{E}^{(a)}}\mathbf{F}^T$$

where J is the dilatation ratio, $\mathbf{F}$ the deformation gradient tensor, $\mathbf{E}^{(a)}$ the Green-Lagrange strain tensor and $W^{(a)}$ the strain-energy density function which is related to the strain invariants by the following relation :

$$W^{(a)} = C_{10}\left(\bar{I}_1 - 3\right) + C_{01}\left(\bar{I}_2 - 3\right) + C_{20}\left(\bar{I}_1 - 3\right)^2 + C_{02}\left(\bar{I}_2 - 3\right)^2 + C_{11}\left(\bar{I}_1 - 3\right)\left(\bar{I}_2 - 3\right) + \frac{\kappa}{2}\left(J_{\mathsf{el}} - 1\right)^2 \tag{4}$$

where $C_{10}, C_{01}, C_{20}, C_{02}$ and C_{11} denotes material parameters extracted by curve fitting from in vitro study [59] and adapted from [60] (see Table 1), $\bar{I}_1$ and $\bar{I}_2$ respectively denotes the first and the second invariant of the isochoric right Cauchy-Green deformation tensor, κ is the initial bulk modulus and J_{el} the elastic volume ratio. The Money-Rivlin constitutive law is based on the assumption of isotropic behavior throughout the deformation history. Note that the numerical values of C_{ij} parameters are provided from a study on human coronary arterial wall, in the lack of such study on human arteriole, we used the same values of C_{ij}. This extrapolation nevertheless remains acceptable since both vessels are of the same nature.

Table 1. Material parameters.

$\rho\,(\mathrm{kg/m^3})$	$\kappa\,(\mathrm{Pa})$	$C_{10}\,(\mathrm{Pa})$	$C_{01}\,(\mathrm{Pa})$	$C_{20}\,(\mathrm{Pa})$	$C_{02}\,(\mathrm{Pa})$	$C_{11}\,(\mathrm{Pa})$
1150	$2.04 \cdot 10^5$	$2.23 \cdot 10^5$	$1.37 \cdot 10^6$	$2.67 \cdot 10^6$	$3.71 \cdot 10^6$	$3.78 \cdot 10^6$

Regarding the external arteriolar wall, we consider a free unconstrained external wall (FEW) where the wall is free to deform and a constrained state where it is surrounded by a muscle which is more realistic. The muscle follows the Neo-Hookean law (5) [62]. Muscle thicknesses considered are $H_m = 5, 10, 15, 20, 27.5, 35$ and 60 μm. The FEW assumption corresponds to $H_m = 0\ \mu$m (no surrounding muscle). As for the arteriolar wall, the zero displacement boundary condition is imposed to the ends of the muscle. Results relative to the FEW assumption and to the muscle-embedded arteriole are given on 4.2 and 4.4, respectively.

2.3 Microparticle model

The studied microparticle consists of a disk-shaped thin membrane (a thickness of $0.27\,\mu$m) enclosing an incompressible Newtonian fluid ($\eta_i = 0.00345\,\mathrm{Pa \cdot s}$ and $\rho_i = 1000\,\mathrm{kg/m^3}$). The membrane is treated as hyperelastic, isotropic and nearly incompressible surface in which the strain-energy density function for a Neo-Hookean material is given by :

$$W^{(m)} = \frac{G}{2}\left(\bar{I}_1 - 3\right) + \frac{\kappa}{2}\left(J_{\mathsf{el}} - 1\right)^2 \tag{5}$$

where the parameter $G\,(\mathrm{N/m^2})$ corresponds to the initial shear modulus. The initial bulk modulus κ and initial shear modulus G are calculated from the surface shear modulus $G_s\,(\mathrm{N/m})$. In this framework the surface shear modulus is varied from the range of 10^{-2} to $10^{-3}\,\mathrm{N/m}$ which is in the same range as experimental extracted modulus [28, 63]. A comprehensive and detailed review of constitutive relations can be found in [64].

In the membrane model, the stresses are integrated across the wall thickness and replaced by tensions, i.e., forces per unit length of the median deformed surface. The deformation of the microparticle is quantified by the Taylor parameter defined as:

$$D = \frac{|L_1 - L_2|}{L_1 + L_2} \tag{6}$$

where L_1 and L_2 respectively designate the axial and the radial length of the capsule (i.e. $D = 0$ for a disk-shaped microparticle). For the initial shape $L_1 = L_2 = 18\,\mu$m. The Taylor parameter strongly depends on the nondimensional capillary number Ca. The latter measures the ratio between the viscous forces applied by the flow and elastic resistance of the membrane:

$$Ca = \frac{\eta\dot{\gamma}L_1}{2G_s} \tag{7}$$

2.4 Fluid-structure interaction

In this paragraph, the dynamic behavior of the suspended microparticle shall be obtained of the judicious interface conditions. Dynamic and kinematic continuity must be satisfied. Hence, the fluid-structure interaction pertaining the fluids is of non-homogeneous Dirichlet condition

$$\begin{aligned}
\mathbf{v}^{(i)} &= \frac{\partial \mathbf{u}^{(m)}}{\partial t} \quad \text{at } (\Gamma_{fm}) \text{ (inside microparticle)} \\
\mathbf{v}^{(o)} &= \frac{\partial \mathbf{u}^{(m)}}{\partial t} \quad \text{at } (\Gamma_{fm}) \text{ (outside microparticle)} \\
\mathbf{v}^{(e)} &= \frac{\partial \mathbf{u}^{(a)}}{\partial t} \quad \text{at } (\Gamma_{fa})
\end{aligned}$$

representing mass conservation throughout the interface, and the fluid-structure interaction for the solids is of non-homogeneous Neumann

$$\begin{aligned}
\boldsymbol{\sigma}^{(i)} \cdot \mathbf{n} &= \boldsymbol{\sigma}^{(m)} \cdot \mathbf{n} \quad \text{at } (\Gamma_{fm}) \text{ (inside microparticle)} \\
\boldsymbol{\sigma}^{(o)} \cdot \mathbf{n} &= \boldsymbol{\sigma}^{(m)} \cdot \mathbf{n} \quad \text{at } (\Gamma_{fm}) \text{ (outside microparticle)} \\
\boldsymbol{\sigma}^{(o)} \cdot \mathbf{n} &= \boldsymbol{\sigma}^{(a)} \cdot \mathbf{n} \quad \text{at } (\Gamma_{fa})
\end{aligned}$$

describing the equivalence of fluids stresses and solids stresses.

3 Numerical method

In the ALE description, the mesh is arbitrary connected to the coordinate system or to the material allowing large deformation state without a mesh distortion. In addition to material configuration R_X and spatial configuration R_x, a third referential configuration R_χ where reference coordinates χ identify the grid points is introduced. The computational gird is allowed to move independently on material motion with a given mesh velocity $\mathbf{v}_m = \partial\mathbf{x}/\partial t$ where $\mathbf{x}$ is the physical coordinates of χ. The difference between both velocities refers to convective velocity $\mathbf{c} = \mathbf{v} - \mathbf{v}_m$ (Note that Eulerian description and Lagrangian description corresponds to $\mathbf{c} = \mathbf{v}$ and $\mathbf{c} = 0$, respectively). At fluid-structure interface, in addition to "classical" conditions given in 2.4, mesh velocity satisfies: $\mathbf{v}_m \cdot \mathbf{n} = \mathbf{v} \cdot \mathbf{n}$ where $\mathbf{n}$ is the unit outward normal. In the moving referential mesh frame R_χ, the material time derivative of a scalar physical quantity f for a given particle X with respect to the moving mesh gird is described by the fundamental equation of ALE :

$$\frac{\partial f}{\partial t}|_X = \frac{\partial f}{\partial t}|_\chi + \frac{\partial f}{\partial x} \cdot \mathbf{c} \tag{8}$$

Regarding time-integration scheme, we used the implicit Backward Differentiation Formula (BDF) scheme (9) derived from the multistep Adams-Moulton scheme

$$\sum_{i=0}^{k} \alpha_i \mathbf{u}_{n-i} = \beta_0 h f(t_n, \mathbf{u}_n) \tag{9}$$

where h is the time-step, the order of accuracy k is varied from (10) :

$$\begin{aligned} &k=1:\alpha_0=1\ ,\ \alpha_1=-1\ ,\ \beta_0=1\ \rightarrow\ \mathbf{u}_n=\mathbf{u}_{n-1}+hf\left(t_n,\mathbf{u}_n\right)\\ &k=2:\alpha_0=1\ ,\ \alpha_1=-\frac{4}{3}\ ,\ \beta_0=1\ ,\ \alpha_2=\frac{1}{3}\ \rightarrow\ \mathbf{u}_n=\frac{4}{3}\mathbf{u}_{n-1}-\frac{1}{3}\mathbf{u}_{n-2}+\frac{2}{3}hf\left(t_n,\mathbf{u}_n\right)\end{aligned} \tag{10}$$

The variables are updated at each time-step using a damped Newton nonlinear method [65]. This method is based on a damping reduction algorithm where the key parameter is the error E : For a new iteration $\mathbf{u}_1=\mathbf{u}_0+\lambda\delta u$ (where $\mathbf{u}_0$ is the initial guess, $10^{-5}\leq\lambda\leq 1$ the damping factor and δu the Newton time-step), the solver computes $Df(x)E=-f(\mathbf{u}_1)$ where $Df(x)$ is the Jacobian matrix and $f(\mathbf{u}_1)$ the residual vector of the solution vector $\mathbf{u_1}$. If E is smaller than the relative error E_r, $\mathbf{u}_1$ is recomputed till the condition $E>E_r$ is satisfied. The nonlinear failures are dealt with the nonlinear controller (STAB) [66] that enables an efficient time-step control in the BDF method and ensures that the accuracy time-step h_{acc} remains smaller than the stability time-step h_{stab}. Mesh deformation is computed using Winslow smoothing nonlinear technique [67], the equations to solve are:

$$\frac{\partial^2 X}{\partial x^2}+\frac{\partial^2 X}{\partial y^2}=0\ ,\quad \frac{\partial^2 Y}{\partial x^2}+\frac{\partial^2 Y}{\partial y^2}=0 \tag{11}$$

x and y are deformed mesh positions and, X and Y the reference coordinates of the material frame. An automatic remeshing procedure enables more extreme deformation states and prevents mesh reversing and tangling that lead to the deterioration of the results. The remeshing is automatically activated beyond a pre-determined cell quality threshold based on the criterion of equiangular skew: $\min\left[1-\left[\max\left(\frac{\theta-\theta_e}{180-\theta_e},\frac{\theta_e-\theta}{\theta_e}\right)\right]\right]<0.01$ where θ is the angle over a vertex in the element and θ_e the angle of the corresponding vertex in an ideal element (zero skewness). The discretization of fluid domain is done with P2/P1 element that gives a quadratic basis for velocity and linear pressure. This element satifyes the LBB (Ladyzhenskaya-Babuska-Brezzi) stability condition. Solving Navier-Stokes equations using finite element method is known to cause (as well as other convection driven problem) numerical instabilities. Therefore, a stabilization is required to circumvent numerical instabilities and solution oscillations. We use two methods of consistant stabilization: streamline diffusion and crosswind diffusion. The first adds artificial diffusion in the streamline direction whereas the second adds diffusion in the cross direction. The added diffusion is a not physical but helps to avoid the mesh refinement and then a huge computational cost.

4 Results and discussion

4.1 Validation of the numerical model

In this section, we report the validation of the present numerical model against the work of Barthes and co-workers on the dynamical behavior of a freely suspended spherical capsule in an unbounded shear flow [68]. In this work, the membrane of the microparticle is neo-Hookean. The external and internal fluids are similar, thus excluding buoyancy effect. The velocity and the pressure of both fluids are governed by Stokes equations ($Re\ll 1$). The FSI problem is solved by the ALE method. We performed a parametric calculation ($Ca=0.075-0.6$) using the commercially available FEM package COMSOL Multiphysics. The evolution of Taylor parameter D is monitored till reaching an asymptotic deformation D^{∞} (see Figure 2). Moreover, this evolution is similar to those reported in [37, 68], where the FSI problem is respectively solved using the boundary element method and the immersed boundary method. Note that the steady deformed shapes shown in Fig. 2 are identical to those illustrated in [68].

4.2 Microparticle confined in human arteriole

The dynamical response of the microparticle is investigated for $Ca=0.01,0.02,0.03,0.04$ and 0.05. As shown in Figure 3(a), when the microparticle is flowing along the arteriole, the Taylor parameter becomes higher as the capillary number is increasing. In response to the sudden start of blood flow, microparticle becomes pebble-shaped: the initial rear end positive curvature (convexity) is decreased till a flattened state and the maximum radial length is significantly more important than the axial one ($t=0.364$ ms in Figure 8(b)). As the microparticle moves from its initial position and starts flowing along the arteriole, it undergoes an axial extension while its radial dimension progressively decreases to compensate axial elongation. The obtained morphology referred to as bullet shape. In the immediate vicinity of the arteriole extremity ($t=1.540$ ms), a concavity is observed at the rear of the microparticle (see Figure 8(b)).

The rear shape transition from the convexity to the flatness and then to the concavity and the increasing of front tapering (see Figure 8(b)) is a consequence of the wall displacement that changes the confinement and then the capillary number. As shown on Figure 4, at $t=1$ ms, the rear end is convex for $Ca=0.01$ while it is flattened for $Ca=0.05$. Regarding the front, it is more pointed for $Ca=0.05$. The decreasing of the initial rear convexity till the concavity and the increasing front

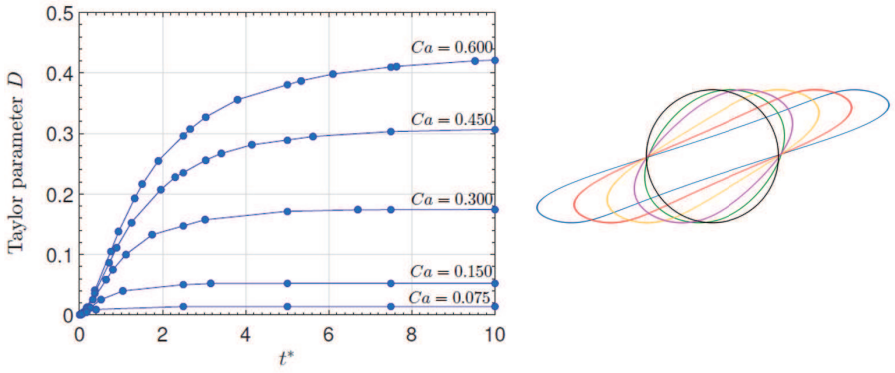

Fig. 2. Taylor parameter versus dimensionless time for a capsule suspended in a shear flow (left). Superposition of obtained steady deformed shapes illustrated by different colors: $Ca = 0.075$ (green) $Ca = 0.15$ (pink), $Ca = 0.3$ (yellow), $Ca = 0.45$ (red) and $Ca = 0.6$ (blue). Black color corresponds to the initial shape (right).

tapering with increasing capillary number is observed in this work by varying "directly" the capillary number (via changing the membrane shear modulus) and "indirectly" (change induced by wall displacement). This behavior is reported in [22, 23] where the shape transition dependence on the capillary number is well described.

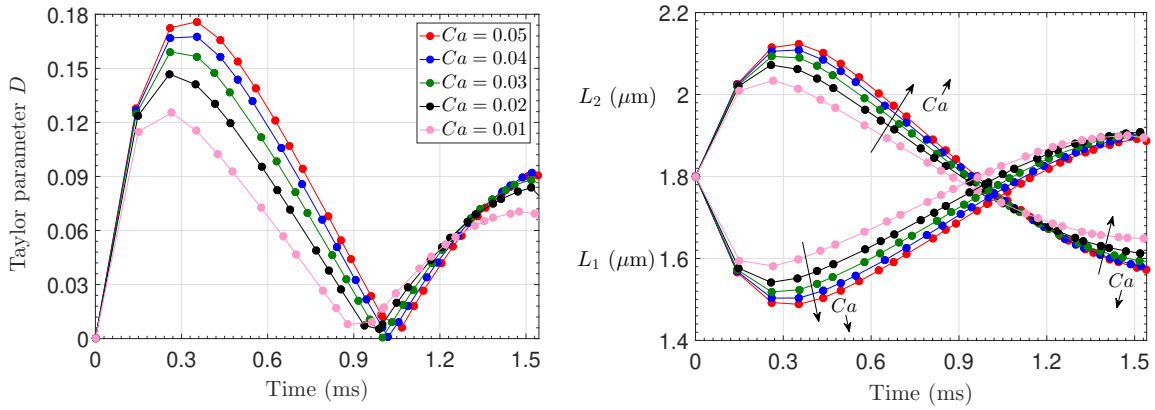

(a) (b)

Fig. 3. Time-evolution of Taylor parameter (a) and of axial and radial lengths (b) for $Ca = 0.01 - 0.05$.

For all Ca, the variations of Taylor parameter versus time are parabolic with decreasing amplitudes. Indeed, the amplitude of the first lobe of the curve is nearly two time greater than the second one. For all curves, the ascending slope of the straight path is similar till roughly 0.15 ms. Above this point, curves deviate from their initial ascending straight path and different amplitudes are observed. Since the curves reached the maximum and starts to decrease, the minimum Taylor parameter is reached firstly for the less important amplitude. Shortly thereafter, curves start to rise with the same slope from the lowest to the highest Ca, reason why in a certain zone, the trend is reversed and the deformation heightens from the lowest to the highest capillary number. Regarding the axial length L_1 and the radial length L_2 time-evolution (see Figure 3(b)), a symmetry with respect to the microparticle centerline is observed due to the surface-area conservation (a radial elongation is systematically compensated by an axial shrinking). The localized axial length tangle is the consequence of the edge effect.

For the purpose of assessing the influence of shear-thinning of blood, we performed a comparison between the Newtonian blood model (so far used) and the Carreau model describing the shear-thinning. Obtained results for $Ca = 0.05$ have shown that deformation overtime is notably similar when the blood is considered as Newtonian or shear-thinning (see Figure 5). The slight discrepancies are due to the differences in the velocity profile and the wall shear stress. When the fluid is shear-thinning, the velocity profile is "flattened" and its slope near the wall is more important comparing to the Newtonian model, thus, the shear stress near the wall is more important.

In order to display the parachute shape (a strongly concave rear end and a highly pointed front), the capillary number is increased until $Ca = 0.1$. Real time-snapshots: $t = 0.206, 1$ and 1.393 ms show respectively: pebble-shape (Figure 6(a)),

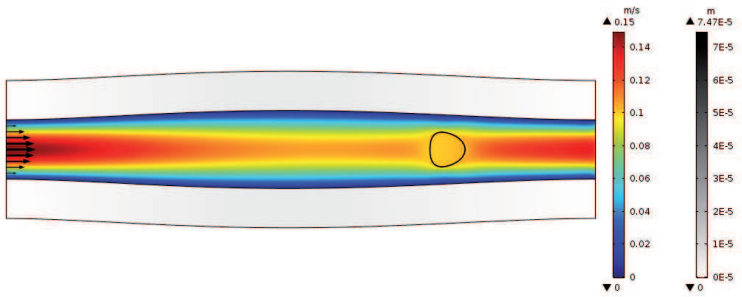

(a) $Ca = 0.01$

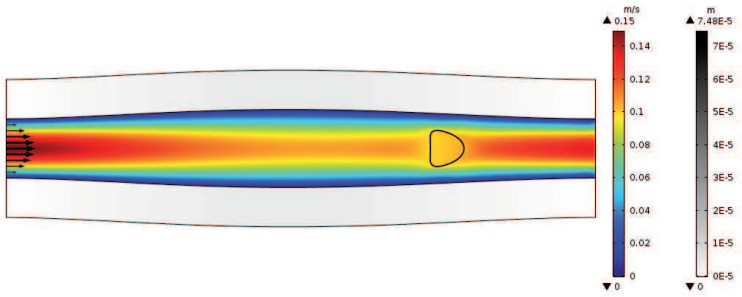

(b) $Ca = 0.05$

Fig. 4. Real time snapshot at $t = 1\,(\mathrm{ms})$. Rainbow color spectrum corresponds to velocity magnitude (m/s) and grey scale color to displacement (m).

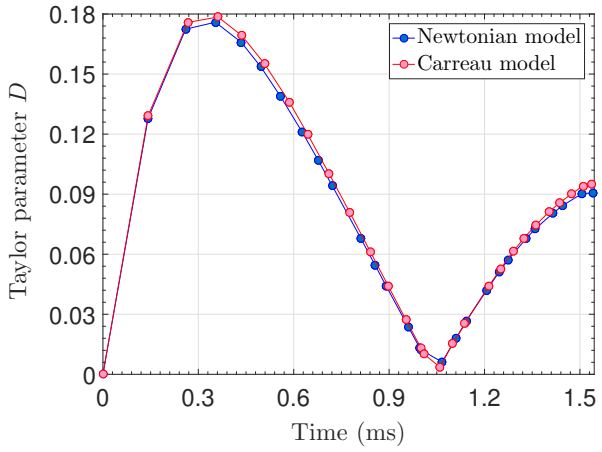

Fig. 5. Influence of the blood viscosity model for $Ca = 0.05$.

bullet shape (Figure 6(b)) and parachute shape (Figure 6(c)). The observation reported above (the increasing concavity with respect to capillary number) is confirmed by the last calculation. Indeed, at $t = 1\,\mathrm{ms}$, we note the transition from the convex rear end ($Ca = 0.01$ in Figure 6(a)), to the flattened rear end ($Ca = 0.05$ in Figure 6(b)) and then to the concave rear end ($Ca = 0.10$ in Figure 6(c)). The increasing front sharpness is also confirmed. Local zoomed mesh illustrated in (Figure 6(d)) affirms the absence of mesh tangling /distortion. All of reported shapes for all capillary numbers are observed for artificial microparticles flowing in rectangular microchannel [22–25], RBCs [19–21] and a cancerous cell (except for the parachute shape) [69].

The effect of increasing arteriole length is evaluated for $L = 900$ and $1800\,\mu$m. As for the initial length $L = 300\,\mu$m, the time-evolution of Taylor parameter is concavity sign changing (Figure 7). One can remarks that for $L = 1800\,\mu$m, the shape of the curve is identical to that of $L = 900\,\mu$m but "stretched". Even if the vascular resistance increases with length, we believe that the unsteadyness of Taylor parameter time-evolution will persists due to the mechanism of expansion-constriction that varies the viscous stresses acting on the microparticle (i.e. the capillary number).

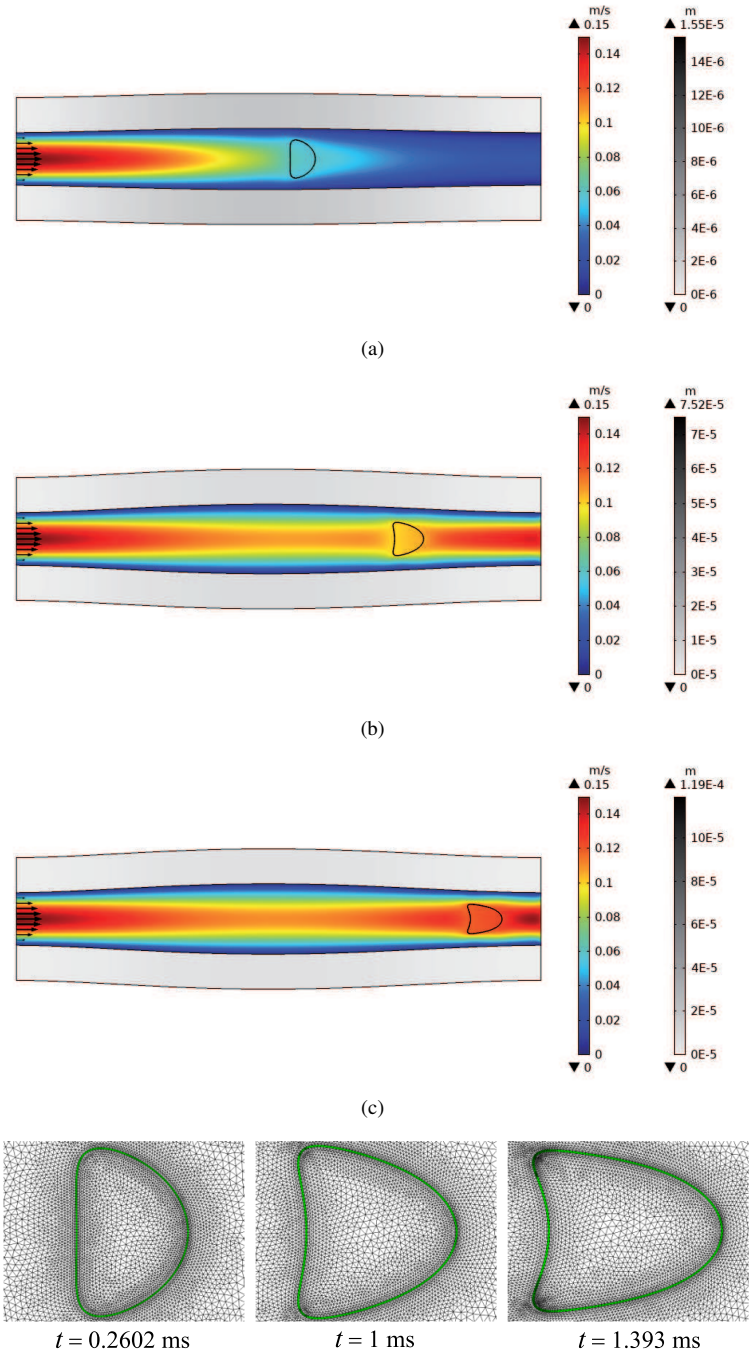

Fig. 6. Pebble-shaped microparticle at $t = 0.2602\,\text{ms}$ (a). Bullet-shaped microparticle at $t = 1\,\text{ms}$ (b). Parachute-shaped microparticle with a strongly concave rear end at $t = 1.393\,\text{ms}$ (c). Corresponding local mesh zoom (d).

4.3 Comparison with rigid microchannel

A comparison with a rigid microchannel is performed for $Ca = 0.05$. It is concluded that for a similar capillary number, the microparticle exhibits a different dynamical behavior. Indeed, when the microparticle is confined in the rigid channel, the Taylor parameter evolution with respect to time is ascending till the microparticle is stopped by the channel extremity (see Figure 8(a)). This evolution is akin when the microparticle is subjected to a shear flow [27, 68] or to an elongational flow [63]. Nevertheless, the horizontal plateau is not observed because of the edge effect. Moreover, various deformed shapes are observed for the hyperelastic arterial wall while the particle confined in the rigid channel is deformed into a quasi-steady shape (see Figures 8(b) and 8(c)). Time-snapshots show that at similar times ($t = 0.364, 0.698$ and $0.910\,\text{ms}$),

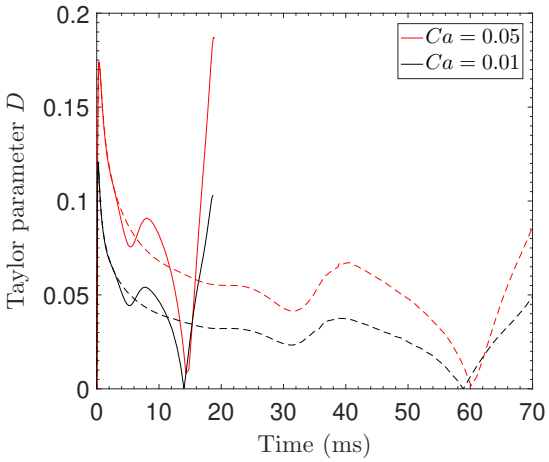

Fig. 7. Arteriole length effect on Taylor parameter. Solid lines are for $L = 900\,\mu$m and dashed lines for $L = 1800\,\mu$m.

deformed shapes are widely different. The deformation soars in the case of arterial wall whilst it progressively increases with respect to time (see Figure 8(a)). On the other hand, when the particle flows along the rigid microchannel, it attains the channel extremity at $t = 0.910\,$ms, while at the same time, the microparticle suspended in the arteriole is in the midway (see Figure 8(b)) which reveals that the microparticle moves with different velocities.

According to the microparticle rear end velocity time-evolution, the flowing particle in the rigid microchannel attains a maximum velocity before it decelerates quasi-instantly and tends to an asymptotic velocity (see Figure 9). Furthermore, the microparticle confined in arteriole accelerates along its course. Curves show that for the highest and the lowest capillary number ($Ca = 0.01$, $Ca = 0.05$), a slight gap exists till a certain time ($t \approx 0.3\,$ms) and the curves finally coincide. This result suggests that for any capillary number, velocity tends to a common magnitude.

All of observed discrepancies are due to the arterial wall distensibility and its hyperelastic response to the flow. The expansion-constriction changes the confinement and therefore the shear rate (i.e. viscous forces applied on the flowing particle). In these conditions, viscous forces applied on the microparticle are related to the wall displacement, leading to different deformed shapes for a same capillary number. In contrast, in the case of rigid microchannel, the microparticle is deformed into a quasi-steady shape. For a deformable wall, it is more appropriate to talk about an initial capillary number that correspond to the undeformed wall state.

4.4 Arteriole embedded in muscle

In this paragraph, we report the effect of the presence of a surrounding muscle on arteriolar wall displacement and on deformation of the microparticle. This configuration is more realistic than the FEW assumption. As expected, it is found that the presence of the muscle that serves as a uniform mechanical load, restricts both arteriolar wall vertical displacement (Figure 10(a)) [70] and microparticle deformation (Figure 10(b)). The higher the muscle thickness the less the arteriolar wall dilation upon blood flow. In the absence of the surrounding muscle, the maximum dilation of the arteriole (34.02%) is within the range of experimental dilation values reported for human coronary arteriole in [71]. The maximum of Taylor parameter is constant starting from $H_m = 35\,\mu$m. A comparison performed for $H_m = 60\,\mu$m and the rigid wall reveals that both configurations are quasi-identical (discrepancies are comprised between 0.89% and 4.31%.)

5 Implications of results in a medical context

Whether in the presence of the surrounding muscle ($H_m < 35\,\mu$m) or in its absence, it is found that microparticle deformation is increased comparing to the rigid wall assumption. In a context of medical application, an important deformation is potentially a risk of premature burst in the vicinity of a non-targeted environment which implies toxic effects on healthy tissues. Regarding the velocity, the arteriolar wall distensibility is found to decelerates the microparticle. Firstly, that means that the particle is in longer contact with RBCs and white blood cells and knowing that these biological cells (whose sizes are comparable to that of the studied microparticle) imposes stresses on microparticle membrane and consequently, a longer contact could result in an additional burst risk. Secondly, the microparticle could impedes bloodstream flow. These findings must imperatively be taken into account while designing microparticles in order to ensure a safe and efficient functioning of the drug-eluting microparticles.

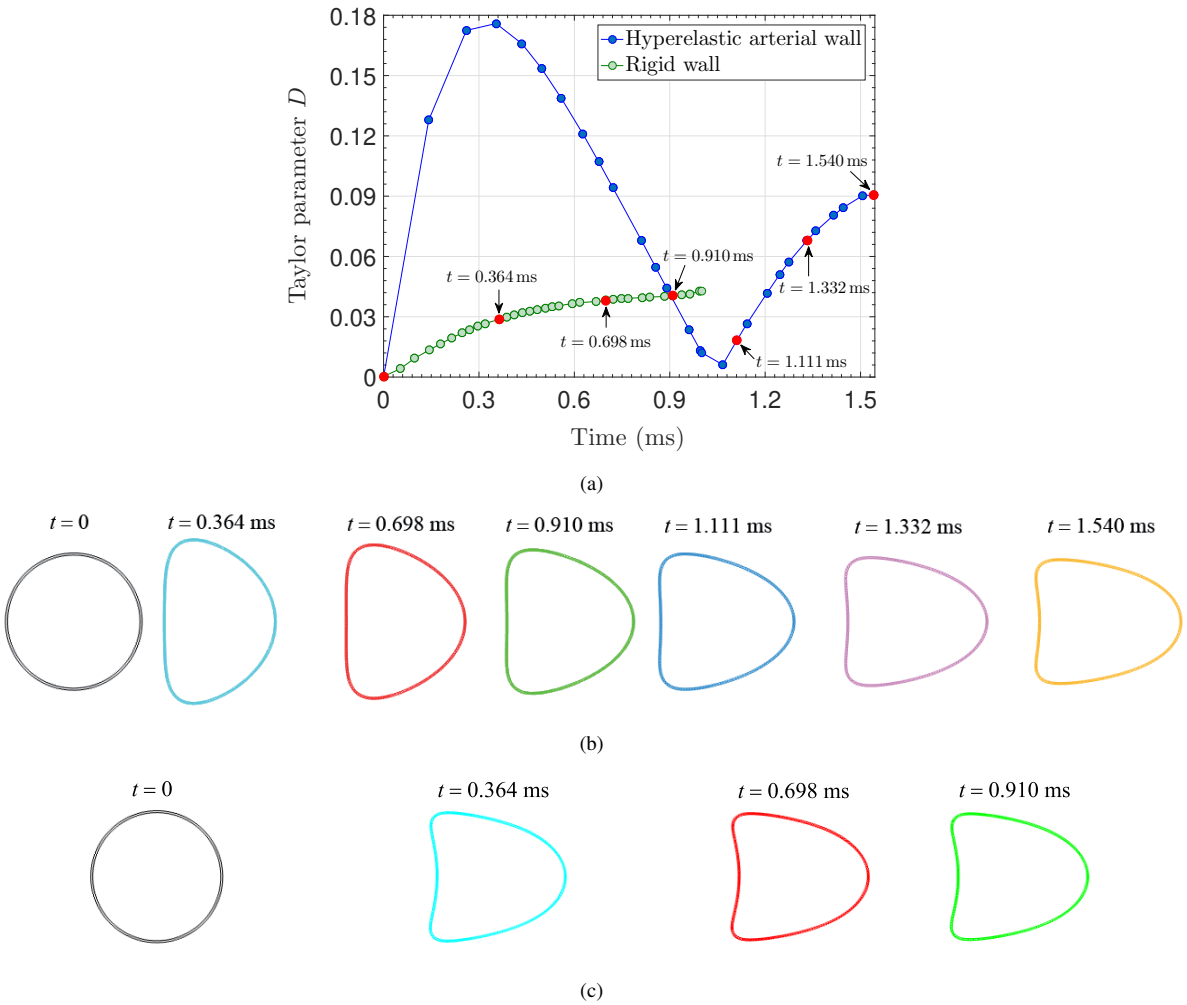

Fig. 8. Taylor parameter and microparticle deformed shapes for $Ca = 0.05$. (a) Red markers at specific times point out snapshot time used to capture deformed shapes. Real time snapshots of the microparticle flowing along the hyperelastic arteriole (b) and along the rigid microchannel (rigid wall) (c).

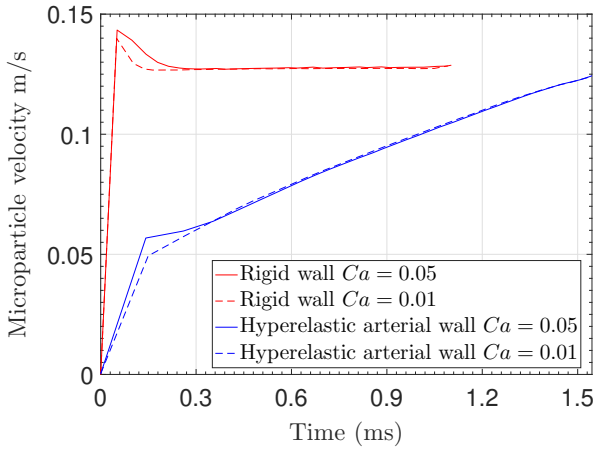

Fig. 9. Microparticle rear velocity for $Ca = 0.01$ and $Ca = 0.05$.

6 Conclusions

In this research paper, we investigate the dynamical behavior of a soft microparticle confined by hyperelastic arterial wall and suspended in blood flow, while fully respecting biomechanical constraints. Finding reveals that the wall distensibility

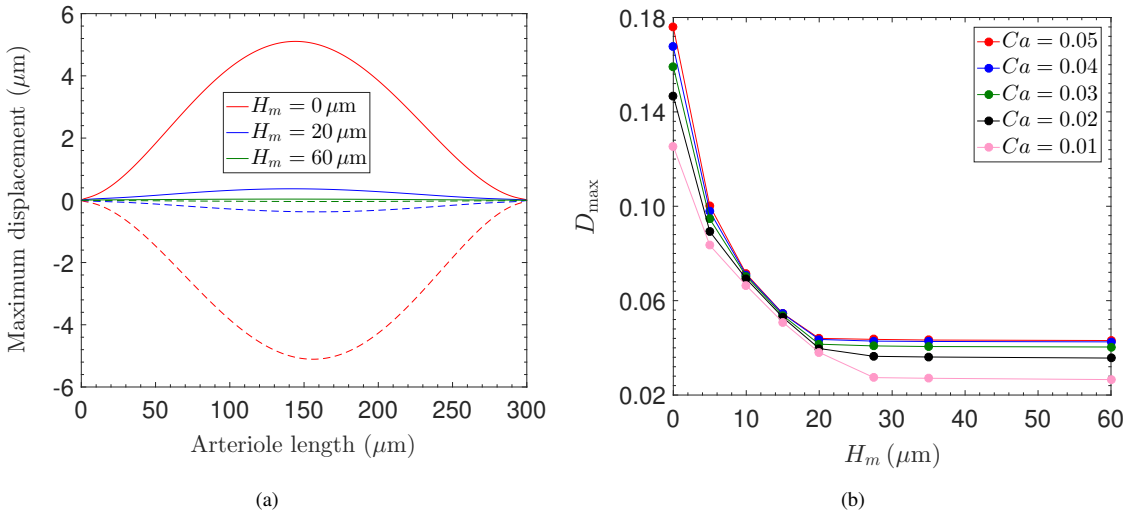

(a) (b)

Fig. 10. (a) Maximum arteriolar wall dilation with respect to arteriole length; Solid lines are for upper wall displacements and dashed lines for lower wall displacements. (b) Effect of varying muscle thickness on maximum Taylor parameter D_{max}.

has a great influence on microparticle deformation (qualitatively and quantitatively) and on its flowing velocity along the arteriole. We unambiguously outline the relevance of the inclusion of biomechanical constrains for an accurate prediction of microparticle dynamics, a prerequisite of a safe and proficient trageted drug-delivery procedure. This study is the first of its kind and further investigation remains necessary, in particular a realistic vessel geometry instead of the idealized geometry used for the sake of simplicity. The following concluding remarks could be drawn :

- The deformation and the velocity of the microparticle depend on mechanical properties of the wall.
- The displacement of the wall changes the shear rate an then the viscous forces applied on the microparticle membrane.
- The microparticle rear end and front shape transition ant their dependence on the capillary number are in good agreement with the numerical and experimental observations reported in numerous published studies.
- Deformed shapes are morphologically in excellent agreement with literature.

References

[1] O. V. Chumakova, A. V. Liopo, V. G. Andreev, I. Cicenaite, B. M. Evers, S. Chakrabarty, T. C. Pappas and R. O. Esenaliev. Composition of PLGA and PEI/DNA nanoparticles improves ultrasound-mediated gene delivery in solid tumors in vivo, *Cancer Lett.* **261**(2), 215–225 (2008).

[2] J. Shao, M. Xuan, T. Si, L. Dai and Q. He. Biointerfacing polymeric microcapsules for in vivo near infrared light-triggered drug release, *Nanoscale.* **7**(45), 19092–19098 (2015).

[3] J. Ma, L. Du, M. Chen, H. Wang, L. Xing, L. Jing and Y. Li. Drug-loaded nano-microcapsules delivery system mediated by ultrasound-targeted microbubble destruction: A promising therapy method, *Biomed. Reports,* **1**(4), 506–510 (2013).

[4] P. Soon-Shiong. Treatment of type I diabetes using encapsulated islet. *Adv. Drug Deliv. Rev.* **35**(2-3), 259–270 (1999).

[5] E. Mihalko, K. Huang, E. Sproul, K. Cheng and A. C. Brown. Targeted treatment of ischemic and fibrotic complications of myocardial infarction using a dual-delivery microgel therapeutic, *ACS Nano.* **12**(8), 7826–7837 (2018).

[6] M. R. Dreher, K. V. Sharma, D. L. Woods, G. Reddy, Y. Tang, W. F. Pritchard, O. A. Chiesa, J. W. Karanian, J. A. Esparza, D. Donahue, E. B. Levy, S. L. Willis, A. L. Lewis and B. J. Wood. Radiopaque Drug-Eluting Beads for Transcatheter Embolotherapy: Experimental study of Drug Penetration and Coverage in Swine, *Journal of Vascular and Interventional Radiology* **23(2)**, 257–264(2012).

[7] A. Hagan, M. Caineb, C. Pressb, W. M. Macfarlanea, G. Phillipsa, A. W. Lloyda, P. Czuczmanb, H. Kilpatrickb, Z. Bascalb, Y. Tangb, P. Garciab and A. L. Lewisb. Predicting pharmacokinetic behaviour of drug release from drug-eluting embolization beads using in vitro elution methods, *European Journal of Pharmaceutical Sciences* **136**, 104943 (2019).

[8] T. de Baere, S. Plotkin, R. Yu, A. Sutter, Y. Wu and G. M. Cruise. An In Vitro Evaluation of Four Types of Drug-Eluting Microspheres Loaded with Doxorubicin, *Journal of Computational Physics 2* **27**, 1425–1431(2016).

[9] K. Fuchs, P. E. Bize, O. Dormond A. Denys, E. Doelker, G. Borchard and O. Jordan. Drug-eluting beads loaded with antiangiogenic agents for chemoembolization: in vitro sunitinib loading and release and in vivo pharmacokinetics in an animal model, *Journal of Vascular and Interventional Radiology* **25(3)**, 379–387 (2014).

[10] R. R. Taylor, Y. Tang, M. V. Gonzalez, P. W. Stratford and A. L. Lewis. Irinotecan drug eluting beads for use in chemoembolization: In vitro and in vivo evaluation of drug release properties, *European Journal of Pharmaceutical Sciences* **30**, 7–14 (2007).
[11] J. M. Sosa, N. D. Nielsen, S. M. Vignes, T. G. Chen and S. S. Shevkoplyas. The relationship between red blood cell deformability metrics and perfusion of an artificial microvascular network, *Clin. Hemorheol. Microcirc.* **57**(3), 291–305 (2014).
[12] J. M. Burns, X. Yang, O. Forouzan, J. M. Sosa and S. S. Shevkoplyas. Artificial microvascular network: A new tool for measuring rheologic properties of stored red blood cells, *Transfusion,* **52**(5), 1010–1023 (2012).
[13] S. Hé, G. Lenormand, A. Richert and F. Ois Gallet. A new determination of the shear modulus of the human erythrocyte membrane using optical tweezers, *Biophysical. Journal.* **76**, 1145–1151 (1999).
[14] R. Hochmuth. Erythrocyte Membrane Elasticity And Viscosity. *Annu. Rev. Physiol.* **49**(1), 209–219 (1987).
[15] R. Waugh and E. A. Evans. Thermoelasticity of red blood cell membrane, *Biophys. Journal.* **26**(1), 115–131 (1979).
[16] E. A. Evans, R. Waugh and L. Melnik. Elastic area compressibility modulus of red cell membrane, *Biophys. Journal.* **6**, 585–595 (1976).
[17] M. A. Peterson, H. Strey and E. Sackmann. Theoretical and phase contrast microscopic eigenmode analysis of erythrocyte flicker: amplitudes, *J. Phys. II,* **2**(5), 1273–1285 (1992).
[18] E. Sackmann. The Seventh Datta Lecture Membrane bending energy concept of vesicle-and cell-shapes and shape-transitions, *FEBS Letters.* **346**(1), 3–16 (1994).
[19] H. Noguchi and G. Gompper. Shape transitions of fluid vesicles and red blood cells in capillary flows, *Proc. Natl. Acad. Sci.* **102**(40), 14159–14164 (2005).
[20] G. Tomaiuolo, L. Lanotte, R. D'Apolito, A. Cassinese and S. Guido. Microconfined flow behavior of red blood cells, *Med. Eng. Phys.* **38**(1), 11–16 (2016).
[21] B. Kaoui, G. Biros and C. Misbah. Why do red blood cells have asymmetric shapes even in a symmetric flow? *Phys. Rev. Lett.* **103**(18) (2009).
[22] G. Coupier, A. Farutin, C. Minetti, T. Podgorski and C. Misbah. Shape diagram of vesicles in poiseuille flow, *Phys. Rev. Lett.* **108**(17) (2012).
[23] S. Kuriakose and P. Dimitrakopoulos. Deformation of an elastic capsule in a rectangular microfluidic channel, *Soft Matter* **9**(16), 4284–4296 (2013).
[24] X. Q. Hu, B. Sévénié, A. V. Salsac, E. Leclerc and D. Barthès-Biesel. Characterizing the membrane properties of capsules flowing in a square-section microfluidic channel: Effects of the membrane constitutive law, *Phys. Rev. E - Stat. Nonlinear, Soft Matter Phys.* **87**(6), (2013).
[25] J. Gubspun, C. de Loubens, R. Trozzo, J. Deschamps, M. Georgelin, F. Edwards-Levy and J. M. Leonetti. Perturbations of the flow induced by a microcapsule in a capillary tube, *Fluid Dyn. Res.* **49**(3) (2017).
[26] M. Rachik, D. Barthès-Biesel, M. Carin and F. Edwards-Levy. Identification of the elastic properties of an artificial capsule membrane with the compression test: Effect of thickness, *J. Colloid Interface Sci.* **301**(1), 217–226 (2006).
[27] M. Husmann, H. Rehage, E. Dhenin and D. Barthès-Biesel. Deformation and bursting of nonspherical polysiloxane microcapsules in a spinning-drop apparatus, *J. Colloid Interface Sci.***282**, 109–119 (2005).
[28] Y. Lefebvre, E. Leclerc, D. Barthès-Biesel, J. Walter and F. Edwards-Lévy. Flow of artificial microcapsules in microfluidic channels: A method for determining the elastic properties of the membrane, *Phys. Fluids,* **20**(12) (2008).
[29] R. M. Kleinberger, N. A. D. Burke, K. Dalnoki-Veress and H. D. H. Stover. Systematic study of alginate-based microcapsules by micropipette aspiration and confocal fluorescence microscopy, *Mater. Sci. Eng. C* **33**(7), 4295–4304 (2013).
[30] M. Carin, D. Barthès-Biesel, F. Edwards-Lévy, C. Postel and D. C. Andrei. Compression of biocompatible liquid-filled HSA-alginate capsules: Determination of the membrane mechanical properties, *Biotechnol. Bioeng.* **82**(2), 207–212 (2003).
[31] Z. Wang, Y. Sui, A. V. Salsac, D. Barthès-Biesel and W. Wang. Motion of a spherical capsule in branched tube flow with finite inertia, *J. Fluid Mech.* **806**, 603–626 (2016).
[32] Y. Lefebvre and D. Barthès-Biesel. Motion of a capsule in a cylindrical tube: Effect of membrane pre-stress, *J. Fluid Mech.* **589**, 157–181 (2007).
[33] D. Barthès-Biesel, A. Diaz and E. Dhenin, Effect of constitutive laws for two-dimensional membranes on flow-induced capsule deformation, *J. Fluid Mech.* **460**, 211–222 (2002).
[34] A. Leyrat-Maurin and D. Barthès-Biesel. Motion of a Deformable Capsule Through a Hyperbolic Constriction, *J. Fluid Mech.* **279**, 135–163 (1994).
[35] Z. X. Gong and C. J. Lu. Research on the spherical capsule motion in 3D simple shear flows, *J. Shanghai Jiaotong Univ.* **15**(6), 702–706, (2010).
[36] X. Q. Hu, A. V. Salsac and D. Barthès-Biesel. Flow of a spherical capsule in a pore with circular or square cross-section, *J. Fluid Mech.* **705**, 176–194 (2012).
[37] P. Pranay, S. G. Anekal, J. P. Hernandez-Ortiz and M. D. Graham. Pair collisions of fluid-filled elastic capsules in shear

flow: Effects of membrane properties and polymer additives, *Phys. Fluids* **22** (2010).
[38] D. Barthès-Biesel and J. M. Rallison. The time-dependent deformation of a capsule freely suspended in a linear shear flow, *J. Fluid Mech.* **113**, 251–267 (1981).
[39] R. Skalak, A. Tozeren, R. P. Zarda and S. Chien. Strain Energy Function of Red Blood Cell Membranes, *Biophys. J.* **13**(3), 245–264 (1973).
[40] E. A. Evans and R. Skalak. *Mechanics and thermodynamics of biomembranes* **35**, CRC Press (1980).
[41] O. H. Yeoh. Some Forms of the Strain Energy Function for Rubber, *RUBBER Chem. Technol.* **66**(5), 754–771 (1993).
[42] A. Diaz, N. Pelekasis and D. Barthès-Biesel. Transient response of a capsule subjected to varying flow conditions: Effect of internal fluid viscosity and membrane elasticity, *Phys. Fluids* **12**(5), 948–957 (2000).
[43] C. Dupont, P. Le Tallec, D. Barthès-Biesel, M. Vidrascu and A. V. Salsac. Dynamics of a spherical capsule in a planar hyperbolic flow: Influence of bending resistance, *Procedia IUTAM* **16**, 70–79 (2015).
[44] S. Kwak and C. Pozrikidis. Effect of membrance bending stiffness on the axisymmetric deformation of capsules in uniaxial extensional flow, *Phys. Fluids* **13**(5), 1234–1242 (2001).
[45] C. Pozrikidis. Effect of membrane bending stiffness on the deformation of capsules in simple shear flow, *J. Fluid Mech.* **440**, 269–291 (2001).
[46] N. Tahiri. Simulation de Globules Rouges modèles, et analyse analytique de modèles de suspensions très concentrées, Université de Grenoble et Université Mohammed V Rabat (2010).
[47] Comsol Multiphysics, Analysis User's Manual Version 5.2 (2016).
[48] D. E. Brooks, J. W. Goodwin and G. V Seaman. Interactions among erythrocytes under shear, *J. Appl. Physiol.* **28**(2), 172–177 (1970).
[49] S. Chien. Shear dependence of effective cell volume as a determinant of blood viscosity, *Science* **168**(3934), 977–979 (1970).
[50] S. A. Berger and L. D. Jou. Flows in Stenotic Vessels, *Annu. Rev. Fluid Mech.* **32**(1), 347–382, (2002).
[51] A. M. Robertson, A. Sequeira and M. V. Kameneva. *Hemodynamical flows Oberwolfach Seminars*, 37th ed. Birkhauser Verlag (2008).
[52] G. Koutsiaris, S. V. Tachmitzi and N. Batis. Wall shear stress quantification in the human conjunctival pre-capillary arterioles in vivo, *Microvasc. Res.* **85**(1), 34–39 (2013).
[53] I. C. Young and R. Kenneth. Effects of the non-Newtonian viscosity of blood on flows in a diseased arterial vessel. Part 1: steady flows, *Biorheology* **28**(199), 241–262 (1991).
[54] J. R. Womersley. Method for the calculation of velocity, rate of flow and viscous drag in arteries when the pressure gradient is known, *J. Physiol* **127**, 553–563 (1955).
[55] C. G. Caro, T. J. Pedley, R. C. Schroter, W. A. Seed. The Mechanics of the circulation, **35**(1st ed. Oxford University Press, 1978).
[56] D. N. Ku. Blood flow in arteries, *Annu. Rev. Fluid Mech.* **29**(1), 399–434 (1997).
[57] K. E. Barrett, S. M. Barman, S. Boitano and H. Brooks. *Ganong's Review of Medical Physiology*, 23th ed. McGraw Hill Medicall (2012).
[58] A. Taki, A. Kermani, S. M. Ranjbarnavazi and A. Pourmodheji, Chapter 4 - Overview of Different Medical Imaging Techniques for the Identification of Coronary Atherosclerotic Plaques, *Computing and Visualization for Intravascular Imaging and Computer-Assisted Stenting* 1st ed. Academic Press (2017).
[59] G. A. Holzapfel, G. Sommer, C. T. Gasser and P. Regitnig. Determination of layer-specific mechanical properties of human coronary arteries with nonatherosclerotic intimal thickening and related constitutive modeling, *Am. J. Physiol. Circ. Physiol.* **289**(5), 2048–2058 (2005).
[60] A. Gholipour, M. H. Ghayesh, A. Zander and R. Mahajan. Three-dimensional biomechanics of coronary arteries, *Int. J. Eng. Sci.* **130**(130), 93–114 (2018).
[61] L. A. Martinez-Lemus. The Dynamic Structure of Arterioles, *Basic Clinical Pharmacology Toxicology* **110**, 5–11(2012).
[62] T. A. Cheema and C. W. Park. Numerical investigation of hyperelastic wall deformation characteristics in a micro-scale stenotic blood vessel, *Korea-Australia Rheology* **25**, 121–127(2013).
[63] C. De Loubens, J. Deschamps, M. Georgelin, A. Charrier, F. Edwards-Levy and M. Leonetti. Mechanical characterization of cross-linked serum albumin microcapsules, *Soft Matter* **10**(25), 4561–4568 (2014).
[64] L. A. Taber. Nonlinear Theory of Elasticity: Applications in Biomechanics, World Scientific Publishing Co Pte Ltd (2004).
[65] P. Deuflhard. A modified Newton method for the solution of ill-conditioned systems of nonlinear equations with alication to multiple shooting, *Numerische Mathematik* **22**, 289–315(1974).
[66] P. K. Moore and L. R. Petzold. A Stepsize Control Strategy for Stiff Systems of Ordinary Differential Equations,*Alied Numerical Mathematics* **15**, 449–463 (1994).
[67] A. M. Winslow. Numerical solution of the quasilinear poisson equation in a nonuniform triangle mesh *Journal of Computational Physics 2* **1(2)**, 149–172 (1967).

[68] E. Lac, D. Barthès-Biesel, N. A. Pelekasis and J. Tsamopoulos. Spherical capsules in three-dimensional unbounded Stokes flows: Effect of the membrane constitutive law and onset of buckling, *J. Fluid Mech.* **35**(516), 303–334 (2004).

[69] M. Dabagh, A. Randles. Role of deformable cancer cells on wall shear stress- associated-VEGF secretion by endothelium in microvasculature, *PLoS ONE.* **14** (2), (2019).

[70] N. Westerhof, C. Boer, R. R. Lamberts and P. Sipkema. Cross-Talk Between Cardiac Muscle and Coronary Vasculature, *Physiological Reviews* **86**, 1263–1308(2006).

[71] H. Miura, R. E. Wachtel, Y. Liu, F. R. Loberiza, T. Saito, M. Miura and D. D. Gutterman. Flow-Induced Dilation of Human Coronary Arterioles Important Role of Ca^2+ Activated K^+Channels, *Circulation* **103**, 1992–1998 (2001).

3.2.2.2 A02

Journal of Mechanics in Medicine and Biology
Vol. 21, No. 8 (2021) 2150062 (25 pages)

DOI: 10.1142/S0219519421500627

World Scientific
www.worldscientific.com

EFFECT OF ARTERIOLAR DISTENSIBILITY ON THE LATERAL MIGRATION OF LIQUID-FILLED MICROPARTICLES FLOWING IN A HUMAN ARTERIOLE

IMANE EL JIRARI*, ADIL EL BAROUDI† and AMINE AMMAR‡
LAMPA, Arts et Metiers Institute of Technology
49035 Angers, France
**imane.eljirari@ensam.eu*
†*adil.elbaroudi@ensam.eu*
‡*amine.ammar@ensam.eu*

Received 28 May 2021
Accepted 5 September 2021
Published 15 October 2021

A promising advance of bioengineering consists in the development of micro-nanoparticles as drug delivery vehicles injected intravenously or intraarterialy for targeted treatment. Proficient functioning of drug carries is conditioned by a reliable prediction of pharmacokinetics in human as well as their dynamical behavior once injected in blood stream. In this study, we aim to provide a reliable numerical prediction of dynamical behavior of microparticles in human arteriole focusing on the crucial mechanism of lateral migration. The dynamical response of the microparticle upon blood flow and arteriolar distensibility is investigated by varying main controlling parameters: viscosity ratio, confinement and capillary number. The influence of the hyperelastic arteriolar wall is highlighted through comparison with an infinitely rigid arteriolar wall. The hydrodynamic interaction in a microparticle train is examined. Fluid–structure interaction is solved by the Arbitrary Lagrangian–Eulerian method using the COMSOL Multiphysics software.

Keywords: Human arteriole; arteriolar distensibility; lateral migration; microparticles; drug delivery.

1. Introduction

Microparticles are artificial microstructures used as drug delivery vectors[1,2] to remedy the limitations of chemotherapy and invasive treatments. Therapeutic applications include targeted treatment of cancerous tumor[3] and thrombus.[4] These microparticles consist of a thin-walled membrane made of lipid, protein or polymer enclosing a small amount of liquid drug and having common physical properties with Red Blood Cell (RBC) and very similar dynamic in flow,[5,6] enabling their use as a simplified model of RBC. The dynamical behavior of the drug carries and

† Corresponding author.

pharmacokinetic behavior of the coated drug is investigated *in vivo*[7] and *in vitro*.[8] The validation and optimization of microparticles functioning to successfully meet higher therapeutic demands require a robust prediction of their dynamical behavior under blood flow and constraints imposed by vascular walls. The inertial lateral migration of microparticle in microfluidic devices in the absence of external force field is a physical phenomenon related to intrinsic hydrodynamical forces and channel geometry. The prominent microfluidic applications are bio-particle manipulation, particularly bioparticle fractionation (e.g., pinched flow fractionation and Dean flow fractionation[9]), filtration[10] and focusing.[11] Lateral migration is a relevant blood viscosity determinant in microvessels (diameter less than 500 μm), where RBCs migrates toward vessel centreline owing the creation of a cell-free layer, thereby decreasing the blood apparent viscosity (Fahræus effect). The lateral migration of microparticles in the absence of inertia or in finite inertia is an intriguing phenomenon that comes with broken microparticle symmetry (fore-aft asymmetric rigid microparticle or deformable microparticle). Numerous studies dealt with non-inertial lateral migration for artificial deformable microparticle[12,13] and for RBC.[14] The lateral migration of RBCs and artficial microparticles in a wall-bounded Poiseuille flow results from an interplay of four lateral forces: wall-induced lift force resulting from the disturbance of flow field induced by the presence of the microparticle and its reflection at the wall (the confinement induced repulsive wall force), shear-gradient lift force due to the curvature of undisturbed fluid velocity profile, Rubinow–Keller lift due to slip-rotation lift force and Saffman lift force due to the interaction of slip velocity and shear. Besides the aforementioned lateral forces, a viscous drag acts in streamlines. Drag results from the relative velocity of the microparticle to the fluid. First revealed in Ref. 15, the deformability induced lift force is responsible of migration of elastic microparticles in the absence of inertia.[16] Deformability-induced lift is the key biomarker factor in malaria diagnosis since malaria-infected RBCs get stiffer and undergo a sidewalls margination while healthy RBCs migrates toward the centerline[17] (artificially hardened RBCs mimic the same behavior[18]). A controlling parameter in migration is the particle Reynolds number Re_p which determine if migration is of inertial or viscous origin. For particle Reynolds number much less than unity, viscous forces dominates and the microparticles drift from streamlines due to their asymmetry while for greater Re_p, the microparticle migrates due to inertial forces. The migration path, velocity and the equilibrium positions are found to depend on elastic properties of the microparticle,[19,20] inertia,[21,22] viscosity contrast between internal and external fluids,[23,24] confinement[20,24] and on the initial microparticle position.[25]

In Ref. 26, Beaucourt and co-workers studied the migration of an artificial microparticle as an RBC simplified model confined in a capillary, for the sake of simplicity, authors limited the contribution of the deformable capillary wall to a local elastic response. Authors show that the elastic capillary wall exerts a normal force compensating the lift force acting on the studied RBC model, guaranteeing equilibrium of the mechanical system. More recently in Ref. 27, authors studied the effect

of the arterial wall distensibility on deformation and velocity of a single microparticle, without any consideration of lateral migration. To our knowledge, apart from the two aforementioned studies none of published papers involve the contribution of vascular wall, let alone the influence of its complex mechanical behavior on lateral migration of microparticles. This paper aims to fill the lack of numerical studies on dynamical behavior of microparticle confined in blood vessels in literature, in particular on the migration process. To achieve this aim, the migration and the overall dynamical behavior are numerically investigated for a single isolated microparticle and for a train of three microparticles confined in a hyperplastic arteriolar wall and in an infinitely rigid arteriolar wall, while varying the confinement, the viscosity ratio and the capillary number. The numerical investigation is performed in COMSOL Multiphysics software package, the 2D fluid–structure interaction FSI nonlinear problem is solved using the Arbitrary Lagrangian–Eulerian method, with a monolithic approach.

2. Mathematical Model

The computational domain (Fig. 1) consists of a thin hyperelastic circular membrane enclosing an internal fluid, freely suspended in a confined external Poiseuille flow (blood). External and internal fluids are similar and the microparticle is neutrally buoyant since there is no contrast between both fluid densities. The idealized straight arteriole $L = 900\,\mu$m is represented by a rectangular channel on which we distinguish the lumen (the interior space of the arteriole through which blood flows) $H_l = 30\,\mu$m and surrounding arteriolar wall $H_a = 20\,\mu$m. The coordinates of the centre of mass (x_c, y_c) are monitored over simulation. At the initial time, the microparticle is placed at $x_c/L = 0.5$ and $y_c/H_l = 0.27$. The inlet velocity v_i and the outlet normal stress are applied at (Γ_i) and at (Γ_o), respectively. Two FSI interfaces are identified: fluid domain-membrane (Γ_{fm}) and fluid-arteriolar wall (Γ_{fa}).

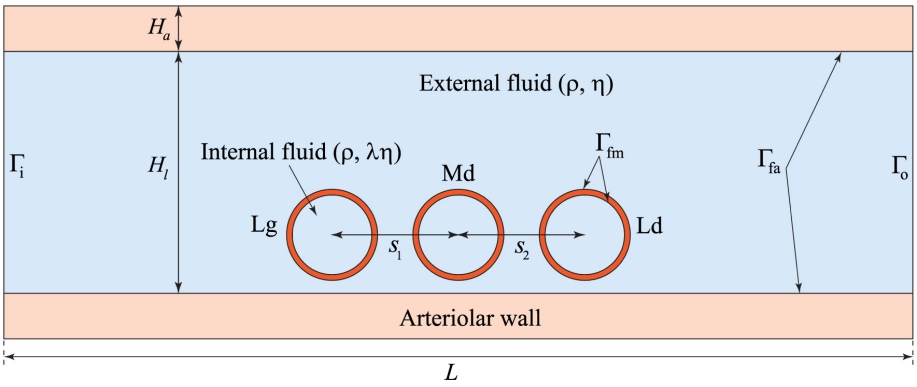

Fig. 1. Schematic drawing of the numerical model. Abbreviations Lg, Md and Ld denote the lagging, the middle and the leading microparticle, respectively. The single isolated microparticle configuration corresponds to an isolated middle microparticle.

2.1. *Arteriolar wall*

Arterioles are muscular blood vessels that are able to dilate for purposes of regulate the vascular tone and maintain vascular permeability. Arteriolar wall comprises three layers (intima, media and adventitia) composed of smooth muscle cells, endothelial cells and collagen fibres. These components are dynamically interconnected making the frontiers blurred between the three layers. We limit the arteriolar wall to the inner layer (the intima) which is modeled as a nearly-incompressible hyperelastic material[28] following the neo-Hookean solid model (Eq. (3)). The equation describing the motion of the arteriolar wall is given by

$$\rho_a \frac{\partial^2 \mathbf{u}^{(a)}}{\partial t^2} = \nabla \cdot \boldsymbol{\sigma}^{(a)}, \tag{1}$$

where $\rho_a = 960$ (kg/m^3) is the arteriolar wall density, $\mathbf{u}^{(a)}$ the displacement vector and $\boldsymbol{\sigma}^{(a)}$ the Cauchy stress tensor

$$\boldsymbol{\sigma}^{(a)} = J^{-1}\mathbf{F}\frac{\partial W^{(a)}}{\partial \mathbf{E}^{(a)}}\mathbf{F}^T. \tag{2}$$

Here, J is the dilatation ratio, $\mathbf{F}$ the deformation gradient tensor, $\mathbf{E}^{(a)}$ the Green–Lagrange strain tensor and $W^{(a)}$ the strain energy density function whose nearly-incompressible form is written as

$$W^{(a)} = \frac{G^{(a)}}{2}(\bar{I}_{1,a} - 3) + \frac{\kappa}{2}(J-1)^2, \tag{3}$$

where $G^{(a)} = 6.2$ (MPa) is the shear modulus, $\bar{I}_{1,a}$ the first invariant of the isochoric right Cauchy–Green deformation tensor and $\kappa = 124$ (MPa) the initial bulk modulus. The deformable arteriolar wall that follows the neo-Hookean law (Eq. (3)) is denoted as DAW, while the infinitely rigid arteriolar wall is denoted as RAW.

2.2. *Blood flow*

In arteriolar blood circulation, the shear rate exceeds 100 (s^{-1}) and blood is Newtonian.[29] In a physiological context, the Womersley number α measures the ratio of unsteady inertial forces to viscous forces, for $\alpha \leq 2$ unsteadiness is neglected and the flow is parabolic ($\alpha \leq 0.04$ in the arteriole), the profile is blunted (plug flow) for $\alpha \leq 10$ (see Ref. 30). A fully-developed Poiseuille flow is imposed at the inlet of the arteriole

$$v_i = 4v_{\max}\frac{y}{H_l}\left(1 - \frac{y}{H_l}\right) \quad \text{at } \Gamma_i (0 \leq y \leq H_l), \tag{4}$$

where y is the ordinate. The maximum velocity $v_{\max} = 17$ (mm/s) located at $y = H_l/2$ is the peak velocity in human arteriol.[31]

The fluids inside and outside microparticle are treated as incompressible, and therefore the mass conservation equation is written in the following form:

$$\nabla \cdot \mathbf{v} = 0. \tag{5}$$

Note that the presence of microparticle has no effect on the density and viscosity of the fluid phases inside and outside microparticle. In addition, the total stress in the fluid is expressed as

$$\boldsymbol{\sigma} = -p\mathbf{I} + \eta[\nabla\mathbf{v} + (\nabla\mathbf{v})^T], \tag{6}$$

where p denotes the fluid pressure, $\mathbf{I}$ the identity tensor, $\mathbf{v}$ the velocity field and $\eta = 0.00345$ (Pa · s) the dynamic viscosity of the external fluid. The product $\lambda\eta$ denotes the internal fluid dynamic viscosity where $\lambda = 0.5 - 2$ is viscosity ratio. Here, the fluid domain is governed by the following Navier–Stokes equation in the absence of body forces

$$\rho\left[\frac{\partial\mathbf{v}}{\partial t} + (\mathbf{v}\cdot\nabla)\mathbf{v}\right] = -\nabla p + \eta\nabla^2\mathbf{v}, \tag{7}$$

where $\rho = 1060$ (kg/m^3) is the fluid density.

2.3. *Microparticle*

The membrane is assumed to be homogeneous, isotropic, impermeable and incompressible. As in Refs. 32 and 33, the membrane is treated as a very thin hyperelastic surface of thickness h devoid of bending stiffness. With neglecting the bending stiffness, we consider that membrane deformation occurs only in-plane and thus the normal vector to the surface remains normal during the deformation. In the absence of bending moment, transverse shear forces vanishes. The bending of a membrane is primarily governed by two elastic parameters: its spontaneous (or preferred) curvature and its bending stiffness κ_b. For artificial microparticles with a thin homogeneous wall, the bending stiffness κ_b is directly related to the membrane thickness h

$$\kappa_b = \frac{E^{(m)}h^3}{12(1-\nu^2)}. \tag{8}$$

The dimensionless form proposed in Ref. 34 is

$$\tilde{\kappa}_b = \frac{h^2}{12(1-\nu^2)R^2}, \tag{9}$$

where $\tilde{\kappa}_b$ is the inverse of the Foppl-von Karman-number. The product $E^{(m)}h$ refers to surface Young's modulus, R denotes the initial microparticle radius and ν the Poisson ratio. In this paper $\tilde{\kappa}_b = 0.0001$, this value is in concordance with experimental values of artificial microparticle membrane ($\tilde{\kappa}_b \simeq 0.00005 - 0.01$)[34,35] and with RBC ($\tilde{\kappa}_b \sim 0.0001$).[34] As in Refs. 20 and 36, the membrane hyperelasticity follows the strain-softening neo-Hookean law, which is found to appropriately model the mechanical behavior of protein-reticulated membranes.[37] Since the membrane is incompressible, Eq. (3) becomes

$$W^{(m)} = \frac{G^{(m)}}{2}(\bar{I}_{1,m} - 3) \tag{10}$$

and Cauchy stress

$$\boldsymbol{\sigma}^{(m)} = \mathbf{F}^{(m)} \frac{\partial W^{(m)}}{\partial \mathbf{E}^{(m)}} \mathbf{F}^{(m)T}. \tag{11}$$

Microparticle dynamics is controlled by dimensionless numbers: confinement $c = 2R/H_l$, particle Reynolds number $\mathrm{Re}_p = \rho v_{\max} R^2/(\eta H_l)$ which gives the relative importance of intertial and viscous forces, viscosity ratio λ between the internal and the external fluids and the capillary number $\mathrm{Ca} = \eta v_{\max}/G^{(m)}/h$ which measures ratio of viscous forces to the elastic resistance of membrane, the time in non-dimensionlized by the shear rate $t^* = \dot{\gamma} t$.

2.4. *Boundary conditions*

A zero-displacement constraint is applied at outer ends of arteriolar wall. The FSI pertaining the fluids satisfies the kinetic continuity

$$\begin{aligned} \mathbf{v} &= \frac{\partial \mathbf{u}^{(m)}}{\partial t} \quad \text{at } \Gamma_{\mathrm{fm}}, \\ \mathbf{v} &= \frac{\partial \mathbf{u}^{(a)}}{\partial t} \quad \text{at } \Gamma_{\mathrm{fa}}, \end{aligned} \tag{12}$$

representing mass conservation throughout the interface, and the FSI for the solids satisfies the dynamic continuity

$$\begin{aligned} \boldsymbol{\sigma} \cdot \mathbf{n} &= \boldsymbol{\sigma}^{(m)} \cdot \mathbf{n} \quad \text{at } \Gamma_{\mathrm{fm}}, \\ \boldsymbol{\sigma} \cdot \mathbf{n} &= \boldsymbol{\sigma}^{(a)} \cdot \mathbf{n} \quad \text{at } \Gamma_{\mathrm{fa}}, \end{aligned} \tag{13}$$

describing the equivalence of fluids stresses and solids stresses. Furthermore, let $\mathbf{v}_m$ denote the dynamic mesh velocity and $\mathbf{n}$ the outer unit normal vector. At FSI interfaces, mesh velocity satisfies

$$\mathbf{v}_m \cdot \mathbf{n} = \mathbf{v} \cdot \mathbf{n}. \tag{14}$$

2.5. *Numerical method*

The ALE was developed to combine the advantages of the purely Eulerian description and the purely Lagrangian description (see Ref. 38). The fundamental equation for ALE gives the variation of a physical quantity f for a given particle X as

$$\left.\frac{\partial f}{\partial t}\right|_X = \left.\frac{\partial f}{\partial t}\right|_\chi + \frac{\partial f}{\partial x} \cdot (\mathbf{v}_m - \mathbf{v}), \tag{15}$$

where χ identifies referential gird coordinates and X denotes the spatial coordinates. The equations of the system are integrated over time using a first or second order accurate multistep implicit Backward Differentiation Formula scheme. The variables are updated at each time-step using a damped Newton nonlinear method.[39] The discretization of the fluid domain is done with P2/P1 element that gives a quadratic

basis for velocity and linear for pressure. In order to prevent numerical instabilities, two consistent stabilization methods were introduced: streamline diffusion and crosswind diffusion. The first adds artificial diffusion in the streamline direction whereas the second adds diffusion in the cross direction. The mesh deformation is calculated using different nonlinear smoothing approaches: Winslow, Hyperelastic and Yeoh. The smoothing method is selected depending on divergence problem that occurs and element distorsion. Hyperelastic and Yeoh smoothing are both inspired by hyperelastic mechanical laws (neo-Hookean and Yeoh, respectively). A remeshing is automatically generated when mesh quality falls below a specified mesh quality threshold based on equiangular skewness or distortion.

3. Results and Discussion

3.1. *Validation*

In this section, we report the validation of the present numerical model by comparing our results to Ref. 20, where microparticle deformation is calculated using a mixed finite-difference/Fourier transform method for the flow solver and a front-tracking method for the deformable interface. The neo-Hookean membrane is incompressible and internal and external fluid are similar (Newtonian and incompressible). The microparticle is confined in a rigid microchannel and migrates upon a pressure-driven Poiseuille flow v_i

$$v_i = -\frac{1}{2\eta}\frac{dp}{dx}(H_l y - y^2), \tag{16}$$

where $dp/dx = \text{cte}$ is the pressure gradient and x the abscissa. The migration history is plotted over a range of capillary numbers $\text{Ca} = 0.1 - 0.8$ in Fig. 2. The discrepancies in temporal evolution of migration between this work and the work of[20]

$$\frac{|\text{Present} - \text{Ref. [20]}|}{\text{Ref. [20]}} \times 100$$

are presented in Table 1. Qualitatively, results are in excellent agreement with Ref. 20. Quantitatively, discrepancies are found to increase with increasing microparticle stiffness (decreasing Ca) but remain acceptable (11.16% at most).

3.2. *Lateral migration in human arteriole*

3.2.1. *Lift and drag*

The lateral migration results from an intricate interplay of wall-induced lift f_W, shear-gradient induced lift f_{SG}, deformability induced lift force f_{Def}, deformable wall force f_{DW} and drag f_{drag}.

The wall exerts a repulsive translational force perpendicular to flow stream on the microparticle that is pushed away from the wall toward the centerline, this force is known as wall-induced lift f_W. The wall repulsive force originates from the stresslet

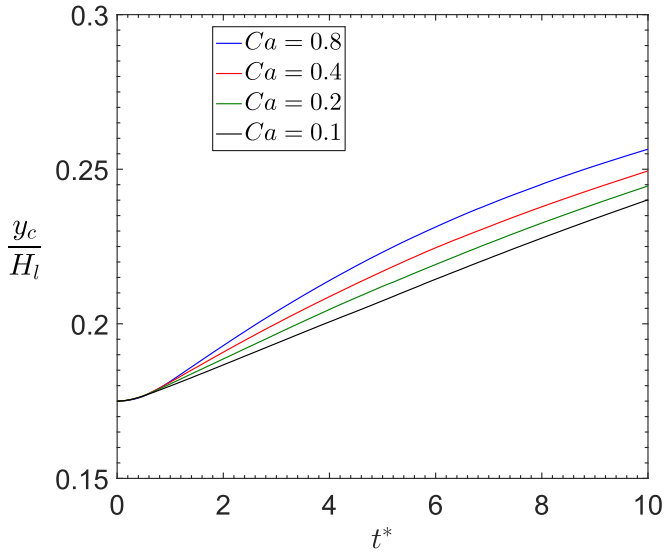

Fig. 2. Microparticle lateral migration history in a pressure-driven flow.

Table 1. Validation: comparison[a] of microparticle lateral position at specific dimensionless times.

	t^*				
Ca	2	4	6	8	10
0.1	0.38%	2.88%	5.63%	8.44%	11.16%
0.2	0.71%	0.82%	1.94%	3.37%	4.97%
0.4	1.13%	0.57%	0.18%	0.78%	1.40%
0.8	0.03%	0.71%	0.04%	0.35%	0.19%

Note: [a]Comparison with Ref. 20.

field induced by the microparticle in presence of the wall[40] (the symmetric component of the first moment of the force per unit area at the microparticle surface). The stresslet contribution is decomposed into viscosity ratio contribution and particle shape contribution. In Ref. 41, authors showed the existence of a viscoelatsic contribution in stresslet. The migration velocity near a rigid wall is inherently dependant on the stresslet since the migration velocity is the wall reflection of the disturbance velocity (stresslet) of the spherical microparticle.

The migration away from the wall leads to a pressure gradient across the microparticle membrane and hence, in a relative velocity magnitude that is higher near the wall where the shear is maximal. This results in an extra lift force directed toward the nearest wall, known as shear-gradient lift force f_{SG}. The contribution of shear gradient is a function of the channel width and distance to the wall, with no dependence on the magnitude of the shear rate or the shear gradient.[24]

Microparticle deformability takes indirectly part in migration via fore-aft symmetry breaking. The presence of the soft microparticle near the wall broke the

fore-aft symmetry, thus permitting the micorparticle to undergo migration in Stokes flow.[16] The fore-aft asymmetry is a generic feature of living organisms and active matters systems that influence the collective and individual properties.[42,43] Due to the reversibility principle of Stokes equations, a single neutrally buoyant rigid microparticle fore-aft symmetric cannot undergo a lateral migration and remains at a unchanged distance from the wall. In contrast, a single rigid fore-aft asymmetric shaped rigid microparticle is able to undergo a lateral migration (Purcell's scallop theorem for micro-swimmers). This theorem states that in a Newtonian fluid a time-reversible motion cannot produce any net force (lift) or net flow. However, in the presence of nonlinear rheological fluid properties, a reciprocal swimming pattern can lead to a net displacement in a shear thinning/thickening) fluid[44] and in a viscoelastic fluid.[45] The deformability lift force is given by the analytical expression[46]

$$f_{\mathrm{Def}} \propto \eta v_{\mathrm{avg}} R \left(\frac{R}{H_l}\right)^2 \left(\frac{d}{H_l}\right), \tag{17}$$

where v_{avg} is the average velocity. Here, d denotes the distance between microparticle and vessel centerline. For the other lift forces, numerical values of Re_p and Ca used in this work are not within the range of validity of analytical expressions available in literature. The contribution of Saffman and Rubinow–Keller forces is neglected since the microparticle is neutrally buoyant[47,48] and the particle Reynolds numbers Re_p are much less than unity[11] ($\mathrm{Re}_p \sim 10^{-3}$ and $\sim 10^{-2}$ for $c = 0.5$ and $c = 0.15$, respectively).

The drag arises from the difference in fore and aft velocities of the microparticle.[49] The wall induces a flow disturbance around the microparticle and tends to accelerate fluid around the microparticle increasing f_{drag} by a factor given by Faxen's correction (see Ref. 50). The drag decays as the microparticle moves away from the wall (relative velocity decreases). Theoretical analysis of drag acting on deformable particle (bubble) is provided in Ref. 51.

3.3. *Single isolated microparticle*

3.3.1. *Deformation*

In response to the parabolic blood flow start the microparticle elongates in the streamlines direction and tilts. As Ca increases, the microparticle stiffness decreases and the microparticle is easily deformed. For $c = 0.5$ and for both arteriolar walls, this deformation enables the development of a pointy tail (cusp-like instability) at its rear-end and the tear-drop shape is observed for the DAW (Fig. 3) and the RAW (Fig. 4(a)). Since this cusp tend to extend closer to the wall, the microparticle is decelerated. As the microparticle moves away from the wall, the cusp relaxes and a roughly ellipsoidal shape is observed. At the vicinity of the centerline, the microparticle exhibits the famous slipper-shape (see Fig. 3). The slipper shape observed for RBCs[52,53] and artificial microparticles[54] is found to result from a loss in stability of the symmetric shape[55] and allows the RBC to move faster in highly confined zones.

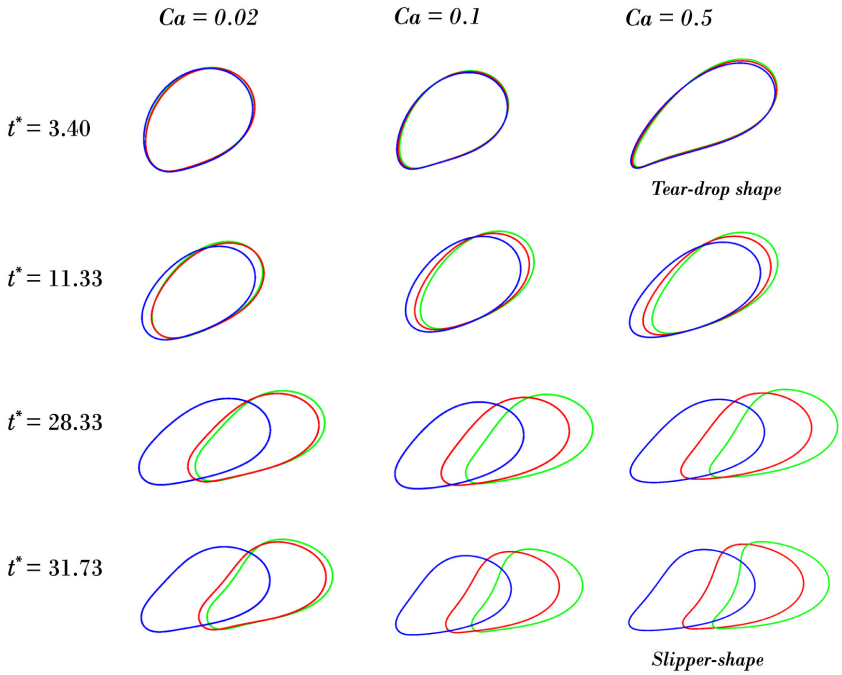

Fig. 3. (Color online) Image sequence of deformed shapes at specific times for $c = 0.5$, DAW. Green color is for $\lambda = 0.5$, red for $\lambda = 1$ and blue for $\lambda = 2$.

The fore-aft asymmetry is much less pronounced for $c = 0.15$ and the microparticle remains roughly ellipsoidal. In fact, due to its size, the smallest microparticle moves at a greater distance from the RAW (even if at $t = 0$ both centers of mass are placed at the same distance to the wall), the influence of the RAW (i.e., asymmetry) on microparticle dynamic is consequently diminished.

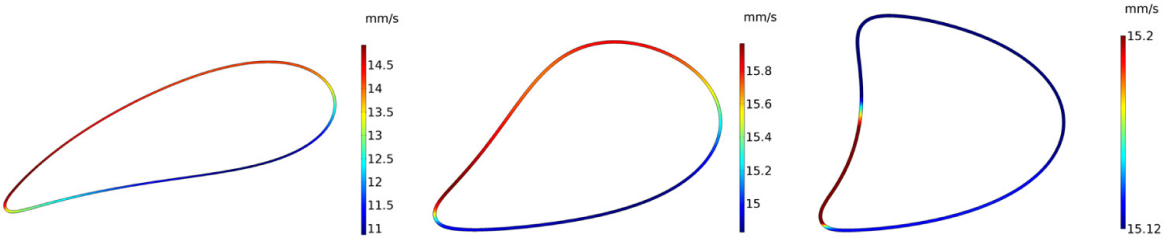

(a) RAW

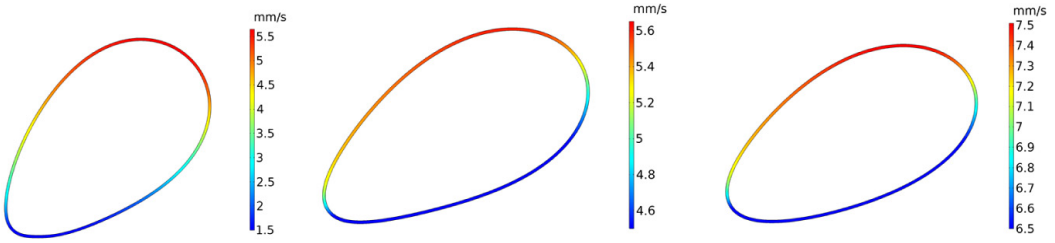

(b) DAW

Fig. 4. Microparticle velocity magnitude ($\lambda = 2, c = 0.5, \mathrm{Ca} = 0.5$) at $t^* = 1.7, 7.94$ and 15.86.

3.3.2. *Migration*

In the presence of the DAW, the initially straight arteriole dilates and develops symmetrically an upper and a lower fusiform-liked bulges (Fig. 5). The maximum arteriolar dilation is of 66% which is in the range of experimental values reported in Ref. 56 for human coronary arteriole. As a consequence of arteriolar dilation, the microparticle is temporarily downward aspired due to its vicinity with the lower wall, thereby, the migration is delayed (Fig. 6).

During the aspiration, f_{DW} and f_{SG} are prominent forces. The aspiration ends at $t^* = 2.5$ and $t^* = 15$ for $c = 0.5$ and $c = 0.15$, respectively, reflecting that the smallest micorparticle is more sensitive to wall distensibility (i.e., to f_{DW}). This effect becomes noticeable in Fig. 6(d). For $c = 0.5$, the zone marking the transition from the aspiration to the effective migration get sharped as Ca increases (Fig. 6(a)). Magnification of this zone reveals that the highest the Ca, the shortest the aspiration (Fig. 6(b)). As shown in Fig. 6(c), this trend is not observed for $c = 0.15$ and the effective migration is observed to start at a common threshold ($t^* = 15$). The influence of λ on migration altitude is accentauted for $c = 0.5$ and is shown to increases with Ca (see Fig. 6(a)). In the presence of the RAW, the migration starts quasi-instantaneously. The smallest microparticle migrates quasi-linearly whilst the migration history shape of the largest one is similar to that of a logarithmic function (refer to Figs. 6(a) and 6(c)). The plateau observed for different Ca corresponds to the equilibrium position morphologically indicated by stable deformation states (i.e., symmetrical parachute shape). The largest microparticle migrates beyond the arteriole centerline ($0.510 \leq y_c/H_l \leq 0.596$). Note that the centerline ($y_c/H_l = 0.5$) is not a stable equilibrium position since a little deflection will never return the microparticles back.[57] For both walls, the largest microparticle moves closer to the arteriole centerline. Regarding the influence of λ, obtained results confirm that λ

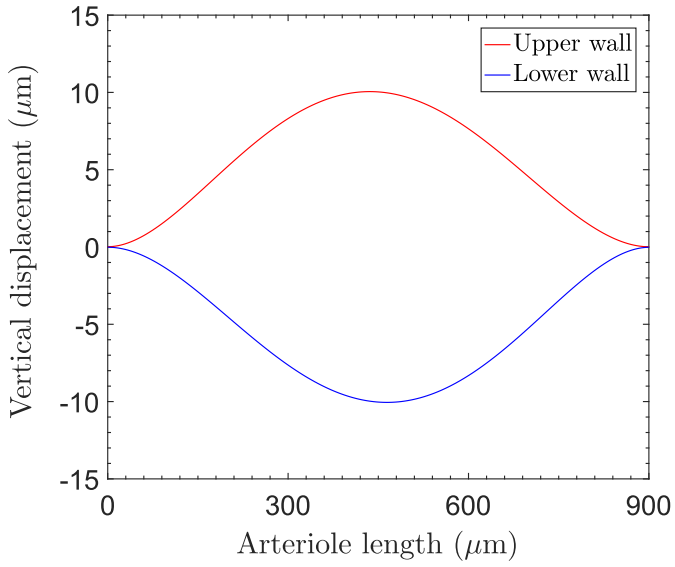

Fig. 5. Maximum arteriolar dilation.

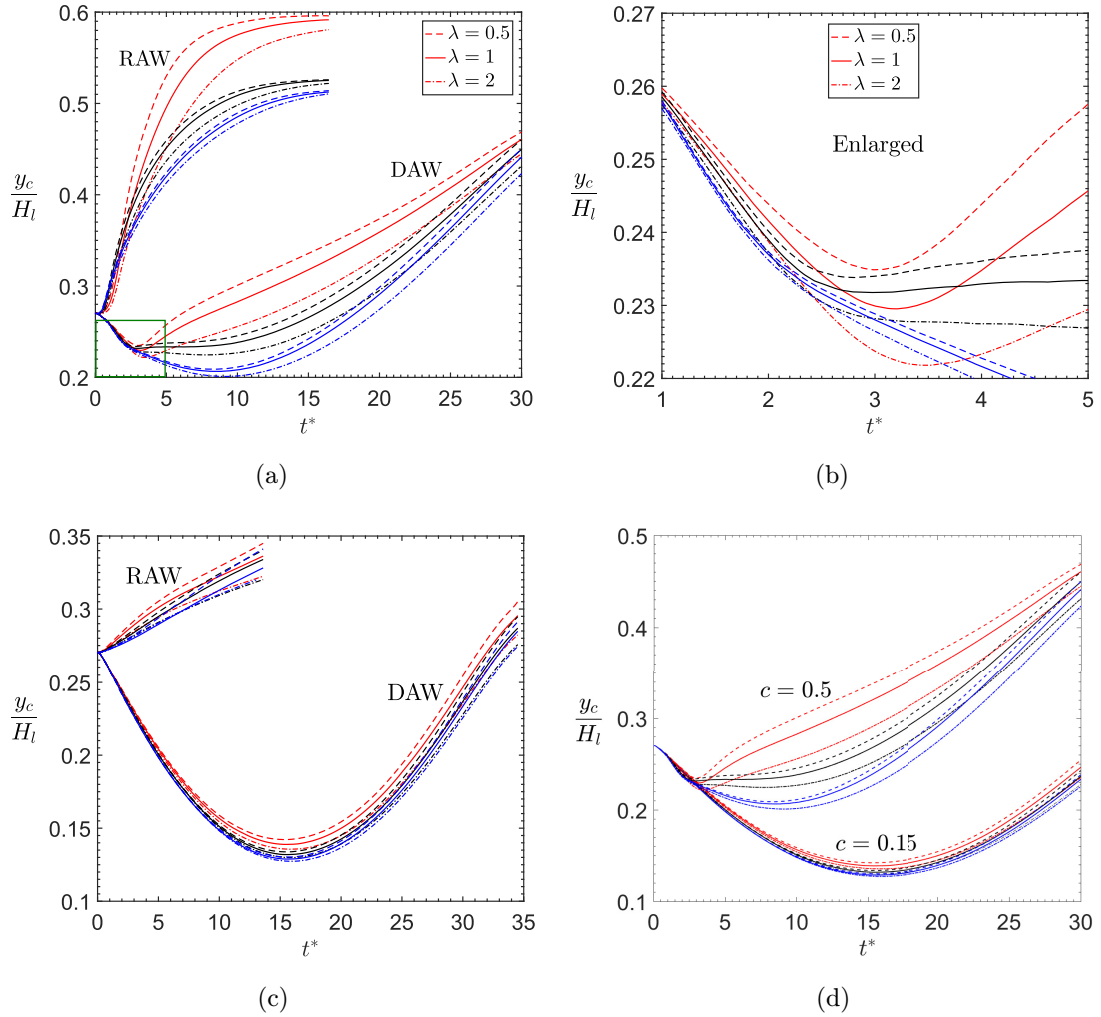

Fig. 6. (Color online) Microparticle migration time evolution: (a) $c = 0.5$, (b) enlarged version of (a), (c)$c = 0.15$, and (d) DAW. Red color is for Ca $= 0.5$, black for Ca $= 0.1$ and blue for Ca $= 0.02$.

restricts microparticles deformation and has an effect on the time required to reach the equilibrium shape (not on the equilibrium shape itself). The influence of λ on migration altitude increases with increasing Ca and c.

3.3.3. *Lateral velocity*

Lateral velocity or migration velocity V_y refers to y-component of membrane velocity. For $c = 0.5$, the "hook" in V_y time evolution in the presence of the RAW is due to f_{SG} that predominates other lift forces at early-times. Interestingly, in the presence of the DAW, V_y history is characterized by a "bump" as the microparticle migrates rapidly ($2.5 < t^* < 5$) before it decelerates (see Fig. 7(a)). For $c = 0.15$ and as previously noticed, the smallest microparticle is more sensitive to f_{DW} and V_y evolves smoothly for both walls (RAW and DAW), expect for $t^* < 2.5$, where numerical instabilities are relatively important for DAW (Fig. 7(b)). For both confinements, V_y tends to vanish as the microparticle moves closer to the equilibrium position.

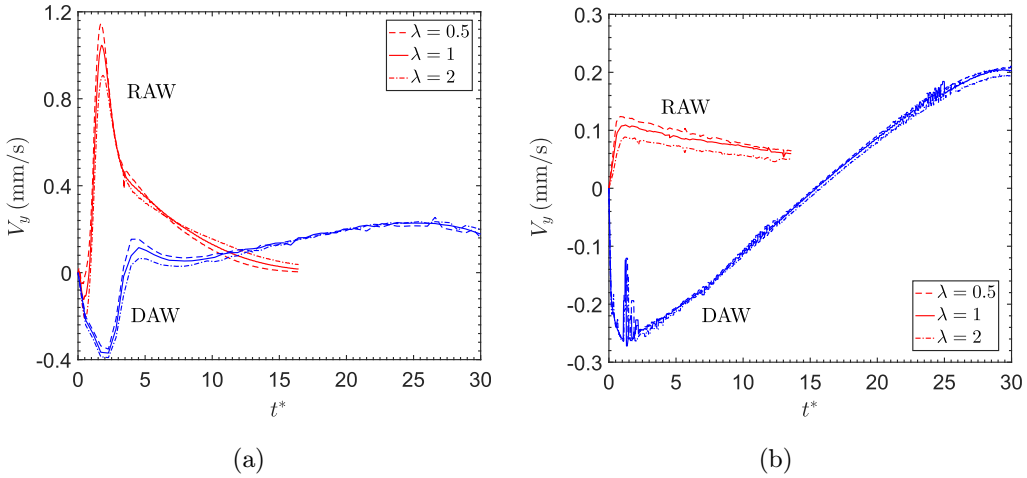

Fig. 7. Microparticle lateral velocity history (a) $c = 0.5$ and (b) $c = 0.15$.

3.4. *Microparticles train*

In this section, we consider a train of three microparticles. The main purpose is to study the influence of the deformable wall on the hydrodynamic inter-particle interaction aiming to assess the risk of inter-particular clustering and/or microparticles adhesion/accumulation near the wall and to clarify the interplay of main parameters in particle-to-particle dynamics for drug-delivery vectors design. Such situations could severely impede the blood stream and eventually, results in a non-targeted release of the drug, thus, toxifying healthy tissues. Let s_1 stand for the centroid–centroid distance between the middle and the lagging microparticle and s_2 the centroid–centroid distance between the middle and the leading microparticle (see Fig. 1). At initial time, both spacing are set to $s_1 = s_2 = 20$ (μm) and $s_1 = s_2 = 6$ (μm) for $c = 0.5$ and $c = 0.15$, respectively, keeping the ratio $a/s_{1,2} = 0.75$ similar for both confinements. For ease of reading, the main results are presented and discussed separately for each confinement in dedicated subdivision ($c = 0.15$ and $c = 0.5$), each one is divided into two paragraphs, the first belongs to the migration/deformation and the second deals with the inter-particle spacing evolution. The section will be concluded by comments related to strain energy density.

3.4.1. $c = 0.15$

An intriguing mechanism is observed for all Ca and λ, the lagging microparticle overtook the middle one. This kinetic consists of an approach phase $t^* = 15 - 20$, a binary collision $t^* \approx 19.5 - 22.66$ and a separating phase $t^* \geq 24$ (Fig. 8). During the approach, phase isolines of pressure distribution showed a high-pressure area between both microparticles resulting in a repulsive force,[58] this force combined with the microparticle position (the lagging microparticle experiences a high-flow strength and hence moves faster) and microparticle size (due to its relative small size, the space is large enough to permit the overtaking process) is a propitious combination to this kinetic. During the binary collision, microparticles lose symmetry and their

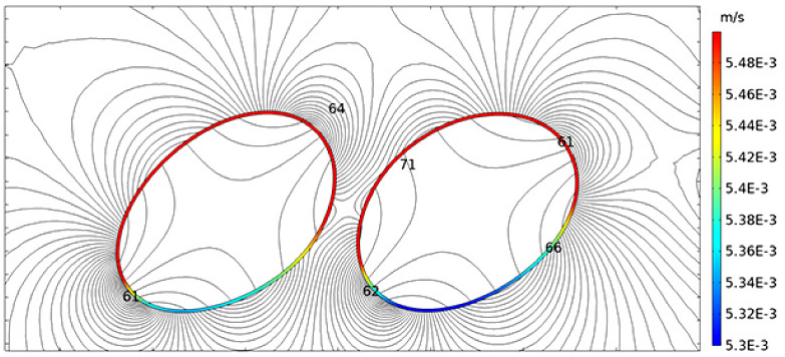

(a) $t^* = 15$

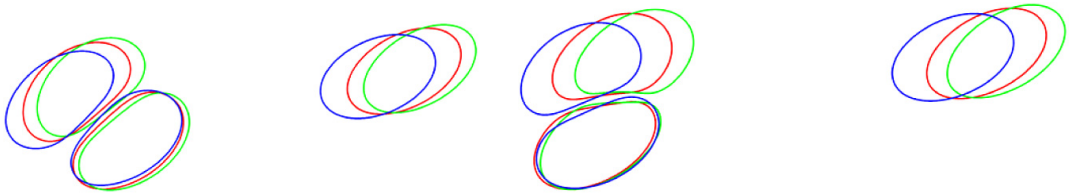

(b) $t^* = 19.83$ (c) $t^* = 21.6$

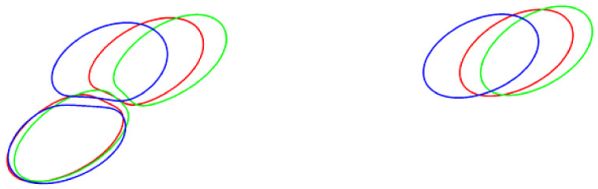

(d) $t^* = 22.66$

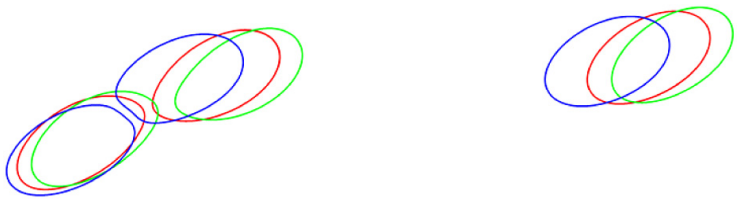

(e) $t^* = 23.8$

Fig. 8. (Color online) Overtaking behavior ($c = 0.15$, Ca $= 0.5$, DAW): (a) Isolines of pressure contour at the approach phase, color legend is for microparticle velocity. (b)–(e) Sequential snapshots of overtaking, green color is for $\lambda = 0.5$, red for $\lambda = 1$ and blue for $\lambda = 2$.

curvature vanishes at opposite faces (Figs. 8(b)–8(d)). The consecutive deformations observed during the binary collision are in excellent agreement with deformation of colliding cells in linear shear flow.[36] The overtaking behavior is indicated on curves by bumps mirrored to each other. For the lagging microparticle, the bumps widens with Ca while for the middle one, the bumps width seems to be independent on Ca (see Fig. 9(a)). For both positions, the apparition of the bumps appears later as Ca decreases and the gap between the studied λ is diminished for Ca $= 0.1$. Upon closer examination of λ effect, for Ca $= 0.02$ and 0.1 the inflection point appears sooner for

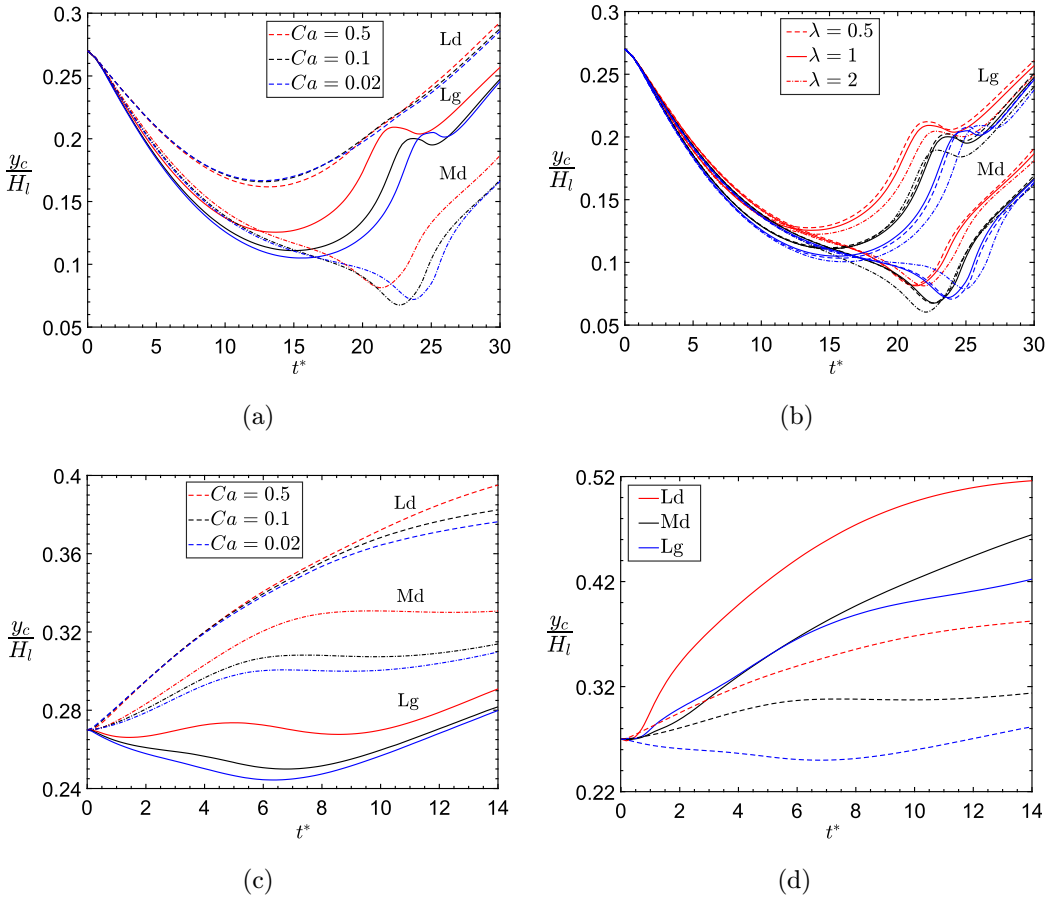

Fig. 9. Microparticles migration histories (a) ($\lambda = 1$, $c = 0.15$, DAW), (b) $c = 0.15$, DAW, (c) ($\lambda = 1$, $c = 0.15$, RAW), and (d) Solid lines are for $c = 0.5$ and dashed lines for $c = 0.15$ ($\lambda = 1$, RAW).

the less important λ and later for $\lambda = 2$. Conversely, the inflection in the bumps for Ca $= 0.1$ first occurs for $\lambda = 2$ followed by $\lambda = 0.5, 1$ (refer to Fig. 9(b)).

Unlike the single isolated configuration, microparticles migrate nonlinearly in the presence of the RAW and unexpectedly, the lagging microparticle hardly migrates. Its migration is even more difficult as Ca decreases and we observe a net aspiration (as in the presence of the DAW), suggesting that in this particular case f_W like f_{DW}, acts as a suction force (Fig. 9(c)). Curiously for Ca $= 0.5$, the lagging microparticle combines upward and downward migration.

The lateral velocity of the leading microparticle evolves quiet similarly to that of the single isolated one, whichever the arteriolar rigidity (RAW or DAW). The same does not apply to the two other microparticles. For the RAW, the lateral velocity changes its monotony and this, more frequently for the lagging microparticle reaffirming its arduous upward migration (Fig. 10(a)). As for the migration (i.e., mirror bumps) V_y, time-evolution of the middle and the lagging microparticle is a rough reflection to each other (Fig. 10(b)). The inflections in each curve ($V_y = f(t^*)$) depict the balancing between the kinetic and the potential energies.

In the presence of the DAW, s_1 and s_2 diverge at $t^* = 10$. As for $c = 0.5$, s_2 manifest an exponential growth. For s_1, the curves slightly decrease with decreasing

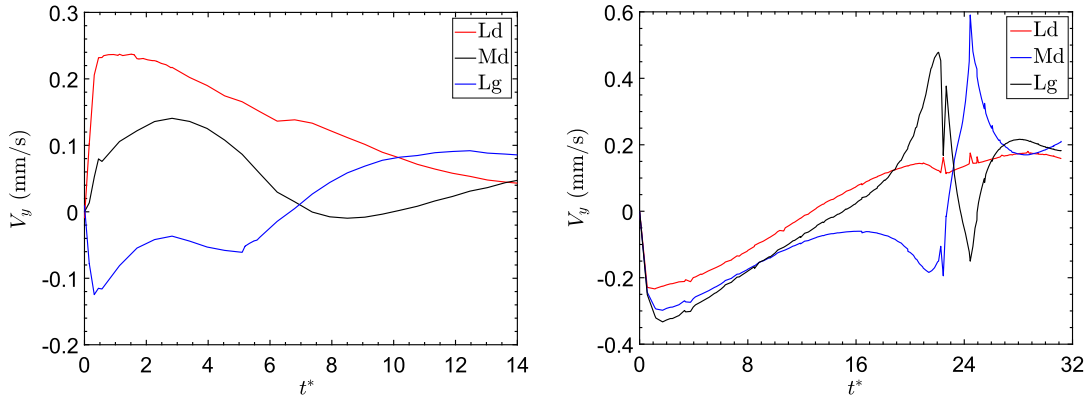

Fig. 10. Microparticles lateral velocity histories ($\lambda = 1$, $c = 0.15$, Ca $= 0.1$): (a) RAW and (b) DAW.

Ca till the overlapping at $t^* \approx 21.6$ (see Fig. 8(c)) and starting from this point, they rise similarly to s_2. Plots shown in (Fig. 11(a)) reveals less membrane shear resistance, less spacing growth. This influence is maintained but minimized for s_1 ($t^* \geq 21.6$). For the RAW, both spacing are growing with time (exponential or logarithmic-like growth) and are observed to expand the most with the highest Ca and the less for the intermediate Ca. In stark contrast to other studied combinations, s_1 widens more rapidly than s_2 (Fig. 11(c)).

3.4.2. $c = 0.5$

Unsurprisingly, we found that the migration altitude is important for the leading microparticle (the middle microparticle is hampered by the presence of too microparticle on its both sides, the lagging one is restrained by too in-front microparticles) (see Fig. 12). The discrepancies in middle and lagging migrations are barely discernible. For the sake of conciseness, we confine ourselves to present the combination Ca $= 0.1$, $\lambda = 1$ in order to evaluate the risk of accumulation near the rigid wall. Plots in Fig. 9(d) confirm the upward migration. Because of the important asymmetry, we chose to quantify the deformation of the microparticles through the deformation gradient $\mathbf{F}^{(m)}$ (instead of the geometric Taylor parameter) that gives information about the local deformation with respect to the non-deformed (referential) state. The main result is microparticle's position influence on arteriolar wall rigidity effect. In fact, the divergence between the deformation gradients for each arteriolar rigidity model widens as the microparticle is placed far from the arteriole entrance (Fig. 13). Qualitatively, quite a few uncommonly observed are characterizing morphological evolution of the largest microparticle. The middle microparticle develops a sharp cusp-like instability as a results to a combination of important softness, quasi-null bending rigidity, infinite wall rigidity and a favorable position. This important local deformation leads to the appearance of a singularity and hence, to convergence issues. We believe that the singularity is a consequence of infinite stress at the cusp that could be fixed by increasing the bending rigidity and/or

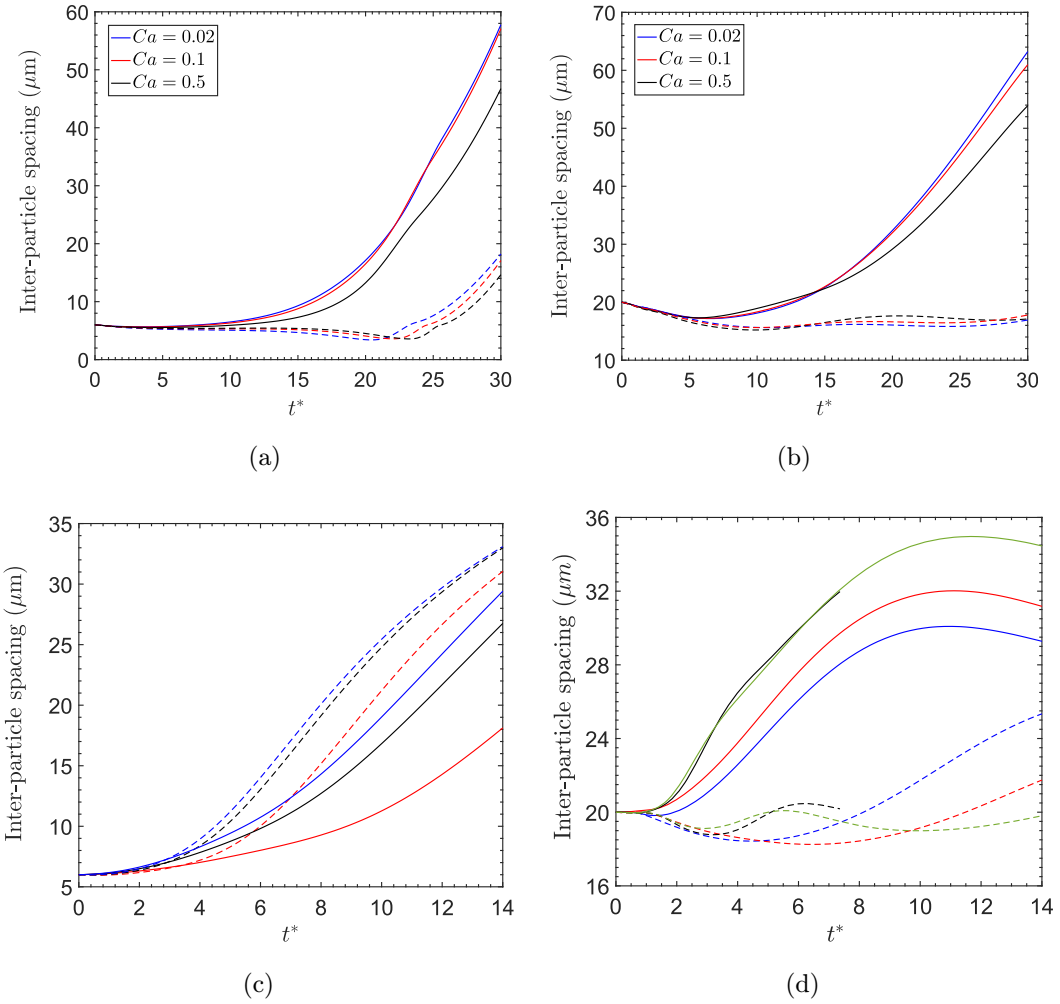

Fig. 11. (Color online) Inter-particle spacing time evolution for $\lambda = 1$, dashed lines are for s_1 and solid ones for s_2 (a) $c = 0.15$, DAW, (b) $c = 0.5$, DAW, (c) $c = 0.15$, RAW and (d) $c = 0.5$, RAW, green color is for Ca $= 0.4$.

modeling the membrane mechanical behavior using a strain-stiffening law (e.g., Skalak *et al.* law), as both restrict microparticle deformation. We opt for a simpler alternative consisting in decreasing the capillary number to Ca $= 0.4$ (by increasing $G^{(m)}$). As for the single isolated configuration, the cusps relax with time (except for the singularity-related case). For Ca ≥ 0.4, the lagging and middle microparticles flatten in a significant way in the immediate vicinity to the RAW, in addition to cusps formation (Fig. 14). The flatness disappears progressively as microparticles move away from the wall. As illustrated in Fig. 15, wall deformability also brings about a localized flatness and cusp formation, the novel observed behavior is the trend to "raise" for Ca $= 0.5$ ($t^* = 4.53$) which relatively restricts the flattened zone in close contact to the wall. This deformation mode is propitious to lateral migration as it helps to circumvent the f_{DW} and the constraints imposed by narrow spacing from neighboring microparticles (i.e., hydrodynamic pressure). Besides giving information about morphological changes in microparticle shape, Fig. 14 also serves to

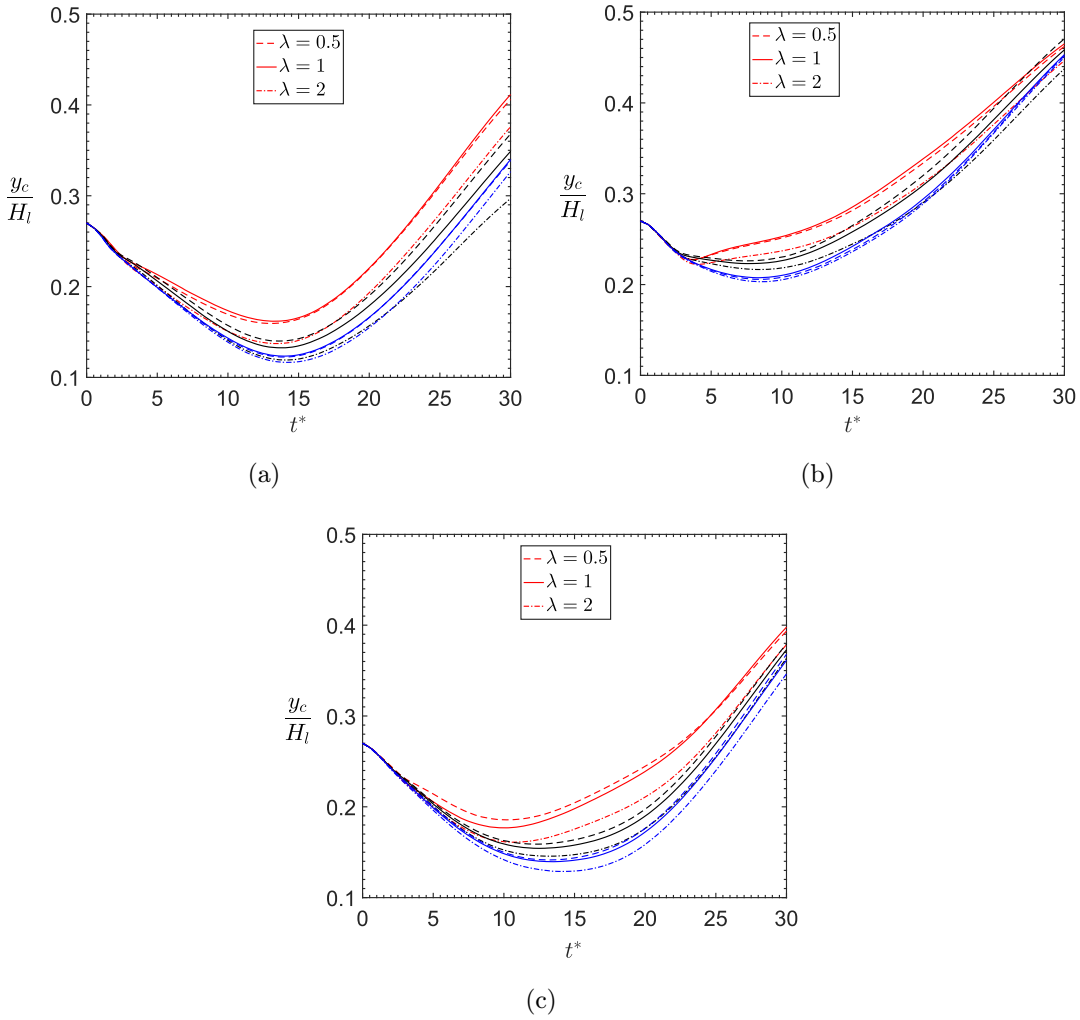

Fig. 12. (Color online) Microparticles migration time evolution $c = 0.5$, DAW: (a) Lg, (b) Ld and (c) Md. Red color is for Ca = 0.5, black for Ca = 0.1 and blue for Ca = 0.02.

concretely describe the evolution of spacing s_1 and s_2 and to show the clustering while Fig. 15 highlights the influence of Ca on microparticles lateral velocities.

In the presence of the DAW, s_1 and s_2 fall below 20 (μm) and diverge at $t^* = 5$, above this point, s_2 increase in an exponential fashion while s_1 evolve quasi-steadily and oscillate between 15.22 (μm) and 17.64 (μm). Apropos of the influence of Ca, it is observed that the higher Ca the less s_2, this influence is not obvious on s_1 (Fig. 11(b)). As regards to the RAW, s_2 evolves in a concave fashion and in contrary to previously noticed for the migration of the lagging and the middle microparticles, the inflection points in s_2 evolution are found to occur sooner as Ca decreases. Surprisingly, the temporal evolution of s_1 and s_2 for Ca = 0.4 and Ca = 0.5 depict an outright concavity change (Fig. 11(d)). The corresponding descending curves are a sign of microparticle clustering. Microparticle deformability plays a major role in clustering and in inter-particle spacing decrease. In fact, a hydrodynamic flow forces amount is absorbed by microparticle deformation, reducing the repulsive force that acts to keep microparticles apart. While the clustering of RBCs is protein-induced

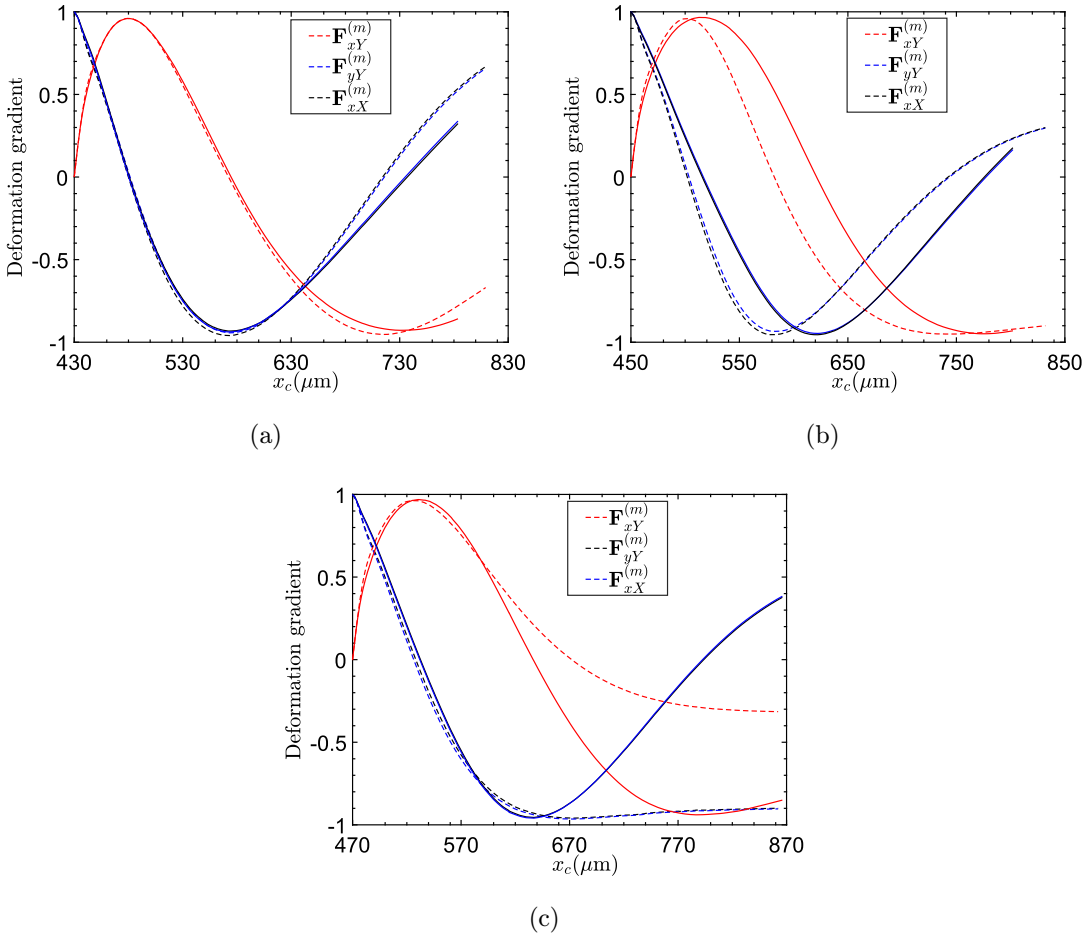

Fig. 13. Deformation gradient ($c = 0.5$, Ca $= 0.1$), x denotes the new location of the material particle and Y denotes the original one (and so on). Solid lines are for RAW and dashed lines for DAW: (a) Lg, (b) Md and (c) Ld.

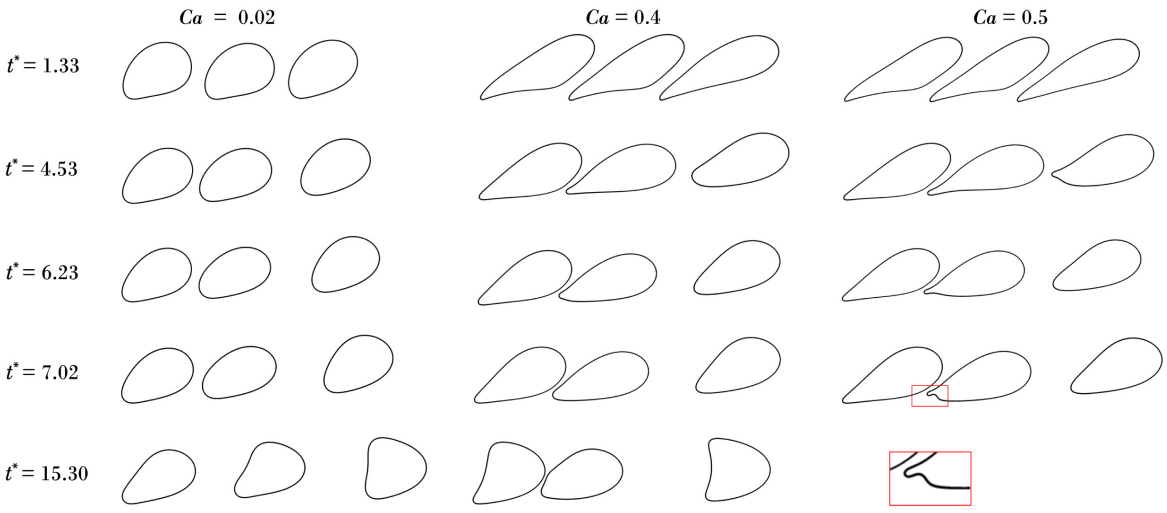

Fig. 14. Sequential snapshots of deformed shapes ($\lambda = 1$, RAW).

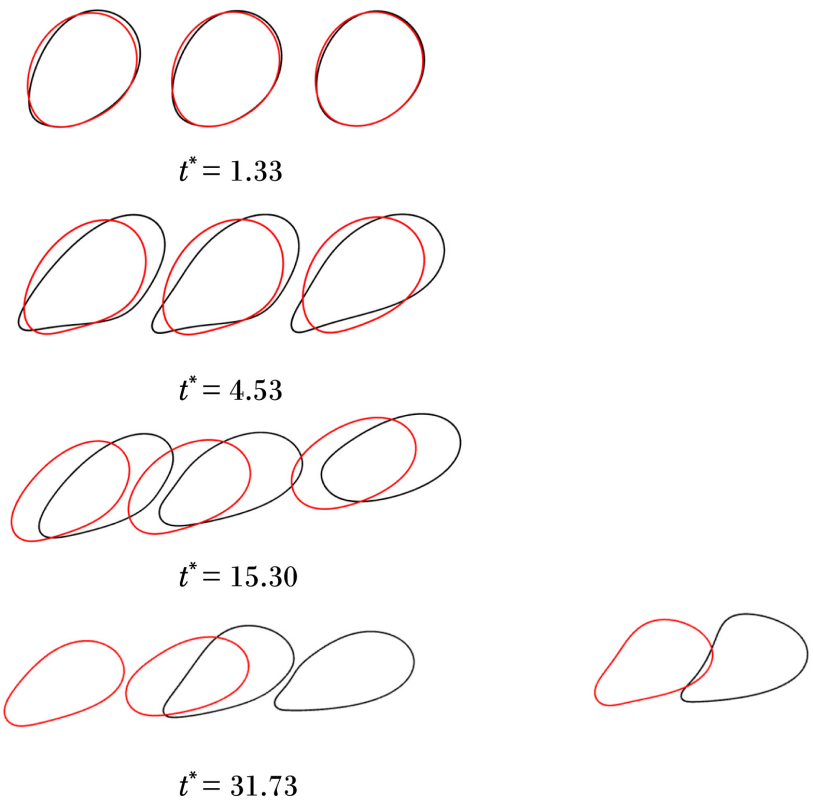

Fig. 15. Sequential snapshots of deformed shapes ($\lambda = 1$, DAW). Red color is for Ca $= 0.02$ and black for Ca $= 0.5$.

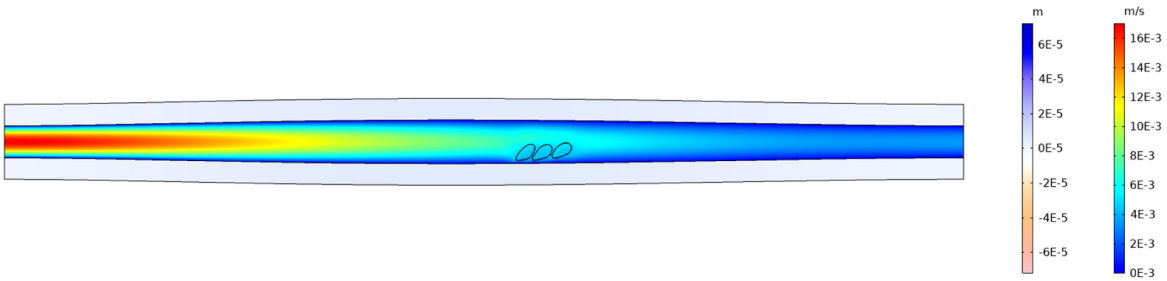

(a) $t^* = 8.5$

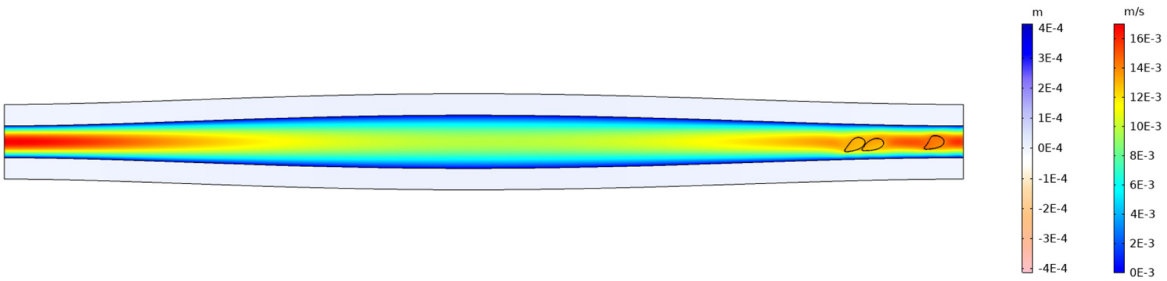

(b) $t^* = 31.17$

Fig. 16. Arteriolar dilation and microparticle lateral migration in the Poiseuille blood flow ($\lambda = 1$, $c = 0.5$, Ca $= 0.5$, DAW). The rainbow color table shows fluid velocity magnitude while the second one represents the vertical displacement of the solid domain.

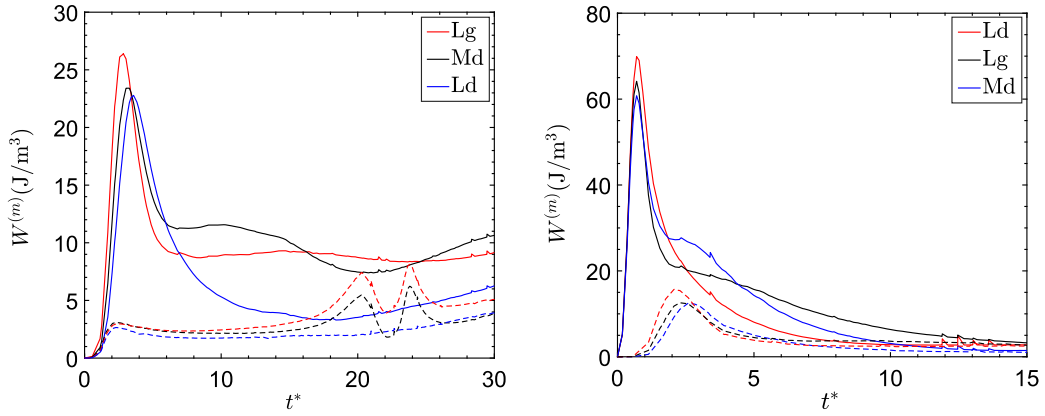

Fig. 17. Elastic energy density $\lambda = 1$: (a) Ca $= 0.1$, solid lines are for RAW and dashed lines are for DAW, (b) Ca $= 0.5$, solid lines are for $c = 0.5$ and dashed lines for $c = 0.15$.

and results from an intricate balancing of "cross-bridging" and depletion forces,[59] the clustering of artificial microparticles is due to the presence of ahead converging vortexes and rear diverging ones.[60]

The elastic strain energy $W^{(m)}$ increases with microparticle deformability, thereby with elastic resistance[61] and microparticle position. The wall rigidity is observed to significantly increase $W^{(m)}$ since the flow strength is exclusively directed toward the microparticle which stores the elastic energy through deformation (Fig. 17(a)). The temporal evolution of $W^{(m)}$ during the three phases composing the overtaking kinetic $(15 \leq t^* \leq 24)$ has a trend similar to microparticle shear stress evolution[62] (Fig. 17(b)).

4. Conclusion

In this work, we studied the influence of arteriolar hyperelasticity on artificial microparticle deformation, trajectory and velocity during the process of lateral migration. Furthermore, we examined the same influence on inter-particle hydrodynamic interactions. Results have revealed the presence of a lift-compensating suction force f_{DW} that modifies the overall microparticle dynamic in flow and brings about a risk of accumulation near the wall. Deformation modes observed for the DAW are in good agreement with those reported in the literature for rigid microchannels (i.e., tear-drop, ellipsoidal and slipper shapes). The suction force magnitude is confinement-dependent and stiffness-dependent, for larger microparticle the force is also viscosity ratio-dependent. Larger microparticle $(c = 0.5)$, relatively stiff (Ca $= 0.02$) and whose viscosity is less than the carrying blood flow viscosity seems to be less sensitive to the aspiration and migrates easily.

Regarding the influence of the arteriolar distensibility on inter-particle interactions, the main findings include the process of overtaking $(c = 0.15)$ and an extra deformation mode $(c = 0.5)$ (Fig. 16). Interesting observations are also made for the

RAW like clustering ($c = 0.5$), the highly pointed rear-end that tends to subdivide into two cusp-like instabilities and the presence of a suction force even in the absence of arteriolar distensibility ($c = 0.15$). Prescribing combinations of microparticle mechanical and rheological properties is necessary in microparticle design to anticipate risky situations in a medical context, in particular clustering and accumulation near the wall. Drawing on the obtained results, the risk of aggregation could solely be discarded for $c = 0.15$ in the presence of the RAW. For this same combination, the risk of microparticles adhesion to wall is unexpectedly present and increases with increasing microparticle stiffness. Blood heterogeneity, larger amount of microparticles and various outflow conditions would provide a deeper knowledge of microparticle dynamics in human blood vessels.

References

1. Zhao Y, Li X, Zhao X, Yang Y, Li H, Zhou X, Yuan W, Asymmetrical polymer vesicles for drug delivery and other applications, *Front Pharmacol* **8**:1–9, 2017.
2. Ma J, Du LF, Chen M, Wang HH, Xing LX, Jing LF, Li YH, Drug loaded nano microcapsules delivery system mediated by ultrasound targeted microbubble destruction: A promising therapy method (Review), *Biomed Rep* **1**:506–510, 2013.
3. Chumakova OV, Liopo AV, Andreev VG, Cicenaite I, Evers BM, Chakrabarty S, Pappas TC, Esenaliev RO, Composition of PLGA and PEI/DNA nanoparticles improves ultrasound-mediated gene delivery in solid tumors *in vivo*, *Cancer Lett* **261**:215–225, 2008.
4. Mihalko E, Huang K, Sproul E, Cheng K, Brown AC, Targeted treatment of ischemic and fibrotic complications of myocardial infarction using a dual-delivery microgel therapeutic, *ACS Nano* **12**:7826–7837, 2018.
5. Coupier G, Farutin A, Minetti C, Podgorski T, Misbah C, Shape Diagram of vesicles in Poiseuille flow, *Phys Rev Lett* **108**:1–5, 2012.
6. Kaoui B, Coupier G, Misbah C, Podgorski T, Lateral migration of vesicles in microchannels: effects of walls and shear gradient, *La Houille Blanche* **5**:112–119, 2009.
7. Taylor RR, Tang Y, Gonzalez MV, Stratford PW, Lewis AL, Irinotecan drug eluting beads for use in chemoembolization: *In vitro* and *in vivo* evaluation of drug release properties, *Eur J Pharmaceut Sci* **30**:7–14, 2007.
8. Fuchs K, Bize PE, Dormond O, Denys A, Doelker E, Borchard G, Jordan O, Drug-eluting beads loaded with antiangiogenic agents for chemoembolization: *In vitro* sunitinib loading and release and *in vivo* pharmacokinetics in an animal model, *J Vasc Interv Radiol* **25**:379–387, 2014.
9. Khoo BL, Warkiani ME, Tan DSW, Bhagat AAS, Irwin D, Lau DP, Lim AST, Lim KH, Krisna SS, Lim WT, Yap YS, Lee SC, Soo RA, Han J, Lim CT, Clinical validation of an ultra high-throughput spiral microfluidics for the detection and enrichment of viable circulating tumor cells, *PLoS One* **9**:1–7, 2014.
10. Browne AW, Ramasamy L, Cripe TP, Ahn CH, A lab-on-a-chip for rapid blood separation and quantification of hematocrit and serum analytes, *Lab Chip* **11**:2440–2446, 2011.
11. Carlo DD, Irimia D, Tompkins RG, Toner M, Continuous inertial focusing, ordering, and separation of particles in microchannels, *PNAS* **104**:18892–18897, 2007.
12. Zhu L, Rabault J, Brandt L, The dynamics of a capsule in a wall-bounded oscillating shear flow, *Phys Fluids* **27**:1–16, 2015.

13. Nix S, Imai Y, Matsunaga D, Yamaguchi T, Ishikawa T, Lateral migration of a spherical capsule near a plane wall in Stokes flow, *Phys Rev E* **90**:1–11, 2014.
14. Hariprasad DS, Secomb TW, Motion of red blood cells near microvessel walls: Effects of a porous wall layer, *J Fluid Mech* **705**:195–212, 2012.
15. Goldsmith HL, Mason SG, Axial migration of particles in Poiseuille flow, *Nature* **190**:1095–1096, 1961.
16. Tam CKW, Hyman WA, Transverse motion of an elastic sphere in a shear field, *J Fluid Mech* **59**:177–185, 1973.
17. Hou HW, Bhagat AAS, Chong AGL, Mao P, Tan KSW, Han J, Lim CT, Deformability based cell margination — A simple microfluidic design for malaria-infected erythrocyte separation, *Lab Chip* **10**:2605–2613, 2010.
18. Namgung B, Ng YC, Leo HL, Rifkind JM, Kim S, Near-wall migration dynamics of erythrocytes *in vivo*: Effects of cell deformability and arteriolar bifurcation, *Front Physiol* **8**:1–10, 2017.
19. Schaaf C, Stark H, Inertial migration and axial control of deformable capsules, *Soft Matter* **13**:3544–3555, 2017.
20. Doddi SK, Bagchi P, Lateral migration of a capsule in a plane Poiseuille flow in a channel, *Lab Chip* **34**:966–986, 2008.
21. He L, Luo Z, Liu WR, Bai B, Capsule equilibrium positions near channel center in Poiseuille flow, *Chem Eng Sci* **172**:603–611, 2017.
22. Amini H, Lee W, Carlo DD, Inertial microfluidic physics, *Lab Chip* **14**:2739–2761, 2014.
23. Li H, Ma G, Modeling performance of a two-dimensional capsule in a microchannel flow: Long-term lateral migration, *Phys Rev E* **82**:1–14, 2010.
24. Nix S, Imai Y, Ishikawa T, Lateral migration of a capsule in a parabolic flow, *J Biomech* **49**:2249–2254, 2016.
25. Coclite A, Ranaldo S, Tullio MD, Decuzzi P, Pascazio G, Kinematic and dynamic forcing strategies for predicting the transport of inertial capsules via a combined lattice Boltzmann-immersed boundary method, *Comput Fluids* **180**:41–53, 2019.
26. Beaucourt J, Biben T, Misbah C, Optimal lift force on vesicles near a compressible substrate, *Europhys Lett* **67**:676–682, 2004.
27. El Jirari I, El Baroudi A, Ammar A, Numerical investigation of the dynamical behavior of a fluid-filled microparticle suspended in human arteriole, *J Biomech Eng* **143**, 2021.
28. Cheema TA, Park CW, Numerical investigation of hyperelastic wall deformation characteristics in a micro-scale stenotic blood vessel, *Korea Aust Rheol J* **25**:121–127, 2013.
29. Brooks DE, Goodwin JW, Seaman GV, Interactions among erythrocytes under shear, *J Appl Physiol* **28**, 1970.
30. San O, Staples AE, An improved model for reduced-order physiological fluid flows, *J Mech Med Biol* **12**, 2012.
31. Westerhof N, Boer C, Lamberts RR, Sipkema P, Cross-talk between cardiac muscle and coronary vasculature, *Physiol Rev* **86**, 2006.
32. Hu XQ, Salsac AV, Barthès-Biesel D, Flow of a spherical capsule in a pore with circular or square cross-section, *J Fluid Mech* **705**:176–194, 2012.
33. Leyrat-Maurin A, Barthes-Biesel D, Motion of a deformable capsule through a hyperbolic constriction, *J Fluid Mech* **279**:135–163, 1994.
34. Knoche S, Kierfeld J, Buckling of spherical capsules, *Phys Rev E* **84**, 2011.
35. Fery A, Dubreuil F, Möhwald H, Mechanics of artificial microcapsules, *New J Phys* **6**, 2004.
36. Jadhav S, Chan KY, Konstantopoulos K, Eggleton CD, Shear modulation of intercellular contact area between two deformable cells colliding under flow, *J Biomech* **40**, 2007.

37. Chu TX, Salsac AV, Leclerc E, Barthès-Biesel D, Wurtz W, Edwards-Lévy F, Comparison between measurements of elasticity and free amino group content of ovalbumin microcapsule membranes: Discrimination of the cross-linking degree, *J Colloid Interface Sci* **355**:81–88, 2011.
38. Hirt CW, Amsden AA, Cook JL, An arbitrary Lagrangian–Eulerian computing method for all flow speeds, *J Comput Phys* **14**:227–253, 1974.
39. Deuflhard P, A modified Newton method for the solution of ill-conditioned systems of nonlinear equations with application to multiple shooting, *Numer Math* **22**:289–315, 1974.
40. Smart JR, Leighton DT, Measurement of the drift of a droplet due to the presence of a plane, *Phys Fluids A* **3**:21–28, 1991.
41. Mukherjee S, Sarkar K, Effects of matrix viscoelasticity on the lateral migration of a deformable drop in a wall-bounded shear, *J Fluid Mech* **727**:318–345, 2013.
42. Chen Q, Patelli A, Chaté H, Ma Y, Shi X, Fore-aft asymmetric flocking, *Phys Rev E* **96**, 2017.
43. Brooks AM, Sabrina S, Bishop JM, Shape-directed dynamics of active colloids powered by induced-charge electrophoresis, *Proc Natl Acad Sci USA* **115**:1090–1099, 2018.
44. Qiu T, Lee T, Mark AG, Morozov KI, Munster R, Mierka O, Turek S, Leshansky AM, Fischer P, Swimming by reciprocal motion at low Reynolds number, *Nat Commun* **5**, 2014.
45. Pak OS, Normand T, Lauga E, Pumping by flapping in a viscoelastic fluid, *Phys Rev E* **81**, 2010.
46. Chan PC, Leal LG, The motion of a deformable drop in a second-order fluid, *J Fluid Mech* **92**:131–170, 1979.
47. Ho BP, Leal LG, Migration of rigid spheres in a two-dimensional unidirectional shear flow of a second-order fluid, *J Fluid Mech* **76**:783–799, 1976.
48. Matas J, Morris J, Guazzelli E, Lateral forces on a sphere, *Oil Gas Sci Technol Rev IFP* **59**:59–70, 2004.
49. Moore DW, Saffman PG, The structure of free vertical shear layers in a rotating fluid and the motion produced by a slowly rising body, *Philos Trans R Soc A* **264**, 1969.
50. Leach J, Mushfique H, Keen S, Leonardo RD, Ruocco G, Cooper JM, Padgett MJ, Comparison of Faxen's correction for a microsphere translating or rotating near a surface, *Phys Rev E* **79**, 2009.
51. Magnaudet J, Takagi S, Legendre D, Drag, deformation and lateral migration of a buoyant drop moving near a wall, *J Fluid Mech* **476**:115–157, 2009.
52. Skalak R, Branemark PI, Deformation of red blood cells in capillaries, *Science* **164**, 1969.
53. Tomaiuolo G, Lanotte L, Ghigliotti G, Misbah C, Guido S, Red blood cell clustering in Poiseuille microcapillary flow, *Phys Fluids* **24**, 2012.
54. Noguchi H, Gompper G, Shape transitions of fluid vesicles and red blood cells in capillary flows, *Proc Natl Acad Sci* **102**:14159–14164, 2005.
55. Kaoui B, Biros G, Misbah C, Why do red blood cells have asymmetric shapes even in a symmetric flow, *Phys Rev Lett* **103**:205909, 2009.
56. Miura H, Wachtel RE, Liu Y, Loberiza FR, Saito T, Miura M, Gutterman DD, Flow-induced dilation of human coronary arterioles important role of ca(2^+)-activated k(+) channels, *Circulation* **103**:1992–1998, 2001.
57. Zhang J, Yan S, Yuan D, Alici G, Nguyen N, Warkianic ME, Li W, Fundamentals and applications of inertial microfluidics: A review, *Lab Chip* **16**:10–34, 2016.
58. Gao T, Hu HH, Deformation of elastic particles in viscous shear flow, *J Comput Phys* **228**:2132–2151, 2009.

59. Lee K, Wagner C, Priezzhev AV, Assessment of the "cross-bridge"-induced interaction of red blood cells by optical trapping combined with microfluidics, *J Biomed Opt* **22**, 2017.
60. Misbah C, Vesicles, capsules and red blood cells under flow, *J Phys Conf Ser* **392**:1–17, 2012.
61. Bryngelson SH, Freund JB, Global stability of flowing red blood cell trains, *Phys Rev Fluids* **3**, 2018.
62. Zhao H, Shaqfeh ESG, The dynamics of a non-dilute vesicle suspension in a simple shear flow, *J Fluid Mech* **725**:709–731, 2013.

3.2.2.3 A03

Predictive dynamical behaviour of liquid-filled microparticles partitioning in the vicinity of a coronary bifurcation under pulsatile blood flow and arterial distensibility

Imane El Jirari[1], Adil El Baroudi[1], and Amine Ammar[1]

[1] Laboratoire Angevin de Mécanique Procédés et innovAtion (LAMPA), HESAM university, Angers, France
E-mail: imane.el_jirari@ensam.eu , adil.elbaroudi@ensam.eu , amine.ammar@ensam.eu

Abstract

A promising advance of bioengineering consists in the development of micro-nanoparticles as drug delivery vehicles injected intravenously or intraarterialy for targeted treatment. Proficient functioning of drug carries is conditioned by a reliable prediction of pharmacokinetics in human as well as their dynamical behavior once injected in blood stream. In this study we aim to provide a reliable numerical prediction of dynamical behavior of microparticles in human left coronary artery focusing on their behavior in the vicinity of the coronary bifurcation. We investigate the velocity, the deformation and the trajectory of three microparticles upon pulsatile blood flow and arterial compliance with varying the capillary number and the initial vertical position. The study is carried out within physiological conditions to provide accurate results. Fluid-structure interaction is solved by the Arbitrary Lagrangian Eulerian method using the COMSOL Multiphysics software.

Keywords: microparticle, coronary bifurcation, pulsatile blood flow

1 Introduction

Microparticles are artificial microstructures used as drug delivery vectors to remedy the limitations of chemotherapy and invasive treatments. It consists of a thin-walled membrane made of lipid, protein or polymer enclosing a small amount of liquid drug. The coated drug is released via membrane rupture or diffuses through permeable membrane. Therapeutic applications include targeted treatment of cancerous tumors [1] and coronary thrombus [2]. For the latter treatment, drug-loaded microparticles are injected in the coronary circulation to dissolve the thrombosis and to reestablish blood flow. The dynamical behavior of the drug carries and pharmacokinetic behavior of the coated drug is investigated $in\ vivo$ and $in\ vitro$ in literature. The validation and optimization of microparticles functioning to successfully (and safely) meet higher therapeutic demands require a robust prediction of the individual and the collective dynamical behavior of microparticles under blood flow and constraints imposed by vascular walls. A challenging task is the prediction of the preferred trajectory of microparticles entering the coronary branches under the action of pulsatile blood flow and arterial compliance. Topics of interest in arterial bifurcation studies include the wall shear stress which is a factor closely associated to pathological lipid cell deposition in artery wall (atherosclerosis), mass transfer and red blood cells separation. Herein, we are interested in the left coronary artery (LCA) whose arterial wall rich in elastic fibers alternates an expansion-recoil as blood is pulsed through it. We aim to predict within physiological conditions, the dynamic behavior of drug-loaded hyperelastic microparticles flowing in the LCA and partitioning at its branches. As far as authors know, this is the first study of this kind. Obtained results related to deformation, velocity and trajectory are briefly summarized and presented in the present paper. The numerical investigation is performed

in COMSOL Multiphysics software package, the 2D fluid-structure interaction non-linear problem is solved using the Arbitrary Lagrangian Eulerian method, with a monolithic approach. This *in silico* approach exempts from the ethical limitations related to *in vivo* studies and complicated experimental setup of *in vitro* studies.

2 Model description

As schematized in Figure 1, the LCA model includes the left main coronary artery (LM) that branches into the left anterior descending branch (LAD) and the left circumflex branch (LCx). The total length of the idealized LCA model is 7 cm. The angle formed by the LM and both daughter branches is set to $142.5°$ and the angle between the LAD and the LCx to $75°$ (values provided by Doutel et al. in [3]). Both branches are tapering toward the outlets, which is a characteristic of the arterial system structure. Three microparticles uniformly spaced are placed at the entrance of the LM at three different vertical positions p_1 or p_2 or p_3 corresponding to $y = H/6, H/2$ and $5H/6$, respectively, where $H = 3.5$ mm is lumen height (lumen is the interior domain of the vessel through which blood flows) and y the ordinate.

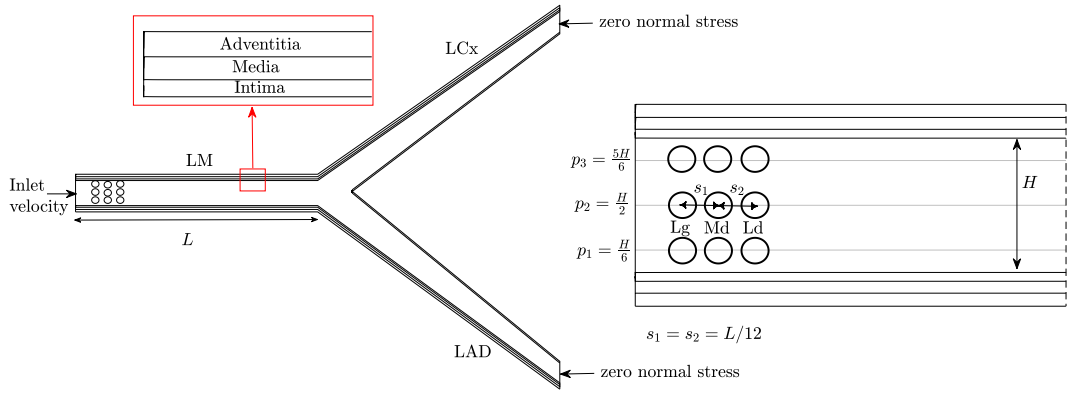

Figure 1: Schematic description showing the idealized LCA geometry and initial positioning of microparticles. Abbreviations Lg, Md and Ld refer to the lagging, the middle and the leading microparticle, respectively.

2.1 Arterial wall

The three layers composing the arterial wall (namely the intima, the media and the adventitia) are hyperelastic. For the sake of simplicity, the three layers are treated as isotropic with a density of $1150\,\mathrm{kg/m^3}$. Arterial hyperelasticity is modeled using the 5-parameters Mooney-Rivlin law where the energy density function $W^{(cor)}$ is expressed in terms of material constants related to the distortional response of the wall C_{ij}, material constant related to the volumetric response D, the first and the second right Cauchy-Green deformation tensor invariants $\bar{I}_1$ and $\bar{I}_2$ and J the determinant of the deformation gradient tensor $\mathbf{F}$. The nearly incompressible form of $W^{(m)}$ could be written as:

$$W^{(cor)} = C_{01}(\bar{I}_2-3)+C_{10}(\bar{I}_1-3)+C_{11}(\bar{I}_1-3)(\bar{I}_2-3)+C_{20}(\bar{I}_1-3)^2+C_{02}(\bar{I}_2-3)^2+\frac{1}{D}(J-1)^2 \ , \quad (1)$$

Material and geometrical properties of the arterial wall are presented in the table below.

Table 1: Arterial wall proprieties (extracted from [4]).

	Height (m)	C_{10} (Pa)	C_{01} (Pa)	C_{11} (Pa)	C_{20} (Pa)	C_{02} (Pa)	D (Pa)
Intima	2.3E-4	2.04E5	2.23E5	3.71E6	1.37E6	2.37E6	0.52E6
Media	3.1E-4	1.17E5	1.28E5	6.72E5	2.24E5	5.69E5	0.92E6
Adventitia	3.4E-4	1.89E5	2.02E5	1.38E6	4.59E5	1.34E6	0.57E6

2.2 Pulsatile blood flow

Human heart contracts to pump blood during systole and relaxes to fill during diastole. This cyclic behavior make blood pulsatile in arterial vascular network. In biofluidics, pulsatility degree is quantified by the non-dimensional Womersley number α representing the ratio of transient inertial forces to viscous forces ($\alpha \approx 2.72$ in the LCA). Throughout a heartbeat, the systolic pressure is stored in the wraparound coronary artery and released at diastole. Consequently, the arterial wall alternates expansion and recoil. The velocity profile imposed at the inlet is written as:

$$V_e = 6V(t)\frac{y}{H}\left(1-\frac{y}{H}\right) \ , \tag{2}$$

where $V(t)$ is the instantaneous pulsatile velocity in the human LCA measured $in\ vivo$ by Bénard in [5], it is expressed as following:

$$V(t) = V_0 + \sum_{n=1}^{8} V_n \cos(n\omega t) + W_n \sin(n\omega t) \ , \tag{3}$$

where $V_0 = 0.16$ m/s is the average blood velocity throughout a heartbeat and $\omega \approx 7.85$ rad/s the angular frequency. The coefficients V_n and W_n are given in Table 2. The signal corresponding to $V(t)$ is plotted in Figure 2, we distinguish the systole ($0 < t$ (s) <0.29) and the diastole ($0.29 < t$ (s) <0.78).

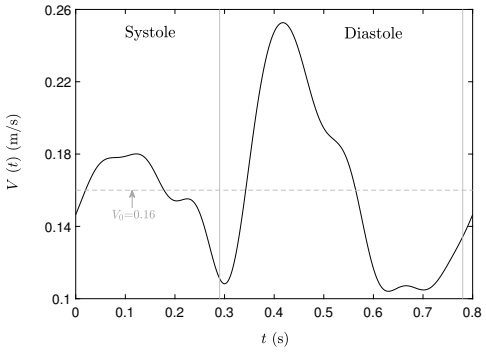

Figure 2: Signal of instantaneous velocity $V(t)$ in the LCA.

n	V_n (m/s)	W_n (m/s)
0	0.15634	0
1	-0.02995	0.00808
2	0.02458	0.03887
3	-0.01182	-0.00838
4	0.00985	0.00280
5	-0.01009	0.00313
6	0.00618	-0.00113
7	0.00133	0.000874
8	-0.00360	-0.000235

Table 2: Numerical values of coefficients V_n and W_n.

In the absence of precise data on physiological outflow conditions in the LCA in literature, a zero normal stress boundary condition is imposed at LCx and LAD ends. This widely used boundary condition means that the outer circulatory domain resistance is neglected and branches ends are exposed to the atmospheric pressure. A Carreau model is employed to model the shear thinning behavior of blood in coronary blood circulation:

$$\eta = \eta_\infty + (\eta_0 - \eta_\infty)[1 + (\lambda\dot{\gamma})^2]^{\frac{k-1}{2}} \ , \tag{4}$$

where $\eta_0 = 0.056\,\mathrm{Pa}\cdot\mathrm{s}$ is the zero shear viscosity, $\eta_\infty = 0.00345\,\mathrm{Pa}\cdot\mathrm{s}$ is the infinite shear viscosity, $\lambda = 3.313$ s and $k = 0.3568$ model parameters and $\dot{\gamma}$ (s^{-1}) is shear rate. Blood density is set to $\rho = 1060\,\mathrm{kg/m^3}$. The shear-thinning implies a flattened velocity profile.

2.3 Microparticles

Microparticles are formed by a thin membrane enclosing a small amount of liquid drug. The homogeneous, isotropic and impermeable membrane is treated as a very thin hyperelastic surface of thickness h devoid of bending stiffness. The membrane hyperelasticity follows the strain-softening neo-Hookean (NH) law whose incompressible form is expressed as:

$$W^{(m)} = \frac{G^{(m)}}{2}\left(\bar{I}_{1,m} - 3\right) \quad , \tag{5}$$

and Cauchy stress:

$$\boldsymbol{\sigma}^{(m)} = \mathbf{F}^{(m)} \frac{\partial W^{(m)}}{\partial \mathbf{E}^{(m)}} \mathbf{F}^{(m)^T} \quad , \tag{6}$$

in which $G^{(m)}$ is the shear modulus, $\mathbf{F}^{(m)}$ the deformation gradient tensor of the membrane and $\mathbf{E}^{(m)}$ the Green-Lagrange strain tensor. The NH law is found to accurately describe mechanical behavior of protein-reticulated membrane [6]. The coated drug is treated as a Newtonian fluid ($\eta = 0.00345\,\mathrm{Pa}\cdot\mathrm{s}$, $\rho = 1060\,\mathrm{kg/m^3}$). The deformation of microparticles is governed by the non-dimensional capillary number Ca which measures the ratio of viscous forces to the elastic resistance of membrane. The capillary number is expressed as $Ca = \eta_\infty V_0/(G^{(m)}h)$. The fluid domain constituted by the coated drug and blood is governed by Navier-Stokes and continuity equations.
At fluid-structure interfaces, stress continuity and velocity continuity are imposed as boundary conditions. A zero-displacement constraint is applied at arterial wall ends.

2.4 Numerical method

The Arbitrary Lagrangian Eulerian (ALE) method combine the advantages of the purely Eulerian description and the purely Lagrangian description. The fundamental equation for ALE gives the variation of a physical quantity f for a given particle X as:

$$\frac{\partial f}{\partial t}|_X = \frac{\partial f}{\partial t}|_\chi + \frac{\partial f}{\partial x} \cdot (\mathbf{v}_m - \mathbf{v}) \tag{7}$$

where χ identifies referential gird coordinates, x denotes the spatial coordinates, $\mathbf{v}_m$ is the dynamic mesh velocity and $\mathbf{v}$ the material velocity. At fluid-structure interfaces mesh velocity satisfies the condition:

$$\mathbf{v}_m \cdot \mathbf{n} = \mathbf{v} \cdot \mathbf{n} \quad , \tag{8}$$

where $\mathbf{n}$ is the outer normal unit vector. Time-integration is done using a first or second order accurate multi-step implicit Backward Differentiation Formula (BDF) scheme and variables are updated at each time-step using a damped Newton nonlinear method (first introduced in [7]). The discretization of the fluid domain is done with P2/P1 element that gives a quadratic basis for velocity and a linear basis for pressure. In order to prevent numerical instabilities, two consistent stabilization methods were introduced: streamline diffusion and crosswind diffusion. The mesh distortion is limited using Laplace [8], Winslow [9] and hyperelastic non-linear smoothing methods. A remeshing is automatically generated when mesh quality falls below a specified mesh quality threshold based on equiangular skewness or distortion.

3 Results and discussion

3.1 Coronary wall deformation

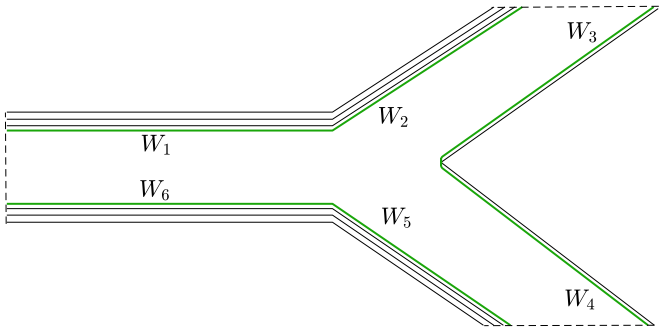

Figure 3: Localization of coronary walls.

The displacements of walls localized in the LM ($W_{1,6}$) and in the branches (W_{2-5}) are plotted in Figure 4.
The walls $W_{1,6}$ alternate deflection and inflection due to blood pulsatile wave propagation. A close look on plots reveals a symmetrical displacement during the systole ($t \leq 0.29$ s) and an asymmetrical evolution during diastole ($t > 0.29$ s). Furthermore successive displacements of wall W_1 during diastole reach a common value indicated by the intersection point I_1 and vary negligibly afterward, while displacement of the wall W_6 displacement vary significantly after intersecting at I_2 and even goes so far as the maximal displacement of 1.25 mm at $t = 0.65$ s, equalizing the maximal value reached during the systole at $t = 0.29$ s.
One can see that walls $W_{3,4}$ expand symmetrically during diastole in a parabolic-like fashion without exceeding 22% of dilation. The symmetry is also observed at early times in systole, which asserts a fully symmetrical behavior.
In the case of walls $W_{2,5}$, the plots provide evidence that displacements during systole are asymmetrical (a gap of 38-48%). The asymmetry is also noted during diastole including early times and excluding $t = 0.29$ s, thus showing the co-existence of asymmetrical and symmetrical deformation in opposite coronary walls even in the LM (excepted walls $W_{3,4}$ bounded by the corner). The height-evolution of $W_{1,2}$ and $W_{5,6}$ plotted in Figure 5 confirms this co-existence.

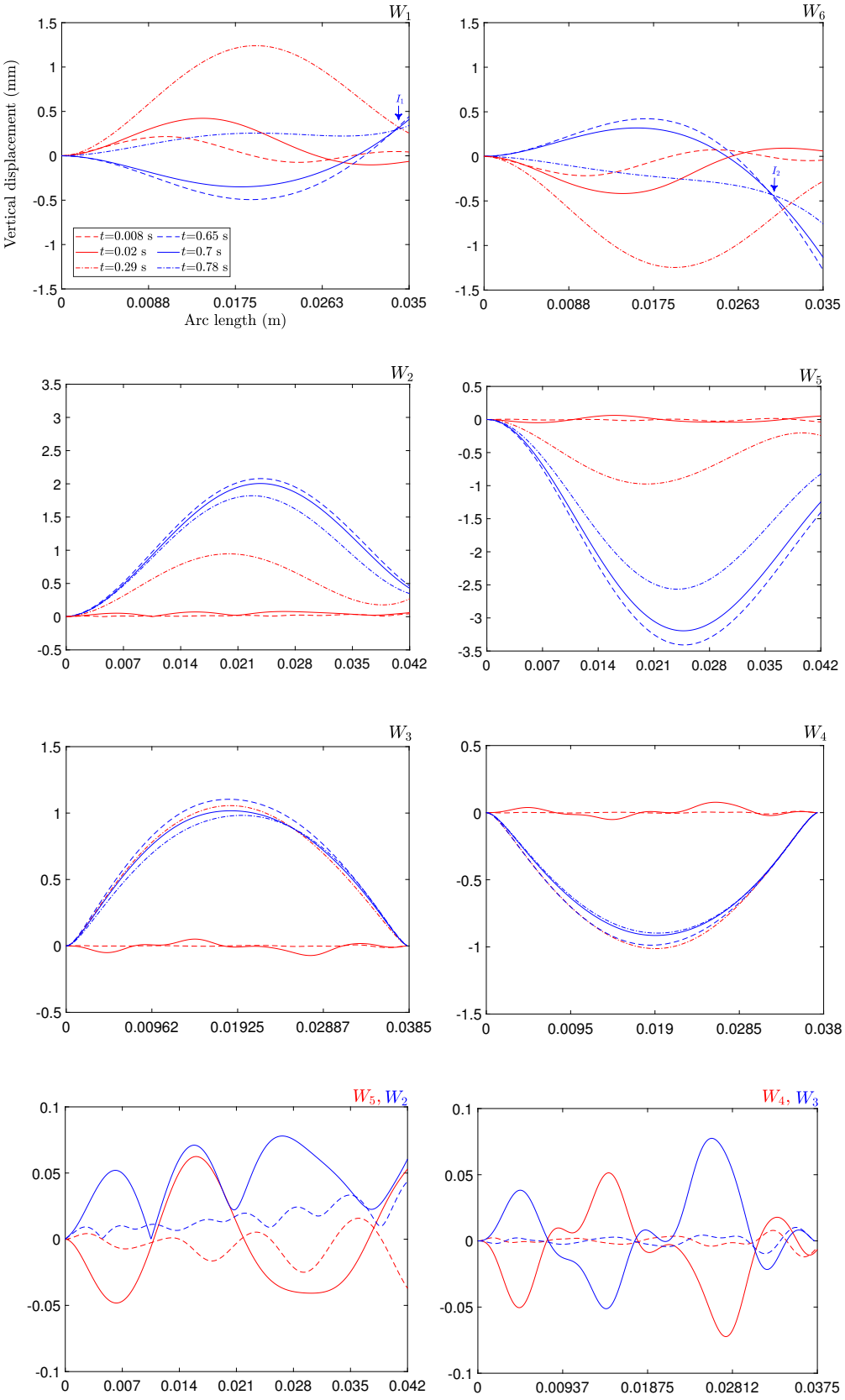

Figure 4: Vertical displacement of coronary walls.

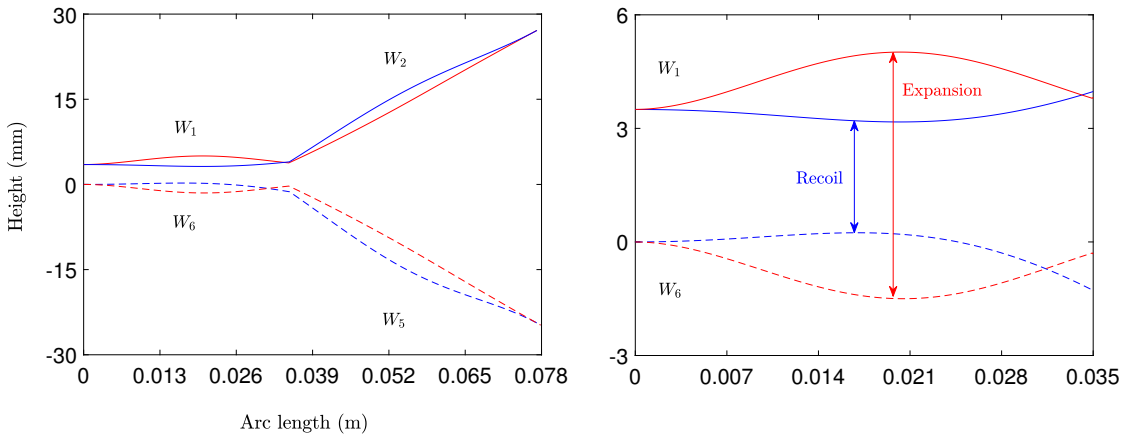

Figure 5: Expansion-recoil at $t = 0.22$ s (red) and $t = 0.60$ s (blue).

Now regarding the flow properties, Figure 6 shows that blood velocity at outlets is higher in the LAD, which thus combines higher flow velocity and higher deformation. The influence of the hyperelastic coronary wall is highlighted through comparison with an infinitely rigid wall. From now on, the abbreviation DCW refers to the hyperelastic coronary wall modeled using the 5-parameters Mooney-Rivlin law (Eq. (1)) while the abbreviation RCW is for the rigid coronary wall. For the LCA, the comparison between the two walls is even more relevant due to the pulsatile character of blood. Furthermore, the wall shear stress (WSS) (the force per unit area exerted tangentially by blood on vascular walls) is found maximal at $W_{3,4}$ and is even more higher in the RCW. Example of WSS distribution is shown in Figure 7. The higher WSS at bifurcating inner walls is a consequence of the velocity skewing toward these same walls as seen in Figure 8. In the RCW skewing vanishes with times and is found to significantly reduces in the DCW. These preliminary results related to coronary wall deformation either in the LM or in daughter branches promise a peculiar dynamical behaviour of microparticles flowing in the LCA.

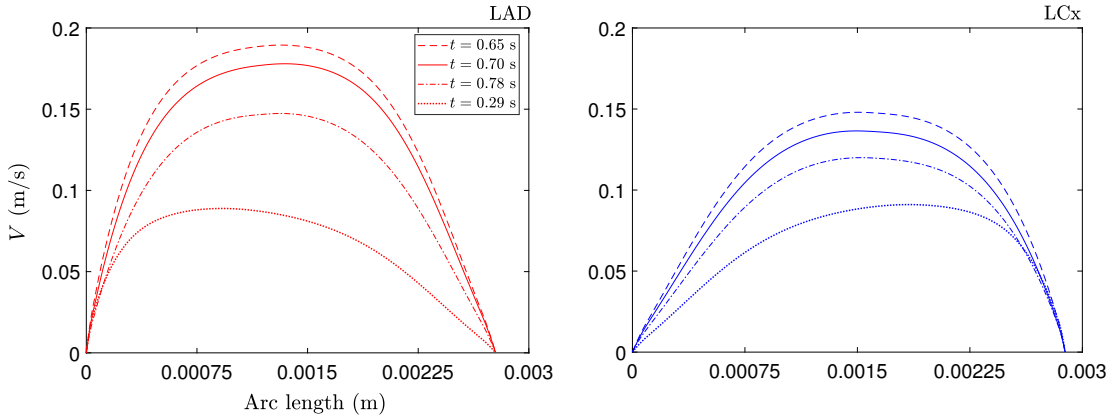

Figure 6: Blood velocity at outlets in daughter branches, DCW.

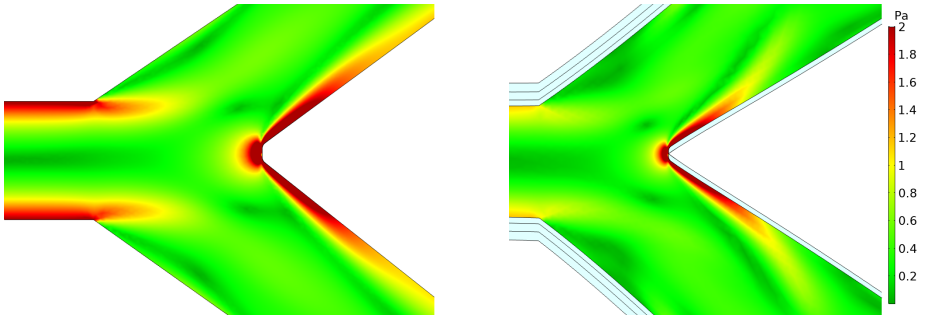

Figure 7: Wall shear stress distribution at $t = 0.4$ s.

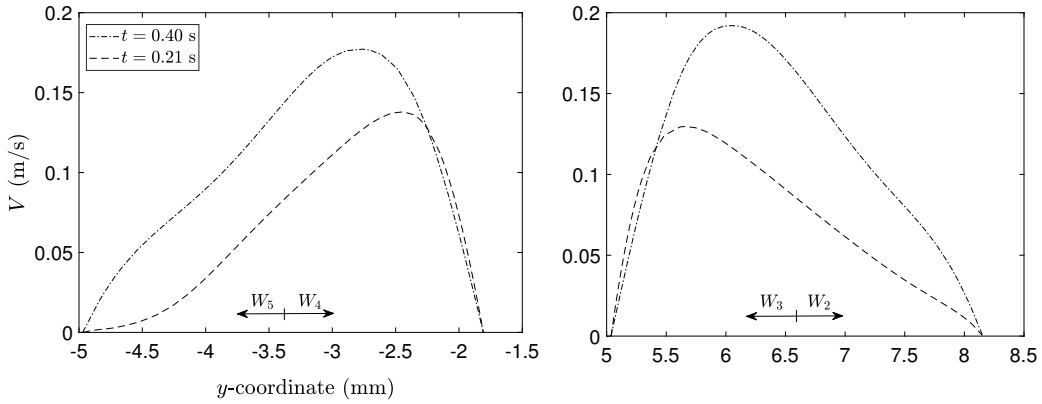

Figure 8: Blood velocity skewing in the DCW.

3.2 Off-centered microparticles

A-Trajectory

The influence of coronary wall rigidity on off-centred microparticles (initially placed at p_1 or p_3) is plotted in Figure 9. It reveals that in the presence of the RCW, trajectories followed by the centers of mass (x_c,y_c) are coincident (Figure 9(a) and 9(b)). Besides, blood being less disrupt in the RCW, trajectories are much more smoother than those obtained in the DCW. In this conditions, microparticles move in a straight pattern in the RCW. Adding to this, overtaking do not occur in the absence of hydrodynamic suction (see [10] for further details). Overtaking in the DCW is preceded by a binary collision characterized by a flattening of sides in tight contact. In the daughter branches where the shear stress is relatively low due to flow splitting at the bifurcation, large oscillatory recirculation zones are observed (two vortexes in each branch). Flow recirculation is accentuated by coronary expansion and viscosity decrease caused by shear-thinning of blood. Vortexes in the LAD are largest due to the higher flow rate and the higher expansion. Interestingly, microparticles are trapped in the formed vortexes as indicated by the hook-like pattern and the loops in the centers of mass trajectories. In contrast to observation in [11] where vortex-trapped microparticles conserve a circular shape and undergo a tank-treading motion during residence in vortex, in the present configuration vortex-trapped microparticles experience a deformation, this deformation might be transitory and vanishes as microparticles orbit repeatedly (which is not reported here as microparticles tank-tread a single time).
On the lateral migration mechanism depicted in Figure 9(c), microparticles flowing in the DCW are aspired due the hydrodynamic suction force near the upper or the lower wall before effectively migrate toward blood vessel centerline. While this behavior is produced on both opposite sides, the resulting curves are mirroring only in the RCW. Now regarding the influence of membrane shear resistance combined to that of the wall, it is

shown in Figure 9(d) that Ca impacts the vortex trapping (especially for p_3) as well as trajectories. Conversely, trajectories in the RCW are insensitive to Ca and the gap between the curves is scarcely discernible. Visual demonstration of off-centered microparticle vortex-trapped in the DCW is given in Figure 10, the figure also shows that once freed from the vortex in the LAD, the Md microparticle exclusively backward flows toward the LM.

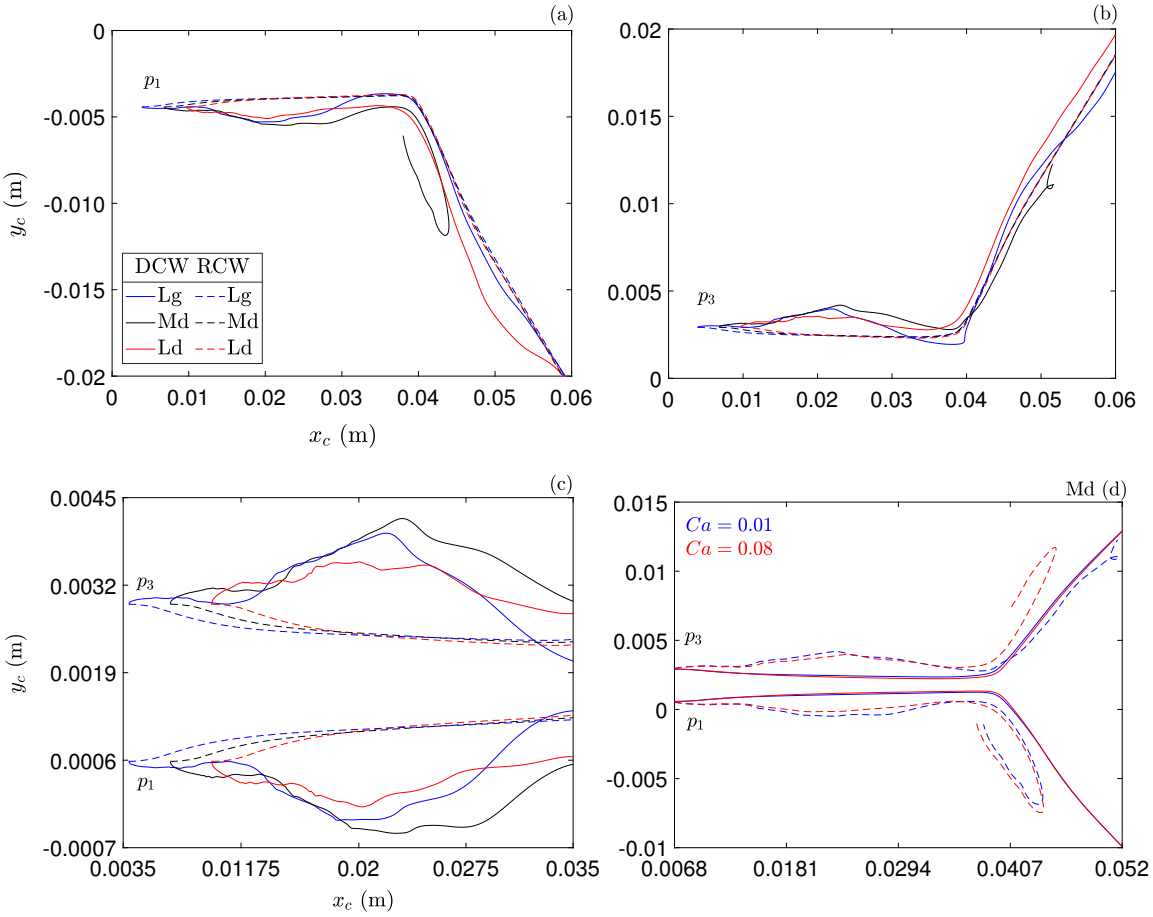

Figure 9: Effect of coronary distensibility for $Ca = 0.01$ (a-c). Effect of the capillary number combined with that of the coronary distensibility on the Md microparticle (d).

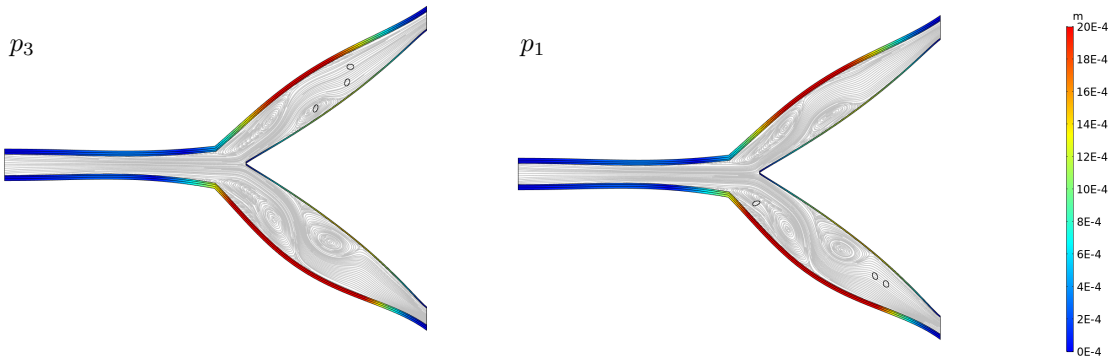

Figure 10: Microparticles vortex-trapped at $t = 0.6$ s for $Ca = 0.01$.

The risk of microparticles clustering is appraised by monitoring particle-particle spacing s_1 (the distance sep-

arating the centers of mass of the Lg and the Md microparticle) and s_2 (the distance separating the centers of mass of the Md and the Ld microparticle) through time (Figure 11). In the RCW, the spacings are found to evolve in a quite similar fashion independently on the initial vertical position. This can also apply for the DCW with the exception that the spacings growth after a first inflection for p_1. Clustering risk is more probable for s_1 independently on the nature of the coronary wall and the initial vertical position. This is attributed to the relatively higher velocity of the Ld microparticle.

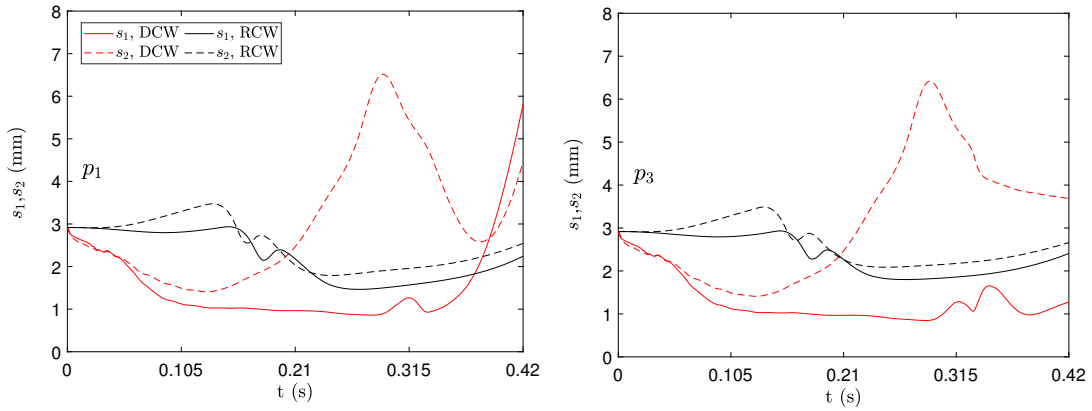

Figure 11: Time-evolution of particle-particle spacing for $Ca = 0.01$.

B-Deformation

Deformation of microparticles is quantified by deformation gradient tensors $\mathbf{F}_{xX}^{(m)}$ and $\mathbf{F}_{xY}^{(m)}$ (Eq. (6)) instead of Taylor parameter because of asymmetrical deformation exhibited in some regions. These quantities are plotted against x_c for meaningful comparison between the rigid and the hyperelastic walls (see Figures 12 and 13). It is clear that microparticles are much more deformed in the presence of the DCW and the corresponding curves present larger inflection points due coronary wall distensibility. In the rigid walled LM ($x_c \leq 0.035$ m), deformation gradients are uniformly dephased (vertical dephasage corresponds to the initial particle-particle spacing). The Lg microparticle is found to reach an asymptotic deformation when flowing in the DCW (but only for p_1). A general observation is plots is the smooth evolution in comparison to the DCW case. Deformation gradients plotted for $Ca = 0.01$, 0.08 in Figure 14 reveals that the influence of membrane shear resistance on the whole microparticle deformation is noteworthier in the presence of the RCW. The same applies for the position p_3. The variations of deformation depending on the initial vertical position stated above ensues from the asymmetrical deformation of walls $W_{1,2,5,6}$. The deformation of microparticles is qualitatively illustrated in Figures 16-18, pointing out a mirroring deformation and particle-particle spacing in the RCW in a stark contrast with the DCW.

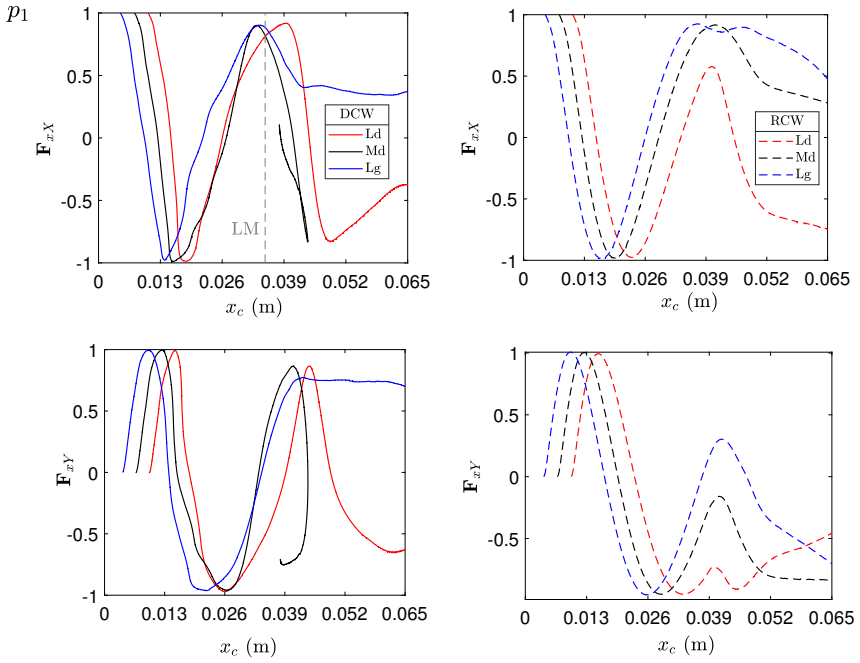

Figure 12: Deformation gradient for $Ca = 0.01$.

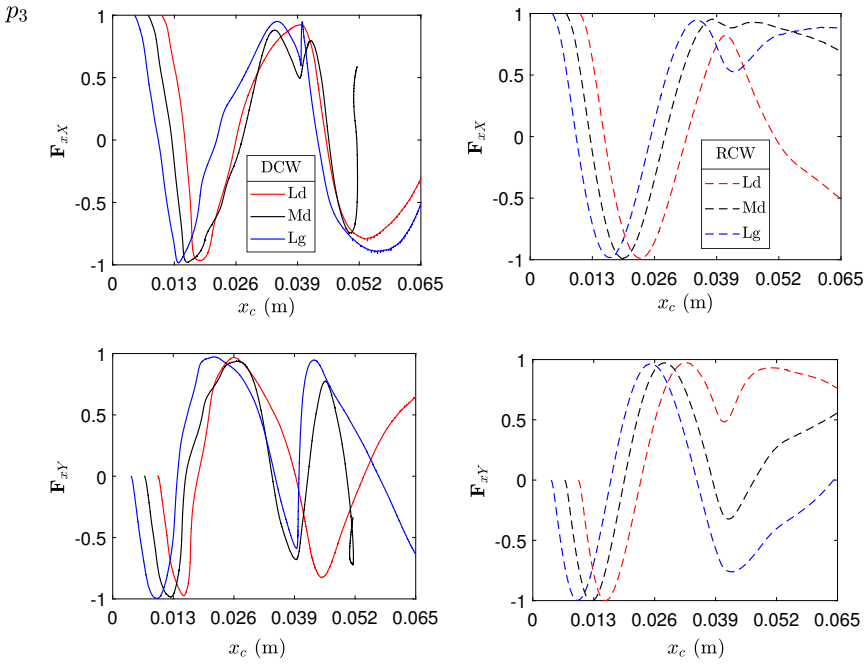

Figure 13: Same as Figure 12 for p_3.

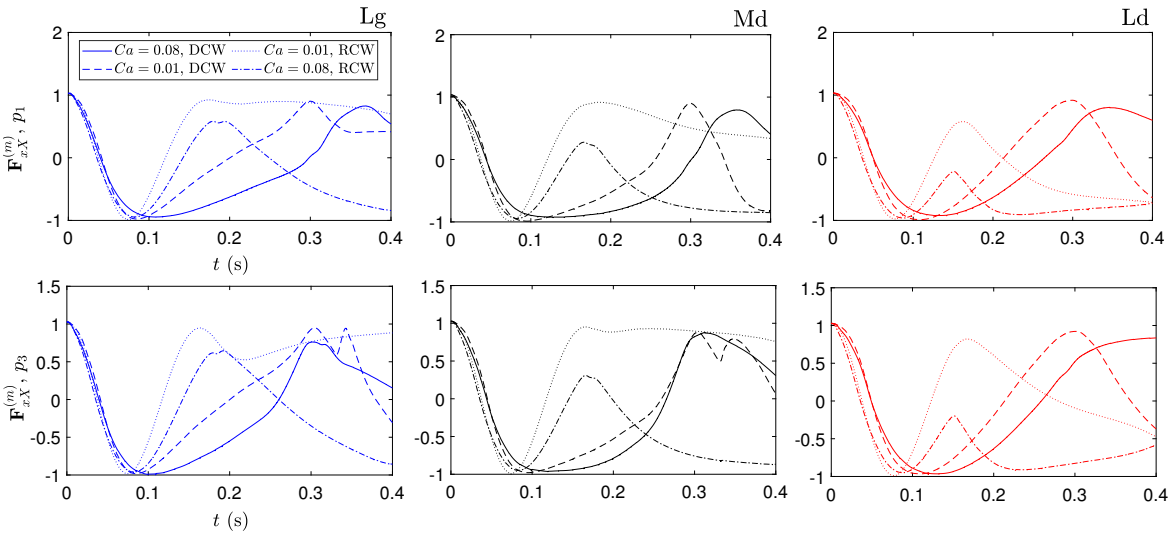

Figure 14: Time-evolution of the deformation gradient of off-centred microparticles.

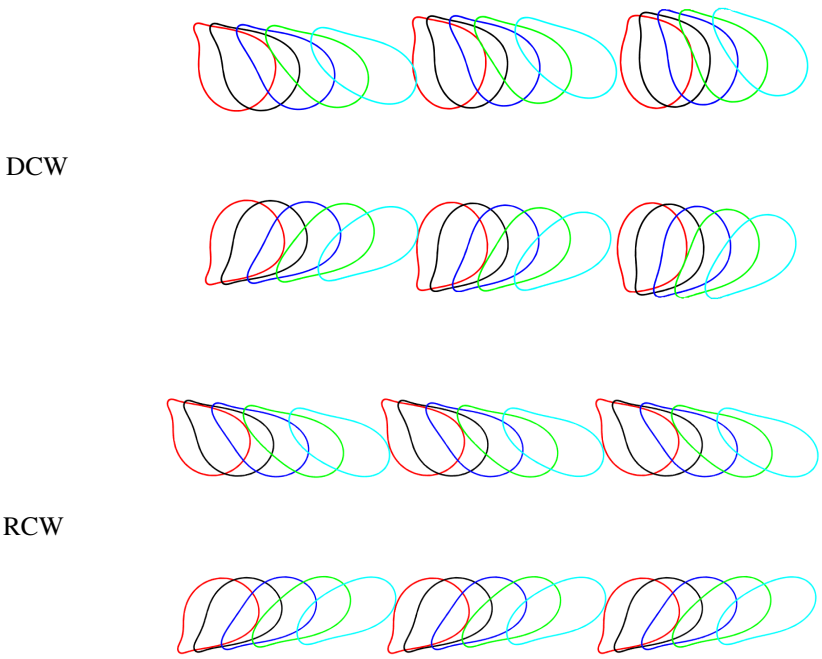

Figure 15: Deformed shapes at $t = 0.007$ s (red), 0.009 s (black), 0.012 s (blue), 0.015 s (green) and 0.019 s (cyan) for $Ca = 0.08$.

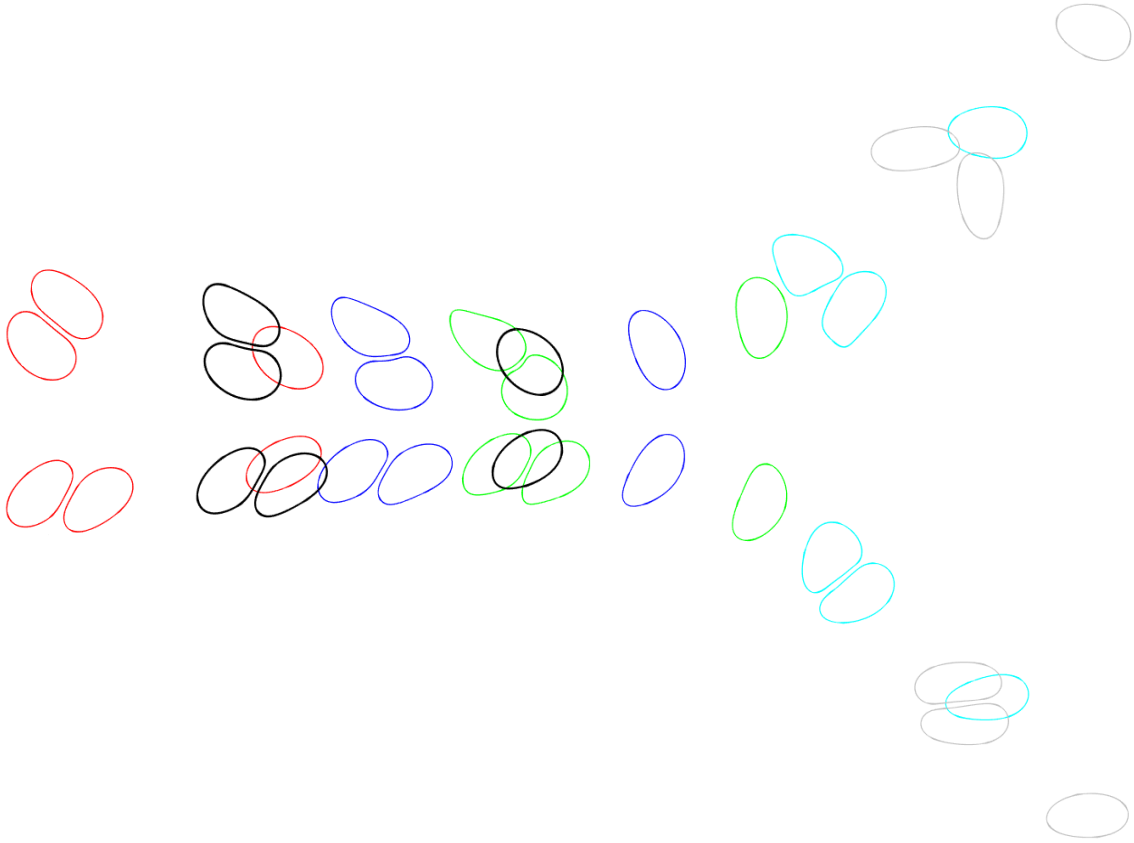

Figure 16: Deformed shapes at $t = 0.25$ s (red), 0.27 s (black), 0.28 s (blue), 0.29 s (green), 0.32 s (cyan) and 0.34 s (gray) for $Ca = 0.08$, DCW

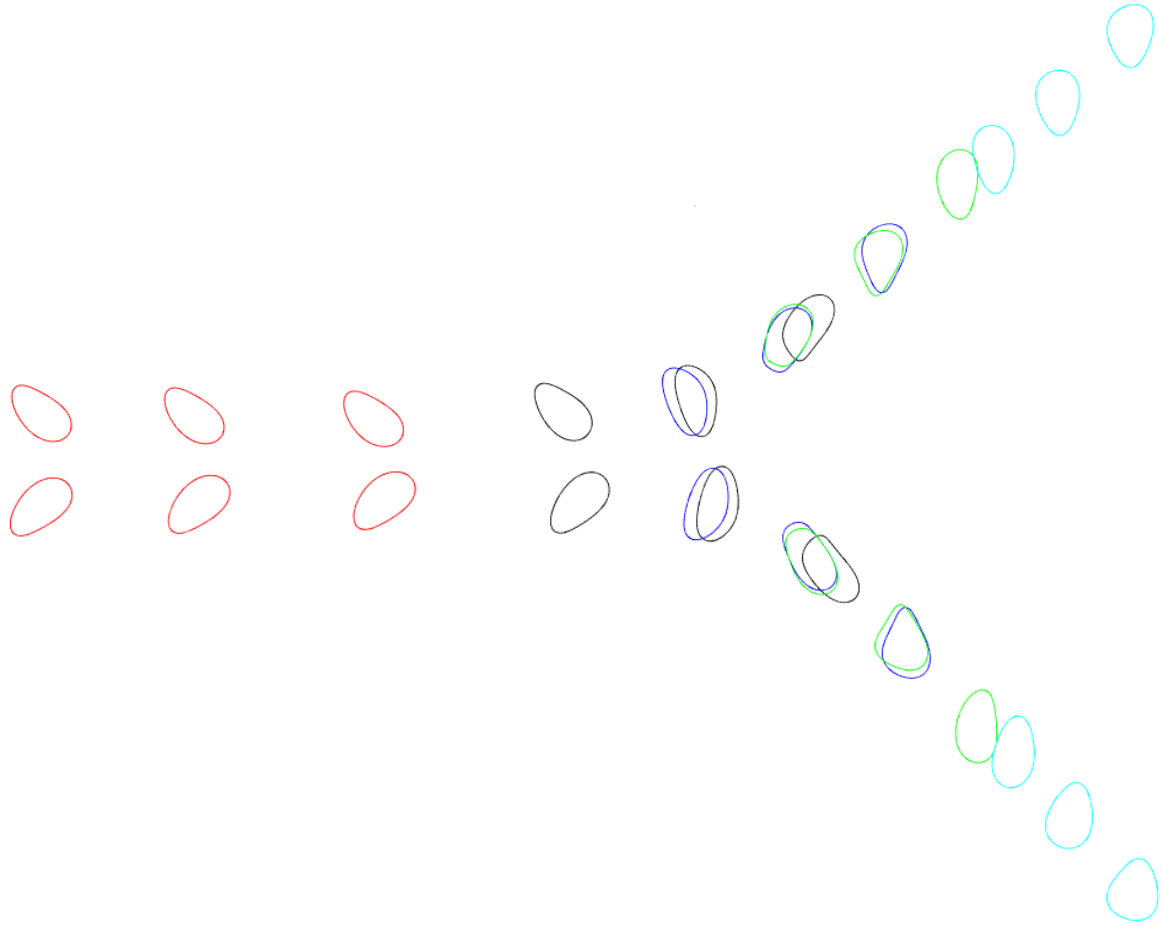

Figure 17: Deformed shapes at $t = 0.12$ s (red), 0.165 s (black), 0.178 s (blue), 0.193 s (green), 0.231 s (cyan) for $Ca = 0.08$, RCW

As seen in Table 3, the microparticles initially placed at p_1 flow faster due to the higher velocity in branch (i.e. the LAD) in the vicinity. Moreover, microparticles with less shear resistance ($Ca = 0.08$) oppose less resistance to deformation and adopt shapes propitious for an easy motion.

Table 3: The average velocities of microparticles.

		Average velocity (m/s)		
	Position	Md	Ld	Lg
$Ca = 0.01$	p_1	0.095	0.119	0.120
	p_3	0.068	0.080	0.092
$Ca = 0.08$	p_1	0.099	0.110	0.118
	p_3	0.070	0.087	0.096

3.3 Centered microparticles

3.3.1 Overall behavior

Coronary wall distensibility foreshadows significant flow disturbance. Blood velocity plotted over specific times in systole at S_1 in Figure 19 reveals blunted velocity profile in the DCW due to the local expansion. Additionally, magnitude of instantaneous velocities is significantly higher in the RCW and its evolution contrast with that of the DCW. Farther down the LCA, velocity integrated along the segment S_2 is found to vary differently in branch entrance depending on the nature of the coronary wall. More precisely, blood moves faster in the rigid-walled LCx as a direct consequence of shear-thinning. The blood velocity along S_2 will be reevaluated later at crucial times (times at which the preferred branch is selected). Before moving further we signal convergence issues at $t \leq$0.278 s for $0.04 < Ca \leq 0.08$, hence calculations are run for $Ca = 0.04$. Results of $Ca = 0.08$ are even exposed before the convergence.

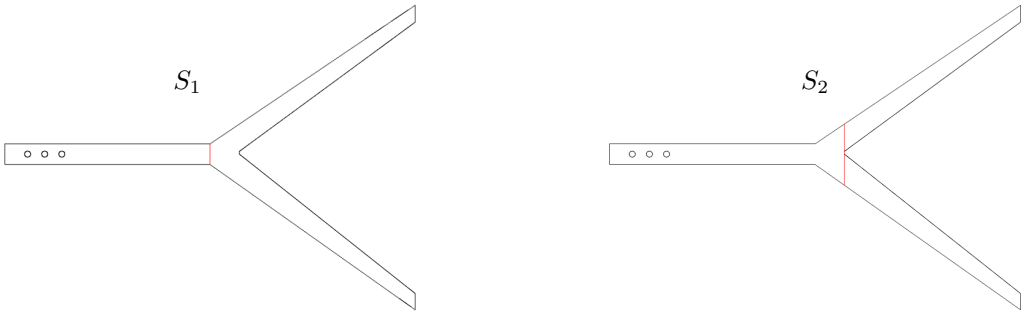

Figure 18: Localization of generating segments S_1 delimiting the end of the LM ($x = 0.035$) and the segment S_2 defined in the bifurcation zone ($x = 0.04$).

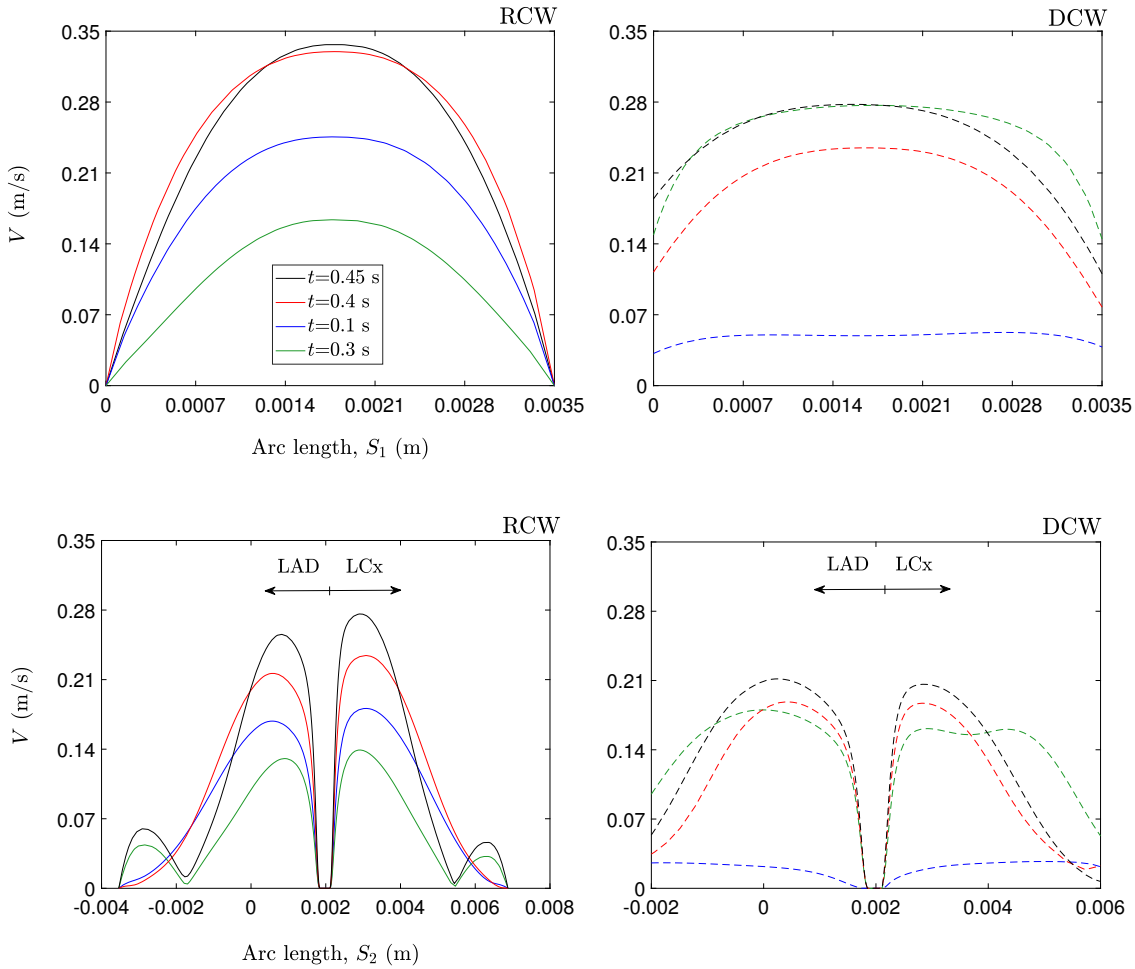

Figure 19: The blood velocity along generating segments S_1 and S_2.

A-Trajectory

In contrast to off-centered microparticles, the centered microparticles enter different branches. In the DCW, two microparticles (Ld and Md) enter the LAD due to the higher flow velocity. Wall rigidity is found to modify the preferred branch of the Ld microparticle, the latter enter the rigid-walled LCx together with the Md microparticle (again due to the higher local velocity). This higher velocity and the induced lower viscosity (due to shear-thinning) are a guarantee of a minimum energy cost. Other local phenomenon is the immediate vicinity of the corner (discussed in 3.3.2) will be found to play a major role in the selection of the preferred branch. It is notable from the zoomed inset in Figure 20(a) and 20(b) that microparticles are kinetically vacillating in the LM while microparticles in the RCW follow a strictly straight path. On another note, microparticles in the hyperelastic-walled LAD experience vortex trapping and overtaking all Ca included (as revealed by plots in Figure 20(b) and illustrated in Figure 21). Both are not reproduced in the RCW, nevertheless trajectories in daughter branches are impacted by local recirculation, giving rise to curvilinear trajectories in some sections of the rigid-walled branches as depicted in Figure 20(c).

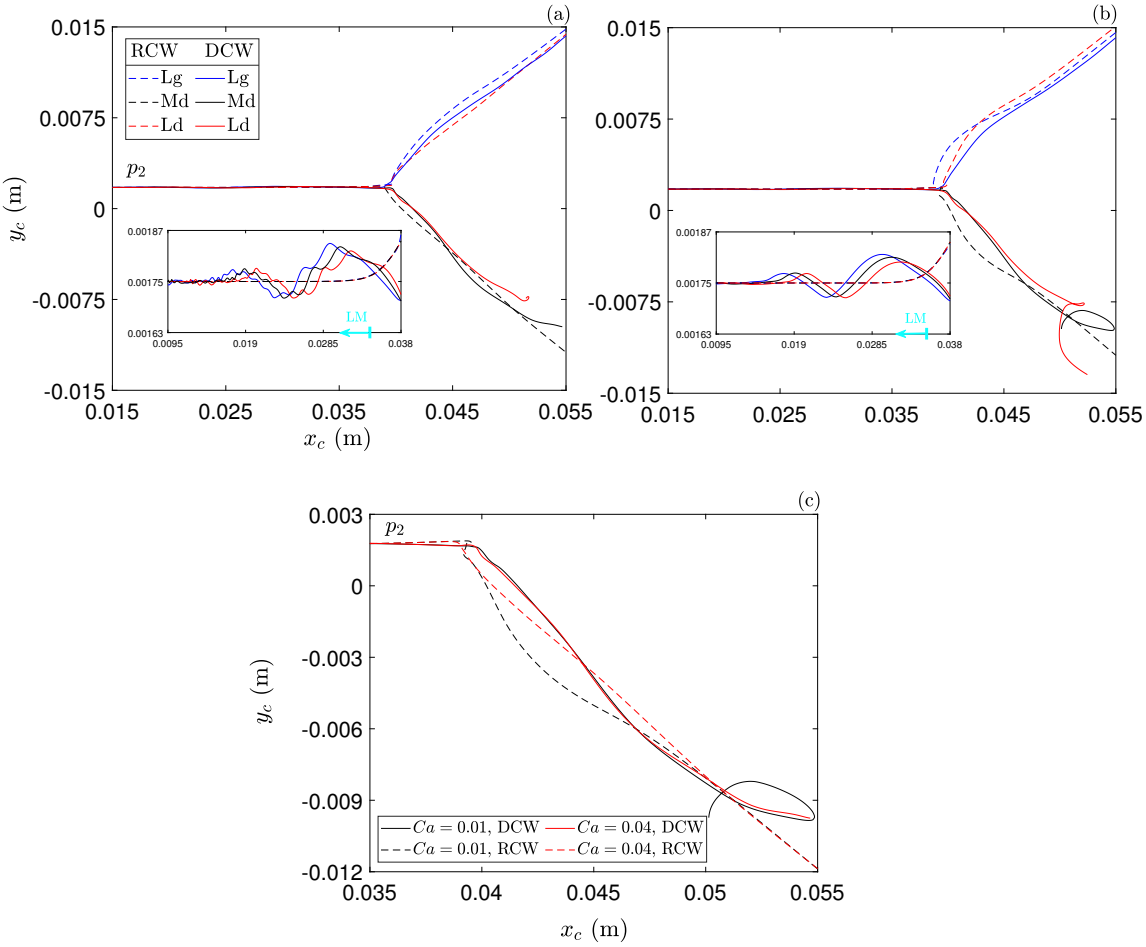

Figure 20: Microparticle trajectories for (a) $Ca = 0.01$ (b) $Ca = 0.04$ (c) Md

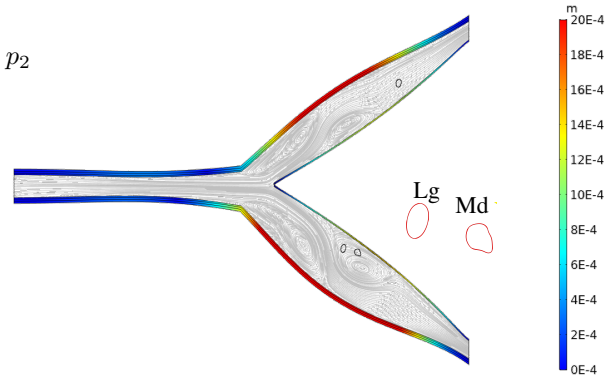

Figure 21: Streamlines at $t = 0.6$ s showing microparticles vortex-trapped in the LAD for $Ca = 0.04$.

B-Deformation

When it comes to the effect of the capillary number combined to that of the wall, it can be seen in Figure 22 that the influence of membrane shear resistance on microparticle deformation is amplified by the RCW which is in

line with the remark previously made for off-centered microparticles. More interestingly, softer microparticles flowing in the RCW are drastically deformed, the corresponding evolution of deformation gradient is unusual in comparison to previously plotted quantities. Morphological changes presented later will aptly illustrate this deformation. Microparticles adopt various symmetrical shapes in the hyperelastic-walled LM: circular, oblate and prolate-like shapes depending on coronary wall deformation (see Figure 23). More precisely, microparticles are oblate-like shaped when the walls expand ($t = 0.11$ s) and prolate-like shaped when the walls recoil ($t = 0.21$ s). Shape transition took place in a breathing-like dynamic due to coronary expansion-recoil, as revealed by the zoomed insets in Figure 22 and confirmed by the time-evolution of Taylor parameter plotted in Figure 24. This behavior is well known in electro-hydrodynamics [12]. In the RCW, stiffer microparticles remain quasi-circle shaped in the LM and deviate progressively from their initial shape to develop the parachute-like shape for $Ca = 0.04$.

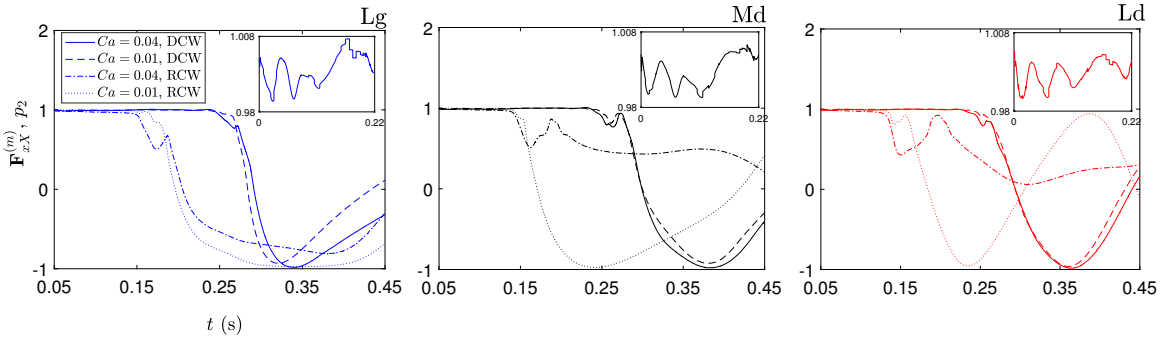

Figure 22: Time-evolution of the deformation gradient of the centered microparticles.

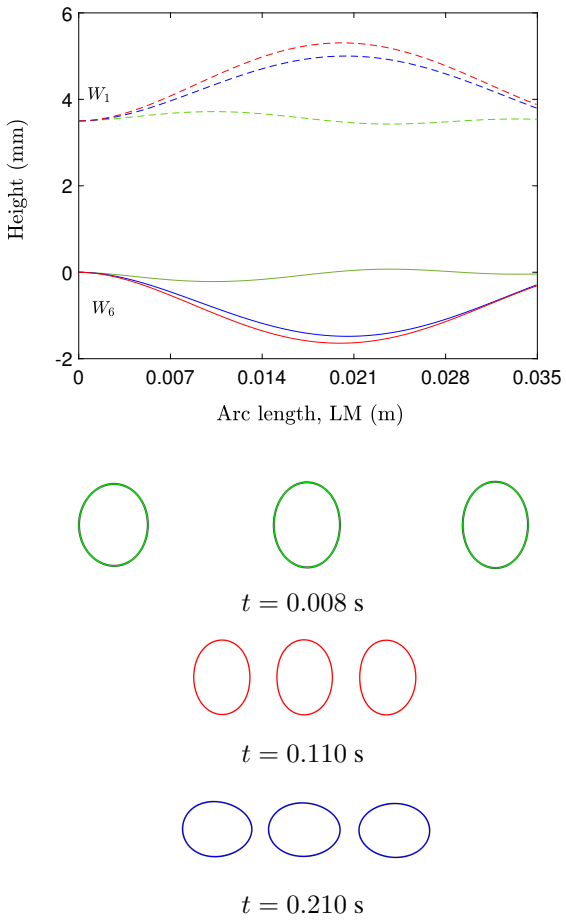

Figure 23: Deformation of the coronary walls $W_{1,6}$ in the LM and the corresponding microparticles deformation.

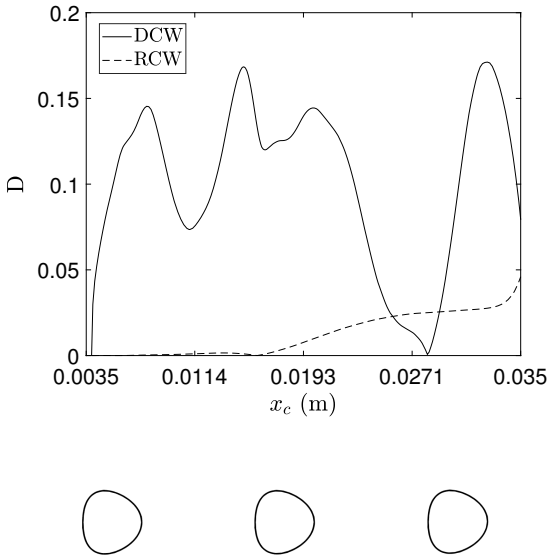

RCW

Figure 24: Time-evolution of Taylor parameter for the Lg microparticle. The snapshot shows the parachute shape at $t = 0.11$ s ($Ca = 0.04$).

The elastic strain energy noted $W^{(m)}$ (Eq. (5)) is another indicator of deformation, this quantity is plotted over time in Figure 25. In the RCW, the elastic strain energy stored in softer membranes is markedly higher, all positions included. Such sharp jump was expected in view of previously noticed elements related to deformation gradients. For the DCW, $W^{(m)}$ is (naturally) higher for $Ca = 0.04$ but the relative difference to $Ca = 0.01$ is quantitatively much more less in comparison to the RCW. Regarding the effect of the initial horizontal position, we found as predicted that the Ld microparticle stores the highest energy, followed by the Md and then the Lg microparticle. We further note that energy storage has a cyclic tendency in the DCW, once again outlining the influence of coronary walls' successive deflection and inflection on microparticle mechanical response.

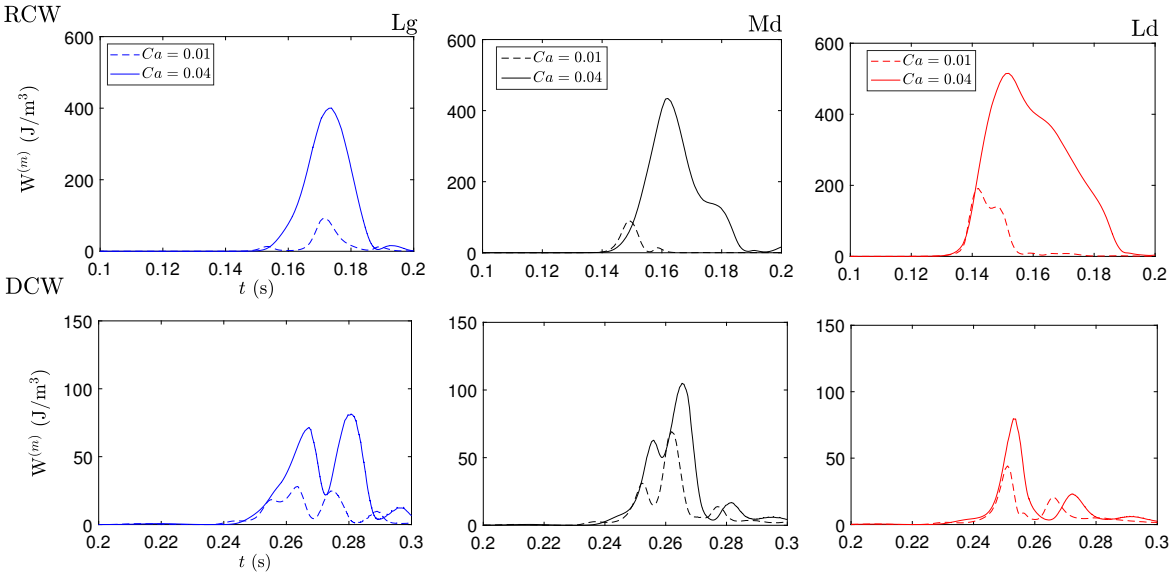

Figure 25: Time-evolution of the density of strain energy of the centered microparticles.

3.3.2 Behavior at the bifurcation zone

The impaction designates the collision of particles against the bifurcation corner or the corner-adjacent walls caused by particle inertia. The interception refers to the contact between partitioning particles and the corner-adjacent walls, initiating the effective entrance in branches. It is related to particle size in that large particles are more likely to experience interception. Impaction and interception are both mechanisms of particle capturing (e.g. particle deposition in the lung [13]) and have been observed $in\ vitro$ for red blood cells (RBCs) bifurcating in microcirculation[14]. Being aware of the relevance of the pre-cited mechanisms and the major role they play in branch selection as well as microparticle behavior through it, we have studied the behavior in the bifurcation zone distinctly from the overall behavior of centered microparticles. Obtained results proved to be very insightful, in particular for softer membranes. We outline that impaction and interception only concern microparticle whose membrane collides with the corner or with the corner-adjacent walls.

A-DCW

a-Trajectory

Before addressing the qualitative deformation of microparticles impacting the corner of the DCW, we observe that microparticles deviate from the centreline and start partitioning in branches simultaneously (Figure 26). After that, they impact the corner one at a time and initiate their entrance in branches in the same order of location (the Ld first followed by the Md and then the Lg). For the two in-front microparticles, the preferred branch in the LAD where the velocity is higher at crucial times (Figure 27), the Lg microparticle enters the LCx as its entrance in the LAD is significantly impeded by the slow sliding in-front microparticles. The slow sliding along the corner is commonly observed for RBCs bifurcating in the microvascular network [15] and for synthetic spherical cells [16], it results from the important shear stress localized at the rear-end. During interception, the Ld and the Md microparticles slide against the immediately adjacent intimal wall of the LAD and start a localized lateral migration to drift away from it, which is in line with the observations reported in [17]. The Lg microparticle reproduces the same behavior in the LCx.

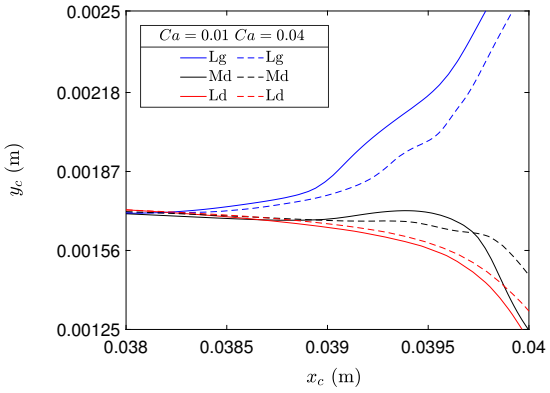

Figure 26: Zoom on microparticle trajectories at the bifurcation zone in the DCW.

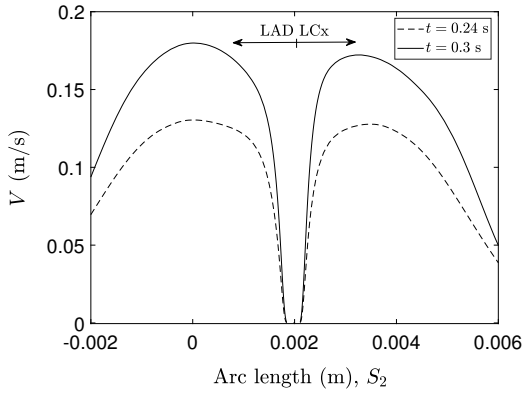

Figure 27: The blood velocity along S_2, DCW.

b-Deformation

Softer microparticles ($Ca = 0.04$ and $Ca = 0.08$) develop an arm-like end at the rear to accommodate the corner shape during sliding (at $t = 0.265$ s and $t = 0.268$ s for $Ca = 0.04$ and at $t = 0.268 - 0.275$ s for $Ca = 0.08$) and to 'claw a way' through the tightening inter-particle space in a crawling like-motion during which the arm-like end is dragged as a tail. The arm-like end slenderize as membrane softness increases. For $Ca = 0.08$, a tip resembling the cusp-like instability reported for migrating microparticles is formed at microparticles back at the very end of arm-like end relaxation. Apart from the functional aspect and from a morphological point of view, the arm-like end make the squeezed microparticles able to exhibit remarkable deformation modes like the center-domed slug shape at $t = 0.275$ s and the sigmoid-shape (tortuous shape) at $t = 0.280$ s both favouring a delicate displacement. A common observation is the tendency of microparticles to cluster as the softness of the membrane increases (see for example deformations at $t = 0.265$ s and $t = 0.275$ s). Back to the convergence problem for $Ca = 0.08$ occurring at $t \approx 0.288$ s, snapshots in Figure 29 at times prior to divergence shows an exaggerated elongation and a central tethering accompanied by thinning of the membrane (even if the latter is modeled as an incompressible solid) leading us to believe that the microparticle is about to break-up. This also due to strain-softening characterizing the here-considered protein membrane induced by structural damage as presented in [18, 19]. In addition to being zones of localized stress, we recall that tether and the cusp are both mathematical instabilities then their co-existence is pronounced to cause significant calculation problems. A similar numerical failure was reported in [20] after the apparition of the tips.

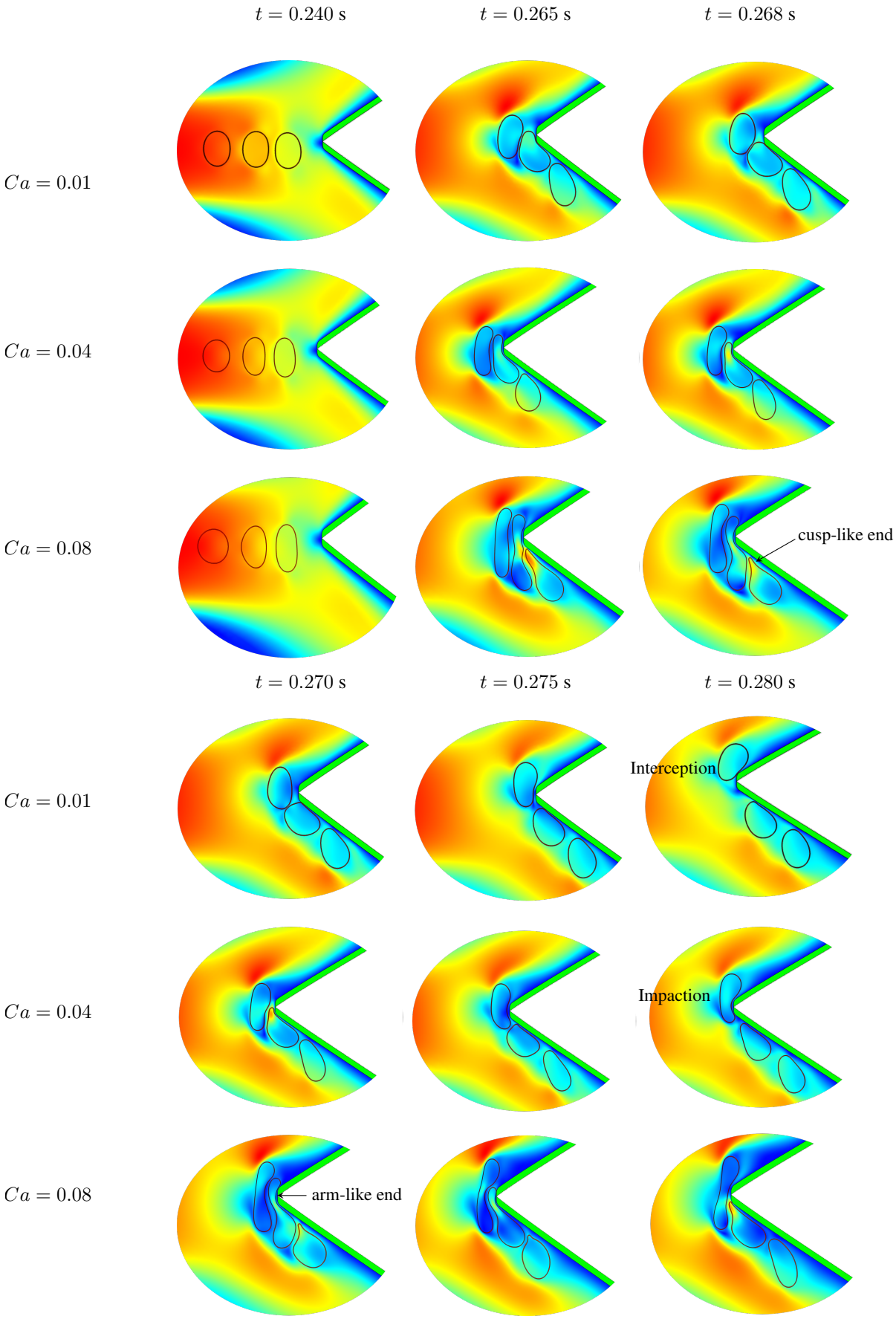

Figure 28: Snapshots in time of microparticles in the bifurcation zone for p_2.

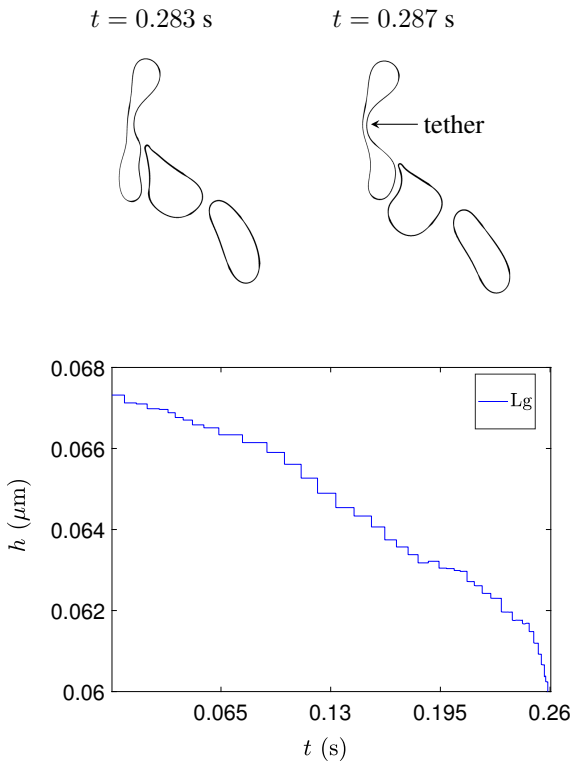

Figure 29: Microparticle deformation showing tethering and excessive elongation for $Ca = 0.08$, DCW (top image). Time-evolution of membrane's thickness (bottom image).

B-RCW

a-*Ca=0.01*

Unlike the DCW, only two microparticles impact the corner. Actually, the Ld microparticle stuck to the corner thus preventing the in-back Md microparticle to experience impaction. The Ld microparticle eventually unstuck from the corner leaving the Lg microparticle to impact the corner at its turn. Microparticles adopt asymmetrical ovaloid-like shapes in the bifurcation zone (Figure 30). The bean shape exhibited by the Ld microparticles when impacting the corner is previously seen in [16]. Another marked difference from the DCW case is that two microparticles enter the LCx Figure 31(a). The Lg microparticles is first to enter the LCx as the instantaneous blood velocity is higher (as seen in Table 4). The immediately contiguous Md microparticle enters the opposite branch as it took advantage from the unoccupied blood space leaved the neighboring microparticle. The Ld microparticle is the last to enter a branch, similarly to the Md microparticle, its preferred branch is more conditioned by the contiguous microparticle deformation than by the instantaneous blood velocity. While the primary purpose was to assess the global effect of the RCW in comparison to the baseline DCW wall, we dwelt on the combination $Ca = 0.04$, RCW in view of unprecedentedly reported deformation modes.

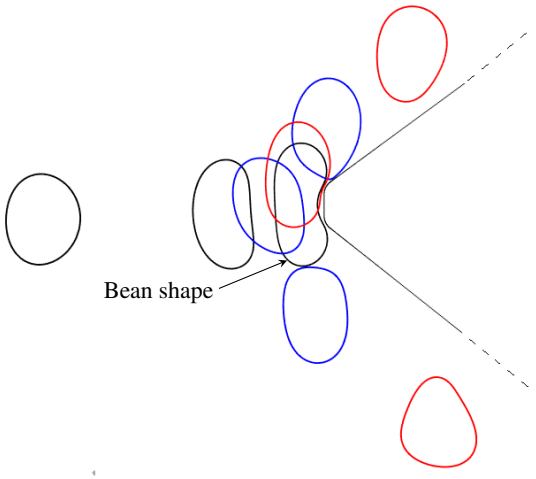

Figure 30: Deformed shapes at $t = 0.145$ s (black), $t = 0.164$ s (blue) and $t = 0.180$ s (red) for $Ca = 0.01$, RCW.

Table 4: The average velocity of shear-thinning blood along S_2 for RCW.

t (s)	V (m/s)	
	LCx	LAD
0.145	**7.18E-2**	5.70E-2
0.158	**3.84E-2**	3.51E-2
0.164	3.39E-3	**3.47E-2**
0.175	**3.87E-2**	3.57E-2
0.180	**3.11E-2**	2.70E-2

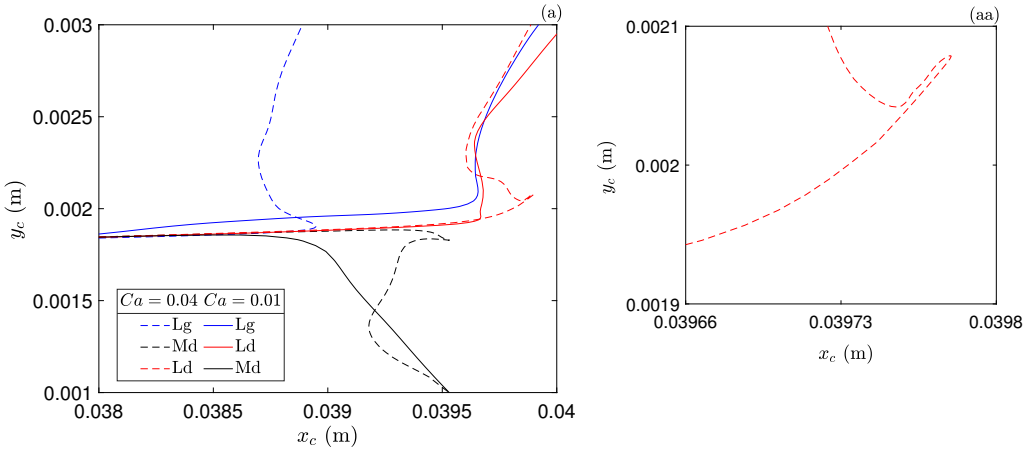

Figure 31: Microparticle trajectories in the bifurcation zone for RCW.

b-*Ca=0.04*

Trajectory

Similarly to stiffer membranes, two microparticles enter the LCx for the same reasons presented above. However, a single microparticle impacts the corner (the Ld microparticle) and remains longer stuck due to its important deformability and strain energy storage capacity. As depicted in Figure 31(aa), the Ld microparticle come unstuck from the corner by performing a 'turning back' enabled by membrane relaxation. The combination between the important membrane deformability and blood velocity, microparticle inertia and size results in microparticle jamming. The later owes the creation of a stagnation zone characterized by blood recirculation (Figure 33). An implication of the local blood recirculation in stagnation zone is the 'bumps' (B_1, B_2 and B_3) in the center of mass trajectories as microparticles have to overcome the recirculation zone to enter a branch. Accordingly, the interception do not occur. We notice that blood recirculation denser in the bottom also favors microparticle entrance to the LCx. To sum up, blood instantaneous velocity in branch entrance determines the preferred branch of the Lg and this latter controls the branch selection of the contiguous microparticles as they benefit from the microparticle-free space created by the in-back bifurcating microparticle, this proves that the instantaneous blood velocity at branch entrance and the deformation mode of neighboring microparticles are both determinants of the preferred branch of microparticles whose membrane is highly deformable.

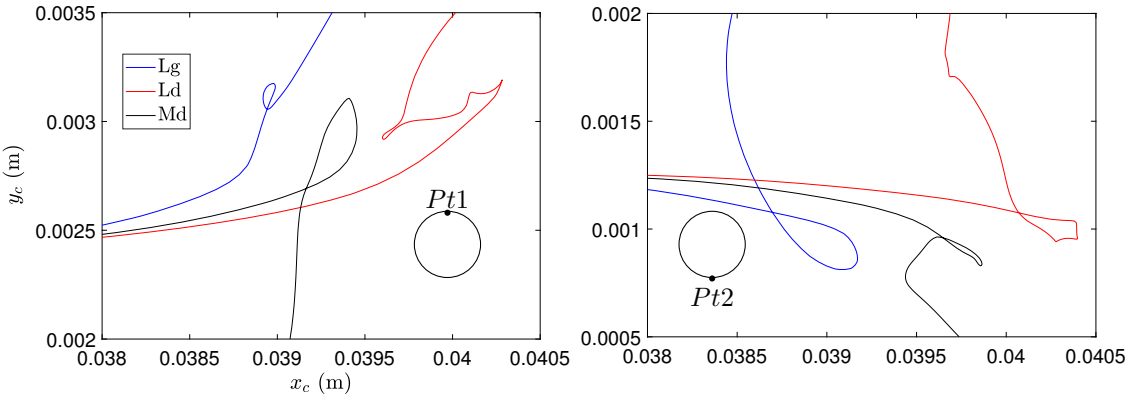

Figure 32: Trajectories of membrane material points $Pt1$ and $Pt2$ in the RCW for $Ca = 0.04$, p_2.

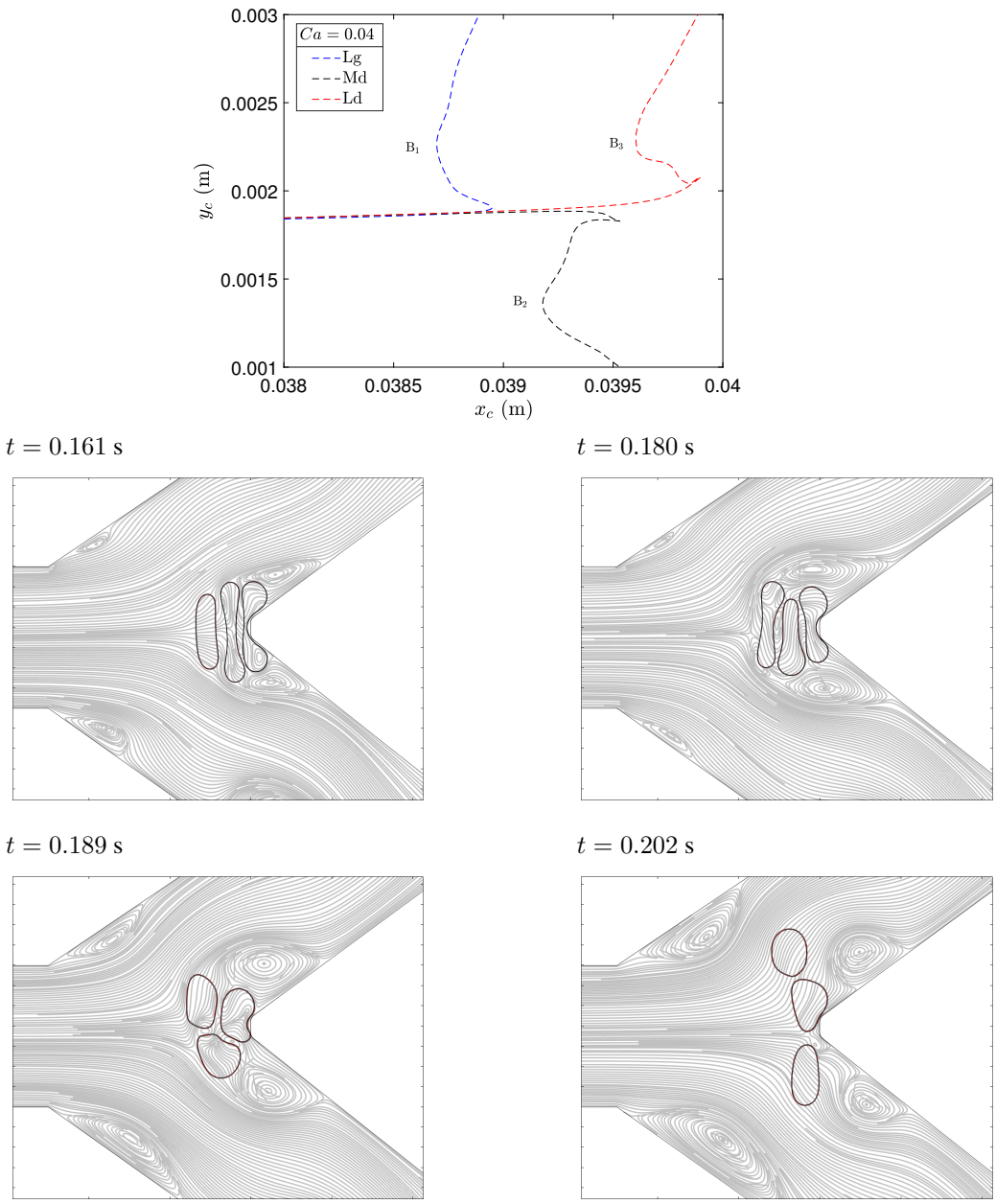

Figure 33: Microparticle trajectories near in the bifurcation zone showing 'bumps'. Images in bottom shows vortexes near the corner at the origin of bumps.

Deformation

The cluster near the corner gives rise to impressive deformation modes displayed in Figures 34 and 35. Microparticles approaching the corner slenderize as they are exposed to elongational stresses imposed by the splitting flow, microparticles progressively evolve from the pebble-shape to an asymmetrical oblate shape (a). When the Ld microparticle impacts the corner, it adopts the stomatocyte-like shape (also known as the cup-shape) (b), the approaching Ld and Md microparticles resemble the tube-like shape (c) while the Ld stomatocyte-shaped microparticle develops a neck (a stretched and thin central area). The in-back microparticle exerts an extra compressive stress on the Ld microparticle making the neck connecting its two symmetrical lobes narrower (d). In soft membrane mechanics this very narrow neck referred to as a tether and accompanies the budding

phenomenon of fluid membranes [21] (corresponding to the creation of a daughter vesicle that pull out from the parent vesicle). The Ld microparticle is jammed by the in-front corner and the microparticles lagging behind. The narrowing of the neck is accompanied by a flattening of the membrane side facing the LM (d). This shape is observed for vesicles interacting with a planar surface [22] and in vesicle phase diagram [23]. By adopting this shape, the Ld microparticle attempts to rid from the corner, then follows a relaxation during which the lobes unstuck symmetrically (then asymmetrically) from the branches and the tether widens (d'). Meanwhile, the Md and the Lg microparticles develop the biconcave shape (e) and the uniconcave shape (e') after transiting by the tubular-like shape (c). The upper part of the tubular-shaped Md microparticle widens to resemble a pending drop (f). The stomatocyte-like shape evolves toward a rotary phone handset shape (d"). The stomatocyte-like shaped microparticle and the uniconcave microparticle simultaneously tilt in opposite directions (the first tilts to the back and the second tilts forward) and rise. This particular elevation owes the creation of a circumflex-like interspace propitious to the deformation of the Md microparticle onto the pear shape (g) while the Lg microparticle becomes P-shaped (golf wedge-like shaped) (h). The Lg microparticle has a very similar shape but it is relatively less bended. The pear shape is reported for lipid vesicles before budding (as a transient shape [23, 22, 24]) and under buoyancy forces (as a stationary shape [25]) and for polymer vesicles (as a stationary shape [26]). Shortly after, the small strangled (pinched) upper area characterizing the pear shape relaxes. Under the present flow conditions, the microparticle developes the pear shape to accelerate (as revealed by the contour plot of microparticle velocity distribution at $t = 0.185$ s). Besides the pear shape, the Lg microparticle shape resemble an alien's head (ovaloid with a narrow side) (i). A part of shape transition above-reported namely the biconcave shape, the uniconcave shape , the prolate-ovoid shape and the stomatocyte shape are reported by several studies among which [27, 28, 29] for lipid vesicle and by [26] for polymer vesicle.

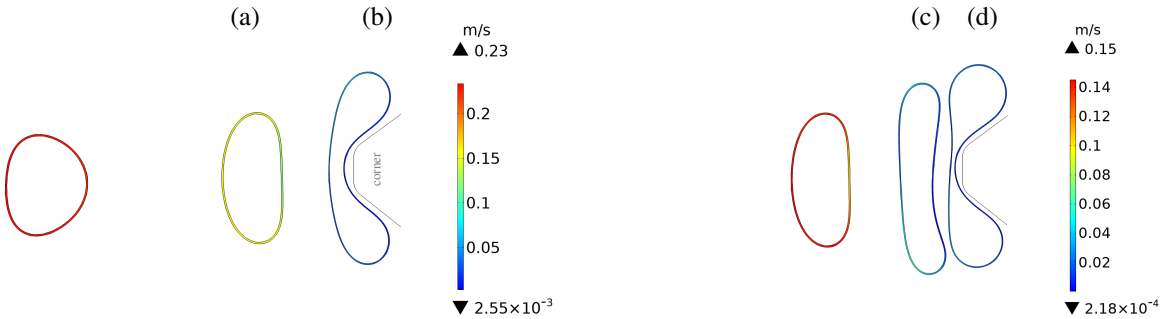

$t = 0.145$ s

$t = 0.155$ s

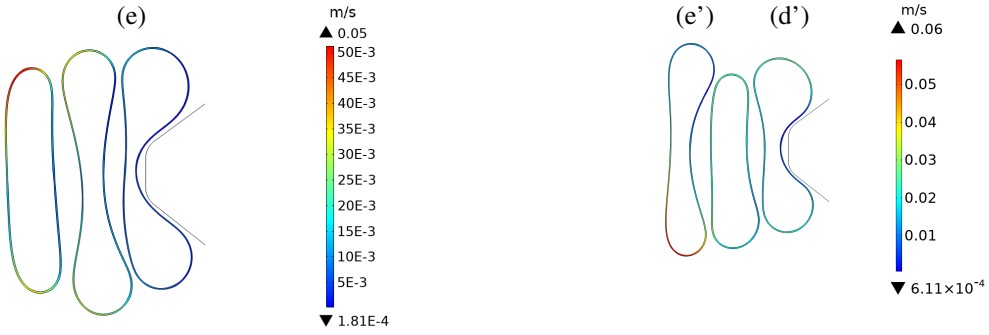

$t = 0.164$ s

$t = 0.175$ s

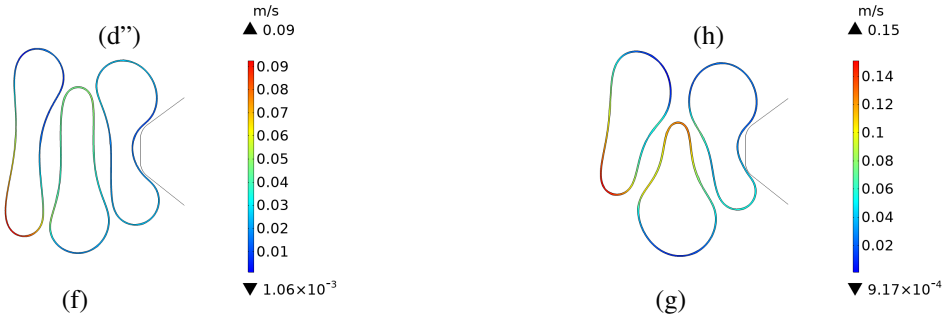

$t = 0.180$ s

$t = 0.185$ s

Figure 34: The impaction against the corner for $Ca = 0.04$, RCW.

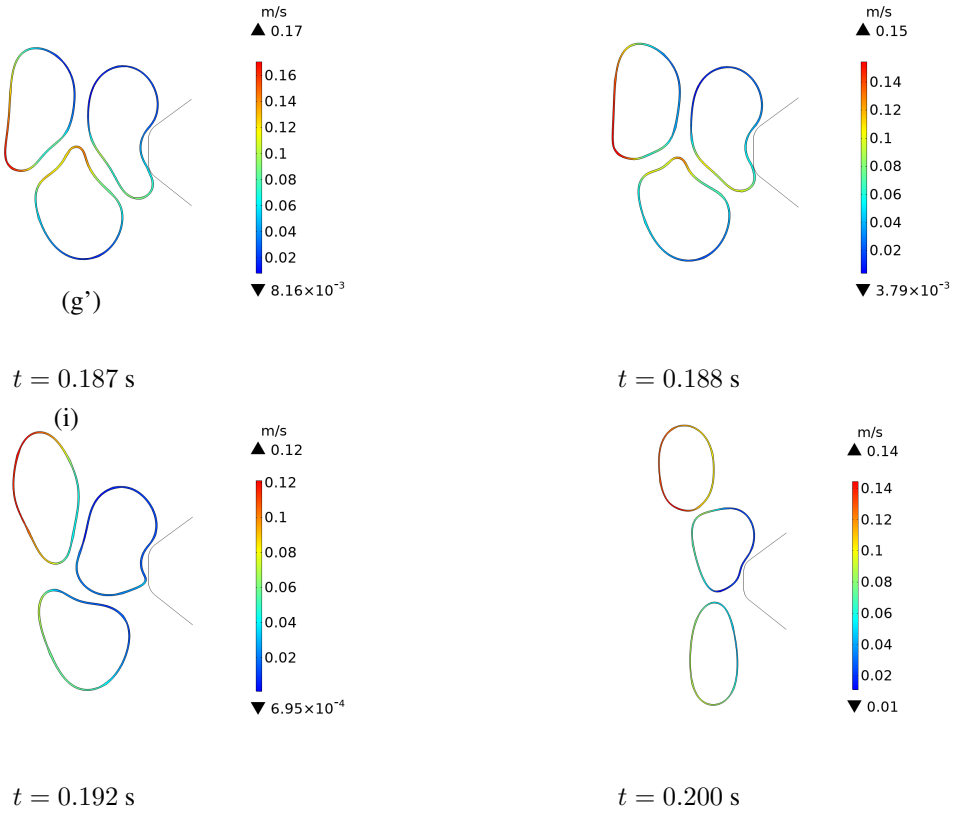

Figure 35: Same as Figure 34 for extended times.

3.3.3 Effect of Blood viscosity on softer membranes

Motivated by the previous observation in the literature [30] outlining the relevant role of suspending blood viscosity (besides membrane deformability) on cell partitioning, the shear-thinning blood model is replaced by a Newtonian model whose constant viscosity is of 0.00345 Pa· s. The aim is to assess the role played by the suspending fluid viscosity on microparticle preferred branch, deformation modes and vortex trapping. The abbreviation STH is for shear-thinning blood and NTH for Newtonian blood.
The blood viscosity is found to influence microparticles partitioning in branches and deformation near the corner when flowing in the RCW. More precisely, the Lg and the Md microparticles enter opposite branches when suspending blood is Newtonian blood. The Lg microparticle is first to enter the LAD due to the higher instantaneous velocity (see Table 5), it is followed by the Md microparticle which enter the LCx. That is to say, the two first microparticles to bifurcate enter opposite branches as previously seen in the STH case. The Ld microparticle is meanwhile stuck to the corner. After a partial relaxation, it is interestingly dynamically-metastable near the corner as illustrated by its center of mass pattern depicted in Figure 36 (aa) that reveals a reluctance to enter the LCx or the LAD (at last enter the LCx). The bumps are re-observed (Figure 36 (ab)). Morphological evolution of microparticles in the bifurcation zone is also affected by blood viscosity as revealed qualitatively in Figure 37 and quantitatively in Figure 38.

Table 5: The average velocity of Newtonian blood at S_2 for RCW.

t (s)	V (m/s)	
	LCx	LAD
0.145	1.29E-2	**6.25E-2**
0.158	**4.10E-2**	3.51E-2
0.164	3.16E-2	**3.24E-2**
0.175	3.87E-2	**4.11E-2**
0.180	3.93E-2	**5.28E-2**

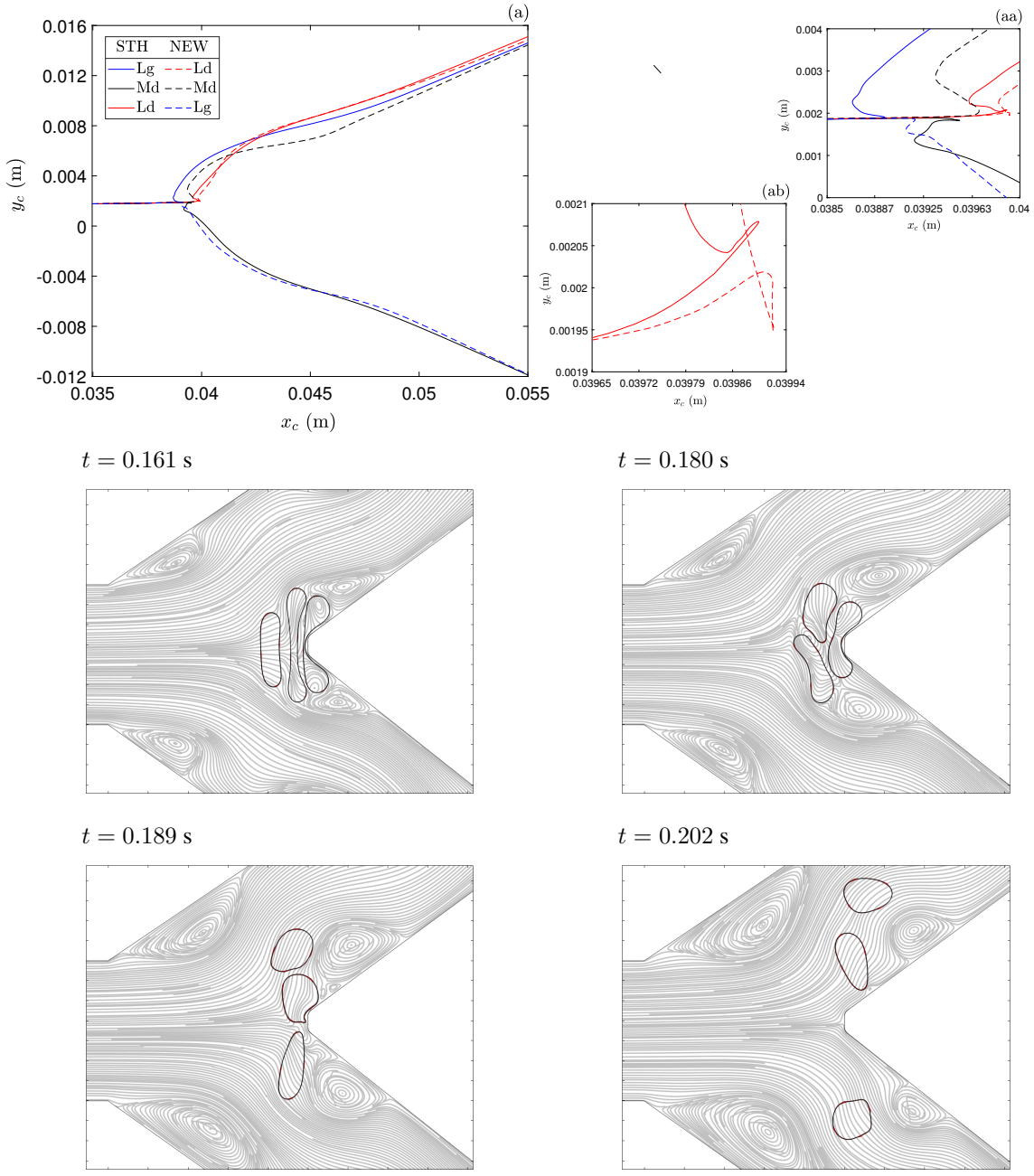

Figure 36: The effect of blood viscosity on microparticle trajectories (a). The magnifications show the 'bumps' (aa) and the metastable equilibrium for the Ld microparticle in the immediate vicinity of the corner (ab). Images in bottom show vortexes in Newtonian blood flow near the corner.

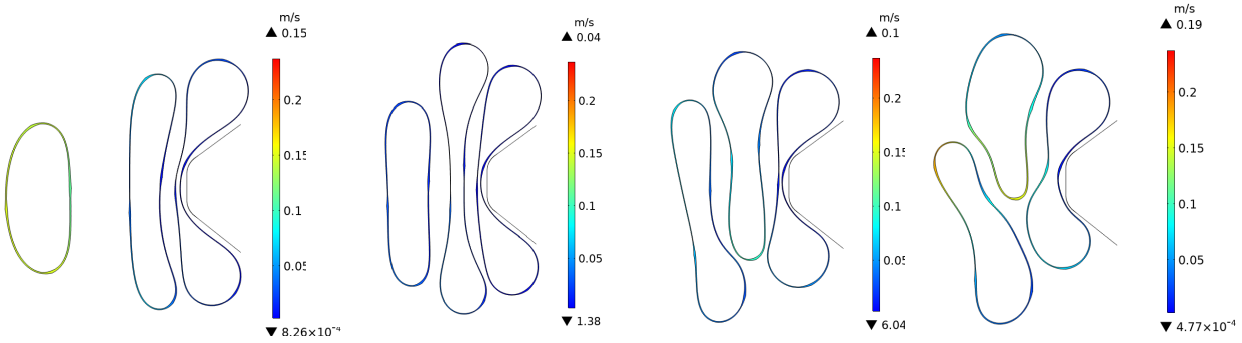

$t = 0.155$ s $t = 0.164$ s $t = 0.175$ s $t = 0.180$ s

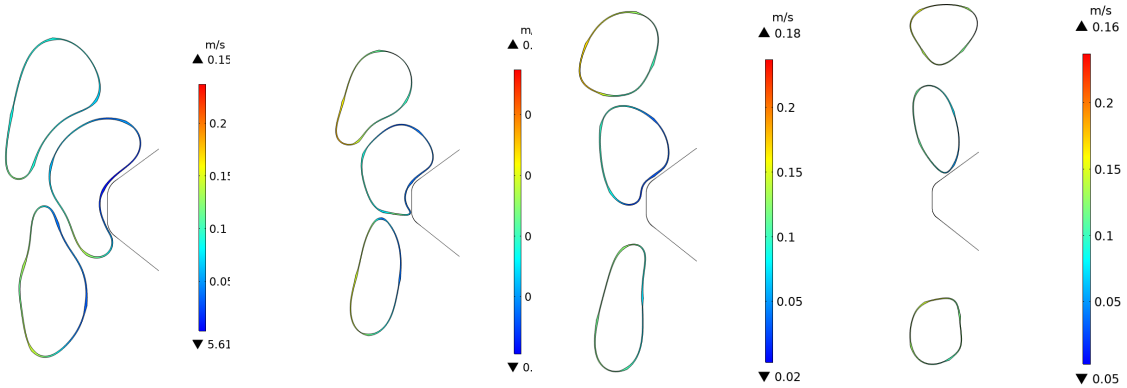

$t = 0.185$ s $t = 0.188$ s $t = 0.192$ s $t = 0.200$ s

Figure 37: Deformed shapes in Newtonian blood near the bifurcation for $Ca = 0.04$.

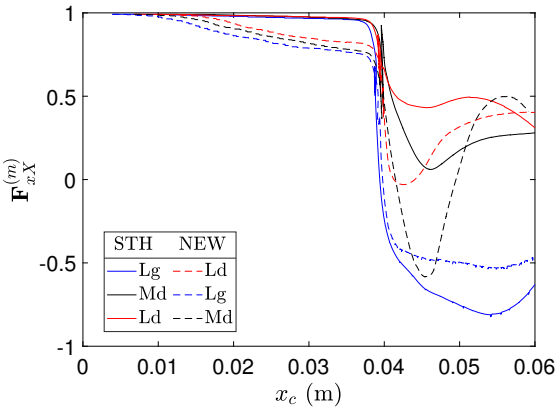

Figure 38: The effect of blood viscosity on microparticles deformation for $Ca = 0.04$, RCW.

The main contribution of the constant viscosity in the DCW is to extend time-residence in the vortexes (Figure 39). Furthermore, the velocity at outlets is investigated at the end of the systole (Figure 40). It reveals that

velocity is higher for NTH which is in agreement with the reported observations in [31]. On velocities of microparticles plotted in Figure 41, it is found that the initial horizontal position (i.e. Lg, Md or Ld) has a negligible effect on velocities in the early stages of microparticles course ($t = 0.008$, 0.02 s). At $t \geq 0.02$ s, the microparticles decelerate till the end of systole $t = 0.29$ s and then accelerate. In the DCW, the microparticles move with different velocities even at early times. At $t \geq 0.02$ s, velocities are descendant. Similarly to RCW, the Newtonian viscosity is found to increase the particle-particle relative velocity and conversely, to accelerate microparticles. Shear-thinning has a different influence depending on the wall. More exactly, microparticles move slower in the DCW and faster in the RCW. The velocity decrease in the DCW is attributed to $i)$ the shear-thinning which makes hydrodynamic forces applied upstream by blood liberated from bulges (formed during the systole) lower than the Newtonian case $ii)$ the flow disruption induced by viscosities and flow interaction with hyperelastic walls $iii)$ the higher time residence in vortexes. These deformable wall-induced elements being absent in the RCW, microparticles naturally move faster as a result of a local lower viscosity and a viscosity ratio of internal viscosity (liquid core) and external viscosity (blood) less or equal to unity.

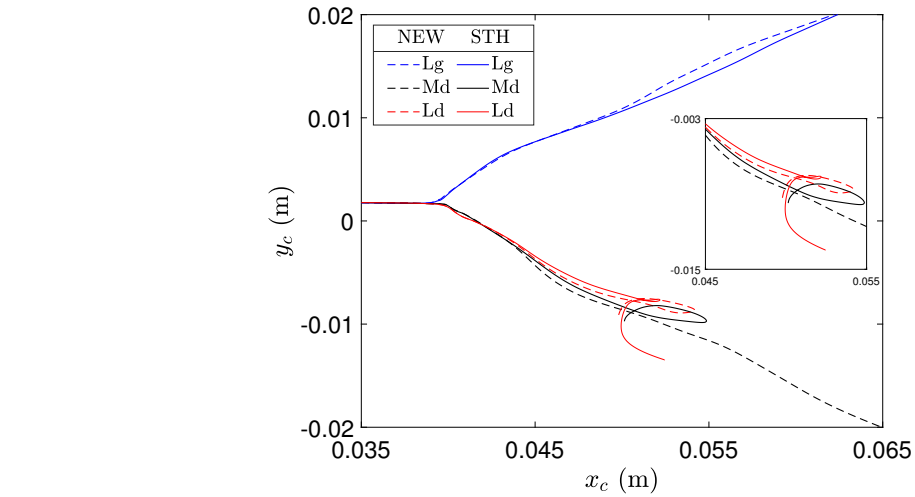

STH, $t = 0.51$ s

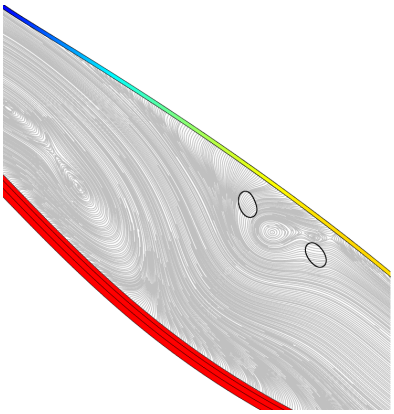

NEW, $t = 0.51$ s

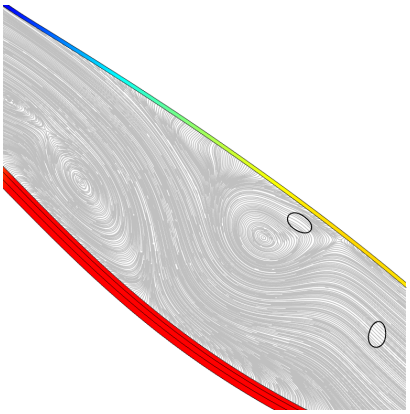

STH, $t = 0.62$ s

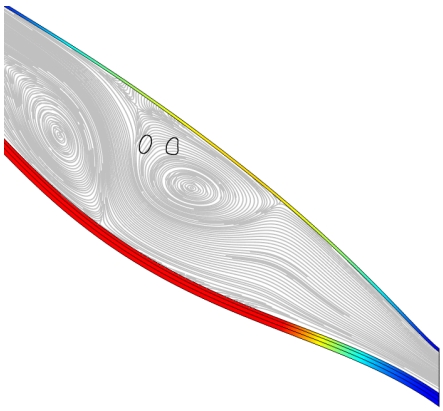

NEW, $t = 0.62$ s

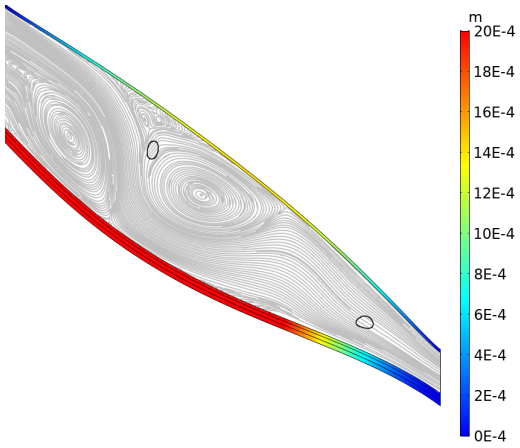

Figure 39: Vortex trapping in the hyperelastic walled LAD. Color legend is for coronary wall displacement and applies for the four presented images.

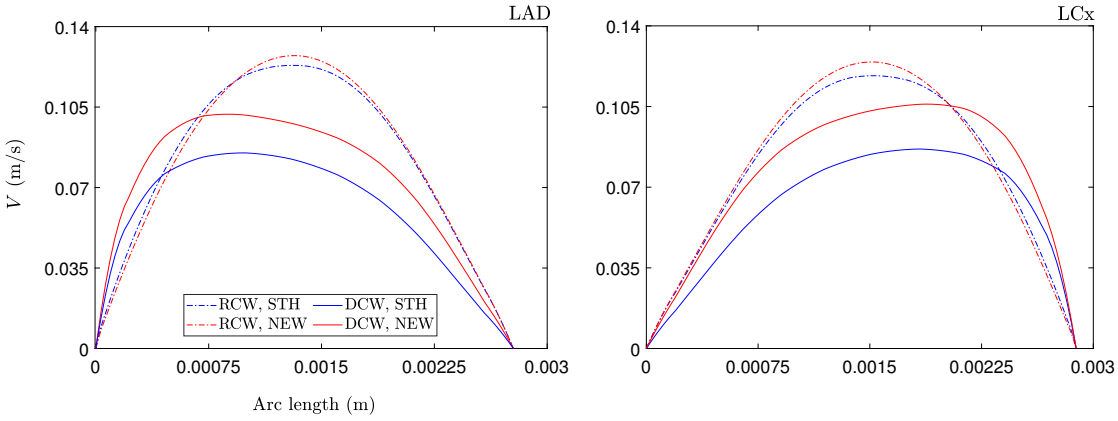

Figure 40: Outlets velocity for Newtonian and shear-thinning blood at $t = 0.29$ s.

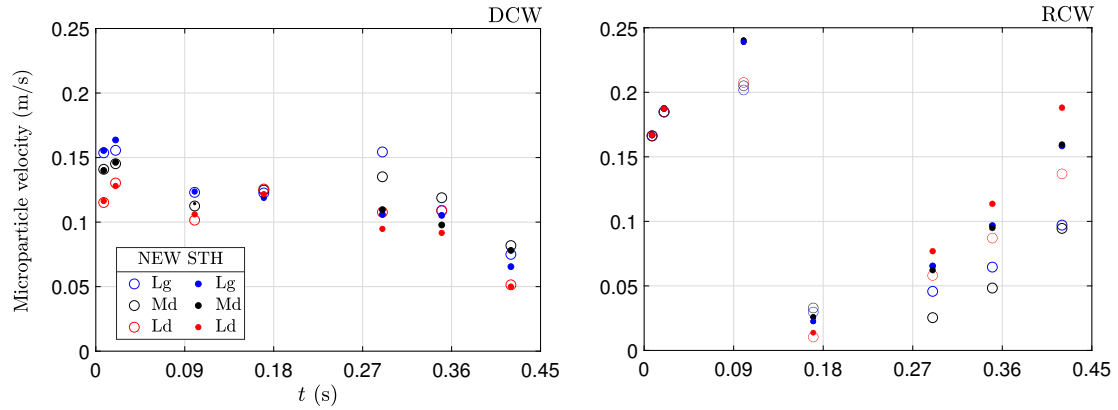

Figure 41: The effect of blood viscosity on velocity of microparticles for $Ca = 0.04$, RCW.

Table 6: A summary table giving an overview on results pertaining centered microparticles. The asterisk designates the microparticles flowing in the Newtonian blood NTH.

		Preferred branch			Impaction Ip			Vortex trapping Vo		
		Lg	Md	Ld	Lg	Md	Ld	Lg	Md	Ld
DCW	$Ca = 0.01$									Vo
	$Ca = 0.04$	LCx	LAD	LAD		All			Vo	Vo
	$Ca = 0.04^*$								Vo	Vo
RCW	$Ca = 0.01$	LCx	LAD	LCx	Ip		Ip			
	$Ca = 0.04$	LCx	LAD	LCx	Ip					
	$Ca = 0.04^*$	LAD	LCx	LCx	Ip	Ip	Ip			Vo

4 Concluding remarks

The dynamical behavior of microparticles flowing in the left coronary artery and partitioning at its Y-bifurcation have been studied in this paper. In a context of intraarterialy targeted drug-delivery, obtained results arouse a particular attention on the risk of microparticles entering a non-targeted branch, clustering at the bifurcation

and prematurely burst due to the important sustained stress. On the basis of the conducted study, the following findings are made:

- The slight surface area difference is found to have a significant impact on coronary wall deformation and to amplify flow asymmetry. As a result off-centered microparticles exhibit an asymmetrical deformation. Oppositely, the juxtaposition of successive deformations of microparticles upper/down placed in the RCW are reflection to each other (in respect to the center-line of the blood vessel);
- For centered microparticles, wall rigidity has a major role on the selection of branch since haemodynamic is found changed;
- In the DCW, the preferred branch of microparticles is directly determined by the instantaneous blood properties and indirectly by the deformation extent of walls in branches and by the kinetics of the contiguous microparticles. For example, a microparticle will enter a branch with a lower instantaneous velocity if it is outpaced by other microparticles, if not the higher velocity branch is selected. The microparticles experience overtaking (and systematically intercept the bifurcating inner walls that are adjacent to the corner) and binary vortex trapping in the branch (all Ca included). When shear thinning blood in considered, the vortex trapping is found to occur exclusively in the DCW;
- The risk of clustering could not be discounted even for off-centered microparticles, especially in the DCW;
- In the RCW, the branch selection is not only impacted by the physical presence of other microparticles but also by their deformation mode, especially for softer membranes. A deformability-induced cluster is observed near the corner whose consequences include stagnation-induced vortex formation and a peculiar deformation modes unprecedentedly seen. The impaction occurrence diminishes as membrane shear resistance decreases, for instance a single microparticle experiences impaction and interception for $Ca = 0.04$ to two microparticles for $Ca = 0.01$;
- A breathing-like deformation is reported for softer membranes ($Ca = 0.04$, 0.08) during flow in the hyperelastic-walled LM;
- Blood viscosity plays a central role especially in the RCW (e.g. different preferred branch and deformation modes), a metastable equilibrium state and a vortex trapping are uniquely reported in the presence of Newtonian blood. In the DCW, the main influence of blood viscosity model is on the time residence in vortexes;
- Dynamical instabilities are omnipresent (e.g. wavering trajectories, cups-like and tether instabilities, wobbling near the corner).

References

[1] O. V. Chumakova, A. V. Liopo, V. G. Andreev, I. Cicenaite, B. M. Evers, S. Chakrabarty, T. C. Pappas, and R. O. Esenaliev. Composition of plga and pei/dna nanoparticles improves ultrasound-mediated gene delivery in solid tumors in vivo. *Cancer Letters*, 261:215–225, 2008. doi: 10.1016/j.canlet.2007.11.023.

[2] E. Mihalko, K. Huang, E. Sproul, K. Cheng, and A. C. Brown. Targeted treatment of ischemic and fibrotic complications of myocardial infarction using a dual-delivery microgel therapeutic. *ACS Nano*, 12 (8):7826–7837, 2018. doi: 10.1021/acsnano.8b01977.

[3] E. Doutel, S. I. S. Pinto, J. B. L. M. Campos, and J. M. Miranda. Link between deviations from Murray's Law and occurrence of low wall shear stress regions in the left coronary artery. *Journal of Theoretical Biology*, 402:89–99, 2016. doi: 10.1016/j.jtbi.2016.04.038.

[4] A. Gholipour, M. H. Ghayesh, A. Zander, and R. Mahajan. Three-dimensional biomechanics of coronary arteries. *International Journal of Engineering Science*, 2018. doi: 10.1016/j.ijengsci.2018.03.002.

[5] N. Bénard. *Analyse de l'écoulement physiologique dans un stent coronarien : Application à la caractérisation des zones de resténose pariétale*. PhD thesis, Université de Poitiers, 2005. URL `https://tel.archives-ouvertes.fr/tel-00012134`.

[6] T. X. Chu, A. V. Salsac, E. Leclerc, D. Barthès-Biesel, H. Wurtz, and F. Edwards-Lévy. Comparison between measurements of elasticity and free amino group content of ovalbumin microcapsule membranes: Discrimination of the cross-linking degree. *Journal of Colloid and Interface Science*, 355(1):81–88, 2011. doi: 10.1016/j.jcis.2010.11.038.

[7] P. Deuflhard. A modified Newton method for the solution of ill-conditioned systems of nonlinear equations with application to multiple shooting. *Numerische Mathematik*, 22:289–315, 1974.

[8] M. Falsafioon, S. Arabi, R. Camarero, and F. Guibault. Comparison of two mesh smoothing techniques for unstructured grids. volume 22. Institute of Physics Publishing, 2013. doi: 10.1088/1755-1315/22/2/022020.

[9] P. M. Knupp. Winslow smoothing on two-dimensional unstructured meshes. *Engineering with Computers*, 15:263–268, 1999. doi: 10.1007/s003660050021.

[10] I. El Jirari, A. El Baroudi, and A. Ammar. Effect of arteriolar distensibility on the lateral migration of liquid-filled microparticles flowing in a human arteriole. *Journal of Mechanics in Medicine and Biology*, 21(8), 2021. doi: 10.1142/S0219519421500627.

[11] P. Marmottant, T. Biben, and S. Hilgenfeldt. Deformation and rupture of lipid vesicles in the strong shear flow generated by ultrasound-driven microbubbles. *Proceedings of the Royal Society A: Mathematical, Physical and Engineering Sciences*, 2008. doi: 10.1098/rspa.2007.0362.

[12] E. M. Kolahdouz and D. Salac. Dynamics of three-dimensional vesicles in DC electric fields. *Physical Review E - Statistical, Nonlinear, and Soft Matter Physics*, 92(1), 2015. doi: 10.1103/PhysRevE.92.012302.

[13] K. M. Kei, M. Y. Cheung, and Y. S. Leung. From aerodynamics to inhalation technique - more about inhaled medication. *Hong Kong Pharmaceutical Journal*, 22(November):98–101, 2015. ISSN 1727-2874.

[14] B. Namgung, Y. C. Ng, H. L. Leo, J. M. Rifkind, and S. Kim. Near-wall migration dynamics of erythrocytes in vivo: Effects of cell deformability and arteriolar bifurcation. *Frontiers in Physiology*, 8, 2017. doi: 10.3389/fphys.2017.00963.

[15] X. Yin, T. Thomas, and J. Zhang. Multiple red blood cell flows through microvascular bifurcations: cell free layer, cell trajectory, and hematocrit separation. *Microvascular Research*, 89:47–56, 2013. doi: 10.1016/j.mvr.2013.05.002.

[16] M. M. Villone, M. Trofa, M. A. Hulsen, and P. L. Maffettone. Numerical design of a T-shaped microfluidic device for deformability-based separation of elastic capsules and soft beads. *Physical Review E*, 2017. doi: 10.1103/PhysRevE.96.053103.

[17] B. Kaoui, G. Coupier, C. Misbah, and T. Podgorski. Migration latérale de vésicules dans des microcanaux: effets des parois et du gradient de cisaillement. Number 5, pages 112–119, 2009. doi: 10.1051/lhb/2009063.

[18] H. Lee, J. M. Ferrer, M. J. Lang, and R. D. Kamm. Molecular origin of strain softening in cross-linked F-actin networks. *Physical Review E - Statistical, Nonlinear, and Soft Matter Physics*, 82(1):1–9, 2010. doi: 10.1103/PhysRevE.82.011919.

[19] B. Saint-Michel, T. Gibaud, and S. Manneville. Predicting and assessing rupture in protein gels under oscillatory shear. *Soft Matter*, 13(14):2643–2653, 2017. doi: 10.1039/C7SM00064B.

[20] W. R. Dodson and P. Dimitrakopoulos. Dynamics of strain-hardening and strain-softening capsules in strong planar extensional flows via an interfacial spectral boundary element algorithm for elastic membranes. *Journal of Fluid Mechanics*, 641:263–296, 2009. doi: 10.1017/S0022112009991662.

[21] U. Seifert, L. Miao, H. G. Döbereiner, and M. Wortis. Budding Transition for Bilayer Fluid Vesicles with Area-Difference Elasticity. 66(2):93–96, 1992. doi: 10.1007/978-3-642-84763-9-19.

[22] R. Lipowsky. The conformation of membranes. *Nature*, 349(6309):475–481, 1991. doi: 10.1038/349475a0.

[23] H. G. Döbereiner. Properties of giant vesicles. *Current Opinion in Colloid and Interface Science*, 5 (February):256–263, 2000. doi: 10.1016/S1359-0294(00)00064-9.

[24] E. Sackmann. The Seventh Datta Lecture Membrane bending energy concept of vesicle-and cell-shapes and shape-transitions. 346:3–16, 1994. doi: 10.1016/0014-5793(94)00484-6.

[25] G. Boedec, M. Leonetti, and M. Jaeger. 3D vesicle dynamics simulations with a linearly triangulated surface. *Journal of Computational Physics*, 2011. doi: 10.1016/j.jcp.2010.10.021.

[26] X. Li. Shape transformations of bilayer vesicles from amphiphilic block copolymers: A dissipative particle dynamics simulation study. *Soft Matter*, 9(48):11663–11670, 2013. doi: 10.1039/c3sm52234b.

[27] A. Sakashita, N. Urakami, P. Ziherl, and M. Imai. Three-dimensional analysis of lipid vesicle transformations. *Soft Matter*, 8(33):8569–8581, 2012. doi: 10.1039/c2sm25759a.

[28] H. Yuan, C. Huang, and S. Zhang. Dynamic shape transformations of fluid vesicles. *Soft Matter*, 6(18): 4571–4579, 2010. doi: 10.1039/c0sm00244e.

[29] L. Mesarec, W. Góźdź, A. Iglič, V. Kralj-Iglič, E. G. Virga, and S. Kralj. Normal red blood cells' shape stabilized by membrane's in-plane ordering. *Scientific Reports*, 9(1):1–11, 2019. doi: 10.1038/s41598-019-56128-0.

[30] W. Xiong and J. Zhang. Two-dimensional lattice Boltzmann study of red blood cell motion through microvascular bifurcation: Cell deformability and suspending viscosity effects. *Biomechanics and Modeling in Mechanobiology*, 11(3-4):575–583, 2012. doi: 10.1007/s10237-011-0334-y.

[31] F. Kabinejadian and D. N. Ghista. Compliant model of a coupled sequential coronary arterial bypass graft: Effects of vessel wall elasticity and non-Newtonian rheology on blood flow regime and hemodynamic parameters distribution. *Medical Engineering and Physics*, 2012. doi: 10.1016/j.medengphy.2011.10.001.

Conclusion

This study is dedicated to asses the dynamical behaviour of hyperelastic microparticles flowing in human arteriole and in the left coronary artery. For all performed calculations, the obtained results are in concordance with literature (when comparison is possible) and reflects very similar dynamical properties with red blood cells. A relevant finding is the major role played by arteriolar hyperelasticity that could not be dismissed, a fortiori when microparticles undergo lateral migration. Actually we found that the deformable wall acts as a suction force that compensates lift. Consequently, the lateral migration away from the wall is impeded. This force is found to be sensitive to viscosities ratio, to membrane shear resistance and to confinement, thus, rendering the lateral migration even more intricate. This vascular hyperelasticity further affects the particle-particle interaction, hence whether or not the clustering is possible. While in the rigid-walled arteriole microparticles are found to develop the cusp-like instability (and an unprecedentedly seen double-cusp like instability), the latter is not observed in the presence of arteriolar distensibility. A novel deformation mode is presented for microparticles migrating in rigid channel as well as a novel mechanism of binary collision and overtaking in Poiseuille flow induced by arteriolar wall hyperelasticity.

Moreover, the dynamical behaviour of microparticles flowing in a coronary bifurcation characterized by an important arterial distensibility is investigated. Therein, the partitioning of microparticles under pulsatile blood flow is examined depending on the initial offset with respect to the coronary wall, membrane shear resistance, haemorheology and coronary wall rigidity. An outcome of interest is that the prediction of the preferred branch is possible at some extent. In point of fact, metastable and unstable equilibrium are found is some prescribed combinations of variable, accordingly rendering the prediction unfeasible. Numerous peculiar deformation modes exhibited near the bifurcation zone are first ever reported while other well-known deformed shapes are first observed in similar flow conditions. Unexpectedly but interestingly, a vortex trapping and an overtaking are observed in the branches. As

for the arteriole, the possibility of occurrence of microparticles clustering, bursting and adhesion to the vascular wall is investigated and favouring conditions are established.

Furthermore, a contribution of the present work might concerns the application of the Arbitrary Lagrangian Eulerian method that is still unpopular due to its conforming nature, particularly when the fluid-structure interaction involves large deformation. The herein presented method is likely to be useful to enforce convergence at a reasonable computational cost.

Résumé détaillé

[Le résumé ci-dessous est rédigé à des fins administratives, sa lecture ne peut en aucun cas remplacer celle du manuscrit]

L'application des concepts d'ingénierie mécanique et de physique à la médecine et à la biologie suscite un intérêt croissant compte tenu des enjeux futurs. Parmi ces applications figure l'administration ciblée de médicaments et la manipulation et la caractérisation de cellules biologiques. Ces exemples sont donnés à dessein puisque tous deux impliquent des microparticules artificielles ou biologiques circulant dans un environnement confiné et soumises à des forces hydrodynamiques. La microencapsulation consiste à enrober une substance active à l'aide d'une fine membrane au moyen de procédures qui peuvent être mécaniques, physico-chimiques ou chimiques. Selon leur taille, les structures sphériques obtenues sont appelées nanoparticules ou microparticules. La membrane est constituée d'un réseau de chaînes de polymères réticulés (polydiméthylsiloxane, poly-L-lysine, alginate, polyacrylates, acide polylactique-coglycolique), de chaînes de protéines (albumine sérique humaine HSA, ovalbumine) ou de molécules lipidiques. Les microparticules constituées de membranes lipidiques sont appelées vésicules et celles constituées de polymères et/ou de protéines sont appelées capsules. Les nano/microparticules sont largement utilisées dans de nombreux domaines industriels, notamment dans l'industrie agro-alimentaire comme composés antibactériens, en pharmaceutique comme vecteurs thérapeutiques et en cosmétique comme micelles nettoyantes. Les avantages comprennent la prévention de l'inactivation de la substance active pendant la fabrication ou le stockage et la libération contrôlée de la substance dans un environnement ciblé. La substance encapsulée est destinée à être libérée soit par rupture de la membrane (déclenchée par une condition prédéterminée comme un seuil de température ou de pression), soit par diffusion lorsque la membrane est de nature poreuse. Parmi les applications les plus prometteuses des nano/microparticules dans le domaine de la pharmaceutique, on trouve l'administration ciblée de médicaments. Il s'agit d'un traitement non invasif basé sur

l'injection directe de nano/microparticules -chargées de substance médicamenteuse- appelées vecteurs thérapeutiques dans la circulation sanguine. Une fois injectés par voie intra-artérielle/veineuse, les vecteurs thérapeutiques se déplacent passivement sous l'action du flux sanguin pour atteindre une cible spécifique (tumeur, thrombose...). Le médicament enrobé est ensuite libéré soit par rupture de la membrane, soit par les pores de cette dernière. La chimioembolisation est un traitement local des tumeurs malignes palliant à la chimiothérapie ou à d'autres traitements invasifs. Au cours de la procédure, des vecteurs thérapeutiques contenant une substance anticancéreuse comme l'irinotécan ou la doxorubicine sont injectés par voie intra-artérielle via un micro-cathéter. La procédure est guidée par rayons afin de surveiller la trajectoire des vecteurs thérapeutiques injectés. Les principaux avantages thérapeutiques de la chimioembolisation sont une concentration maximisée du médicament absorbé par la tumeur, une toxicité réduite pour les tissus sains ainsi qu'une incidence moins élevée des effets secondaires systémiques. La technique d'administration ciblée de médicaments fut inspirée par le mécanisme d'endocytose-exocytose et le globule rouge GR. L'endocytose est le processus immunologique par lequel une cellule utilise sa membrane pour engloutir et entourer des particules cibles dans l'environnement fluide extracellulaire. La vésicule formée (de rayon $0{,}5-5$ μm) migre vers le cœur de la cellule pour y être détruite. Le transport vésiculaire dans le sens inverse est connu sous le nom d'exocytose au cours duquel la vésicule sécrétoire libère des protéines ou des débris dans le milieu liquide extracellulaire. Quant au GR, il s'agit d'un système naturel encapsulé (une fine membrane déformable renfermant une solution aqueuse d'hémoglobine) dont le rôle principal est de délivrer de l'oxygène. Les techniques d'administration ciblée de médicaments ont fait preuve d'une grande efficacité thérapeutique, néanmoins, elles requièrent une surveillance continue *in situ* pour une prise en charge rapide en cas de complications telles que la formation d'embole susceptible d'entraver la circulation sanguine et l'éclatement prématuré ou tardif de la membrane. Des études supplémentaires sont nécessaires pour optimiser la procédure, l'étendre à d'autres zones affectées, remédier aux contre-indications et faire la lumière sur les mécanismes à l'origine des complications couramment rencontrées ou du moins, sur les conditions qui favorisent leur survenue. Pour ce faire, il est nécessaire d'inclure les caractéristiques hémorhéologiques et hémodynamiques. Le choix idéal serait certainement une approche *in vivo*, mais ce choix est vite écarté par la communauté scientifique en raison de problèmes éthiques évidents. Une alternative consiste à reproduire les conditions physiologiques au moyen d'une approche *in vitro*. Cependant, les propriétés biophysiques de la paroi artérielle et les caractéristiques

géométriques du réseau vasculaire comme la tortuosité et les bifurcations, sont très difficiles, voire impossibles, à reproduire expérimentalement. De plus, une telle approche est coûteuse et nécessite d'importantes ressources matérielles et humaines. L'approche *in silico* basée sur la modélisation et la simulation numérique permet de remédier aux limitations susmentionnées, elle est employée comme une approche alternative ou auxiliaire en biophysique et en ingénierie biomécanique. Les études *in silico* reposent sur deux piliers pour une représentation précise des phénomènes physiques complexes dans le système circulatoire humain à savoir, la robustesse et la satisfaction du concept de problème bien posé. Elles pourraient constituer un outil de prédiction du comportement dynamique des vecteurs thérapeutiques, de la pharmacocinétique et permettre de comprendre les mécanismes encore ambigus à l'origine des complications liées à l'administration ciblée de médicaments. En outre, une modélisation numérique paramétrique permet aux scientifiques et aux ingénieurs d'évaluer assez rapidement le rôle d'un groupe de paramètres sur l'évolution d'un large éventail de quantités physiques.

Le comportement dynamique de microparticules constituées d'une fine membrane hyperélastique enrobant une gouttelette et soumises à des sollicitations hémodynamiques est étudié dans le cadre de cette thèse au moyen d'une modélisation numérique physiologiquement (et raisonnablement) réaliste. L'objectif est de combler le manque d'études portant sur la réponse mécanique de microparticules circulant dans des vaisseaux sanguins humains distensibles, en particulier dans les artérioles et les artères coronaires. Les conditions physiologiques dans les deux types de vaisseaux sanguins sont prises en compte dans la mesure où les données sont disponibles dans la littérature. Le comportement dynamique des microparticules dans différents types d'écoulement a été largement étudié dans la littérature, sans toutefois prendre en compte la contribution des parois vasculaires sur la réponse mécanique globale des microparticules. A notre connaissance, les rares études portant sur la dynamique de microparticules dans les vaisseaux sanguins se sont limitées aux capillaires sanguins (microvaisseaux caractérisés par une fine paroi rigide), motivées par une confrontation numérique/analytique-expérimentale relativement commode (le capillaire étant assimilable à un microcanal rigide). Ainsi, nous avons mis un point d'honneur quant à l'inclusion de la contribution des parois vasculaires épaisses et distensibles. Nous avons examiné, entre autres, le mécanisme de migration latérale et le partitionnement particulaire dans une bifurcation coronarienne en la présence de parois vasculaires distensibles. De plus, l'interaction particule-particule est étudiée dans des trains réduits de microparticules tout en évaluant le risque d'agrégation interparticulaire, d'adhérence aux parois et de rupture prématurée

de la membrane. Dans l'artériole, nous avons étudié l'influence de la paroi artériolaire isolée ou enrobée par un muscle sur une microparticule centrée et, plus intéressant encore, sur le mécanisme de migration latérale d'un train réduit de microparticules. L'influence de la distensibilité artériolaire sur l'interaction particule-particule pendant la migration latérale est étudiée en plus de l'interaction particule-paroi en fonction des paramètres non dimensionnels clefs, à savoir le rapport entre les forces visqueuses du fluide dans lequel la microparticule est immergée et la résistance au cisaillement de la membrane, le rapport entre les viscosités externe et interne et le confinement. Une autre contribution de ce travail concerne l'évaluation du comportement dynamique de microparticules circulant au niveau d'une bifurcation coronarienne sous l'action d'un écoulement sanguin pulsatile. L'accent est mis sur la prédiction de la branche préférée des microparticules interagissant avec la pulsatilité du sang, avec les microparticules voisines et avec la paroi coronarienne vacillante en fonction de l'excentrement vertical initial et de la résistance au cisaillement de la membrane. Pour les deux vaisseaux sanguins considérés, la contribution de la distensibilité de la paroi vasculaire est mise en évidence par le biais d'une comparaison avec des parois vasculaires rigides. Les quantités physiques d'intérêt sont -entre autres- la vitesse des microparticules, leur déformation (quantitative et qualitative), leur trajectoire et l'énergie élastique emmagasinée le long de leur course dans le vaisseau sanguin. Au vu du contexte thérapeutique, le risque de formation d'agrégats, d'adhésion à la paroi et de rupture membranaire prématurée sont évalués. Le problème transitoire de l'interaction fluide-structure est résolu dans le cadre du formalisme arbitrairement lagrangien eulérien ALE. L'ensemble des calculs est effectué à l'aide du code éléments finis Comsol Multiphysics® suivant une approche monolithique.

Les propriétés physiques et mécaniques des membranes sont des facteurs clefs dans la réponse des microparticules aux contraintes externes. Les tissus biologiques tels que les protéines et les polymères naturels et synthétiques sont capables de supporter des taux de déformation importants sans subir de dissipation d'énergie interne. Ce comportement est décrit par des lois de comportement hyperélastiques, incluant les non-linéarités géométriques et matérielles. L'élasticité des membranes constituées de protéines réticulées et de polymères est purement entropique, ce qui signifie que leur élasticité découle de l'entropie conformationnelle (un changement de forme et de dynamique des molécules) induite par une contrainte externe. Afin d'emmagasiner l'énergie mécanique induite par la déformation, la distance entre les chaînes augmente et l'entropie est diminuée. Les polymères sont connus pour manifester un adoucissement sous charge cyclique (effet Mullins) et un écrouissage sous des contraintes

importantes. Le premier comportement résulte de la composante viscoélastique des polymères et de l'altération de la structure macromoléculaire. En fonction de la tacticité, le second comportement est attribué soit à la cristallinité, soit à l'extensibilité finie de la chaîne et est sensible à la température et à la concentration moléculaire. Les lois de comportement décrivant la réponse d'un solide hyper-élastique sont basées sur une approche phénoménologique (Mooney-Rivlin, Ogden, Gent...), expérimentale (Hart-Smith...) ou physique (Aruda-Boyce...). Les lois phénoménologiques sont basées sur le développement mathématique de la fonction de densité d'énergie élastique tandis que les lois découlant d'une approche physique sont quant à elles, basées sur une approche micromécanique statistique. Les propriétés physiques de la membrane sont intrinsèquement déterminées par le procédé de fabrication qui peut être mécanique, physico-chimique ou chimique. Les propriétés élastiques de la membrane et la rhéologie du noyau déterminent les propriétés globales des microparticules (capsules et vésicules) et par conséquent leur réponse mécanique aux contraintes externes appliquées (compression, cisaillement, traction...). Une comparaison directe entre le comportement mécanique des microparticules à membrane polymérique ou protéinique est dépourvue de sens étant donné que la nature moléculaire est loin d'être le seul déterminant des propriétés élastiques des membranes. En effet, ces dernières dépendent de la concentration moléculaire, du degré de réticulation et de la taille des microparticules. D'autant plus, la fragilité, la finesse et l'instabilité de la membrane la rendent très sensible aux forces appliquées par les instruments de mesure; ainsi, les propriétés mécaniques intrinsèques interfèrent avec les forces appliquées et donnent lieu à des propriétés élastiques différentes selon la technique de mesure employée. Les propriétés élastiques des membranes sont déterminées au moyen de plusieurs techniques basées sur la mesure de la déformation des microparticules sous une contrainte locale ou globale, dont la sélection est tributaire de la taille de la microparticule et de la fragilité de sa membrane. Les propriétés mécaniques des particules de taille micrométrique sont principalement extraites par des méthodes microfluidiques. Ces méthodes consistent à faire circuler des microparticules dans un canal microfluidique dont la dimension transversale est comparable au diamètre des microparticules et de suivre les variations de déformation, de volume et de vitesse. Les propriétés de la membrane sont récupérées au moyen d'une analyse inverse (via un modèle numérique), puis en choisissant une loi de comportement adéquate pour s'adapter aux profils expérimentaux extraits et pour relier l'extension aux tensions subies par la membrane. Le GR est le principal élément figuré du sang ($\approx 45\%$). Il s'agit d'une cellule anucléée contenant une solution d'hémoglobine (cytoplasme) en suspension dans la

partie liquide du sang (plasma). La principale fonction du GR est l'apport d'oxygène. Sa membrane est constituée d'une bicouche phospholipidique ancrée à un squelette de réseau de filaments de spectrine. La solution d'hémoglobine encapsulée est newtonienne et incompressible. La forme normale du GR est discoïde biconcave, une solution spéciale de l'équation de forme des vésicules lipidiques. Cette forme particulière correspond à la minimisation de l'énergie de flexion de Helfrich. D'un point de vue physiologique, le GR humain pourrait avoir développé la forme biconcave pour maximiser sa surface, et ainsi optimiser l'apport d'oxygène dans les petits vaisseaux sanguins. La configuration métastable de la forme discoïde biconcave est la forme dite de stomatocyte. Le GR est facilement déformable ($10 - 100$ pN) et ses propriétés mécaniques globales sont principalement déterminées par la bicouche phospholipidique et le squelette de spectrine qui composent sa membrane. La bicouche phospholipidique se comporte comme un fluide bidimensionnel décrit par le modèle de la mosaïque fluide (les phospholipides sont libres de se déplacer comme des molécules fluides tandis que les protéines sont ancrées). La bicouche phospholipidique est semi-perméable et possède la propriété de perméabilité sélective. Le squelette est topologiquement organisé comme un réseau hexagonal et pentagonal de filaments de spectrine. La résistance au cisaillement du squelette proviendrait de la résistance au cisaillement intrinsèque des filaments de spectrine et de la topologie particulière du réseau. Les propriétés combinées de la bicouche phospholipidique et du squelette de spectrine permettent au GR de subir de grandes déformations dans le système microvasculaire composé de capillaires sans subir de rupture. La membrane des vésicules est constituée d'une ou de plusieurs couches de phospholipides qui se courbent spontanément au contact du milieu aqueux en raison du caractère amphiphile de la couche: la membrane s'auto-assemble en une forme sphérique de telle sorte que les extrémités hydrophobes ne soient pas en contact avec le milieu aqueux. La membrane vésiculaire est comparable à une membrane de GR dépourvue de squelette et agit de ce fait, comme un fluide bidimensionnel. Les formes au repos des vésicules initialement sphériques sont caractérisées par le volume réduit (ou surface réduite) quantifiant le degré de dégonflement par rapport à une sphère.

La réponse dynamique globale des microparticules soumises à des contraintes hydrodynamiques dépend de plusieurs éléments dont l'inertie du fluide dans lequel elles sont immergées, l'élasticité de la membrane, le confinement et la rhéologie du fluide encapsulé. Le comportement dynamique des microparticules initialement sphériques immergées dans un écoulement de Poiseuille a été largement étudié dans la littérature profitant -entre autres- du développement des dispositifs microfluidiques. La

déformation des microparticules centrées reste symétrique par rapport l'axe du canal. Sous l'action de l'écoulement, la partie arrière initialement convexe commence à d'aplatir et change de signe de courbure pour donner lieu à une fossette au fur et à mesure que les contraintes augmentent. Pour des seuils de contraintes encore plus importants, la fossette s'approfondie davantage et la partie avant de la microparticule diminue sa taille transversale afin de se déplacer plus facilement. Lorsque la microparticule est soumise à un cisaillement simple, elle adopte une forme ellipsoïdale. L'angle d'inclinaison par rapport à la ligne centrale du canal initialement de 90° diminue continuellement. La microparticule est susceptible d'exhiber un mouvement dit de chenille de char défini comme un mode de rotation où la membrane tourne incessamment autour du fluide intérieur. Par conséquent, les éléments du fluide intérieur tournent d'une manière purement rotative. À des contraintes modérées à élevées, la microparticule est plus étirée et développe une pointe supérieure et une pointe inférieure alignées avec les lignes de courant. Un autre mode de rotation qui pourrait être observé lorsqu'une microparticule centrée est soumise à un écoulement de cisaillement simple est le mouvement de *tumbling* au cours duquel la microparticule bascule autour de son centre de masse. Contrairement au mode de rotation en chenille de char au cours duquel la microparticule agit comme un fluide, la microparticule a un comportement de corps rigide au cours du *tumbling*. Les deux modes de rotation sont observés pour les microparticules centrées et excentrées. Les microparticules excentrées subissent une migration latérale, un mécanisme complexe employé dans une multitude de techniques de manipulation bio-cellulaire comme le fractionnement, la filtration et la focalisation. La trajectoire de migration des microparticules, leur vitesse et leurs positions d'équilibre dépendent de plusieurs éléments intrinsèques et des conditions d'écoulement: propriétés élastiques de la microparticule, inertie, contraste de viscosité entre les fluides interne et externe, confinement et position initiale de la microparticule. La migration latérale est un mécanisme crucial dans la microcirculation sanguine où les GRs migrent vers la ligne centrale du vaisseau sanguin tandis que les globules blancs dont la membrane est significativement plus rigide subissent une migration vers les parois appelée margination. Cette dernière est nécessaire au processus immunologique de diapédèse durant lequel des globules blancs franchissent la paroi vasculaire (extravasation) pour aller dans les tissus inflammatoires environnants. En l'absence d'inertie ou pour une inertie finie, la migration latérale de microparticules à flottabilité neutre suspendues dans un écoulement confiné de Poiseuille résulte de l'interaction de trois forces latérales : *i*) la force de portance induite par la paroi; *ii*) la force de portance induite par la déformabilité ; et

iii) la force de portance induite par le gradient de cisaillement. Contrairement aux deux premières forces de portance, la portance induite par le gradient de cisaillement pousse la microparticule vers la paroi la plus proche. Pour les microparticules à flottabilité non neutre et/ou pour un écoulement inertiel, la force de portance de Rubinow-Keller et la force de portance de Saffman sont également impliquées dans la migration latérale. Les microparticules déformables initialement excentrées présentent des formes asymétriques avant-arrière propices à la migration et ce, en raison du gradient de pression entre l'avant et l'arrière. Contrairement aux formes de balle ou de parachute exhibées par les microparticules centrées dans un écoulement de Poiseuille, les formes asymétriques avant-arrière sont également asymétriques par rapport à la ligne centrale du canal. La microparticule adopte les formes de balle et de parachute (et les formes symétriques intermédiaires) lorsque (et uniquement lorsque) sa position d'équilibre coïncide avec l'axe du canal. La déformation asymétrique rappelant la forme d'une pantoufle largement observée aussi bien pour les microparticules artificielles que pour les GRs résulte d'une perte de stabilité. Cette forme est particulièrement propice à la migration et pourrait même s'accompagner d'un mouvement de chenille de char sous certaines conditions, par exemple en dessous d'un rapport critique de viscosités.

Les vaisseaux sanguins sont des tissus mous, comme les ligaments et la peau. Le système sanguin artériel est constitué de grosses artères et d'artérioles musculaires et élastiques, tandis que le système veineux transportant le sang désoxygéné est composé de grosses veines et de veinules. Ces deux systèmes sont reliés par des capillaires, des microvaisseaux à une seule couche dont la largeur est comparable (voire inférieure) à celle du GR. Dans le cadre de la thèse, l'accent est mis sur les vaisseaux sanguins artériels. Les parois vasculaires sont structurellement et biologiquement différentes selon la fonction du vaisseau. De manière générale, la paroi artérielle est divisée en trois couches: la tunique intima, la tunique media et la tunique adventice (tunique externe). La première est la couche la plus interne qui tapisse la lumière (le domaine du vaisseau sanguin dans lequel le sang circule), elle est principalement composée de cellules endothéliales. La deuxième est composée de muscles lisses. La troisième est la couche la plus externe, composée de collagène et d'élastine, tous deux permettent aux vaisseaux de subir de grandes déformations pour réguler le flux sanguin. Les couches sont séparées par deux couches élastiques internes très fines. Les éléments composant les parois vasculaires sont répartis de manière hétérogène sur les différentes couches selon la fonction de l'artère. Les artères de gros et moyen calibre sont capables de dilater leur lumière par un amincissement de la paroi artérielle

(vasodilatation) ou, à l'inverse, de la rétrécir par un épaississement de la paroi artérielle (vasoconstriction). Ces deux mécanismes sont contrôlés par la contraction du muscle lisse et visent à contrôler la pression artérielle et donc, d'adapter le flux sanguin en toutes circonstances. Par ailleurs, les artères et artérioles sont sujettes à l'expansion alors que les artères musculaires dont le rôle principal est la résistance au flux sanguin sont relativement moins enclines à l'expansion que les artères élastiques. Très peu d'études expérimentales ont été menées pour extraire les propriétés mécaniques des parois vasculaires en raison des restrictions légales liées à l'expérimentation sur les tissus humains, des limitations éthiques et des manipulations extrêmement délicates requises. De telles expérimentations sont d'autant plus complexifiées par les variations anatomiques et biochimiques d'un spécimen à l'autre ainsi que par la sensibilité accrue des tissus mous biologiques. Ceci explique la rareté des données relatives aux propriétés mécaniques des parois artérielles humaines dans la littérature. À l'échelle microscopique, les parois artérielles sont une structure fibreuse dont les fibres sont orientées et distribuées différemment, un caractère judicieusement décrit par le formalisme anisotrope. Cependant, selon l'orientation et la distribution des fibres et surtout selon l'application en question, la paroi artérielle pourrait être considérée comme homogène et isotrope. Les parois artérielles sont non-linéaires en raison de leur structure physiologique et de leur capacité à subir de grandes déformations. Similairement aux GRs et aux protéines, les parois artérielles ont la capacité de s'écrouir, empêchant ainsi leur rupture dans certaines conditions comme l'hypertension artérielle. Comme pour les membranes déformables, l'élasticité artérielle est décrite dans le cadre théorique de l'hyperélasticité. À notre connaissance, les données expérimentales sur les propriétés mécaniques des artérioles humaines font défaut dans la littérature. D'un point de vue physiologique, la paroi artériolaire pourrait être considérée comme une paroi monocouche. Plus précisément, les constituants artériolaires s'avèrent être fonctionnellement interdépendants et dynamiquement interconnectés, rendant ainsi les frontières séparant les couches artériolaires confuses. Cette particularité est confirmée par les physiologistes qui considèrent que la paroi des plus petites artérioles se limite à une seule couche intimale incomplète composée de cellules lisses. En ce qui concerne leur réponse mécanique au flux sanguin, les artérioles révèlent des capacités de distensibilité qui sont moins importantes par rapport aux grandes artères. Le sang humain est une suspension de cellules appelées éléments figurés dans un liquide aqueux jaunâtre (le plasma sanguin). Les éléments figurés sont les GRs (majoritaires), les leucocytes (globules blancs) et les thrombocytes (plaquettes). Les propriétés rhéologiques du sang dont la rhéofluidification, la thixotropie et

la viscoélasticité sont déterminées par les propriétés mécaniques inhérentes des éléments figurés mais également par les interactions inter-intracellulaires. La rhéofluidification est une conséquence du processus d'agrégation et de désagrégation des GRs contrôlé par le taux de cisaillement. En effet, pour de faibles taux de cisaillement, les GRs s'agglomèrent et forment de longues structures appelées rouleaux qui se désagrègent lorsque le taux de cisaillement augmente. En conséquence, la viscosité sanguine augmente pendant l'agrégation et diminue pendant la désagrégation. Il est admis que l'écoulement sang est laminaire à $Re<$ 2000 et turbulent à $Re>$3000. Cependant, la turbulence peut apparaître localement (et occasionnellement) comme dans les artères sténosées. L'étude de l'interaction cellulaire des composants du sang ainsi que des propriétés hémodynamiques et hémorhéologiques à une échelle micrométrique nécessite un modèle d'écoulement multiphasique. Néanmoins, l'hypothèse d'un fluide homogène monophasique est acceptable dans certains cas et permet de s'affranchir de la variation de l'hématocrite (pourcentage de GRs par rapport au volume sanguin total).

Pour résoudre le problème d'interaction fluide-structure, plusieurs méthodes numériques peuvent être utilisées. La plus populaire est sans doute la méthode des frontières immergées IBM, une méthode à maillage non conforme introduite à l'origine pour décrire l'interaction entre les valves cardiaques et le flux sanguin. La méthode IBM traite la membrane comme une fibre élastique formée par une série de marqueurs lagrangiens à masse nulle immergés dans un maillage eulérien à travers lequel s'écoule le domaine fluide. La membrane peut se déplacer à travers le maillage fixe. La méthode IBM n'est compatible qu'avec des membranes très fines et avec des écoulements visqueux. De plus, la membrane n'est pas traitée comme une entité physique mais est approximée à l'aide de fonctions de Dirac. Le domaine fluide est généralement résolu par la méthode des différences finies ou par la méthode de lattice Boltzmann tandis que la force élastique de la membrane est généralement obtenue par la méthode des éléments finis. Alternativement, la méthode ALE pourrait être utilisée pour remédier aux limites de la méthode IBM. Il s'agit d'une méthode à maillage conforme qui implique un remaillage continu. Il n'y a aucune restriction ni sur l'inertie de la membrane ni sur celle du fluide. Le maillage peut se déplacer pour suivre la déformation et le déplacement de la frontière immergée. La méthode ALE combine les avantages de la description purement eulérienne et de la description purement lagrangienne. Dans ce travail, la discrétisation temporelle suit le schéma d'Euler retardé d'ordre 2. Les variables sont approximées par la méthode de Newton amortie ayant la propriété de convergence globale.

Pour l'ensemble des calculs effectués, les résultats obtenus sont en concordance avec la littérature

(lorsque la comparaison est possible) et reflètent des propriétés dynamiques très similaires à celles des GRs. Parmi les résultats les plus importants figure le rôle majeur de l'hyperélasticité artériolaire dans le processus de migration latérale. En effet, nous avons montré que la paroi déformable induit une force d'aspiration qui s'oppose à la portance, entravant ainsi la migration latérale des microparticules. Cette force d'aspiration est sensible au rapport des viscosités, à la résistance au cisaillement de la membrane et au confinement, ce qui rend la migration latérale encore plus complexe. En outre, l'hyperélasticité vasculaire s'avère avoir une influence significative sur la dynamique individuelle des microparticules ainsi que sur les interactions hydrodynamiques interparticulaires. Par ailleurs, nous avons montré que la prédiction de la branche préférée des microparticules circulant dans une bifurcation coronarienne est possible dans une certaine mesure. Toujours au niveau de la bifurcation, de nombreux modes de déformation inédits ont été observés, en plus de la capture des microparticules dans les tourbillons formés aux branches ascendante et descendante. Enfin, une contribution et pas des moindres, concerne la proposition d'une méthode de résolution qui permet de renforcer la convergence à un coût de calcul raisonnable.

Bibliography

[1] Dolçà C, Ferrándiz M, Capablanca L, Franco E, Mira E, López F, García D. 2015 Microencapsulation of rosemary essential oil by co-extrusion/gelling using alginate as a wall material. *Journal of Encapsulation and Adsorption Sciences* **05**, 03, 121–130. (doi:10.4236/jeas.2015.53010).

[2] Giri TK. 2016 Alginate containing nanoarchitectonics for improved cancer therapy. In: *Nanoarchitectonics for Smart Delivery and Drug Targeting*, pp. 565–588. William Andrew Publishing. (doi:https://doi.org/10.1016/B978-0-323-47347-7.00020-3).

[3] Hawkins S, Wolf M, Guyard G, Greenberg S, Dayan N. 2005 Microcapsules as a delivery system. In: *Delivery System Handbook for Personal Care and Cosmetic Products*, pp. 191–213. William Andrew Publishing. (doi:https://doi.org/10.1016/B978-081551504-3.50014-6).

[4] Soon-Shiong P. 1999 Treatment of type I diabetes using encapsulated islet. *Advanced Drug Delivery Reviews* **35**, 259–270. (doi:10.1016/s0169-409x(98)00076-3).

[5] Mihalko E, Huang K, Sproul E, Cheng K, Brown AC. 2018 Targeted treatment of ischemic and fibrotic complications of myocardial infarction using a dual-delivery microgel therapeutic. *ACS Nano* **12**, 8, 7826–7837. (doi:10.1021/acsnano.8b01977).

[6] Ashrafi K, Tang Y, Britton H, Domenge O, Blino D, Bushby AJ, Shuturminska K, den Hartog M, Radaelli A, Negussie AH, *et al.* 2017 Characterization of a novel intrinsically radiopaque Drug-eluting Bead for image-guided therapy: DC Bead LUMI™. *Journal of Controlled Release* **250**, 36–47. (doi:10.1016/j.jconrel.2017.02.001).

[7] Ma J, Du LF, Chen M, Wang HH, Xing LX, Jing LF, Li YH. 2013 Drug-loaded nano-microcapsules delivery system mediated by ultrasound-targeted microbubble destruction: A promising therapy method. *Biomedical Reports* **1**, 506–510. (doi:10.3892/br.2013.110).

[8] Bilbao J, Martínez-Cuesta A, Urtasun F, Cosín O. 2006 Complications of embolization. *Seminars in Interventional Radiology* **23**, 126–142. (doi:10.1055/s-2006-941443).

[9] Urry DW. 1988 Entropic elastic processes in protein mechanisms. i. elastic structure due to an inverse temperature transition and elasticity due to internal chain dynamics. *J Protein Chem* **7**, 1–34. (doi:10.1007/BF01025411).

[10] Gardel ML, Shin JH, MacKintosh FC, Mahadevan L, Matsudaira P, Weitz DA. 2004 Elastic behavior of cross-linked and bundled actin networks. *Science* **304**, 5675, 1301–1305. (doi:10.1126/science.1095087).

[11] Marckmann G, Verron E, Gornet L, Chagnon G, Charrier P, Fort P. 2002 A theory of network alteration for the Mullins effect. *Journal of the Mechanics and Physics of Solids* **50**, 2011–2028. (doi:10.1016/S0022-5096(01)00136-3).

[12] Jaspers M, Dennison M, Mabesoone MFJ, MacKintosh FC, Rowan AE, Kouwer PHJ. 2014 Ultra-responsive soft matter from strain-stiffening hydrogels. *Nature Communications* **5**. (doi:10.1038/ncomms6808).

[13] Lee H, Ferrer JM, Lang MJ, Kamm RD. 2010 Molecular origin of strain softening in cross-linked F-actin networks. *Physical Review E - Statistical, Nonlinear, and Soft Matter Physics* **82**, 1, 1–9. (doi:10.1103/PhysRevE.82.011919).

[14] Saint-Michel B, Gibaud T, Manneville S. 2017 Predicting and assessing rupture in protein gels under oscillatory shear. *Soft Matter* **13**, 14, 2643–2653. (doi:10.1039/C7SM00064B).

[15] Ingber DE. 1997 Tensegrity: the architectural basis of cellular mechanotransduction. *Annual Review of Physiology* **59**, 1, 575–599. (doi:10.1146/annurev.physiol.59.1.575).

[16] Motte S, Kaufman LJ. 2013 Strain stiffening in collagen I networks. *Biopolymers* **99**, 1, 35–46. (doi:10.1002/bip.22133).

[17] Sun YL, Luo ZP, Fertala A, AN KN. 2004 Stretching type II collagen with optical tweezers. *Journal of Biomechanics* **37**, 11, 1665–1669. (doi:10.1016/j.jbiomech.2004.02.028).

[18] Storm C, Pastore JJ, MacKintosh FC, Lubensky T, Janmey PA. 2005 Nonlinear elasticity in biological gels. *Nature* **435**, 7039, 191–194. (doi:10.1038/nature03521).

[19] Gardel ML, Shin JH, MacKintosh FC, Mahadevan L, Matsudaira P, Weitz DA. 2004 Elastic behavior of cross-linked and bundled actin networks. *Science* **304**, 1301–1305. (doi:10.1126/science.1095087).

[20] Zhang Y, Huang C, Kim S, Golkaram M, Dixon WAM, Tilley L, Li J, Zhang S, Suresh S. 2015 Multiple stiffening effects of nanoscale knobs on human red blood cells infected with Plasmodium falciparum malaria parasite. *Proceedings of the National Academy of Sciences of the United States of America* **112**, 19, 6068–6073. (doi:10.1073/pnas.1505584112).

[21] Xu J, Tseng Y, Wirtz D. 2000 Strain Hardening of Actin Filament Networks **275**, 46, 35886–35892. (doi:10.1074/jbc.M002377200).

[22] Mooney M. 1940 A theory of large elastic deformation. *Journal of Applied Physics* **11**, 9, 582–592. (doi:10.1063/1.1712836).

[23] Rivlin RS. 1948 Large elastic deformations of isotropic materials iv. further developments of the general theory. *Philosophical Transactions of the Royal Society of London* **241**, 379–397. (doi:10.1098/rsta.1948.0024).

[24] Russo S, Aggarwal SL, Allen SG. 1996 *Comprehensive polymer science*. Pergamon, 2nd ed.

[25] Treloar LRG. 1943 The elasticity of a network of long-chain molecules—ii. *Trans. Faraday Society* **39**, 241–246. (doi:10.1039/TF9433900241).

[26] Boyce MC, Arruda EM. 2000 Constitutive models of rubber elasticity: A review. *Rubber Chemistry and Technology* **73**, 504–523.

[27] Gent AN. 1996 A new constitutive relation for rubber. *Rubber Chemistry and Technology* **69**, 1, 59–61. (doi:10.5254/1.3538357).

[28] Ogden RW. 1973 Large deformation isotropic elasticity - on the correlation of theory and experiment for incompressible rubberlike solids. *Rubber Chemistry and Technology* **46**, 2, 398–416. (doi:10.5254/1.3542910).

[29] Rooij RD, Kuhl E. 2016 Constitutive modeling of brain tissue: current perspectives. *Applied Mechanics Reviews* **68**. (doi:10.1115/1.4032436).

[30] Arruda EM, Boyce MC. 1993 A three-dimensional constitutive model for the large stretch behavior of rubber elastic materials. *Journal of the Mechanics and Physics of Solids* **41**, 2, 389–412. (doi:10.1016/0022-5096(93)90013-6).

[31] Skalak R, Tozeren A, Zarda RP, Chien S. 1973 Strain Energy Function of Red Blood Cell Membranes. *Biophysical Journal* **13**, 3, 245–264. (doi:10.1016/S0006-3495(73)85983-1).

[32] Hochmuth RM, Mohandas N. 1972 Uniaxial loading of the red-cell membrane. *Journal of Biomechanics* **5**, 5. (doi:10.1016/0021-9290(72)90007-3).

[33] Loubens CD, Deschamps J, Georgelin M, Charrier A, Edwards-Levy F, Leonetti M. 2014 Mechanical characterization of cross-linked serum albumin microcapsules. *Soft Matter* **10**, 25, 4561–4568. (doi:10.1039/c4sm00349g).

[34] Husmann M, Rehage H, Dhenin E, Barthès-Biesel D. 2005 Deformation and bursting of nonspherical polysiloxane microcapsules in a spinning-drop apparatus. *Journal of Colloid and Interface Science* **282**, 1, 109–119. (doi:10.1016/j.jcis.2004.08.129).

[35] Leick S, Henning S, Degen P, Suter D, Rehage H. 2010 Deformation of liquid-filled calcium alginate capsules in a spinning drop apparatus. *Physical Chemistry Chemical Physics* **12**, 12, 2950–2958. (doi:10.1039/b921116k).

[36] Pieper G, Rehage H, Barthès-Biesel D. 1998 Deformation of a capsule in a spinning drop apparatus. *Journal of Colloid and Interface Science* **202**, 2, 293–300. (doi:https://doi.org/10.1006/jcis.1998.5438).

[37] Rachik M, Barthes-Biesel D, Carin M, Edwards-Levy F. 2006 Identification of the elastic properties of an artificial capsule membrane with the compression test: Effect of thickness. *Journal of Colloid and Interface Science* **301**, 1, 217–226. (doi:10.1016/j.jcis.2006.04.062).

[38] Chang KS, Olbricht WL. 1993 Experimental studies of the deformation of a synthetic capsule in extensional flow. *Journal of Fluid Mechanics* **250**. (doi:10.1017/S0022112093001570).

[39] Hu XQ, Sévénié B, Salsac AV, Leclerc E, Barthès-Biesel D. 2013 Characterizing the membrane properties of capsules flowing in a square-section microfluidic channel: Effects of the membrane

constitutive law. *Physical Review E - Statistical, Nonlinear, and Soft Matter Physics* **87**, 6. (doi:10.1103/PhysRevE.87.063008).

[40] Lefebvre Y, Leclerc E, Barthès-Biesel D, Walter J, Edwards-Lévy F. 2008 Flow of artificial microcapsules in microfluidic channels: A method for determining the elastic properties of the membrane. *Physics of Fluids* **20**, 12. (doi:10.1063/1.3054128).

[41] Carin M, Barthès-Biesel D, Edwards-Lévy F, Postel C, Andrei DC. 2003 Compression of biocompatible liquid-filled HSA-alginate capsules: Determination of the membrane mechanical properties. *Biotechnology and Bioengineering* **82**, 2, 207–212. (doi:10.1002/bit.10559).

[42] Kleinberger RM, Burke NAD, Dalnoki-Veress K, Stöver HDH. 2013 Systematic study of alginate-based microcapsules by micropipette aspiration and confocal fluorescence microscopy. *Materials Science and Engineering C* **33**, 7, 4295–4304. (doi:10.1016/j.msec.2013.06.033).

[43] Olbricht WL. 1993 Experimental studies of the deformation of a synthetic capsule in extensional flow. *Journal of Fluid Mechanics* **250**, 587–608. (doi:10.1017/S0022112093001570).

[44] Hwang MY, Kim SG, Lee HS, Muller SJ. 2018 Elastic particle deformation in rectangular channel flow as a measure of particle stiffness. *Soft Matter* (doi:10.1039/c7sm01829k).

[45] Hu XQ, Salsac AV, Barthès-Biesel D. 2012 Flow of a spherical capsule in a pore with circular or square cross-section. *Journal of Fluid Mechanics* **705**, 176–194. (doi:10.1017/jfm.2011.462).

[46] Chu TX, Salsac AV, Leclerc E, Barthès-Biesel D, Wurtz H, Edwards-Lévy F. 2011 Comparison between measurements of elasticity and free amino group content of ovalbumin microcapsule membranes: Discrimination of the cross-linking degree. *Journal of Colloid and Interface Science* **355**, 1, 81–88. (doi:10.1016/j.jcis.2010.11.038).

[47] Li XZ, Barthes-Biesel D, Helmy A. 1988 Large deformations and burst of a capsule freely suspended in an elongational flow. *Journal of Fluid Mechanics* **187**, 179–196. (doi:10.1017/S0022112088000394).

[48] Risso F, Collé-Paillot F, Zagzoule M. 2006 Experimental investigation of a bioartificial capsule flowing in a narrow tube. *Journal of Fluid Mechanics* **547**, 149–173. (doi:10.1017/S0022112005007652).

[49] Knoche S, Kierfeld J. 2011 Buckling of spherical capsules. *Physical Review E - Statistical, Nonlinear, and Soft Matter Physics* **84**. (doi:10.1103/PhysRevE.84.046608).

[50] Mohandas N, Gallagher PG. 2008 Red cell membrane: past, present, and future **112**, 3939–3948. (doi:10.1182/blood-2008).

[51] Elgsaeter A, Stokke BT, Mikkelsen A, Branton D. 1986 The molecular basis of erythrocyte shape. *Science* **234**, 4781, 1217–1223. (doi:10.1126/science.3775380).

[52] Canham PB. 1970 The minimum energy of bending as a possible explanation of the biconcave shape of the human red blood cell. *Journal of Theoretical Biology* **26**, 61–81. (doi:10.1016/s0022-5193(70)80032-7).

[53] Uzoigwe C. 2006 The human erythrocyte has developed the biconcave disc shape to optimise the flow properties of the blood in the large vessels. *Medical Hypotheses* **67**, 1159–1163. (doi:10.1016/j.mehy.2004.11.047).

[54] Hochmuth RM. 2000 Micropipette aspiration of living cells. *Journal of Biomechanics* **33**, 15–20. (doi:10.1016/S0021-9290(99)00175-X).

[55] Evans EA, Waugh R, Melnik L. 1976 Elastic area compressibility modulus of red cell membrane. *Biophysical Journal* **16**, 585–595. (doi:10.1016/S0006-3495(76)85713-X).

[56] Hansen JC, Skalak R, Chien S, Hoger A. 1996 An elastic network model based on the structure of the red blood cell membrane skeleton. *Biophysical Journal* **70**, 146–166. (doi:10.1016/S0006-3495(96)79556-5).

[57] Lenormand G, Hénon S, Richert A, Siméon J, Gallet F. 2003 Elasticity of the human red blood cell skeleton. *Biorheology* **40**, 247–251.

[58] Hansen JC, Skalak R, Chien S, Hoger A. 1997 Influence of network topology on the elasticity of the red blood cell membrane skeleton. *Biophysical Journal* **72**, 5, 2369–2381. (doi:10.1016/S0006-3495(97)78882-9).

[59] Skalak R, Branemark PI. 1969 Deformation of red blood cells in capillaries. *Science* pp. 717–719. (doi:10.1126/science.164.3880.717).

[60] Hochmuth RM, Buxbaum KL, Evans EA. 1980 Temperature dependence of the viscoelastic recovery of red cell membrane. *Biophysical Journal* **29**, 1, 177–182.

[61] Dintenfass L. 1968 Internal viscosity of the red cell and a blood viscosity equation. *Nature* **219**, 5157, 956–958. (doi:10.1038/219956a0).

[62] Hwang WC, Waugh RE. 1997 Energy of dissociation of lipid bilayer from the membrane skeleton of red blood cells. *Biophysical Journal* **72**, 149–173. (doi:10.1016/S0006-3495(97)78910-0).

[63] Waugh R, Evans EA. 1979 Thermoelasticity of red blood cell membrane. *Biophysical Journal* **26**, 1, 115–131. (doi:10.1016/S0006-3495(79)85239-X).

[64] Meiselman HJ, Evans EA, Hochmuth RM. 1978 Membrane mechanical properties of atp-depleted human erythrocytes. *Blood* **52**, 499–504. (doi:https://doi.org/10.1182/blood.V52.3.499.499).

[65] Dulińska I, Targosz M, Strojny W, Lekka M, Czuba P, Balwierz W, Szymoński M. 2006 Stiffness of normal and pathological erythrocytes studied by means of atomic force microscopy. *Journal of Biochemical and Biophysical Methods* **66**, 1–11. (doi:10.1016/j.jbbm.2005.11.003).

[66] Fedosov DA. 2010 *Multiscale modeling of blood flow and soft matter*. Ph.D. thesis, Brown University.

[67] Peng Z, Asaro RJ, Zhu Q. 2010 Multiscale simulation of erythrocyte membranes. *Physical Review E - Statistical, Nonlinear, and Soft Matter Physics* **81**, 3. (doi:10.1103/PhysRevE.81.031904).

[68] Knoche S, Kierfeld J. 2014 Osmotic buckling of spherical capsules. *Soft Matter* **10**, 41, 8358–8369. (doi:10.1039/c4sm01205d).

[69] Tsekov R, Stukan MR, Vinogradova OI. 2008 Osmotic pressure acting on a semipermeable shell immersed in a solution of polyions. *Journal of Chemical Physics* **129**, 24, 1–9. (doi:10.1063/1.3046679).

[70] Kuriakose S, Dimitrakopoulos P. 2013 Deformation of an elastic capsule in a rectangular microfluidic channel. *Soft Matter* **9**, 16, 4284–4296. (doi:10.1039/c3sm27683j).

[71] Farutin A, Misbah C. 2013 Analytical and numerical study of three main migration laws for vesicles under flow. *Physical Review Letters* **110**, 10. (doi:10.1103/PhysRevLett.110.108104).

[72] Vlahovska PM, Podgorski T, Misbah C. 2009 Vesicles and red blood cells in flow: From individual dynamics to rheology. *Comptes Rendus Physique* **10**, 775–789. (doi:10.1016/j.crhy.2009.10.001).

[73] Kaoui B, Tahiri N, Biben T, Ez-Zahraouy H, Benyoussef A, Biros G, Misbah C. 2011 Complexity of vesicle microcirculation. *Physical Review E - Statistical, Nonlinear, and Soft Matter Physics* **84**, 4. (doi:10.1103/PhysRevE.84.041906).

[74] Noguchi H, Gompper G. 2005 Shape transitions of fluid vesicles and red blood cells in capillary flows. *Proceedings of the National Academy of Sciences* **102**, 14159–14164. (doi:10.1073/pnas.0504243102).

[75] Barthès-Biesel D. 2009 Capsule motion in flow: Deformation and membrane buckling. *Comptes Rendus Physique* **10**, 8, 764–774. (doi:10.1016/j.crhy.2009.09.004).

[76] Dupont C, Salsac AV, Barthès-Biesel D. 2013 Off-plane motion of a prolate capsule in shear flow. *Journal of Fluid Mechanics* **721**, 180–198. (doi:10.1017/jfm.2013.62).

[77] Kessler S, Finken R, Seifert U. 2008 Swinging and tumbling of elastic capsules in shear flow. *Journal of Fluid Mechanics* **605**, 207–226. (doi:10.1017/S0022112008001493).

[78] Misbah C. 2006 Vacillating breathing and tumbling of vesicles under shear flow. *Physical Review Letters* **96**, 2. (doi:10.1103/PhysRevLett.96.028104).

[79] Warkiani ME, Khoo BL, Tan DSW, Baghat AAS, Irwin D, Lau DP, Lim AST, Yap YS, Lee SC, Soo RA, *et al.* 2014 Clinical validation of an ultra high-throughput spiral microfluidics for the detection and enrichment of viable circulating tumor cells. *Plos One* **9**, 1–7. (doi:10.1371/journal.pone.0099409).

[80] Browne AW. 2011 A lab-on-a-chip for rapid blood separation and quantification of hematocrit and serum analytes. *Lab on a Chip* **11**, 14, 2440–2446. (doi:10.1039/c1lc20144a).

[81] Carlo DD, Irimia D, Tompkins RG, Toner M. 2007 Continuous inertial focusing, ordering, and separation of particles in microchannels. *Proceedings of the National Academy of Sciences* **104**, 48, 18892–18897. (doi:10.1073/PNAS.0704958104).

[82] Schaaf C, Stark H. 2017 Inertial migration and axial control of deformable capsules. *Soft Matter* **13**, 3544–3555.

[83] Doddi SK, Bagchi P. 2008 Lateral migration of a capsule in a plane poiseuille flow in a channel. *Lab ob a Chip* **34**, 10, 966–986.

[84] He L, Luo Z, Liu WR, Bai B. 2017 Capsule equilibrium positions near channel center in poiseuille flow. *Chemical Engineering Science* **172**, 23, 603–611.

[85] Amini H, Lee W, Carlo DD. 2014 Inertial microfluidic physics. *Lab on a Chip* **14**, 2739–2761.

[86] Li H, Ma G. 2010 Modeling performance of a two-dimensional capsule in a microchannel flow: Long-term lateral migration. *Physical Review E* **82**, 1–14.

[87] Nix S, Imai Y, Ishikawa T. 2016 Lateral migration of a capsule in a parabolic flow. *Journal of Biomechanics* **49**, 11, 2249–2254.

[88] Coclite A, Ranaldo S, Tullio MD, Decuzzi P, Pascazio G. 2019 Kinematic and dynamic forcing strategies for predicting the transport of inertial capsules via a combined lattice boltzmann - immersed boundary method. *Computers and Fluids* **180**, 41–53. (doi:10.1016/j.compfluid.2018.12.014).

[89] Kaoui B, Biros G, Misbah C. 2009 Why do red blood cells have asymmetric shapes even in a symmetric flow? *Physical Review Letters* **103**, 18. (doi:10.1103/PhysRevLett.103.188101).

[90] Hariprasad DS, Secomb TW. 2015 Prediction of noninertial focusing of red blood cells in poiseuille flow. *Physical Review E* **92**, 3. (doi:10.1103/PhysRevE.92.033008).

[91] Holzapfel GA, Sommer G, Gasser CT, Regitnig P. 2005 Determination of layer-specific mechanical properties of human coronary arteries with nonatherosclerotic intimal thickening and related constitutive modeling. *American Journal of Physiology-Heart and Circulatory Physiology* **289**, 5, 2048–2058. (doi:10.1152/ajpheart.00934.2004).

[92] Holzapfel GA, Gasser TC, Ogden RW. 2000 A new constitutive framework for arterial wall mechanics and a comparative study of material models. *Journal of Elasticity* **61**, 1–48. (doi:10.1023/A:1010835316564).

[93] Delfino A, Stergiopulos N, Moore JE, Meister JJ. 1997 Residual strain effects on the stress field in a thick wall finite element model of the human carotid bifurcation. *Journal of Biomechanics* **30**, 8, 777–786. (doi:https://doi.org/10.1016/S0021-9290(97)00025-0).

[94] Carmines DV, McElhaney JH, Stack R. 1991 A piece-wise non-linear elastic stress expression of human and pig coronary arteries tested in vitro. *Journal of Biomechanics* **24**, 10, 899–906. (doi:https://doi.org/10.1016/0021-9290(91)90168-M).

[95] Gholipour A, Ghayesh MH, Zander A, Mahajan R. 2018 Three-dimensional biomechanics of coronary arteries. *International Journal of Engineering Science* **130**, 93–114. (doi:10.1016/j.ijengsci.2018.03.002).

[96] Watton PN, Ventikos Y, Holzapfel GA. 2009 Modelling the mechanical response of elastin for arterial tissue. *Journal of Biomechanics* **42**, 9, 1320–1325. (doi:10.1016/j.jbiomech.2009.03.012).

[97] Volokh KY. 2007 Hyperelasticity with softening for modeling materials failure. *Journal of the Mechanics and Physics of Solids* **55**, 10, 2237–2264. (doi:10.1016/j.jmps.2007.02.012).

[98] Martinez-Lemus LA. 2012 The dynamic structure of arterioles **110**, 5–11. (doi:10.1111/j.1742-7843.2011.00813.x).

[99] Biga LM, Dawson S, Harwell A, Hopkins R, Kaufmann J, Lemaster M, Matern P, Morrison-Graham K, Quick D, Runyeon J *Anatomy & Physiology.* Openstax/Oregon State University.

[100] Miura H, Wachtel RE, Liu Y, Loberiza FR, Saito T, Miura M, Gutterman DD. 2001 Flow-Induced Dilation of Human Coronary Arterioles Important Role of Ca 2-Activated K Channels. *Circulation* **103**, 1992–1998.

[101] Miller FJ, Dellsperger KC, Gutterman DD. 1997 Myogenic constriction of human coronary arterioles. *American Journal of Physiology-Heart and Circulatory Physiology* **273**, 257–264. (doi:10.1152/ajpheart.1997.273.1.H257).

[102] Whitmore RL. 1968 *Rheology of the circulation.* Oxford, New York, Pergamon Press.

[103] Huang CR, Fabisiak W. 1976 Thixotropic parameters of whole human blood. *Thrombosis Research* **8**, 1–8. (doi:10.1016/0049-3848(76)90041-4).

[104] Thurston GB. 1972 Viscoelasticity of Human Blood. *Biophysical Journal* **12**, 9, 1205–1217. (doi:10.1016/S0006-3495(72)86156-3).

[105] S Chien S. 1970 Shear dependence of effective cell volume as a determinant of blood viscosity. *Science* **168**, 977–979. (doi:10.1126/science.168.3934.977).

[106] de Morales-Marinkovic MP, Turner KT, Butler JP, Fredberg JJ, , Suresh S. 2007 Viscoelasticity of the human red blood cell. *American Journal of Physiology-Cell Physiology* **293**, 597–605. (doi:10.1152/ajpcell.00562.2006).

[107] Barrett KE, Barman SM, Boitano S, Brooks H. 2012 *Ganong's Review of Medical Physiology.* McGraw Hill Medicall.

[108] Ku DN. 1997 Blood Flow in Arteries. *Annual Review of Fluid Mechecanics* **29**, 399–434. (doi:10.1146/annurev.fluid.29.1.399).

[109] Tan J, Keller W, Sohrabi S, Yang J, Liu Y. 2016 Characterization of nanoparticle dispersion in red blood cell suspension by the lattice boltzmann-immersed boundary method. *Nanomaterials* **6**, 2, 12–16. (doi:10.3390/nano6020030).

[110] Boyle J. 1988 Microcirculatory hematocrit and blood flow. *Journal of Theoretical Biology* **131**, 2, 223–229. (doi:10.1016/S0022-5193(88)80238-8).

[111] Gabriel SA, Ding Y, Feng Y, Gear J. 2014 Comparative analysis of pulsatile and steady flow on arterial mass transport. In: *19th Australasian Fluid Mechanics Conference.*

[112] Frank O. 1899 Die grundform des arteriellen pulses (the basic form of the arterial pulse). *Zeitschrift für Biologie* **37**, 483–526.

[113] Frank O. 1930 Schätzung des schlagvolumens des menschlichen herzens auf grund der wellen-und windkesseltheorie. *Zeitschrift für Biologie* **90**, 405–409.

[114] Womersley JR. 1955 Method for the calculation of velocity, rate of flow and viscous drag in arteries when the pressure gradient is known. *The Journal of physiology* **127**, 3, 553–563. (doi:10.1113/jphysiol.1955.sp005276).

[115] Womersley JR. 1955 XXIV. Oscillatory motion of a viscous liquid in a thin-walled elastic tube—I: The linear approximation for long waves. *The London, Edinburgh, and Dublin Philosophical Magazine and Journal of Science* **46**, 199–221. (doi:10.1080/14786440208520564).

[116] Womersley JR. 1957 An elastic tube theory of pulse transmission and oscillatory flow in mammalian arteries. Tech. rep., Aeronautical Research Laboratory.

[117] Bénard N. 2005 *Analyse de l'écoulement physiologique dans un stent coronarien : Application à la caractérisation des zones de resténose pariétale.* Ph.D. thesis, Université de Poitiers.

[118] Chabi F, Champmartin S, Sarraf C, Noguera R. 2015 Critical evaluation of three hemodynamic models for the numerical simulation of intra-stent flows. *Journal of Biomechanics* **48**, 10, 1769–1776. (doi:10.1016/j.jbiomech.2015.05.011).

[119] Peskin CS. 1977 Numerical analysis of blood flow in the heart. *Journal of Computational Physics* **25**, 220–252. (doi:10.1109/icicic.2006.483).

[120] Yazdani AZK, Kalluri KM, Bagchi P. 2011 Tank-treading and tumbling frequencies of capsules and red blood cells. *Physical Review E - Statistical, Nonlinear, and Soft Matter Physics* **83**, 4, 569–595. (doi:10.1103/PhysRevE.83.046305).

[121] Wang Z, Sui Y, Salsac AV, Barthès-Biesel D, Wang W. 2016 Motion of a spherical capsule in branched tube flow with finite inertia. *Journal of Fluid Mechanics* **806**, 603–626. (doi:10.1017/jfm.2016.603).

[122] Sigüenza J, Mendez S, Ambard D, Dubois F, Jourdan F, Mozul R, Nicoud F. 2016 Validation of an immersed thick boundary method for simulating fluid–structure interactions of deformable membranes. *Journal of Computational Physics* **322**, 723–746. (doi:10.1016/j.jcp.2016.06.041).

[123] Hirt CW, Amsden AA, Cook JL. 1974 An arbitrary Lagrangian-Eulerian computing method for all flow speeds. *Journal of Computational Physics* **14**, 3, 227–253. (doi:10.1016/0021-9991(74)90051-5).

[124] Donea J, Giuliani S, Halleux JP. 1982 An arbitrary lagrangian-eulerian finite element method for transient dynamic fluid-structure interactions. *Computer Methods in Applied Mechanics and Engineering* **33**, 689–723. (doi:10.1016/0045-7825(82)90128-1).

[125] Donea J, Fasoli-Stella P, Giuliani S. 1977 Lagrangian and Eulerian finite element techniques for transient fluid-structure interaction problems. In: *Trans. 4th Int. Conf. on Structural Mechanics in Reactor Technology.*

[126] Villone MM, Greco F, Hulsen MA, Maffettone PL. 2014 Simulations of an elastic particle in Newtonian and viscoelastic fluids subjected to confined shear flow. *Journal of Non-Newtonian Fluid Mechanics* **210**, 47–55. (doi:10.1016/j.jnnfm.2014.05.003).

[127] Villone MM, Greco F, Hulsen MA, Maffettone PL. 2016 Numerical simulations of deformable particle lateral migration in tube flow of Newtonian and viscoelastic media. *Journal of Non-Newtonian Fluid Mechanics* **234**, 105–113. (doi:10.1016/j.jnnfm.2016.05.006).

[128] Villone MM. 2019 Lateral migration of deformable particles in microfluidic channel flow of Newtonian and viscoelastic media: a computational study. *Microfluidics and Nanofluidics* **23**. (doi:10.1007/s10404-019-2212-3).

[129] Cetin A, Sahin M. 2019 A monolithic fluid-structure interaction framework applied to red blood cells. *International Journal for Numerical Methods in Biomedical Engineering* **35**, 2. (doi:10.1002/cnm.3171).

[130] Gao T, Hu HH. 2009 Deformation of elastic particles in viscous shear flow. *Journal of Computational Physics* **228**, 6, 2132–2151. (doi:10.1016/j.jcp.2008.11.029).

[131] Ni A, Cheema TA, Park CW. 2015 Numerical study of RBC motion and deformation through microcapillary in alcohol plasma solution. *Open Journal of Fluid Dynamics* **5**, 01, 26–33. (doi:10.4236/ojfd.2015.51004).

[132] Turek S, Hron J. 2008 Numerical techniques for multiphase flow with liquid-solid interaction. In: *Oberwolfach Seminars*, vol. 37 of *Hemodynamical Flows : Modeling, Analysis and Simulation*, pp. 379–492. Birkhaüser Verlag Basel. (doi:10.1007/978-3-7643-7806-6).

[133] Donea J, Huerta A, Ponthot JP, Rodriguez-Ferran A. 2004 *Arbitrary Lagrangian-Eulerian Methods*, chap. 14. John Wiley & Sons, Ltd. (doi:10.1002/0470091355.ecm009).

[134] Souli M, Benson DJ. 2010 *Arbitrary Lagrangian Eulerian and Numerical Simulation-Fluid-structure Interaction*. ISTE-Wiley & sons.

[135] Bazilevs Y, Calo VM, Hughes TJR, Zhang Y. 2008 Isogeometric fluid-structure interaction: Theory, algorithms, and computations. *Computational Mechanics* **43**, 3–37. (doi:10.1007/s00466-008-0315-x).

[136] Thoutireddy P. 2003 *Variational Arbitrary Lagrangian Eulerian method.* Ph.D. thesis, California Institute of Technology. (doi:10.7907/DQT0-5104).

[137] dos Santos ND. 2013 *Numerical methods for fluid-structure interaction problems with valves.* Ph.D. thesis, Université Pierre et Marie Curie - Paris VI.

[138] Franck RM, Lazarus RB. 1964 Mixed eulerian-lagrangian method. *Methods in computational physics* **3**, 47–67.

[139] Kennedy JM, Belytschko TB. 1982 Theory and application of a finite element method for arbitrary Lagrangian-Eulerian fluids and structures. *Nuclear Engineering and Design* **68**, 2, 129–146. (doi:10.1016/0029-5493(82)90026-7).

[140] Souli M, Ouahsine A, Lewin L. 2000 ALE and fluid–structure interaction problems. *Computer Methods in Applied Mechanics and Engineering* **190**, 659–675. (doi:10.1016/S0045-7825(99)00432-6).

[141] Michler C, van Brummelen EH, Hulshoff SJ, Borst RD. 2003 The relevance of conservation for stability and accuracy of numerical methods for fluid-structure interaction. *Computer Methods in Applied Mechanics and Engineering* **192**, 4195–4215. (doi:10.1016/S0045-7825(03)00392-X).

[142] Piperno S, Farhat C. 2001 Partitioned procedures for the transient solution of coupled aeroelastic problems - part II: Energy transfer analysis and three-dimensional applications. *Computer Methods in Applied Mechanics and Engineering* **190**, 3147–3170. (doi:10.1016/S0045-7825(00)00386-8).

[143] Küttler U, Förster C, Wall WA. 2006 A solution for the incompressibility dilemma in partitioned fluid-structure interaction with pure dirichlet fluid domains. *Computational Mechanics* **38**, 4-5, 417–429. (doi:10.1007/s00466-006-0066-5).

[144] Chen L. 2014 A simple construction of a Fortin operator for the two dimensional Taylor-Hood element. *Computers and Mathematics with Applications* **68**, 10, 1368–1373. (doi:10.1016/j.camwa.2014.09.003).

[145] Winslow AM. 1967 Numerical Solution of the Quasilinear Triangle. *Journal of Computational Physics* **2**, 149–172. (doi:10.1016/0021-9991(66)90001-5).

[146] Knupp P. 1999 Winslow smoothing on two-dimensional unstructured meshes. *Engineering with Computers* **15**, 263–268. (doi:10.1007/s003660050021).

[147] Curtiss CF, Hirschfelder JO. 1952 Integration of Stiff Equations. *The Proceedings of the National Academy of Sciences* **38**, 3, 235–243. (doi:10.1073/pnas.38.3.235).

[148] Deuflhard P. 1974 A Modified Newton Method for the Solution of Ill-Conditioned Systems of Nonlinear Equations with Application to Multiple Shooting. *Numerische Mathematik* **22**, 289–315. (doi:10.1007/BF01406969).

[149] Dupont C, Salsac AV, Barthes-Biesel D, Vidrascu M, Tallec PL. 2015 Influence of bending resistance on the dynamics of a spherical capsule in shear flow. *Physics of Fluids* **27**. (doi:10.1063/1.4921247).

[150] Moore PK, Petzold LR. 1994 A stepsize control strategy for stiff systems of ordinary differential equations. *Applied Numerical Mathematics* **15**, 449–463. (doi:10.1016/0168-9274(94)00042-5).

[151] Cheema TA, Park CW. 2013 Numerical investigation of hyperelastic wall deformation characteristics in a micro-scale stenotic blood vessel. *Korea Australia Rheology Journal* **25**, 3, 121–127. (doi:10.1007/s13367-013-0012-y).

[152] M Jahangiri MS, Sadeghi MR. 2015 Numerical study of turbulent pulsatile blood flow through stenosed artery using fluid-solid interaction. *Computational and Mathematical Methods in Medicine* (doi:10.1155/2015/515613).

[153] Lewis AL, Dreher MR. 2012 Locoregional drug delivery using image-guided intra-arterial drug eluting bead therapy. *Journal of Controlled Release* **161**, 338–350. (doi:10.1016/j.jconrel.2012.01.018).

[154] Souli M, Zolesio JP. 1993 Shape derivative of discretized problems. *Computer Methods in Applied Mechanics and Engineering* **108**, 187–199. (doi:10.1016/0045-7825(93)90001-E).

[155] Yeoh OH. 1993 Some forms of the strain energy function for rubber. *Rubber Chemistry and Technology* **66**, 5, 754–771. (doi:10.5254/1.3538343).

Arts et Métiers Sciences et Technologies

Imane EL JIRARI

Computational study of dynamical behaviour of liquid-filled hyperelastic microparticles flowing under haemodynamical and vascular constraints

HESAM UNIVERSITÉ

Résumé : Cette thèse est dédiée à l'étude du comportement dynamique de microparticules à membrane hyperélastique chargées d'une substance liquide et soumises à des contraintes hémodynamiques et vasculaires. L'étude qui est basée sur une modélisation numérique suffisamment fidèle aux conditions physiologiques a pour but de combler le manque d'études sur la réponse mécanique de microparticules en écoulement dans des vaisseaux sanguins distensibles (hyperélastiques), en particulier dans une artériole et une artère coronaire. Les travaux menés dans le cadre de cette thèse ont contribué à l'étude de l'influence de la distensibilité vasculaire sur le mécanisme de migration latérale dans une artériole ainsi que sur le partitionnement de microparticules soumises à un écoulement pulsatile au niveau d'une bifurcation coronarienne. Le problème instationnaire d'interaction fluide-structure est résolu suivant le formalisme arbitrairement lagrangien eulérien.

Mots clés : Microparticule, interaction fluide-structure, paroi vasculaire, écoulement sanguin, hyperélasticité, modélisation numérique, microfluidique.

Abstract : In this thesis the dynamical behaviour of microparticles made of a thin hyperelastic membrane enclosing a liquid medium and subjected to haemodynamical solicitations is studied by means of physiologically and reasonably realistic numerical modelling. The aim is to fill the gap in studies addressing the mechanical response of microparticles flowing in distensible human blood vessels, particularly in arterioles and coronary arteries. Contributions of the present work include the appraisement of the influence of arteriolar distensibility on the mechanism of lateral migration in arteriole and on microparticles partitioning in a coronary bifurcation under the action of a pulsatile blood flow. Numerous physical quantities of interest are evaluated quantitatively and qualitatively over time. Considering the therapeutic context, the risk of clustering, adhesion to wall and premature burst are assessed. The unsteady fluid structure-interaction problem is solved within the Arbitrary Lagrangian Eulerian framework.

Keywords : Microparticle, fluid-structure interaction, vascular wall, blood flow, hyperelasticity, numerical modelling, microfluidics.